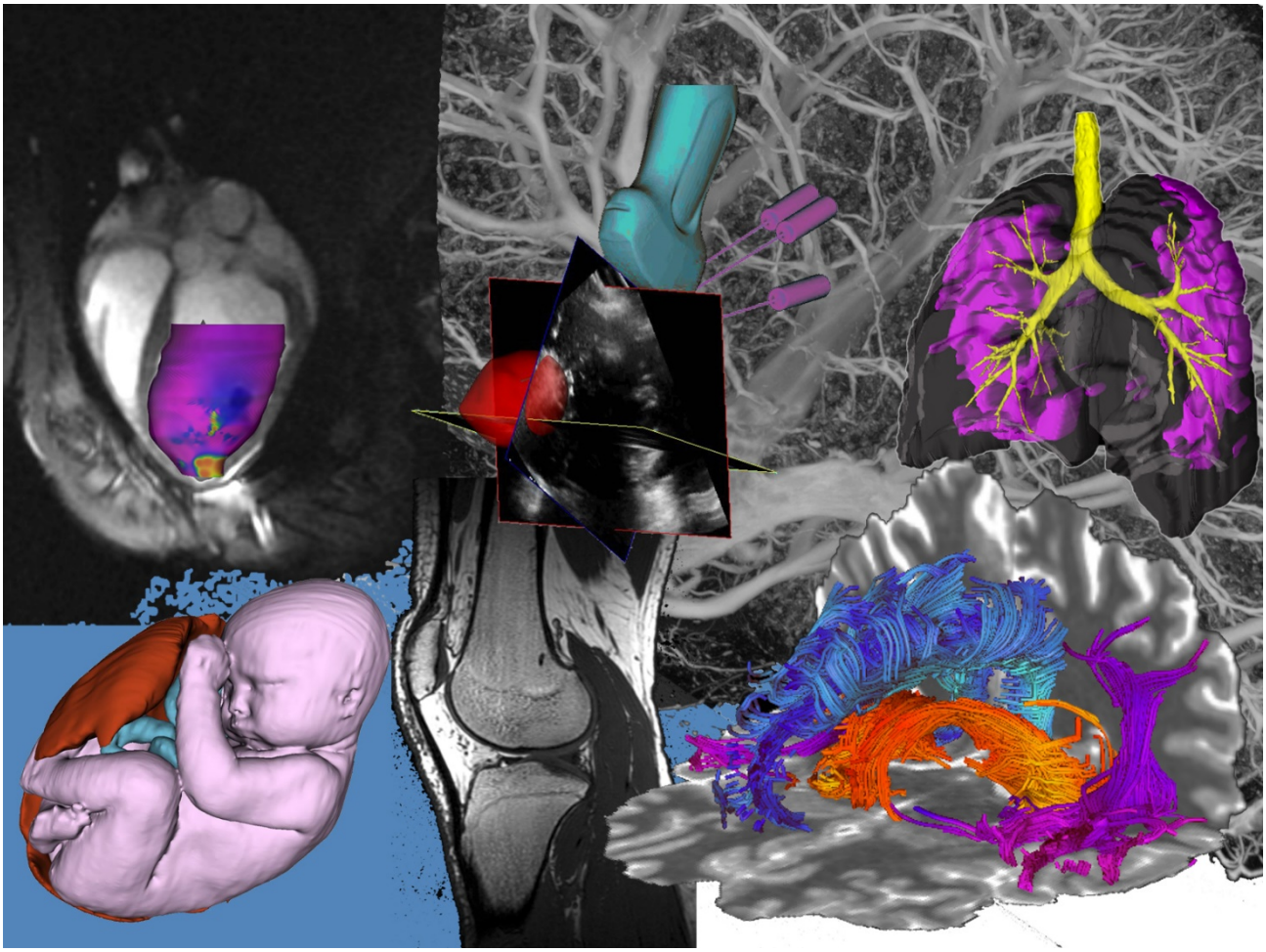

Proceedings of the

16th Annual Symposium

Imaging Network Ontario

March 28 – 29, 2018

Chestnut Residence and Conference Centre

Toronto, ON

Silver Sponsors

7D Surgical is a Toronto based company that develops advanced optical technologies and machine vision-based registration algorithms to improve surgical workflow and patient care. 7D Surgical's Machine-vision Image Guidance System (MvIGS) delivers profound improvement to workflows in spine surgery, providing the promise of future advancements in other surgical specialtie

ClaroNav (formerly Claron Technology), headquartered in Toronto, is dedicated to the development and global sales and marketing of surgical navigation solutions. Its current product line includes MicronTracker, an optical tracking system, Navident, the leading dental navigation system and NaviENT, a cranial navigation system.

GE Healthcare Tomorrow's MR, the SIGNA™ Premier, an advanced MR system equipped with innovative coil and gradient technology that directly links to cloud-based analytics. It's the future of MR technology and it's ready today. Visit us and see our latest in Air Coils live on the Exhibits floor!

Bronze Sponsor

NVIDIA's invention of the GPU in 1999 sparked the growth of the PC gaming market, redefined modern computer graphics and revolutionized parallel computing. More recently, GPU deep learning ignited modern AI — with the GPU acting as the brain of computers, robots and self-driving cars that can perceive and understand the world.

Academic Sponsor

Western University's **Bone and Joint Institute** aims for lifelong mobility by engaging in high-impact transdisciplinary research that will enhance active living, mobility and movement; investigate causes, prevention, diagnosis, and treatment options; and improve support systems and palliation for a wide range of MSK conditions.

Table of Contents

Welcome Letter

March 28, 2018

Dear ImNO 2018 Attendees:

Welcome to the Imaging Network Ontario (ImNO) 2018 Symposium. This year marks our 16th annual meeting.

ImNO is an initiative created in response to a request by the Ontario Research Development Challenge Fund – now the Ontario Research Fund – for assistance in harmonizing its investments in imaging research. The establishment of ImNO provides a means of harnessing and focusing the intellectual and innovative capabilities at Ontario universities in partnerships with emerging and established medical imaging companies to create a strong and sustainable internationally competitive imaging industry based on scientific excellence in Ontario.

Since its inception in 2003, the annual ImNO meeting has welcomed invited presentations from world-class scientists and proffered presentations from Ontario and across the county. This year, we are pleased to thank the five consortia for supporting our conference:

- Development of Novel Therapies for Bone and Joint Diseases;
- Heart Failure: Prevention through Early Detection Using New Imaging Methods;
- Imaging for Cardiovascular Device Intervention;
- Ontario Institute for Cancer Research Imaging Program; and
- NIH – NICHD Human Placenta Project – Hyperpolarized 13C MRI of Placental Metabolic Abnormalities Resulting from the Western Diet.

For the 2018 meeting, we received a total of 158 submitted abstracts that were reviewed by an average of 3 reviewers. The ImNO 2018 Scientific Committee then assembled the final program: 6 keynote speakers, 57 oral presentations and 103 poster presentations

In closing, we would like to acknowledge the significant contributions made by the members of the Scientific and Organizing Committees. Together they have worked very hard to bring us this year's meeting. We hope you enjoy this year's program and world-renowned keynote speakers.

Sincerely,

Anne Martel and Gabor Fichtinger
Co-Chairs, Scientific Committee, 2018 ImNO Symposium

Sponsoring Consortia

The Annual Meeting of Imaging Network Ontario (ImNO) promotes Canada's role as a leader in medical imaging innovation by cultivating synergy among consortia and partnerships between Ontario and other Canadian imaging entities.

The following consortia and programs supported the 2018 ImNO Symposium financially.

Development of Novel Therapies for Bone and Joint Diseases

Director: Dr. David Holdsworth **Ontario Research Fund**

Musculoskeletal disorders are the most common cause of severe long-term pain and physical disability, affecting hundreds of millions of people around the world. The economic burden is high; joint diseases cost the Ontario economy more than $2 billion per year. To reduce this disease burden, this Ontario Research Fund Research Excellence program focuses on the "Development of Novel Therapies for Bone and Joint Diseases," including improved diagnostic imaging techniques and new approaches for image-guided therapy. A multidisciplinary team of imaging scientists, biomedical engineers, physical therapists, and orthopaedic surgeons work together on key research projects, including the development of new ways to post-process 3D MRI and CT data to guide surgery, dynamic imaging of moving joints (under load), and image- based design of "patient-specific" orthopaedic components.

Heart Failure: Prevention through Early Detection Using New Imaging Methods

Director: Dr. Frank Prato **Ontario Research Fund**

Consortium partners: Lawson Health Research Institute, Sunnybrook Research Institute and University of Ottawa Heart Institute. Ten percent of Ontarians over 60 have heart failure. One quarter will die within one year of diagnosis and almost all in ten years. Our LHRI/SRI/UOHI consortium is developing combined PET and MRI imaging methods for early diagnosis when treatment is still possible. The imaging methods developed are being commercialized and will benefit Ontario by improving the health of its citizens and creating new jobs.

Imaging for Cardiovascular Device Intervention

Director: Dr. Graham Wright **Ontario Research Fund**

Cardiovascular diseases have evolved from an acute killer to a chronic disease challenge. In recent years, there have been major advances in less invasive treatments, placing an emphasis on the development of imaging and tracking technologies. Focusing on electropathophysiology, percutaneous procedures, and valve replacement, researchers at Sunnybrook and Robarts Research Institutes, working with local, national, and multinational diagnostic imaging and interventional device companies, are advancing the state-of-the-art in image acquisition and analysis with ultrasound, MRI, x-ray, and CT methods, including the design of visualization platforms and associated communication and control interfaces for interventional guidance, facilitating fusion and manipulation of prior and real-time imaging and device information. The ultimate goal is more

effective utilization of imaging to improve outcomes for patients with chronic ischemia, complex arrhythmias, and heart failure related to structural heart diseases.

Ontario Institute for Cancer Research Imaging Program

Directors: Dr. Aaron Fenster/Dr. Martin Yaffe **Ontario Institute for Cancer Research**

The OICR Imaging Program (OICR IP) accelerates the translation of research into the development of new imaging innovations for earlier cancer detection and diagnosis and treatment through four major projects: probe development and commercialization, medical imaging instrumentation and software, pathology validation, and imaging for clinical trials. The Imaging Program facilitates improved screening and treatment options for cancer patients by streamlining advances of medical imaging through the complex pipeline from discovery through clinical translation and ultimately to clinical use.

NIH – NICHD Human Placenta Project - Hyperpolarized 13C MRI of Placental Metabolic Abnormalities Resulting from the Western Diet

Director: Dr. Charles McKenzie **NICHD**

Over 30% of all pregnancies in North America occur in women that are obese. Maternal obesity is often a result of lifelong consumption of an obesity-promoting Western Diet. Altered placental metabolism contributes to increased rates of adverse outcomes in these Western Diet exposed pregnancies, but there is currently no method available to non-invasively measure placental metabolism. The goal of this project is to develop and validate an MRI based method that can be used in human pregnancy to distinguish the placenta with normal metabolism from one where metabolic function is abnormal due to exposure to the Western Diet. Ultimately this will allow improved diagnosis and monitoring of metabolically compromised pregnancies and allow improved treatment that will reduce the rates of adverse outcomes.

Keynote Speakers

Keynote Speaker 1 – Wednesday, March 28 at 8:40

Jeffrey H. Siewerdsen, PhD, Professor of Biomedical Engineering, Department Computer Science & Russell H. Morgan Department of Radiology, Johns Hopkins University

Dr. Siewerdsen is the Vice-Chair and John C. Malone Professor of Biomedical Engineering at Johns Hopkins University, with cross-appointment in the Malone Center for Engineering in Healthcare, the Armstrong Institute for Patient Safety and Quality, and the Departments of Computer Science, Radiology, and Neurosurgery. He is also Co-Director for the Carnegie Center for Surgical Innovation (http://carnegie.jhu.edu) supporting research and education collaborations between engineering and surgery at Johns Hopkins Hospital and is a Principal Investigator in The I-STAR Lab (http://istar.jhu.edu). His research focuses on the development of new 3D imaging technologies and registration methods for diagnostic and image-guided interventions, including cone-beam CT, deformable registration methods, and the development of data-intensive approaches for patient-specific planning and outcomes assessment. He was previously Senior Scientist at the Ontario Cancer Institute and Associate Professor in Medical Biophysics at the University of Toronto, where he helped to form the GTx Program for collaborative research in image-guided therapies.

Keynote Speaker 2 – Wednesday, March 28 at 9:25

Sandy Napel, PhD, Professor, Department: Rad/Integrative Biomedical Imaging Informatics, Stanford University

Dr. Napel is Professor of Radiology and Electrical Engineering and Medicine (Biomedical Informatics). He obtained his BS in Engineering from the State University of New York at Stony Brook and his MS and PhD in Electrical Engineering from Stanford University. Originally appointed as an Assistant Professor at UCSF, he became Vice President of Engineering at Imatron Inc., manufacturer of the first commercial cardiac CT scanner. He was a Visiting Scientist at the Robarts Research Institute in London Ontario before joining Stanford's Radiology Department in 1991. He founded the Radiology Department 3D and Quantitative Imaging Lab in 1996, which developed many fundamental approaches to volumetric visualization and now processes over 2200 Stanford Medicine patient cases per month, creating alternative visualizations and tracking quantitative measurements from cross-sectional imaging exams for many medical conditions. He also co-leads Stanford Radiology's Division of Integrative Biomedical Imaging Informatics at Stanford (IBIIS).

Keynote Speaker 3 – Wednesday, March 28 at 13:30

Imogen Coe, PhD, Dean, Faculty of Science, Ryerson University

Dr. Imogen R. Coe is the founding dean of the Faculty of Science at Ryerson University and a professor in the Department of Chemistry and Biology. Her research group studies the biology of drug transport proteins, which facilitate the entry into cells of drugs used in the treatment of cancer, viral infections and parasitic infections. Dr. Coe is internationally recognized as an advocate for the engagement, retention, recruitment and promotion of girls and women in science. In fall 2016 she was recognized by WXN as one of Canada's Top 100 Women, in the Trail Blazer category for her advocacy work promoting equity in STEM and in 2017, she was one of the "Canada150 Women" in the best-selling publication of the same name.

Keynote Speaker 4 – Thursday, March 29 at 8:55

Reza Razavi, MD, Vice President & Vice Principal (Research), King's College London

Professor Razavi completed his medical training at the University of London. He was awarded a Professorship at King's College London in 2004, and by 2007 headed the School of Biomedical Engineering and Imaging Sciences, leading the 10 year transformation from 20 to over 400 active researchers in this now world class research centre. Currently, he is the Director of the Wellcome Trust/ EPSRC Centre for Medical Engineering and has research strategy roles as Vice-President and Vice-Principal (Research) at King's College London, and Director of Research at King's Health Partners. He also continues clinical practice to treat patients as an honorary clinical consultant cardiologist / paediatric cardiologist. The main focus of Professor Razavi's research is imaging and biomedical engineering related to cardiovascular disease, specialising in cardiac MRI, congenital heart disease, and image guided intervention. His group was the first to perform MRI guided cardiac catheterisation and intervention in patients, and continues to use imaging, computational imaging, and modelling, to develop new and transformative tools for patient care.

Keynote Speaker 5 – Thursday, March 29 at 9:40

Dinesh M. Shah, MD, Professor, & Director, Maternal-Fetal Medicine, University of Wisconsin

Dr. Dinesh Shah is a tenured professor in the department of Obstetrics and Gynecology at the University of Wisconsin School of Medicine and Public Health in Madison, WI. He holds an MD from the University of Bombay and is a Board certified Maternal-Fetal Medicine specialist. His clinical work includes the care of high-risk pregnancies and sonographic imaging. His research is focused on the mechanism of preeclampsia with a specific interest in the role of the renin-angiotensin system and renal injury in preeclampsia using a mouse model. He is the PI on the placenta function project at UWSMPH.

Keynote Speaker 6 – Thursday, March 29 at 13:35

Parvin Mousavi, PhD, Director, School of Computing, Queen's University

Dr. Parvin Mousavi is a professor of Computer Science and Electrical and Computer Engineering at Queen's University, Canada, and a member of the Royal Society of Canada, College of New Scholars, Artists and Scientists. Her research interests are in machine learning, medical image computing, computational biology and integrative modeling of large-scale heterogeneous data, with applications in oncology, computer-assisted surgery, and neurology. She is the General Co-Chair of Information Processing in Computer Assisted Interventions (IPCAI) from 2017-2019, a satellite Co-Chair for Medical Image Computing and Computer Assisted Interventions (MICCAI) in 2017 and 2020 and a founding member of Women in MICCAI.

Scientific and Organizing Committees

Co-Chairs **Anne Martel** **Gabor Fichtinger**

Scientific Committee

Maria Drangova
Aaron Fenster
David Holdsworth
Charlie McKenzie
Frank Prato
Aaron Ward
Graham Wright
Martin Yaffe

Organizing Committee

Johanne Langford
Carol Richardson
Jean Rookwood
Janette Wallace
Yulia Yerofeyev

Judges - Oral & Poster

Elvis Chen
Marcus Couch
Chuck Cunningham
Mamadou Diop
Homa Fashandi
Gabor Fichtinger
Nilesh Ghugre
Donna Goldhawk
Amanda Hamilton
Andras Lasso
Liz Lorusso
Charles McKenzie
Gerald Moran
Parvin Mousavi
Terry Peters
Csaba Pinter
Mihaela Pop
Tim Scholl
Dinesh Shah
Nasim Shams
Eric Schrauben
Stephen Strother
Jonathan Thiessen
Hussain Uzair
Aaron Ward
Raimond Wong
Yiming Xiao
Martin Yaffe

Abstract Reviewers

Shazia Akbar
Natasha Alves-Kotzev
Stephen Breen
Tim Burkhart
Elvis Chen
Chuck Cunningham
Robert DeKemp
Mamadou Diop
Pascal Fallavollita
Gabor Fichtinger
Stewart Gaede
Nilesh Ghugre
Donna Goldhawk
Michael Hardisty
Therese Heinonen
Tyna Hope
April Khademi
Ali R. Khan
Emily Lalone
Andras Lasso
M Louis Lauzon
Ting Lee
Chris Macgowan
James Mainprize
Michael Noseworthly
Csaba Pinter
Mihaela Pop
Giles Santyr
Tim Scholl
Navneet Singh
Matthew Teeter
Jonathan Thiessen
Tamas Ungi
Glenn Wells
Martin Yaffe
Ivan Yeung

Program

Day 1 - Wednesday, March 28, 2018

7:00	**Registration**	Colony Grand Foyer
7:00 – 8:30	**Poster Set-Up & Light Breakfast**	Colony Grande West
8:30 – 8:40	**Opening Remarks**	Colony Grande Centre and East
	Anne Martel and Gabor Fichtinger, ImNO 2018 Scientific Committee Chairs	
	Keynote Session	Colony Grande Centre and East
	Chairs: David Holdsworth, Robarts Research Institute; Cari Whyne, Sunnybrook Research Institute	
8:40 – 9:25	**Novel CT Systems at the Point-of-Care** Jeffrey Siewardsen, PhD, Johns Hopkins University	
9:25 – 10:10	**Radiomic/Radiogenomics: Tools and Techniques** Sandy Napel, PhD, Stanford University	
10:10 – 11:10	**Poster Session & Nutrition Break**	Colony Grande West

		Colony Grand Centre		Colony Grande East
		1 - Image Guided Intervention		**2 - Deep Learning for Medical Image**
		Chairs: Tamas Ungi, Queen's University; Meaghan O'Reilly, Sunnybrook Research Institute		Chairs: Shazia Akbar, Graham Wright, Sunnybrook Research Institute
11:10 – 11:24	1-1	**Dynamic Navigation for Dental Implantation** Arish Qazi, ClaroNav	2-1	**Tumor Bed Segmentation from Whole Slide Images of Breast Cancer After Neoadjuvant Therapy** Mohammad Peikari, Sunnybrook Research Institute
11:24 – 11:38	1-2	**Configurable Overall Skill Assessment in Ultrasound-Guided Needle Insertion** Matthew Holden, Queen's University	2-2	**Automatic Whole Heart MRI Segmentation: CNN Augmented with Continuous Max-flow** Fumin Guo, Sunnybrook Research Institute
11:38 – 11:52	1-3	**360° 3D Transvaginal Ultrasound System for Intraoperative Verification of Needle Positions During High-Dose-Rate Interstitial Gynecologic Brachytherapy** Jessica Rodgers, Robarts Research Institute	2-3	**Semi-Automatic Segmentation of the Myocardial Scar from 3D Late Gadolinium Enhancement Magnetic Resonance Images using a Deep Learning Approach** Fatemeh Zabihollahy, Carleton University
11:52 – 12:06	1-4	**Confocal, Multifrequency Ultrasound Strategies for Controlled MR-Guided Blood-Spinal Cord Barrier Disruption** Stecia-Marie Fletcher, Sunnybrook Research Institute	2-4	**Motion Correction in MRI using Deep Learning** Patricia Johnson, Robarts Research Institute
12:06 – 12:20	1-5	**A CT-Based Simulation for Predicting Trans-Vertebral Ultrasound Propagation** Rui Xu, University of Toronto	2-5	**Synthetic-CT using Conditional Generative Adversarial Neural Networks for MRI-Guided Radiotherapy** Matt Hemsley, University of Toronto

12:20 – 13:20	**Lunch**	Giovanni
	Keynote Session	Colony Grande Centre and East
	Chair: Maria Drangova, Robarts Research Institute	
13:20 – 13:50	**Embedding Equity, Delivering Diversity, Saving Science** Imogen Coe, PhD, Ryerson University	
13:50 – 14:35	Discussion	
14:35 – 15:35	**Poster Session & Nutrition Break**	Colony Grande West

Day 1 - Wednesday, March 28, 2018

		Colony Grand Centre	Colony Grande East
		3 - Bone and Joint Imaging	**4 - Cancer Imaging**
		Chairs: Margarete Akens, TECHNA Institute; Michael Hardisty, Sunnybrook Research Institute	Chairs: Tyna Hope, Sunnybrook Research Institute; Jonathan Thiessen, Lawson Research Institute
15:35 – 15:49	3-1	**Machine Vision Image Guided Surgery – Lighting the Way** Beau Standish, 7D Surgical	4-1 **Automatic Prostate Cancer Detection and Localization on Digital Histopathology Imaging** Wenchao Han, Western University
15:49 – 16:03	3-2	**Validating 3D Face Morphing Towards Improving Pre-Operative Planning in Facial Reconstruction Surgery** Zachary Fishman, University of Toronto - Sunnybrook Research Institute	4-2 **Early Detection of Lung Cancer Recurrence after Stereotactic Ablative Radiation Therapy: Radiomics System Design** Salma Dammak, Western University
16:03 – 16:17	3-3	**Soft Tissue Strain Measurement in Human Cadaveric Knees using Embedded Radiopaque Markers** Alexandra Blokker, Robarts Research Institute	4-3 **Online Assessment of Dose Changes in Head and Neck Radiotherapy without Dose Re-Computation using Deformable Image Registration** Jason Vickress, Western University
16:17 – 16:31	3-4	**Knee Osteophyte Depiction using 3D Ultrasound Imaging Compared to Computed Tomography** Valeria Vendres, Queen's University	4-4 **Case Report: Hyperpolarized 13C Imaging of a Castration-Resistant Prostate Cancer Patient** Casey Lee, University of Toronto
16:31 – 16:45	3-5	**Measuring Joint Blood Flow with DCE-NIRS: Application to Rheumatoid Arthritis Treatment Monitoring** Seva Ioussoufovitch, Western University	4-5 **Longitudinal Assessment of Single-Dose Radiation-Induced Tumour Vascular Changes with Functional Optical Coherence Tomography** Valentin Demidov, University of Toronto
16:45 – 17:00		**Break**	
		Colony Grand Centre	Colony Grande East
		5 - Augmented Reality	**6 - New Contrast Agents**
		Chairs: Elvis Chen, Robarts Research Institute; Pascal Fallavollita, University of Ottawa	Chairs: Savita Dhanvantari, Donna Goldhawk, Lawson Research Institute
17:00 – 17:14	5-1	**Accuracy of the Microsoft Hololens for Neurosurgical Burr Hole Placement** Emily Rae, Queen's University	6-1 **A New Family of Small Manganese (III) Porphyrin Based MRI Contrast Agents and the Analyses of the Binding to Human Serum Albumin** Piryanka Sasidharan, University of Toronto
17:14 – 17:28	5-2	**Ultrasound-Guided Needle Insertion Simulator with Tracking- and Video-Based Skill Assessment** Sean Xia, Queen's University	6-2 **Engineering Non-Integrating Lentiviral Vectors for Safe Reporter-Based Imaging of Mesenchymal Stem Cells** Amanda Hamilton, Robarts Research Institute
17:28 – 17:42	5-3	**Comparison of a Mixed-Reality Technology to Cadavers for Gross Anatomy Learning** Mustafa Haiderbhai, University of Ottawa	6-3 **Developing tumour-activatable minicircles as novel reagents for prostate cancer detection** TianDuo Wang, Western University
17:42 – 17:56	5-4	**Using Augmented-Reality for Self-Directed Surgical Skills Training in Competency-Based Medical Education** Regina Leung, Queen's University	6-4 **Lanthanide Nanoparticles as Vascular Contrast Agents for Microcomputed Tomography** Charmainne Cruje, Robarts Research Institute

Day 2 - Thursday, March 29, 2018

7:00	**Registration**	Colony Grande Foyer
8:00 – 8:50	**Poster Set-Up & Light Breakfast**	Colony Grande West
8:50 – 8:55	**Opening Remarks**	Colony Grande Centre and East
	Anne Martel and Gabor Fichtinger, ImNO 2018 Scientific Committee Chairs	
	Keynote Session	Colony Grande Centre and East
	Chairs: Mike Seed, The Hospital for Sick Children; Graham Wright, Sunnybrook Research Institute	
8:55 – 9:40	**Treating Ventricular Tachycardia with MR guided ablation: clinical advantages and technical challenges** Reza Razavi, MD, King's College London	
9:40 – 10:25	**Advanced Imaging Approach to Define Placenta Function** Dinesh Shah, MD, University of Wisconsin	
10:25 – 11:25	**Poster Session & Nutrition Break**	Colony Grande West

		Colony Grand Centre		Colony Grande East
		7 - Cardiovascular Imaging		**8 - Maternal - Fetal Imaging**
		Chairs: Maria Drangova, Robarts Research Institute; Mihaela Pop, Sunnybrook Research Institute		Chairs: Christopher Macgowan, The Hospital for Sick Children; Charlie McKenzie, Western University
11:25 – 11:39	7-1	**Characterization of T2, T2* Relaxation and Strain in Disease Progression Post Acute Myocardial Infarction** Dipal Patel, Sunnybrook Research Institute	8-1	**Fetal Cardiac Hemodynamics: Initial Experience using 4D Flow MRI** Eric Schrauben, Hospital for Sick Children
11:39 – 11:53	7-2	**Investigating the Correlation Between Cellular Iron Content and Magnetic Resonance Signal using THP-1 Monocytes to Model the Inflammatory Response** Praveen Sankajith Dassanayake, Western University	8-2	**Imaging Fetal Congenital Heart Disease using Motion Compensated MRI** Christopher Roy, Hospital for Sick Children
11:53 – 12:07	7-3	**Analysis of Flow and Oscillating Wall Shear Stress in the Carotid Bifurcation using Particle Image Velocimetry: Effects of Stenosis Severity and Waveform Pulsatility** Amanda Dicarlo, Western University	8-3	**A Novel Optical Neuromonitor for Simultaneous and Real-Time Quantification of Cerebral Saturation, Perfusion, and Metabolism at the Bedside** Ajay Rajaram, Western University
12:07 – 12:21	7-4	**Evaluation of Sympathetic Function with PET 11C-Hydroxyephedrine (HED) and Ammonia (13N-NH3) in A Canine Pacing Model of Atrial Fibrillation** Robert Miner, Ottawa Heart Institute	8-4	**Generating A 3D Ultrasound Panorama to Monitor Neonatal Post-Hemorrhagic Ventricle Dilation** Andrew Harris, Robarts Research Institute
12:21 – 12:35	7-5	**Direct Measurement of Blood Flow Reflections by Ultrasound** Luxi Wei, University of Toronto	8-5	**3D Water-Fat MRI Detection of Developmental Maturity in Fetal Adipose Tissue Compartments** Stephanie Giza, Western University

12:35 – 13:35	**Lunch**	Giovanni
	Keynote Session	Colony Grande Centre and East
	Chair: Anne Martel, Sunnybrook Research Institute	
13:35 – 14:20	**The Chronicles of Prostate Cancer Detection and Grading** Parvin Mousavi, PhD, Queen's University	

Day 2 - Thursday, March 29, 2018

		Colony Grand Centre	Colony Grande East
		9 - New MRI Approaches	**10 - Neuroimaging**
		Chairs: Hai-Ling Margaret Cheng, University of Toronto; Giles Santyr, Hospital for Sick Children	Chairs: April Khademi, Ryerson University; Ali Khan, Robarts Research Institute
14:25 – 14:39	9-1	**Quantitative MR: Application to Concussion Studies** Scott Hinks, GE Healthcare	10-1 **Effect of Scan Duration on CT Perfusion-Derived Hemodynamic Parameters and Infarct Volume** Eric Wright, Western University
14:39 – 14:53	9-2	**Optimizing Signal-to-Noise Ratio for Hyperpolarized Carbon-13 MRI using a Hybrid Flip Angle Scheme** Lauren Smith, Western University	10-2 **Design and Evaluation of a Diffusion MRI Fibre Phantom using 3D Printing** Uzair Hussain, Robarts Research Institute
14:53 – 15:07	9-3	**Accelerated 3D Spiral-Ideal Imaging Approach for Breath-Hold Hyperpolarized 129Xe Lung MRI** Brandon Zanette, Hospital for Sick Children	10-3 **Between- and Within-Site MRI Scanner Stability Investigated using EPI fMRI Phantom Scans** Aras Kayvanrad, University of Toronto
15:07 – 15:21	9-4	**Under-Sampling and Reconstruction Effects in 31P-MRSI using Flyback-EPSI with Compressed Sensing** Diana Harasym, McMaster University	10-4 **Relating Hippocampal Glutamate to Structural Changes and Cognitive Performance in Alzheimer's Disease: A 7T MRI Study** Dickson Wong, Robarts Research Institute
15:21 – 15:35	9-5	**Density-Adapted 3-Dimensional Radial Multiple Gradient-Echo Acquisition Scheme for 23Na MRI** Alireza Akbari, Western University	10-5 **Magnetic Resonance Spectroscopy in a Rodent Concussion Model** Amy Schranz, Robarts Research Institute
15:35 – 16:30		**Poster Session & Nutrition Break**	Colony Grande West
		Colony Grand Centre	Colony Grande East
		11 - Tissue Characterization	**12 - Instrumentation and Technology**
		Chairs: Mamadou Diop, Lawson Research Institute; Alex Vitkin, University Health Network	Chairs: Christine Demore, Sunnybrook Research Institute; Tamie Poepping, Western University
16:30 – 16:44	11-1	**Magnetic Resonance Imaging of the Microbiome using MagA-Expressing Bacteria** Sarah Donnelly, Lawson Health Research Institute	12-1 **Apodized-Aperture Pixel: A Novel X-Ray Detector Design to Improve Cancer Detection in Mammography** Tomi Nano, Robarts Research Institute
16:44 – 16:58	11-2	**An Investigation into the Biosynthesis Pathway of Serotonin using CEST MRI** Ryan Oglesby, Sunnybrook Health Sciences Centre	12-2 **3D Verification of Flow in Microfluidic Devices using Micro-PIV** Kayla Soon, Western University
16:58 – 17:12	11-3	**The Growth Hormone Secretagogue Receptor, Ghrelin, and Biochemical Signaling Processes in Human Heart Failure** Rebecca Sullivan, Lawson Health Research Institute	12-3 **Transmit Coil Impedance Measurements to Estimate Radiofrequency Induced Currents on Wires in MRI** Brandon Coles, University of Toronto
17:12 – 17:26	11-4	**MRI of Magnetically Labeled Alveolar-Like Macrophages in Rat Lungs using Hyperpolarized Xe-129: Confirmation with Histology** Vlora Riberdy, Hospital for Sick Children	12-4 **Parametric Modeling and Metal 3D Printing of Anti-Scatter Grids for Cone-Beam CT** Santiago Cobos, Western University
17:26 – 17:40	11-5	**Blood Clot Hematocrit and Age Differentiation in Vitro using R2* and Quantitative Susceptibility Mapping** Spencer Christiansen, Robarts Research Institute	12-5 **Array-Based Dual Frequency Acoustic Angiography** Jing Yang, University of Toronto
17:40 – 18:00		**Awards and Closing Remarks**	Colony Grande Centre and East
18:00 – 18:30		**Poster Take Down**	Colony Grande West

Oral Presentation Abstracts

(in order of presentation)

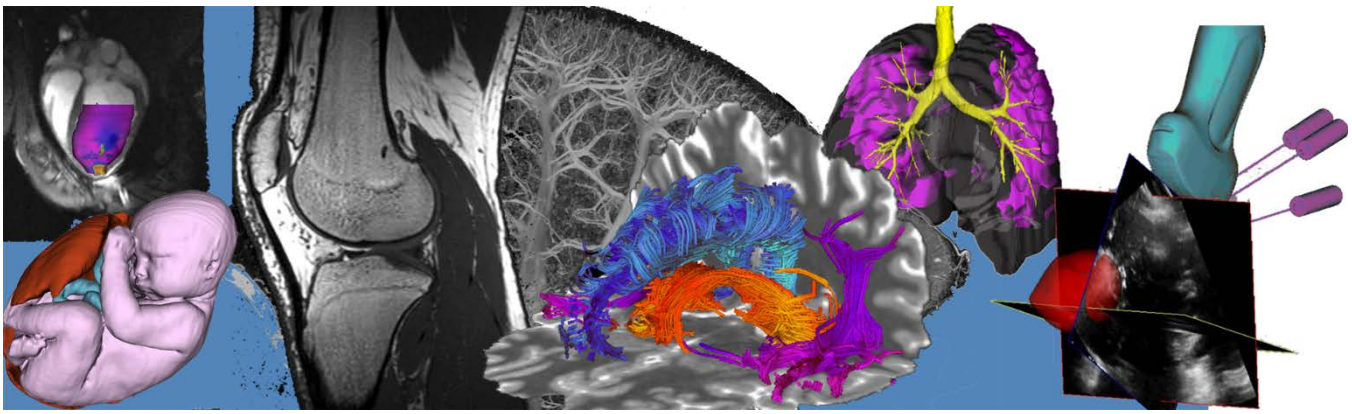

Oral Presentation Abstracts

Session 1: Image Guided Intervention

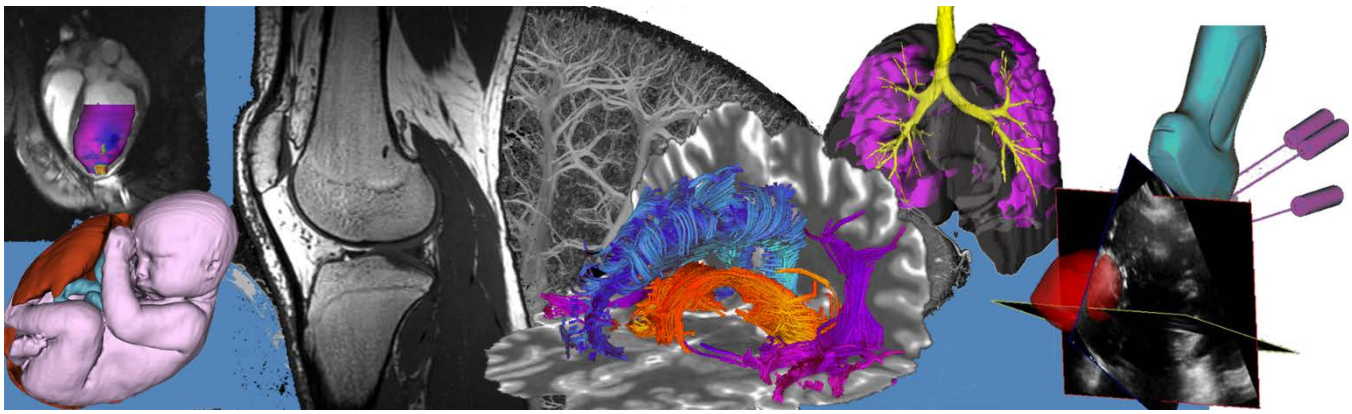

Dynamic Navigation for Dental Implantation

Dental implants have become a common way to anchor the replacement of lost teeth. Currently, dental implants are placed without guidance, requiring cutting the gums widely to expose the jaw bone in order to avoid major drilling errors. This results in increased risk of infection, increased patient discomfort and implant placement inaccuracies which make the final restoration more difficult or less attractive. In this talk, we will present our dental navigation solution, Navident, which enables rapid surgery planning using 3D CT image data, registering the 3D image and plan to the real jaw, then guiding, to within less than 500 microns, the drilling and implant placement. In particular, we will present ñTrace and Placeò, a technique we recently developed to overcome the major barriers to adoption of Navident by dentists.

Presenter:

Arish A. Qazi, PhD
Head of R&D, Navident

Configurable Overall Skill Assessment in Ultrasound-Guided Needle Insertion

Matthew S. Holden[1], Hillary Lia[1], Sean Xia[1,2], Zsuzsanna Keri[1], Tamas Ungi[1], Gabor Fichtinger[1]

[1]Laboratory for Percutaneous Surgery, School of Computing, Queenôs University, Kingston, ON, Canada
[2]School of Medicine, Queenôs University, Kingston, Canada

INTRODUCTION: Computer-assisted training for ultrasound-guided interventions has proliferated over the last several years due to its efficiency over supervised training. Objective skill assessment can be used to monitor trainee performance as they follow a training course without the need for a preceptor. The interaction of trainees and preceptors with computer-assisted training systems, however, has not been well defined. We suggest that computer-assisted training systems must remain configurable and transparent such that instructors may configure the assessment to emphasize particular skills and both instructors and trainees may understand traineesô progression through the curriculum and how to interpret results into action.

METHODS: We implemented three configurable and transparent methods for overall skill assessment. The first method uses a weighted combination of percentile ranked metric values, where the weight associated with each performance metric is configurable. The second method uses a k-nearest neighbours approach, where the scale in each dimension of metric space is configurable. The third method uses a fuzzy inference system with kernel density estimates as the membership functions, where the user may add, remove, or weight fuzzy different if-then rules. These methods were all implemented within the Perk Tutor platform (www.perktutor.org) which allows the input performance metrics and parameters to be configured. Furthermore, these methods are connected directly to the training system to provide immediate feedback.

We conducted a retrospective validation study to compare the accuracy of skill assessment with each of these methods using equal weights. Twenty medical trainees and eight experts performed either in-plane or out-of-plane ultrasound-guided needle insertion on a vascular access phantom, and were assessed using 10 performance metrics (**Figure 1**). We validated each method for classification of participants as novice or expert using the leave-one-out method, and we compared these results with the well-accepted SVM method [1]. Area under the sensitivity-specificity curve (AUC) was used as the measure of accuracy.

Figure 1. Trainee practicing out-of-plane needle insertion under ultrasound-guidance with augmented reality 3D display.

RESULTS: For classification into the novice and expert categories, AUC was 0.88 for the combination of percentile ranks method, 0.80 for the k-nearest neighbours method, and 0.83 for the fuzzy inference system method. This compares favourably to the 0.86 AUC for the well-accepted SVM method.

CONCLUSION: Configurable and transparent skill assessment methods allow trainees and preceptors to understand results and configure them to emphasize particular skills. We have shown that overall skill assessment accuracy using configurable methods and using well-accepted black box methods is comparable; thus, configurable methods may be adopted into practice without compromising accuracy. We expect accuracy to improve further when the methods are optimized based on expert knowledge.

[1] B. Allen, V. Nistor, E. Dutson, G. Carman, C. Lewis, and P. Faloutsos, ñSupport vector machines improve the accuracy of evaluation for the performance of laparoscopic training tasks,ò *Surg Endosc*, vol. 24, no. 1, pp. 170ï 178, Jan. 2010.

360Á3D transvaginal ultrasound system for intraoperative verification of needle positions during high-dose-rate interstitial gynecologic brachytherapy

Jessica R. Rodgers[1,2], Jeffrey Bax[2], Vikram Velker[3], Kathleen Surry[3], David DôSouza[3], Eric Leung[4], Aaron Fenster[1,2]

[1]Biomedical Engineering Graduate Program, Western University, London, Ontario, Canada; [2]Robarts Research Institute, Western University, London, Ontario, Canada; [3]London Regional Cancer Program, London, Ontario, Canada; [4]Odette Cancer Centre, Toronto, Ontario, Canada

Introduction: Treatment for gynecologic cancers, particularly vaginal malignancies, may include brachytherapy, which enables higher doses of radiation to be delivered to the tumor and nearby area relative to the surrounding healthy tissues. One method of brachytherapy is high-dose-rate (HDR) perineal interstitial brachytherapy where hollow needles are inserted through a template on the perineum and a ^{192}Ir radioactive source is temporarily placed at planned positions along the needles to deliver the therapy. Given the close proximity of organs, including the bladder, rectum, and bowel, precise placement of needles is important to avoid overexposure of these organs and deliver optimal treatment. Adjacent pairs of needles are ideally parallel with 10 mm spacing, though spacing of 10 Ñ5 mm is typically clinically acceptable. Currently, patients receive a post-insertion x-ray computed tomography (CT) scan to visualize the needles; however, there is no standard approach to visualizing the needles intraoperatively during needle placement. Implementation of an intraoperative needle verification tool would allow for organs at risk (OAR) to be avoided and allow needle placements to be refined, potentially improving the quality of the implant. We have developed a three-dimensional (3D) transvaginal ultrasound (TVUS) system that produces a 360º 3D image through a template-compatible sonolucent vaginal cylinder and propose its use for intraoperative needle placement verification during HDR interstitial gynecologic brachytherapy.

Methods: We developed a 3D TVUS system that uses a motorized mechanism to rotate a two-dimensional side-fire transrectal ultrasound (US) probe 360Á, generating a ring-shaped 3D US image (voxel size: 0.126 Ǐ 0.126 Ǐ 0.126 mm^3) and enabling visualization of needles placed on all sides of the US probe. A bearing on the probe cradle mitigates any interference between the probe motion and the placed needles. Before acquisition, the probe is inserted into the hollow core of a sonolucent polymethylpentene cylinder compatible with the clinical perineal template, mimicking the geometry of the current template vaginal cylinder, stabilizing and separating the vaginal walls. The 3D scan takes approximately 20 s and allows the user to view the image immediately after acquisition with the option to update subsectors of the image.

In accordance with the approved protocols, three patients receiving HDR interstitial gynecologic brachytherapy for vaginal malignancies at the London Regional Cancer Program were imaged using the 3D TVUS system. For each needle placed, the point where the needle entered the image and either the exit or tip position were identified in both the 3D TVUS image and the corresponding, clinical post-insertion CT image (voxel size: 0.57 Ǐ 0.57 Ǐ 1.5 mm^3), which was rigidly registered to the 3D TVUS. Corresponding entrance and exit points between the modalities were established for each needle and used to assess the trajectory and distance errors in the needle paths identified. As the needles are considered linear within the image field-of-view, the maximum difference was calculated using the point pair (entrance or exit) with the larger difference for each needle.

Results: Features of interest, including the patientôs rectum, urethra, and bladder with an inserted Foley catheter, were clearly visualized in the 3D TVUS images, in addition to the needles (Figure 1). The mean angular difference Ñstandard deviation (SD) between needle paths in the two modalities was 1.67 Ñ0.75 º for the 28 needles placed, and there were no trends in the direction of the differences relative to the image planes. The mean entrance point difference ÑSD was 1.98 Ñ0.92 mm and the mean exit point difference ÑSD was 1.92 Ñ0.81 mm. The mean maximum difference ÑSD between the needles in the two modalities was 2.33 Ñ0.78 mm.

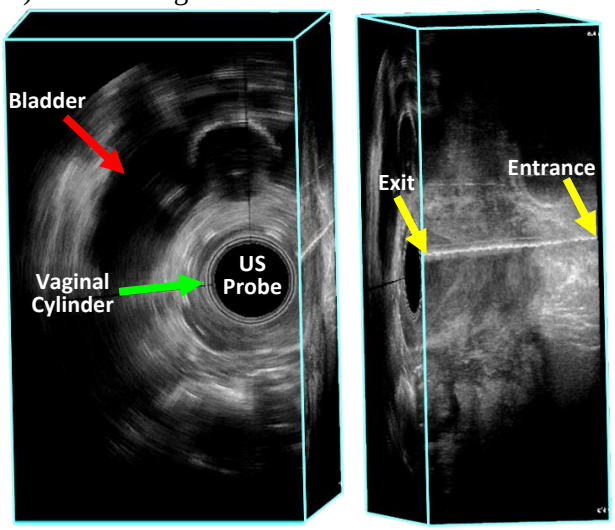

Figure 1. Patient 3D TVUS image, with key features including bladder, US probe, entrance and exit points, indicated.

Conclusions: Based on this preliminary patient study, 360º 3D TVUS may be a feasible option for intraoperatively localizing needles during HDR interstitial gynecologic brachytherapy needle placement and the proof-of-concept patient study with 15 patients is ongoing.

Confocal, Multifrequency Ultrasound Strategies for Controlled MR-Guided Blood-Spinal Cord Barrier Disruption

Stecia-Marie P. Fletcher[1,2] and Meaghan A. OôReilly[1,2]*
[1]*Department of Medical Biophysics, University of Toronto;* [2]*Sunnybrook Research Institute; *supervisor*

Introduction. The Blood-Spinal Cord Barrier (BSCB) consists of a neurovascular unit characterized by non-fenestrated vascular endothelial cells with tight junctions between them, and neuronal accessory structures[1]. It is similar in morphology to the Blood-Brain Barrier (BBB) and has an important role in maintaining a specialized and selective environment in the spinal cord. However, it poses a major challenge to drug delivery[1]. Existing methods to circumvent the BSCB have a range of disadvantages including invasiveness, difficultly achieving therapeutic concentrations, and non-targeted effects[2]. Microbubble mediated MR-guided focused ultrasound (MRgFUS) can produce targeted, consistent, reproducible, and reversible BBB disruption (BBBD)[3]. The feasibility of this technique for BSCB disruption (BSCBD) has also been demonstrated[4]. A major challenge to clinical application is achieving ultrasound delivery through the human spine. Sub-megahertz frequencies required to minimize attenuation and aberration as ultrasound propagates through bone[5], correspond to long focal zones compared to the size of the spinal canal, and may result in the formation of standing waves which can lead to lack of control over the focus, off focal effects, and the inability to accurately predict focal pressures in situ[6]. Research indicates that multifrequency ultrasound and modulated pulses can reduce focal depth of field and suppress standing waves[5,7,8,9].

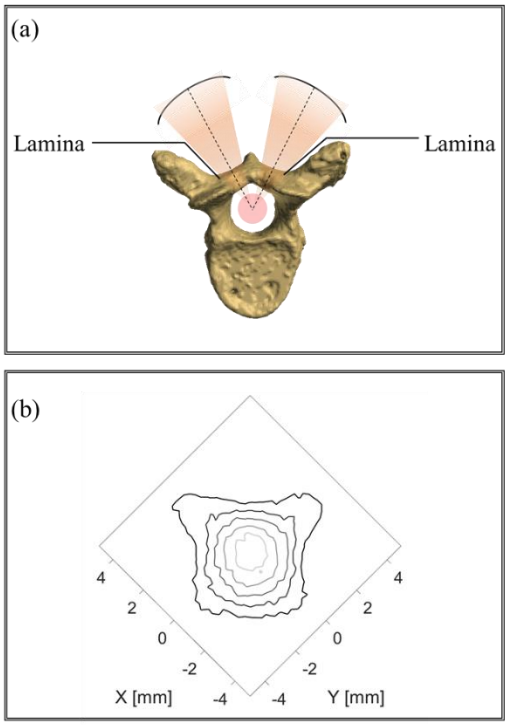

Fig. 1 (a) Confocal approach for focusing in vertebrae. **(b)** Normalized max. pressure contours (50, 60, 70, 80, 90%) in 1st thoracic vertebra using confocal approach and short pulses combined with QPSK.

Methods. The effects of confocal, dual-frequency ultrasound on focal depth-of-field have been investigated at clinically relevant frequencies (250kHz, 500kHz) both numerically using k-Wave, and experimentally by performing ultrasound field measurements with a 0.5mm needle hydrophone in a tank of deionized and degassed water. The effects of standing waves have been investigated in a cylindrical acrylic tube phantom and in odd-numbered *ex-vivo* human thoracic vertebrae. Linear chirp pulses, random quadrature phase shift keying (QPSK), and a range of short burst excitations have been investigated for mitigating the effects of standing waves in benchtop experiments.

Results. Confocal transducers with a centre frequency (f) of 500kHz, frequency difference (qpf) of 30kHz, and angular separation (d) of 90Áhave been shown to reduce the width of the 70% maximum pressure distribution by approximately 85%, when compared to a single transducer. For a single transducer (f = 514kHz), short burst excitations (2 cycles) have shown a greater reduction in standing wave content when compared to quasi-continuous wave methods (30 cycles) ï ~60% vs. ~35%. Under confocal exposures (f = 514kHz), closely timed short pulses (PRP = 50ɛs) accompanied by random QPSK at the start of each pulse has been demonstrated to mitigate standing waves in ex-vivo vertebrae, while maintaining a uniform ellipsoidal focal spot.

Conclusions. The feasibility of using confocal ultrasound exposures to create a controlled focus within the human thoracic spine has been demonstrated in ex-vivo vertebrae. Techniques used here can be adapted for MRgFUS induced BSCBD for drug-delivery to the human spinal cord.

References. [1] V. Bartanusz, *et al.* ***Ann. Neurol.,*** 70, 2011; [2] A. Burgess & K. Hynynen ***Expert Opin. Drug Deliv.,*** 11(5), 2014; [3] K. Hynynen, *et al.* ***Radiology,*** 220(3), 2001; [4] J. Wachsmuth, *et al.* ***AIP Conference Proceedings,*** 1113, 2009; [5] S. Pichardo, *et al.* Phys. Med. Biol., 56(1), 2011; [6] M. OôReilly & K. Hynynen ***Phys. Med. Biol.,*** 55(18), 2010; [7] J. Sutton, *et al.* ***J. Acoust. Soc. Am.,*** 138(3), 2015; [8] F. Mitri, *et al.* ***IEEE Trans. Med. Imaging,*** 24(10), 2005; [9] S. Tang & G. Clement ***J. Acoustic. Soc. Am.,*** 126(4), 2009

A CT-Based Simulation for Predicting Trans-Vertebral Ultrasound Propagation

Rui Xu[1,2], Meaghan O'Reilly[1,2]
[1]Medical Biophysics, University of Toronto, [2]Sunnybrook Research Institute, Toronto, ON, Canada

Introduction. The blood spinal cord barrier (BSCB) prevents the passage of approximately 98% of small molecule drugs and 100% of large molecule drugs, making most molecular treatments of the central nervous system ineffective [1]. Focused ultrasound can transiently open the blood brain barrier (BBB) for the transport of therapeutics across the BBB in animal models. This technique has recently reached clinical trials and has the potential to drastically increase the possibilities for targeted drug therapies in the brain [2, 3]. The extension of this technique to the human BSCB may similarly revolutionize targeted therapies to the spinal cord [4, 5]. However, clinical translation remains an issue. The human vertebral column is irregularly shaped and has drastically different acoustic properties than the surrounding soft tissues, making focusing ultrasound through the vertebral column to the spinal cord a challenge [6, 7]. It may be possible to focus trans-vertebral ultrasound using phased arrays with appropriate phase and amplitude corrections. We envision a method in which phase and amplitude corrections are calculated non-invasively using a numerical model based on the Rayleigh-Sommerfeld integral and patient-specific preoperative CT scans. This numerical model is being developed and the simulation accuracy has been quantified through comparison with experimental measurements of ultrasound propagation through *ex vivo* human vertebrae.

Methods. Even numbered *ex vivo* thoracic vertebrae were degassed and individually placed in degassed and deionized water, then sonicated with a spherically focused transducer (diameter = 5cm, f-number = 1.2, frequency = 514kHz) oriented facing the posterior elements of the vertebrae. Ultrasound field scans were conducted inside the vertebral foramen for multiple transducer-vertebra configurations. The vertebrae were CT scanned at 0.5mm isotropic resolution. Vertebral geometries were extracted using semi-automatic segmentation, and CT intensity was used to determine bone density and acoustic properties using known relationships from skull bone [7, 8]. Simulation systems were registered to the experiment setups using Horn transforms based on anatomical markers visible in experiment and CT space. The Rayleigh-Sommerfeld integral method was used to propagate ultrasound from the transducer, through the posterior elements of vertebrae, into the vertebral foramen. Pressures were calculated at measurement locations for direct comparison between experiment and simulation.

Results. Average simulation error in maximum pressure location and a weighted >50% pressure location were 1.9 mm and 1.4 mm, respectively. Simulation error was more widely distributed along the vertical axis than the frontal axis.

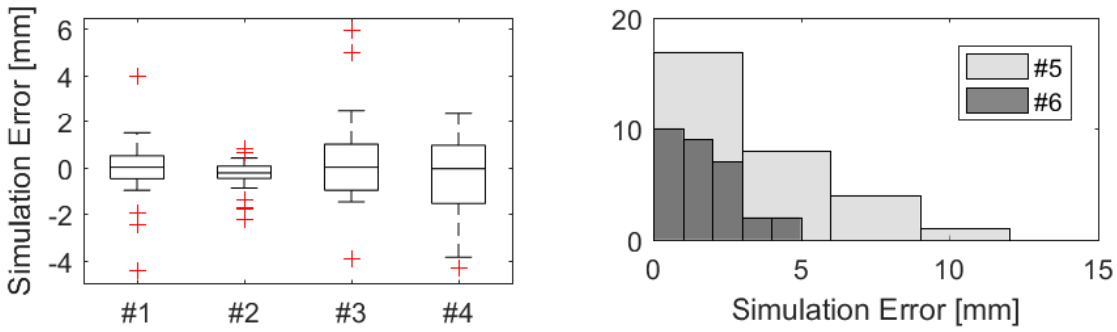

Simulation error in frontal axis (#1, #2), vertical axis (#3, #4), and frontal plane (#5, #6) in maximum pressure location and weighted >50% pressure location respectively, for five measurement positions in each even-numbered thoracic vertebrae.

Conclusions. Simulation error suggests that the Rayleigh-Sommerfeld integral method and skull acoustic properties provide an adequate approximation for modeling trans-vertebral ultrasound propagation, although greater accuracy might be achieved by determining vertebrae specific acoustic properties. Demonstrating the accuracy of a numerical model of trans-vertebral ultrasound propagation is a critical first step in the development of the methodology for using phased arrays to deliver ultrasound to the spinal cord for BSCB disruption and to improve the delivery of therapeutics to the spinal cord.

References [1] Bartanusz, V. *Annals of neurology* **70**, 194–206 (2011). [2] Poon, C. *Neuropharmacology* **120**, 20–37 (2017). [3] Huang, Y. *ISMRM*, (2016). [4] Wachsmuth, J. *ISTU* (2009). [5] Weber-Adrian, D. *Gene therapy* **22**, 568–577 (2015). [6] Nicholson, P. *Phys. Med. Biol* **39**, 1013–1024 (1994). [7] Pichardo, S. *Phys. Med. Biol* **56**, 219–250 (2010). [8] Pichardo, S. *Phys. Med. Biol* **62**, 6938–6962 (2017). [9] Horn, B. *JOSA A*, **5** 1127-1135 (1988).

Oral Presentation Abstracts

Session 2: Deep Learning for Medical Image Analysis

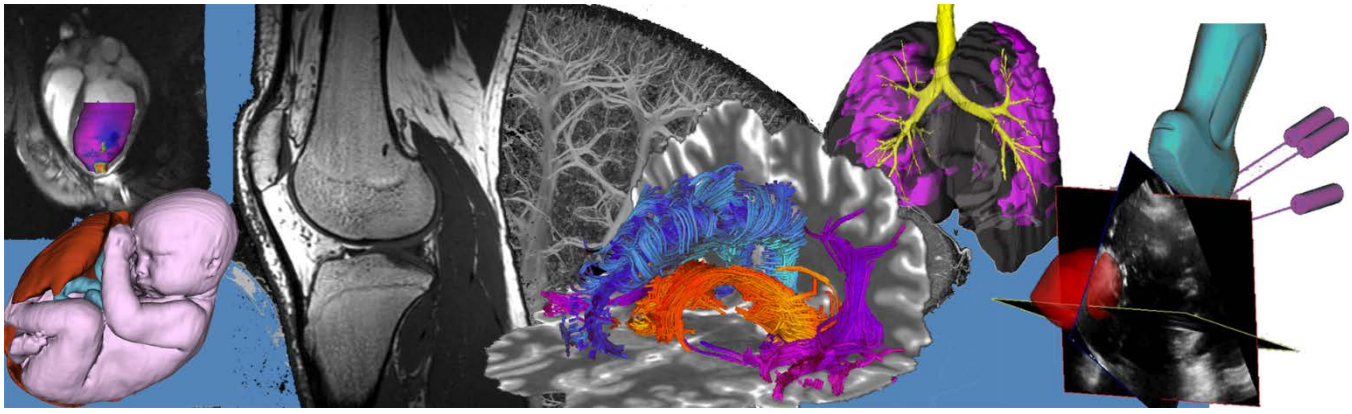

Tumor Bed Segmentation from Whole Slide Images of Breast Cancer After Neoadjuvant Therapy

Mohammad Peikari, Azadeh Yazdanpanah, Anne L. Martel
Department of Medical Biophysics, University of Toronto, Sunnybrook Research Institute

Introduction: Neoadjuvant therapy (NAT) is a treatment of choice for selected high-risk and/or locally advanced breast cancer patients. The goal of NAT is to downsize the tumor, allowing for less extensive surgical operation resulting in better cosmetic outcomes and reduced postoperative complications. NAT also allows the efficacy of new therapeutic agents to be assessed *in vivo* [1]. Currently, residual tumor burden assessment is done manually by pathologists on hematoxylin and eosin (H&E) stained tissue sections through a qualitative and time-consuming process [2]. The first step in assessing tumor burden by pathologists is to identify the tumor bed region from H&E stained tissue slides. Tumor bed is defined as the region which would have been occupied by cancer cells prior to treatment. The task of identifying tumor bed after NAT is highly subjective. Regions with features like the high concentration of fibroblast cells within fibrosis, foamy macrophages with pigments, calcifications, aggregates of lymphocytes, areas of tumor necrosis, thin collagen bundle strands, and small capillaries are indications for the tissue that is part of the tumor bed. The purpose of this study is to automatically identify tumor bed regions from post-NAT H&E stained pathology slides.

Methods: It would be challenging to address this problem using traditional machine learning approaches since all the aforementioned features must be identified and included in the learning model. Convolutional Neural Network (CNN) approaches, on the other hand, are capable of learning appropriate features that can best differentiate between normal tissue, residual tumor and areas where cancer cells have been successfully treated. Therefore, in this study, a CNN approach was taken to identify tumor bed regions.

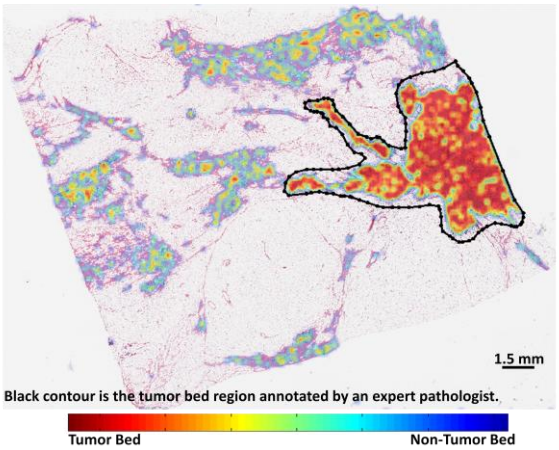

Figure 1- result of applying CNN on a post-NAT whole slide image from our validation set.

We used n = 92 whole slide images (WSIs) for training a CNN method and n = 30 additional images for testing the model. All WSIs were scanned at 20X magnification. Tumor bed regions from all images in the train and test sets were annotated by an expert pathologist (black contour in the image). Patches of size s = 512x512 pixels were cropped from inside and outside of the tumor bed regions to form two classes of data. The cropped patches were then used to fine-tune top layers of an InceptionV3 network with preloaded ImageNet weights. The model was then validated using the test set.

Results and Conclusion: Over n = 606,000 training patches were used to train the network and n = 128,000 image patches were used to validate the model. The achieved classification accuracy on the validation set was about 75%. The above figure shows tumor bed segmentation result on a whole slide image in the validation set. Regions with a higher probability of belonging to tumor bed regions are colored as hot red and regions with a lower probability of belonging to tumor bed regions are shown as cold blue. This shows that using CNN based techniques it is possible to identify tumor bed regions after NAT.

Acknowledgements: This research is funded by the Canadian Cancer Society (grant number 703006).

[1] F Faneyte et al. *British journal of cancer, 88(3):406-412, 2003.*
[2] Abrial C et al. *Journal of Clinical Oncology, 26(18):3093-3094, 2008.*

Automatic whole heart MRI segmentation: CNN augmented with continuous max-flow

Fumin Guo[1], Matthew Ng[1], Nii Okai Addy[2], William R. Overall[2], Juan M. Santos[2], Mihaela Pop[1], and Graham A. Wright[1]

[1]Sunnybrook Research Institute; Medical Biophysics, University of Toronto, Canada; [2]HeartVista Inc., USA

Introduction: Cardiac magnetic resonance imaging (MRI) is routinely used in the clinics for disease diagnosis and therapy guidance. Whole heart segmentation (WHS) is required as a first step to quantify cardiac indices [1]. However, this step is challenging because of complex geometry, large shape variation of the heart, imaging noise and motion artefacts [2]. The objective of this work is to combine a recently developed convolutional neural network and a continuous max-flow segmentation algorithm with spatial coherence information for fully automatic WHS.

Methods: The MRI dataset were acquired using a cine SSFP sequence at 1.5T and 3.0T, and consisted of 100 patients from five categories: normal condition, myocardial infarction, dilated cardiomyopathy, hypertrophic cardiomyopathy, and abnormal right ventricle from the Automated Cardiac Diagnosis Challenge [3]. Seventy subjects (n=14 patients from each category) were used to train the HeartVista neural network [4]. The network consists of several layers of learned convolutional filters to extract image features, which are then de-convolved and up-sampled to generate probability maps of each region. Thirty subjects were tested using the trained network and the generated probability maps were refined using a continuous max-flow segmentation algorithm [5] that minimizes the voxel-wise data terms and the segmentation surface area. The data term employs image signal intensity and X-Y spatial location information to compensate for signal intensity heterogeneity and generate spatially compact segmentation. The resulting high dimensional features were classified using a kernel k-means in the embedding space for linear separation and the high-order data term was simplified through upper-bound relaxation [6]. The derived voxel-wise data term using high-dimensional features and the regularization term generated using image edge information were entered into a multi-region continuous max-flow algorithm. The objective function was optimized in an iterative manner and the output from the current iteration was used to re-initialize the next iteration until convergence.

Results: Figure 1 shows representative left ventricle (LV), right ventricle (RV) and myocardium (Myo) segmentation results in a short axis image, as well as rendered in 3D. Table 1 provides a summary of the segmentation performance by comparing algorithm masks with expert manual outputs using Dice similarity coefficient (DSC), mean absolute distance (MAD) and absolute percent volume error (δVp). For 30 subjects, we achieved DSC of 89.3%, 86.7% and 93.6% and MAD of 3.0 mm, 2.2 mm and 2.5 mm for RV, Myo and LV, respectively. Algorithm volumes were strongly and significantly correlated with manual results with Pearson correlation coefficients (V_A-V_M Corr.) of 0.98, 0.963, and 0.995 (all $p < 0.01$) and small δVp of 9.7%, -5.7% and -3.8% for RV, Myo and LV, respectively. The neural network required ~24 hours for training, ~1s to generate the probability maps and ~12s to refine the results using the kernel k-means based continuous max-flow algorithm.

Conclusion: Our novel segmentation approach successfully combines the power of deep neural network and continuous max-flow, and automatically generated spatially compact and smooth whole heart MRI segmentation, with accuracy and computational efficiency that may be clinically acceptable.

References: [1] Peng et al., MAGMA, 2016. [2] Zhuang et al., J. Healthc Eng., 2013. [3] https://www.creatis.insa-lyon.fr/Challenge/acdc/databases.html. [4] www.heartvista.com. [5] Yuan et al., ECCV, 2010. [6] Tang et al., ICCV, 2015.

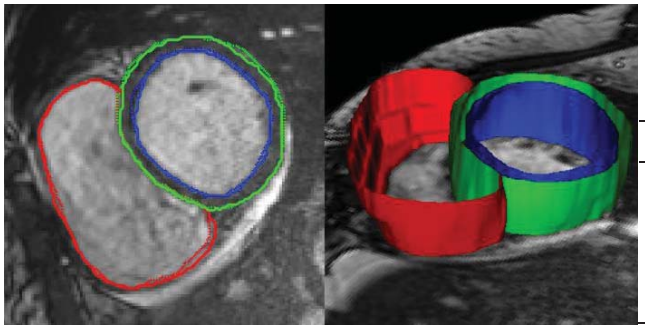

Figure 1. Representative RV (red), Myo (green) and LV (blue) segmentation results in a short axis image (left) and in 3D (right). Solid and dashed contours represent algorithm and expert manual segmentation, respectively.

Table 1. Algorithm segmentation performance: comparison with the expert manual segmentation (mean ÑSD)

	RV	Myo	LV
DSC (%)	89.3Ñ6.2	86.7Ñ3.5	93.6Ñ4.9
MAD (mm)	3.0Ñ2.3	2.2Ñ1.0	2.5Ñ2.3
δVp (%)	9.7Ñ16.1	-5.7Ñ8.7	-3.8Ñ8.3
V_A-V_M Corr.	0.980	0.963	0.995

Semi-Automatic Segmentation of the Myocardial Scar from 3D Late Gadolinium Enhancement Magnetic Resonance Images Using a Deep Learning Approach

Fatemeh Zabihollahy[1], James A. White[2], Eranga Ukwatta[1]
[1]Department of System and Computer Engineering, Carleton University, Ottawa, Canada
[2]Stephenson Cardiac Imaging Centre - Libin Cardiovascular Institute of Alberta, University of Calgary, Calgary, Canada

Introduction: Segmentation of left ventricular (LV) myocardial scar from Late Gadolinium Enhancement Magnetic Resonance (LGE-MR) has an important role for clinical decision making and procedural planning in patients with ischemic cardiomyopathy. While currently, 2-dimensional 2D LGE MR is primarily used for this purpose, 3D LGE-MR has emerged with improved, isotropic spatial resolution, enabling more accurate spatial representation and quantification. However, techniques for 3D LGE segmentation are lacking.

Methods: The proposed method employed a deep learning algorithm for semi-automated segmentation of myocardial scar from 3D LGE-MR images. In particular, we developed an algorithm based on convolutional neural network (CNN), which is comprised of four convolutional layers and one pooling layer followed by a standard two layers neural network with 128 nodes in the hidden layer. We used 3D LGE-MR images from 34 patients with chronic myocardial infarction (MI) and a mean left ventricular ejection fraction (LVEF) of 32.1 Ñ12.7%. The datasets were then divided into a training set (N=10) and a testing set (N=24). The segmentation generated through our proposed method was compared with manual delineations performed by experienced experts. Furthermore, we compared the performance of the proposed algorithm with previously described signal intensity thresholding-based methods including full width at half maximum (FWHM) and signal threshold to reference mean (STRM) approaches, which are widely employed in the literature due to their efficiency and ease of use.

Results: We validated our method using 24 unobserved 3D LGE-MR datasets. Example results of CNN-based scar segmentation for 3D LGE-MR images from three patients are shown in Fig. 1. Visually, the algorithm-generated boundaries closely matching those of manual expert delineations. Validation metrics, average of Dice similarity coefficient (DSC), precision, and recall were computed as 93.63 Ñ2.61%, 94.17 Ñ 2.32%, and 93.54 Ñ 2.71% versus manually expert segmentation, respectively. Furthermore, the developed algorithm yielded a mean absolute volume difference (AVD) of 16.71 Ñ14.31% of manual scar volume. Table I summarizes the results of comparisons performed between the developed algorithm versus FWHM and STRM signal threshold-based techniques.

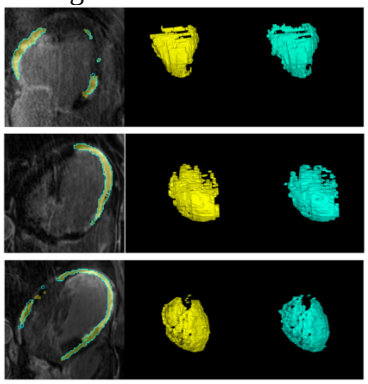

Table I Performance of All 3d Scar Segmentation Methods against Expert Manual Segmentation.

Method	DSC (%)	AVD (%)
CNN	93.63 ± 2.61	16.71 ± 14.31
FWHM	61.77 ± 9.81	33.22 ± 28.16
STRM + 2SD	48.33 ± 17.68	201.96 ± 173.41
STRM + 3SD	57.71 ± 14.42	91.45 ± 81.55
STRM + 4SD	62.44 ± 10.67	36.96 ± 47.57
STRM + 5SD	61.16 ± 9.95	34.01 ± 26.31
STRM + 6SD	54.08 ± 11.94	46.30 ± 21.25

Fig. 1 Exemplary results of scar segmentation from 3D LGE-MR images in three patients. Left: expert manual segmentation of scar (shown for one slice extracted from 3D LGE-MR) shown in yellow, and contours computed by the CNN-based method shown in cyan. The middle and right columns show volume rendered expert manual segmentation and CNN generated scar regions, respectively.

Conclusions: Our results showed that the described CNN-based algorithm yielded high accuracy for segmentation of myocardial scar from 3D LGE-MR images. As compared to the most widely used signal intensity-based methods, such as FWHM and STRM, our method achieved higher accuracy for scar segmentation versus manual expert delineation.

Motion correction in MRI using deep learning

PM Johnson and M Drangova
Robarts Research Institute, London, ON, Canada
Department of Medical Biophysics, Western University, London, ON, Canada

Introduction: Subject motion in MRI remains an unsolved problem; motion during image acquisition may cause artefacts that severely degrade image quality. In the clinic, if an image with motion artefacts is acquired, it will often be reacquired. This provides a source from which a large number of motion-degraded images, along with their respective re-scans, could be collected. These pairs of images could be used to train a neural network to identify the mapping relationship between an image with motion artefacts and a high quality, artefact free image. Inspired by previous work demonstrating MR image reconstruction with machine learning,[1,2] our objective is to train a neural network to perform motion corrected image reconstruction on image data with simulated motion artefacts. In this work, motion is simulated in previously acquired brain images; the image pairs (corrupted + original) are used to train a deep neural network (DNN).

Methods: An open source MRI data set[3] comprising T2* weighted, FLASH magnitude and phase brain images for 53 patients, each with 128 non-overlapping image slices was used to provide thousands of 2D complex images.

Motion Simulation: Each complex 2D image, from the data set described above, was Fourier transformed to simulate the acquired k-space data. To simulate rigid motion, k-space lines were rotated and phase shifted, simulating the k-space inconsistencies that would occur if the subject were moving. The motion profiles were parameterized by the time, magnitude and direction of motion and were randomly generated with constraints to keep the motion within the realm of realistic head motion. A unique 3D motion profile was applied to each image.

Network architecture and training: The DNN (Fig 1) was developed and trained using the TensorFlow library.[4] To correct for 3D motion in a 2D slice, data relocated to other slices due to through plane motion was recovered by incorporating neighbouring slices in the input. Each training pair was made up of a 2D ground truth image and its corresponding motion-corrupted, k-space, with 2 neighbouring slices in each direction. The input to the network has 5 channels; each channel contains the data from one k-space slice. The network training set consisted of 2048 image pairs; 64 pairs were reserved for validation and testing. The network was trained for 4 hrs using the SHARCNET computing network. Memory limitations required that the input data be under-sampled by a factor of approximately 4.

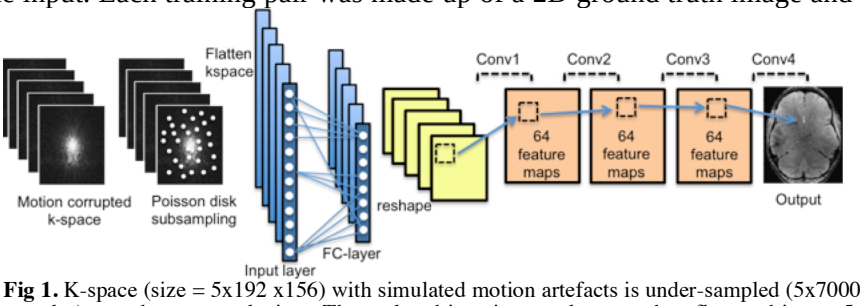

Fig 1. K-space (size = 5x192 x156) with simulated motion artefacts is under-sampled (5x7000 samples) to reduce network size. The real and imaginary values are then flattened into a 5-channel 1 dimensional vector (5x14000), which is the input layer of the DNN. The input layer is fully connected to the first hidden layer (FC-layer, size=5x7488), which is reshaped into 2D arrays (5x96x78) and then up sampled to the dimensions of the original images (5x192x156). The next 3 layers are all identical convolutional layers with 64 5x5 filters. The output of the network is the reconstructed, motion corrected magnitude image.

Results: The images predicted by the DNN, have improved image quality compared to the motion-corrupted images. The mean absolute error (MAE) between the motion corrupted and ground-truth images was 32% of the image mean value, while the (MAE) between the DNN-predicted and ground-truth images was only 11%. Most of the predicted images have significantly improved image quality; representative examples are shown in Fig. 2a and 2b. However, in some cases the network-predicted images have substantial blurring; a representative example is shown in Fig. 2c.

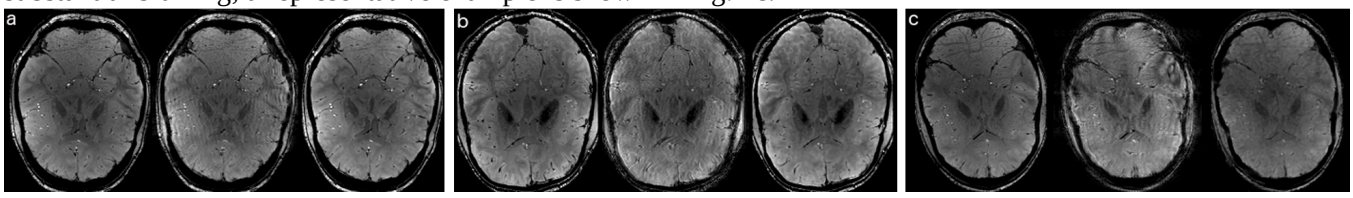

Fig 2. Examples of motion correction using the trained DNN. Image sets **a**, **b** and **c** represent three different examples from the test set. Ground truth, simulated-motion, and DNN-reconstructed images are shown in the first, middle and third columns, respectively. In both **a** and **b**, excellent artefact suppression is achieved. Image set **c**, is an example of unsuccessful motion correction. The network output in this example has substantial blurring.

Discussion: Motion-corrected image reconstruction was successfully achieved on brain images with simulated motion artefacts. This work represents the first time machine learning has been used to perform motion correction of MR images. Improving the consistency of the network performance is the focus of ongoing work.

References: [1] Zhu, Bo. et al., Image reconstruction by domain transform manifold learning, 2017 [2] Hammernik K, et al., Learning a Variational Network for Reconstruction of Accelerated MRI Data, 2017 [3] Forstmann BU, et al., Multi-modal ultra-high resolution structural 7-Tesla MRI data repository. 2014 [4] Abadi M. et al., TensorFlow, 2015.

Acknowledgements: The authors thank Compute Canada for access to SHARCNETôs computing resources.

Synthetic-CT using conditional generative adversarial neural networks for MRI-guided radiotherapy

Matt Hemsley*, Angus Lau

Department of Medical Biophysics, University of Toronto, Toronto, ON
Physical Sciences, Sunnybrook Research Institute, Toronto, ON

Introduction - Computed tomography (CT) is the conventional imaging modality for radiotherapy planning (RTP). CT is used to determine the electron density of imaged objects, a requirement for radiation dose calculations. Additional requirements for modern RTP are soft-tissue contrast, accurate gross tumor volume delineation and measurement of tumor function. This is provided by magnetic resonance imaging (MRI), but lack of electron density information precludes MRI from the sole RTP imaging modality. Methods for electron density assignment to MR images (synthetic-CT) have been reported [1, 2]. However most published methods place strict anatomical constraints on patients, and are impractical for clinical use due to high computational costs. The purpose of this study is to develop a computationally efficient method to generate synthetic-CTs for real-time adaptive radiotherapy, with no anatomical restrictions on patients.

Methods - The conditionally generative adversarial neural network (cGAN) configuration described by Isola *et al.*[3] was used to generate synthetic-CTs from input MR images. The cGAN architecture consists of two competing networks, a *generator* which generates candidate images based on a model distribution and a *discriminator* which discriminates between the candidate and ground truth images. The model is updated until images produced by the generator can not be distinguished from ground truth by the discriminator.

Data was comprised of brain images (n=7 patients) collected retrospectively from the Sunnybrook radiation therapy program. The images (3D T1w post-Gd MRI and planning CTs) were acquired using a Philips Ingenia MR-RT 1.5 T MRI and Philips Brilliance CT. The matching MR and CT image pairs were registered and sorted into two groups, 1) to train the neural network correlation model from input MR space to output CT space, and 2) to apply the model and qualitatively validate the accuracy of the synthetic-CTs.

Results - A cGAN configuration converting single MR slices to single CT slices was successfully implemented. Figure 1 shows qualitative feasibility. Notably, the patients bone structure which is invisible on MRI, but bright on CT, is well represented in the synthetic-CT, and the signal within the white and grey brain matter is relatively uniform similar to the traditional CT, in contrast to the complex MR representation. Training the cGAN to determine the correlation mapping on a paired MR/CT image set of 200 took roughly 90 minutes. Once the network was trained, a whole synthetic-CT brain volume (roughly 500 slices) could be generated per second.

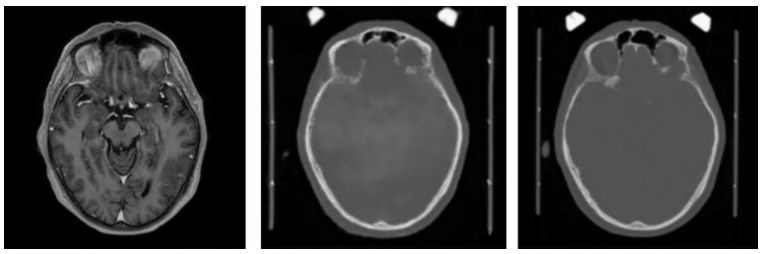

Figure 1. ***Left,*** MRI input to cGAN ***Centre,*** Synthetic-CT generated by cGAN ***Right,*** Traditional CT

Conclusions ï Assignment of electron density to MR images using a trained cGAN is feasible at clinically viable speeds. Future work includes training with a larger data set, and quantitative assessment by comparing calculated dose distributions made using the synthetic-CTs with those calculated with traditional CT and through applying similarity metrics.

References

[1] Uh, J., et al, (2014). Medical Physics, 41(5), 051711.
[2] Edmund, J. M., & Nyholm, T. (2017). Radiation Oncology (London, England), 12, 28.
[3] Isola, P., et .al, (2017). Retrieved from https://arxiv.org/abs/1611.07004v2

Oral Presentation Abstracts

Session 3: Bone and Joint Imaging

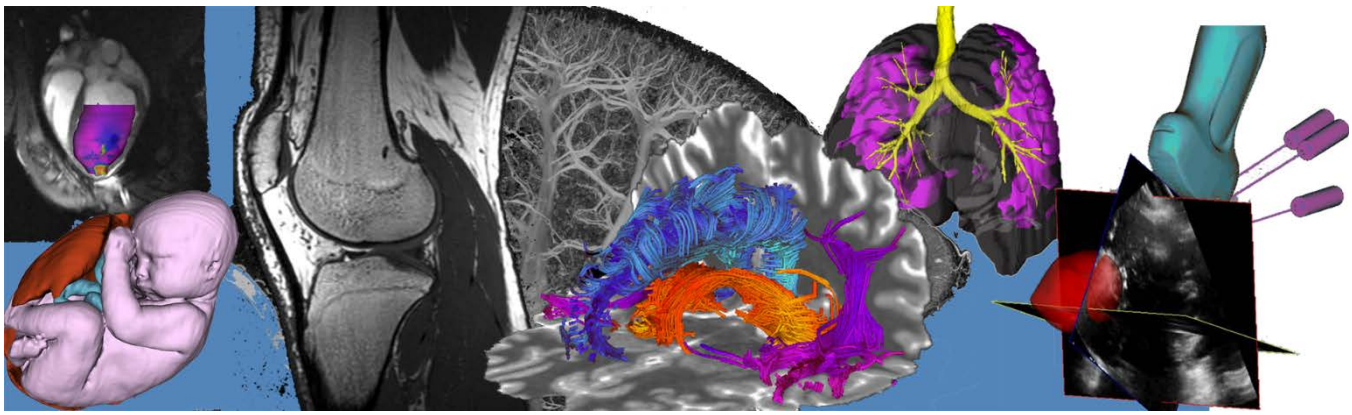

Title: Machine Vision Image Guided Surgery – Lighting the Way

Presenter: Beau Standish, Chief Executive Officer, 7D Surgical

Abstract:

Spine surgery is inherently difficult and is especially challenging when working on large deformity or complex procedures. Surgeons create a pre-operative plan to optimize patient outcome, but currently lack intraoperative feedback relating to the position of the spine as it's alignment is altered throughout the procedure. The limited feedback that exists requires ionizing radiation through the use of extensive fluoroscopy (2D planer views), but even then, the feedback in most cases is qualitative. Intraoperative CT navigation technologies may provide some 3D anatomical information, however, their lengthy set up time and cumbersome workflow has led to their low adoption rate. In addition, using ionizing radiation in the OR exposes harmful radiation to not only the patients, but also to the surgical staff.

There exists a need to provide surgeons with fast and accurate intraoperative feedback for complex multilevel spinal deformity cases without the use of ionization radiation. 7D Surgical's Machine-vision Image Guided Surgery (MvIGS) system for spine surgery employs cutting-edge 3D optical imaging technologies and machine vision algorithms to determine the location of individual vertebrae on the patient and automatically registers these anatomical landmarks to preoperative CT images. This enables an intraoperative radiation-free workflow, where patient registration and surgical navigation can occur in less than 20 seconds.

In this presentation we will review the 7D Surgical imaging platform, discuss our pipeline of innovations for intraoperative imaging and present existing challenges associated with real-time spine deformity characterization.

Validating 3D face morphing towards improving pre-operative planning in facial reconstruction surgery

Z Fishman [1,2], J Pope [1], OM Antonyshyn [3], JA Fialkov [3,4], CM Whyne [1,2]

1. Orthopaedic Biomechanics Laboratory, Sunnybrook Research Institute, Toronto, ON; 2. Institute of Biomaterials and Biomedical Engineering, University of Toronto, Toronto, ON; 3. Department of Surgery, University of Toronto, Toronto, ON; 4. Division of Plastic Surgery, Sunnybrook Health Sciences Center, Toronto, ON

Introduction: The face and craniofacial skeleton (CFS) is a complex 3D structure that is important to human function and cosmesis. Traumatic injury to the facial skeleton can be devastating and requires fracture treatment to both allow the recovery of mechanical function and restoration of pre-injury appearance. This work aims to add new imaging tools to the plastic surgeonôs workflow to help enable improved patient results. A patient would rarely have 3D imaging of their face or skull prior to the trauma they experienced, which results in missing shape information for guiding the reconstruction surgery. Furthermore, the pre-trauma photos that a patient commonly submits to the plastic surgeon upon consultation rarely include side views of the face since people generally ósmile at the cameraô. The face shape is especially lacking in cases where the mirror image of the head cannot be used, such as bi-frontal injuries, pan-facial fractures and nose traumas. Morphable models are capable of estimating a 3D face shape from a pre-trauma 2D photograph. The 3D face morphable model can fill in a missing gap in pre-operative planning for craniofacial reconstruction but validation is required for the high expectation of accuracy required for restoring the human face.

Methods: Using a collection of existing photos (range 5 to 50 per individual), we first detect and landmark the face in the picture. The Surrey Face Model (SFM) [1] is utilized to morph a trained average face shape to coincide with the landmarked points on the face. A 3D scan geometry was captured using a structured light scanner for each subject (Einscan-Pro) which was considered as a gold-standard for true facial shape. Accuracy of the SFM method was evaluated by comparing surface distances (per-vertex Euclidean distance) to rigidly registered (ICP) 3D scanned geometries. Distance errors less than 2 mm are target values deemed acceptable and comparable to a plastic surgeonôs manual results.

Results: Sixty-six percent of modelled points generated from the SFM were within 2.5mm of the closest point on the optically scanned face surface (N=10). Low distance errors (<1 mm) were found for the forehead region, around the eyes and nasal bridge, as these points are anchored well by landmarks. High distance error (> 3 mm) was measured around the cheeks due to a lack of landmarking information there, and at the nose tip due to a lack of perspective. A small number of well-chosen photos were found to perform as well as a larger photo collection.

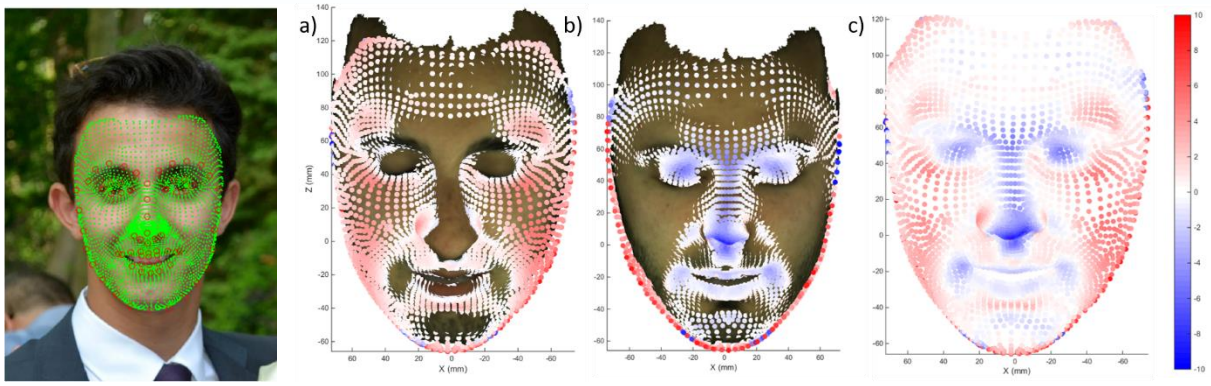

Figure 1. (Left) Projected 3D face mesh obtained from a 2D photo. (Right) Visualizing the 3D distance error between the face model and the registered 3D scan. The colormap corresponds to error ranging from -10 mm to +10 mm, where red is in front and blue is behind.

Conclusions: The 3D morphable model obtained from 2D patient photos was demonstrated to yield clinically acceptable accuracy (< 2 mm) in regions found around the eyes and forehead. Errors greater than 3 mm are caused by lack of regional landmarking (e.g. the cheeks) or perspective (e.g. nose tip). The 3D face shapes provided by this work are being developed into translational tools to help guide craniomaxillofacial reconstruction.

1. Huber, P.; Hu, G.; Tena, R.; Mortazavian, P.; Koppen, W. P.; Christmas, W. J.; Rªtsch, M.; Kittler, J. A Multiresolution 3D Morphable Face Model and Fitting Framework. *Proc. 11th Jt. Conf. Comput. Vision, Imaging Comput. Graph. Theory Appl.* **2016**, 79ï86.

Soft Tissue Strain Measurement in Human Cadaveric Knees Using Embedded Radiopaque Markers

Alexandra Blokker[a,b], Ryan Wood, MD[c,e], Timothy Burkhart, PhD[b,c,e] , David Holdsworth, PhD[a,b,c,d], Alan. Getgood, MD[c,e]
[a]Robarts Research Institute, [b]Dept of Biomedical Engineering, [c]Dept of Surgery [d]Dept. of Medical Biophysics,
[e]Fowler Kennedy Sports Medicine Clinic, Western University, London, ON, Canada

Introduction. Despite significant advancements in anterior cruciate ligament reconstruction (ACLR) methods, upwards of 14% experience acute failure, and 60% develop osteoarthritis in the knee joint. These conditions may be partly attributed an incomplete understanding of soft tissue mechanical properties (i.e., tissue strain), leading to potential changes in the jointôs kinematic profile. Traditionally, non-destructive material testing directly instrumented the tissue, but was limited in the type, number, and regions of tissues tested. Radiostereometric analysis (RSA) has been used to non-invasively quantify soft tissue strain by following radio-opaque beads distributed throughout the tissue. This method is highly accurate and useful, but cannot generate three-dimensional finite element models (FEM) of the joint. Micro-computed tomography (micro-CT) imaging generates non-invasive, high resolution, three-dimensional images which can be used to create and validate FEMs. Therefore, the purpose of this research was to non-invasively quantify knee joint soft tissue strains in response to applied loading patterns using radio-opaque beads and micro-CT imaging.

Methods. Small diameter zirconium dioxide beads (0.8 mm diameter) were arthroscopically placed into the anteromedial bundle (AMB) of the ACL of fresh-frozen human cadavers (N=4, mid-tibia to mid-femur, age: 59Ñ9 years, 1 male, 2 right) by an experienced orthopedic fellow. Beads were also embedded in several other structures not described here (Fig. 1). The beads were implanted 3 mm apart and approximately 3 mm deep (depth controlled by embedding an 18 gauge needle tip to the end of the bevel). Beads were arranged in two rows along the length of the ACL as follows: i) 4 in the femoral insertion; ii) 6 in the mid-substance; and iii) 4 in the tibia insertion. Three beads each were embedded in the femur and tibia to create rigid coordinate systems. The joints were then loaded using a previously validated micro-CT compatible, five degree-of-freedom motion simulator to the following force targets while maintaining a 10 N compressive load: i) 5 Nm internal rotation; ii) 100 N anterior translation; and iii) a combined load of 100 N compression, 5 Nm internal rotation, 10 Nm valgus rotation, and 100 N anterior translation. The loads were applied at 0Á 15Á and 30Áof knee flexion. Images were acquired on a cone beam micro-CT scanner (GE Locus Ultra, London, Ontario) with a standard anatomical protocol (16 s, 80 kVp, 50 mA, 0.15 mm isotropic voxels) at baseline and each load target; this was repeated five times for each condition. A custom program thresholded and located the centroid of each bead in the scanner coordinate system for each image, then inter-bead distances were measured before and after load application to quantify tissue strain. Strains were calculated both globally, along the entire length of the ligament, and regionally (at the femoral footprint, mid-substance, and tibial footprint). Trans-axial strain was also calculated. The axial strain values from a 5 Nm internal rotation load applied at a 0ę flexion angle are presented here to demonstrate the method, but these calculations can be repeated for all joint conditions tested.

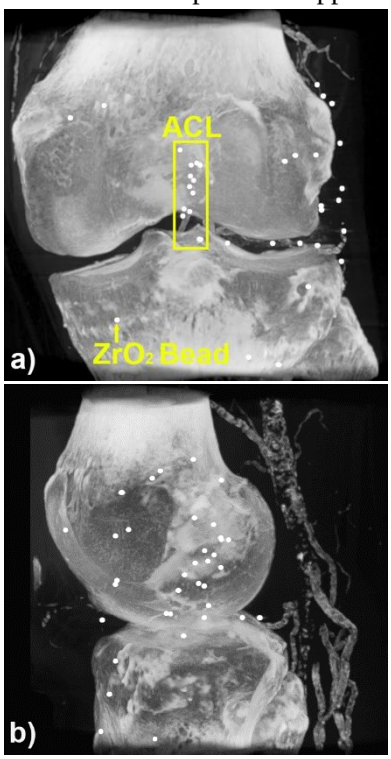

Fig 1. Maximum intensity projection of a) coronal and b) sagittal views of an unloaded human cadaveric knee joint (right) at 0ę flexion with ZrO_2 beads embedded in soft tissue structures.

Results. All images showed the entire joint capsule, with all beads easily thresholded from surrounding tissue. The majority of the beads remained embedded within the tissue throughout the entire testing protocol. There was no significant difference in the strains calculated across the five trials ($p>0.05$ for all) for each region. The standard deviations in the measured strains did not exceed 3.2 % strain for all regions. The regional strains were 2.0 (0.22) % in the femoral insertion, 2.9 (2.7) % in the mid-substance, and 3.1 (1.9) % at the tibial insertion. The greatest variation in strains measured was in the ligament mid-substance.

Conclusions. The method presented here facilitates non-invasive, high resolution quantification of both global and regional soft tissue strains. It allows strain measurement in multiple regions of each tissue, and in multiple tissue structures simultaneously. This method furthers the study of the ACL and other soft tissues because it allows researchers to non-invasively quantify regional tissue strains and create and validate high detail FEMs that will allow for further understanding of the joint.

Knee Osteophyte Depiction using 3D Ultrasound Imaging Compared to Computed Tomography

Authors: Vendries, V (MSc, BSc), Ungi, T (PhD, MD), Harry, J, Kunz, M (PhD), MacKenzie, L (PhD), Venne, G (PhD, D.O)
Affiliations: Anatomical Sciences Program & Department of Biomedical and Molecular Sciences Queenôs University, Kingston, Ontario, Canada K7L 3N6
School of Computing, Queenôs University, Kingston, Ontario, Canada K7L 3N6
Department of Anatomy and Cell Biology, McGill University, Montreal, Quebec, Canada, H3A 0G4

Background: Osteophytes (marginal bony outgrowths) are a common radiographic marker of osteoarthritis (OA) and joint degeneration[1]. However, due to their variable morphologic composition, osteophytes are not accurately depicted using conventional imaging modalities[1,2]. This represents problems for evaluating the anatomical changes of the osteoarthritic joint, and for the design of surgical interventions that rely on the accuracy of pre-operative images[2]. Studies have shown that ultrasound is a promising tool to detect articular changes such as the presence of osteophytes, and to monitor the progression of OA[1]. Furthermore, 3D ultrasound (3DUS), a tool for volume rendering and surface representation[3], can potentially offer a means to quantify and depict osteophytes.

Objective: To compare osteophyte depiction in the knee joint using 3DUS and conventional Computed Tomography (CT) and to evaluate the ability of 3DUS at quantifying osteophyte surface depiction.

Methods: Eleven fresh-frozen-thawed human cadaveric knees were pre-scanned for the presence of osteophytes according to a previously validated US semi-quantitative grading system[1]. Five knee sides with visible signs of OA were selected; 3DUS and CT images were obtained, segmented and digitally 3D reconstructed. The knees were dissected and Structured Light Scanner (SLS) images of the physical joint surface were obtained. Using a custom software, surface matching and Root Mean Square Error (RMSE) analyses were performed to assess the accuracy of each of the evaluated modalities in capturing the anatomy of the bone surface at the sites of osteophytes. 3DUS and CT models were compared to the SLS model, which was used as ground truth.

Results: The average RMSE for 3DUS to SLS and for CT to SLS model comparisons were 0.87mm and 0.95mm respectively. No statistical difference was found between 3DUS and CT (p=0.43). Comparative observation of imaging modalities set against each other suggests that 3DUS is superior in depicting osteophytes with cartilage and fibrocartilage tissue characteristics compared to CT.

Conclusions: 3D Ultrasound can depict features of OA such as osteophytes together with their cartilaginous portion, which is not accurately represented using CT. It is feasible to compare 3DUS to conventional imaging for bone surface depiction within the knee joint. Lastly, 3DUS can provide useful information about not only the presence, but the extent of osteophytes.

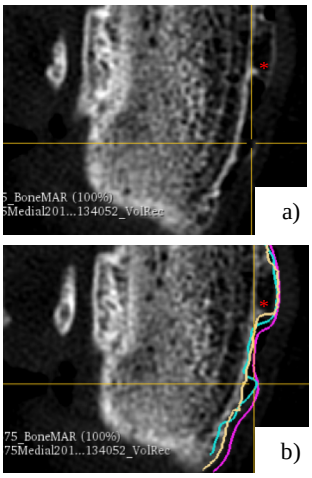

Axial view of CT scan (a), with superimposed contours from the 3DUS (blue), LS (purple) and CT (yellow) models (b). *= posterior osteophyte; += anterior osteophyte

References: 1. Koski J, Kamel A, Waris P, et al. Atlas-based knee osteophyte assessment with ultrasonography and radiography: relationship to arthroscopic degeneration of articular cartilage. Scandinavian Journal of Rheumatology.2015;45(2):158-164. doi:10.3109/03009742.2015.1055797.
2. Kunz M, Balaketheeswaran S, Ellis RE, Rudan JF. The influence of osteophyte depiction in CT for patient-specific guided hip resurfacing procedures. International Journal of Computer Assisted Radiology and Surgery. 2015;10(6):717-726. doi:10.1007/s11548-015-1200-7.
3. Cruz LB. Basics on 3D Ultrasound. Donald School Journal of Ultrasound in Obstetrics & Gynecology. 2008:1-5. doi:10.5005/jp-journals-10009-1071.

Measuring Joint Blood Flow with DCE-NIRS: Application to Rheumatoid Arthritis Treatment Monitoring

Seva Ioussoufovitch[1*], Laura B. Morrison[2], Keith St Lawrence[2,3], Ting-Yim Lee[2,3,4], Mamadou Diop[2,3]
[1]Department of Biomedical Engineering, Western University, London, Ontario, N6A 5C1, Canada
[2]Imaging Program, Lawson Health Research Institute, London, Ontario, N6A 4V2, Canada
[3]Department of Medical Biophysics, Western University, London, Ontario, N6A 5C1, Canada
[4]Imaging Program, Robarts Research Institute, London, Ontario, N6A 5K8, Canada
**Primary Author*

Introduction: Over the past three decades, the emergence of biologic drugs has reduced the burden of rheumatoid arthritis (RA) and made remission a clinically achievable goal. While these drugs are one of the most effective RA therapies currently available, they are expensive and do not work in 30% of patients [Rubbert-Roth & Finckh (2009), Arthritis Res. Ther., **11**]. Due to a lack of convenient and sensitive treatment monitoring tools, patients can spend months on biologics before treatment ineffectiveness is identified [Singh et al. (2012), Arthritis Care Res. (Hoboken)., **64**]. Considering the high cost of biologic drugs and the risk of further joint damage associated with the use of ineffective therapies, there is a clear need for identifying patients who are unresponsive to biologic treatments. Chronic hypoxia, which is a hallmark of RA, is a potent signal for blood flow [Konisti et al. (2012) Nat. Rev. Rheumatol., **8**]; based on this, we previously developed a non-invasive dynamic contrast-enhanced time-resolved near-infrared spectroscopy (DCE TR-NIRS) technique for measuring joint blood flow (BF) and subsequently showed that it can distinguish healthy from arthritic joints within one week of onset [Rajaram et al. (2016), Biomed. Opt. Express, **7**]. Building on this advancement, our current objective is to investigate whether joint BF, as measured by our DCE TR-NIRS technique, can be used as an early biomarker of treatment response in RA.

Methods: Arthritis was induced in adult male Lewis rats using the well-established adjuvant-induced arthritis (AIA) rat model [Bendele (2001), J. Musculoskelet. Neuronal Interact., **1**]. Animals acclimated for 5ï 7 days prior to the start of experiments. Two baseline measurements were acquired 21 and 15 days prior to adjuvant injection on day 0. Thereafter, ankle joint BF was measured every 5 days until the end of the study on day 30. Caliper measurements of ankle joint width were also performed to assess joint inflammation. Starting on day 20 after adjuvant injection, rats were treated with etanercept (EnbrelÈ: 0.5 ml/kg; intramuscular injection) 3 times with a constant interval of 5 days. The TR-NIRS system was composed of a picosecond diode laser emitting at 805nm with a frequency of 80MHz; the laser output was coupled into a 400ε m emission fiber. Light transmitted through the ankle joint was collected with a detection probe composed of a fiber bundle coupled to a hybrid photomultiplier tube and a time-resolved detection module. Measurements were acquired by positioning the emission and detection probes transversely across the rat ankle joint. A 0.15mL bolus of Indocyanine Green (ICG: 0.25 mg/kg) solution was injected into a tail vein 10 seconds after starting a measurement. Temporal changes in tissue ICG concentration and arterial ICG concentration were acquired using the TR-NIRS system and a dye densitometer placed on the animalôs contralateral paw, respectively. Tissue and arterial ICG concentrations curves were used as inputs into a previously reported deconvolution algorithm to extract joint BF [Cenic et al. (1999), Am. J. Neuroradiol. **20**]. Friedmanôs test and paired-sample *t*-tests were conducted on the BF data to determine presence of significant differences.

Results: Thirty-four ankle joint BF measurements were acquired over a 51-day period. Mean ankle joint BF increased significantly ($p<0.05$) from 5.64 mL/min/100g at baseline to 16.71 mL/min/100g during arthritis induction; mean ankle width increased by 1.36mm over this period. Mean ankle joint BF dropped by 5.65 mL/min/100g within 10 days of treatment, which represented a 34% decrease in BF. In contrast to BF, ankle width continued increasing during treatment for an additional 10 days prior to regression. The significant increase in joint BF upon arthritis induction and the subsequent 34% decrease in mean joint BF over a 10-day treatment period were consistent with the known pathophysiology of RA. Notably, joint BF measurements demonstrated greater sensitivity to treatment onset than decreases in joint inflammation measured using calipers.

Conclusion: Arthritis induction caused a significant and consistent increase in joint BF; initiation of treatment with etanercept resulted in a 34% decrease in mean joint BF within 10 days. In addition, reduction of BF in response to treatment was observed 10 days prior to any change in joint inflammation measured by calipers. This is an ongoing study and the promising preliminary results reported here support the potential of our joint BF technique to be a highly sensitive RA treatment monitoring tool.

Oral Presentation Abstracts

Session 4: Cancer Imaging

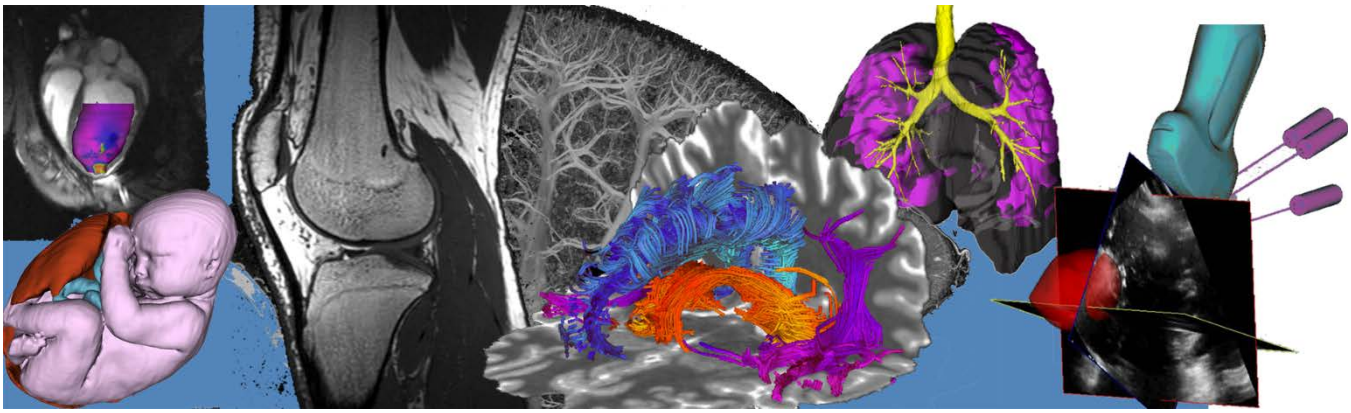

Automatic Prostate Cancer Detection and Localization on Digital Histopathology Imaging

Wenchao Han[1,2,6], E. Gibson[7], M. Gaed[5], J. A. Gomez[5], M. Moussa[5], J. L. Chin[4,5], S.E. Pautler[4,5], G. Bauman[2,5], A. D. Ward[1,2,5,6] (research supervisor)

[1]Baines Imaging Research Laboratory, London Regional Cancer Program, Depts. of [2]Medical Biophysics, [3]Pathology, [4]Surgery, [5]Oncology, Western University, [6]Lawson Health Research Institute, London, Ontario, Canada; [7]Centre for Medical Image Computing, University College London, London, UK

Introduction: Automatic detection and localization of cancerous lesions on digital histology images from radical prostatectomy specimens would facilitate quantitative and graphical pathology reporting that potentially benefits prognosis and adjuvant therapy planning which relates to tumour volumes, locations, and their Gleason grades.[1,2] It also supports image studies validating in vivo imaging against gold-standard histopathology.[3] Our objective is to develop a fully automatic system for cancer detection and localization on digital histology images, which is sufficiently efficient, robust to staining variations of the specimens, and well-validated to be embedded into everyday clinical use in the pathology workflow.

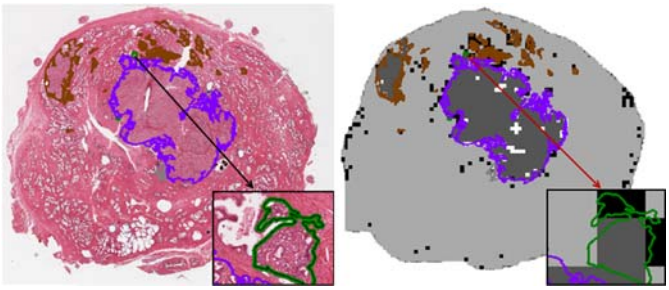

Fig. 1: WSI (left) and cancer map (right) one patient. Coloured contours are the expert-drawn reference standard (with colours different indicating different Gleason grades). Light and dark grey: Correctly labeled normal and cancerous tissues. Black and white: false positive and false negative cancer tissues. Note the detection of a very small cancerous region.

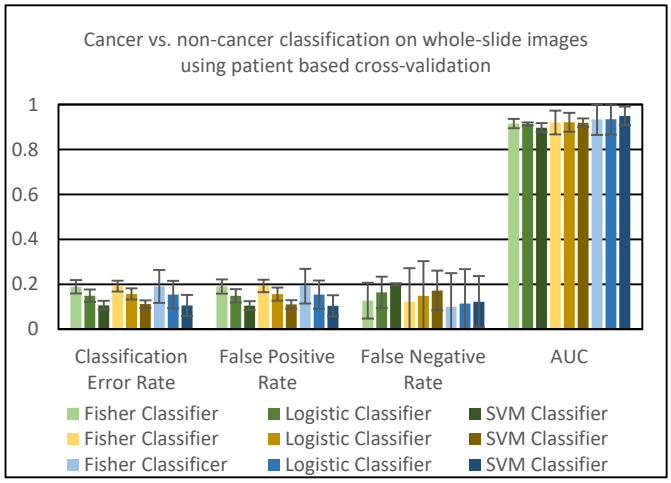

Fig. 2: Cancer detection performance estimation using WSIs.

Methods: 199 mid-gland whole-slide-images (WSIs) were obtained from 49 radical prostatectomy specimens. The surgically removed prostates were sectioned at $4\mu m$, stained with hematoxylin and eosin (H&E) and scanned at 20X ($0.5\mu m/pixel$). Computations were conducted independently on $480\mu m \times 480um$ sub-images covering each WSI completely. 33 WSIs from 8 patients were used for system tuning and a separate 41 patient data set comprising 703,745 $480\mu m \times 480\mu m$ sub-images across 166 whole-slide images (WSIs) were used for validation. Computation proceeded in following steps. (1) Labeling each tissue component as nucleus, lumen, and stroma/other by applying colour deconvolution and a novel adaptive thresholding algorithm for nucleus segmentation; global thresholding for lumen segmentation; and allocating all the rest as stroma/other. (2) Extracting first- second-order statistical features from labeled tissue component sub-images and selecting the 13 top-ranked features by backward feature selection using a Fisher classifier on the tuning data set. (3) Classifying cancerous vs. non-cancerous sub-images using supervised machine learning with three different classifiers [Fisher classifier, logistic classifier, and support vector machine (SVM) classifier]. (4) Validating the system against expert-drawn contours via leave-one-patient-out, 2-fold, and 5-fold cross-validation using each classifier on the validation data set. Contours annotated cancerous regions at very high precision and were verified by a genitourinary pathologist. All samples in the data set were grouped on a per-patient basis.

Results: Our system can generate graphical whole-slide cancer maps as shown in Fig.1. The best performing SVM classifier gives an error rate of $10.6\% \pm 4.7\%$, AUC of 0.95 ± 0.04, false negative rate of $12.3\% \pm 11.4\%$, and false positive rate of $10.5\% \pm 4.7\%$ in leave-one-patient-out CV as Fig. 2 shows.

Conclusion: In general, our system demonstrated good performance in cancer detection on mid-gland prostate WSIs despite staining variations. Experiments showed the system is robust to different classifiers and varying sample sizes (i.e. varying the number of CV folds). Ongoing work includes automatic Gleason grading.

References: [1]L. Egevad et al, Modern Pathology 24(1), 1ï 5, 2011; [2]T. H. van der Kwast et al, Modern Pathology 24(1), 16ï 25, 2011. [3] Gibson, E., et al. Int J Radiat Oncol Biol Phys, 2016. 96(1): 188-196.

Early detection of lung cancer recurrence after stereotactic ablative radiation therapy: radiomics system design

Salma Dammak[1], Dr. David Palma[1], Dr. Sarah Mattonen[2], Dr. Suresh Senan[3], Dr. Aaron D. Ward[1]
[1]The University of Western Ontario, [2]Stanford University, [3]VU University Medical Center

Introduction: Stereotactic ablative radiotherapy (SABR) is a guideline-recommended treatment option for patients with Stage I non-small cell lung cancer who are inoperable [1]. This treatment, however, has a high likelihood of introducing a type of benign radiation-induced lung injury (RILI), that can be difficult to differentiate from disease recurrence on follow-up computed tomography (CT) scans. Figure 1 shows an example of each outcome. In a preliminary study (n = 45) with an unbalanced training set (1 recurrence : 2 RILI), we have shown that radiomics coupled with machine learning shows promise for differentiating RILI from recurrence in the 2ï 5 month period post-SABR [2]. We hypothesized that there exist machine learning parameters producing a system that does this with an area under the receiver operator characteristic curve (AUC) > 0.80 on a balanced training and testing set.

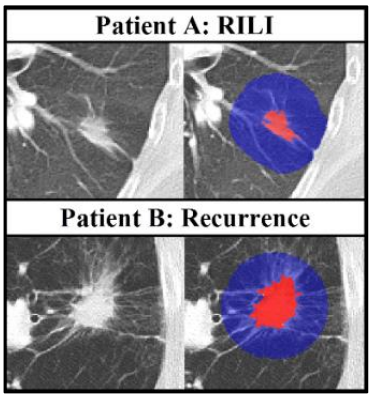

***Figure 1**: Original (left) and contoured (right) two patients' CT scans A with RILI and B with recurrence*

***Table 1:** Features used by both systems from consolidative (C) and peri-consolidative (P) regions*

Order	Feature Name	Region
1	MeanGradientValue	c
2	GLCM Cluster Prominence	p
3	GLRLM Short Run High Gray Level Emphasis	p
4	Surface Area	c
5	GL 1-Percentile	c
6	GLCM Contrast	p
7	GL Bimodality Coefficient	p
8	GL 99-Percentile	p
9	GL Bimodality Coefficient	c

Methods: This study was approved by our institutional human subjects research ethics board. We obtained contrast-enhanced follow up CT scans (taken closest to 3 months, and no later than 6 months, post-SABR) from a balanced set of 52 patients. We conducted our analysis within two regions of interest: the consolidative region (shown in red in Figure 1) and the peri-consolidative region (shown in blue in Figure 1), which we obtained using a semi-automated algorithm we have previously published [3]. This algorithm segmented the peri-consolidative region by thresholding the 3D distance transform of the consolidation with a threshold of 16 mm based on our previous observation that classification results do not change much with differing volume and shape above this threshold [4]. From these regions, we extracted a 136 features, which we reduced using supervised greedy forward feature selection with four different criteria for minimization of error, obtaining four sets of 10 features. Then for each of those sets, we used leave-one-out (LOO) and 2-fold cross validation (CV) to investigate seven common classifiers in separating RILI from recurrence. Using the resulting AUC, we determined the best performing system (highest AUC). Then, we determined the most robust system by finding the set of features with least variation in AUC across all classifiers that had a mean AUC > 0.80, and chose the classifier with the best error metrics for that set.

Results: The best performing system had an AUC of 0.89 and used the top 8 features from Table 1 with the radial basis support vector machine (SVM) classifier. The most robust combination had an AUC of 0.85 and used all features in Table 1 with the nu-type SVM classifier. Error metrics [AUC, error, false negative rate (FNR) and false positive rate (FPR)] from LOO CV and two-fold CV for both systems are shown in Figure 2. The more robust system has less variability in error metrics with changing training and testing set sizes, suggesting that it is likely to be generalizable. As seen in Table 1, both systems used features from the consolidative region and peri-consolidative region to arrive at these results.

Conclusions: Analysis of 52 patients with an equal split of outcomes confirmed that radiomics combined with machine learning provides a promising solution to differentiating RILI from recurrence within the first 5 months post-SABR with an AUC > 0.80 whether looking for the best performing or most robust system. Both systems relied on features from the peri-consolidative region and the consolidative region which indicates that they are both important for further study.

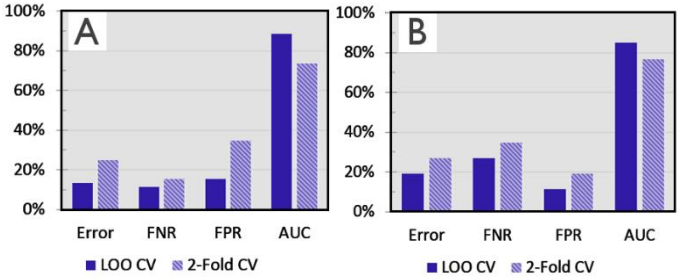

***Figure 2:** Error metrics for the best performing system (A) and most robust system (B) with LOO-CV vs. 2-fold CV*

References:

1. Ettinger DS *et al.*, NCCN. 2017.
2. Mattonen SA *et al.*, Int J Radiat Oncol Biol Phys., 2016: 94(5):1121-8.
3. Mattonen SA *et al.*, J Med Imaging (Bellingham), 2015:2(4):041010.
4. Mattonen SA *et al*, SPIE 9038, 2014.

Online assessment of dose changes in head and neck radiotherapy without dose re-computation using deformable image registration.

Jason Vickress[1], Rob Barnett[1,2,3], Jerry Battista[1,2,3], Slav Yartsev[1,2,3]
Departments of [1]Medical Biophysics and [2]Oncology, Western University and
[3]London Regional Cancer Program, London Health Sciences Centre, London, Ontario

Background: Head and neck cancer is commonly treated with radiation, when visible volume changes are detected, plan adaptation may be required during the course of treatment. Currently plan adaptations consume significant clinical resources and it is difficult to determine if they are clinically justified. Head and neck radiotherapy is typically performed with cone-beam CT (CBCT) image guidance. Daily pre-treatment CBCT imaging is routinely used to qualitatively assess anatomy change, but no quantitative assessment is available without repeated diagnostic CT studies and dose re-calculation. We propose to use deformable image registration (DIR) performed between the planning CT (PCT) and daily CBCT studies with the planned dose distribution to provide a fast assessment of the necessity for plan adaptation.

Methods: This study involved 18 head-and-neck cancer patients treated with CBCT image guidance who had their treatment plan modified on day X based on an additional CT simulation (ReCT). Anatomical changes were analyzed using DIR between pairs of image sets (fixed to moving) i) PCT to day X CBCT and ii) PCT to ReCT. DIR was performed using the commercial DIR algorithm from MIM (MIM version 6.5). Dose effects were calculated using dose distributions calculated on either the PCT or ReCT taken from a Pinnacle treatment planning system (version 9.10) and rigidly registered to the moving image. Both pairs of images and two dose distributions produced four methods to predict dose change (figure 1) with the gold standard method being the DIR from PCT to ReCT with the recomputed dose on the ReCT (method A). Changes in the dose to ipsilateral and contralateral parotid glands and spinal cord were evaluated for each method and compared to the gold standard through voxel-by-voxel dose changes. The necessity of plan adaptation was assessed by predicting the dose to 95% (D95) of the planning target volume and the mean dose to the parotids. Adaption was triggered if the D95 was below the prescribed dose or the mean dose to the parotids was above 26 Gy.

Results: Compared to the gold standard the simplest approach, method C yielded a voxel-wise dose error of 13%, 13%, and 6% for the ipsilateral and contralateral parotids, and spinal cord, respectively, whereas method D yielded a dose error correspondingly of 7%, 8%, and 4%. Results for the ipsilateral parotid are shown as a box plot in figure 2 for methods C and D. The treatment plans for all 18 patients were adapted clinically but our analysis showed that only 6 needed an adaptation according to the gold standard yielding 12 potential unnecessary adaptations. Using method C had four unnecessary adaptations and method D had two unnecessary adaptations and both methods missed no required adaptations.

Conclusion: The current practice is to qualitatively assess pre-treatment CBCT imaging to determine when to proceed with plan adaption but a quantitative alternative is needed. Using a daily CBCT in place of a ReCT can provide a fast quantitative assessment of the necessity of plan adaptation even without re-computing dose.

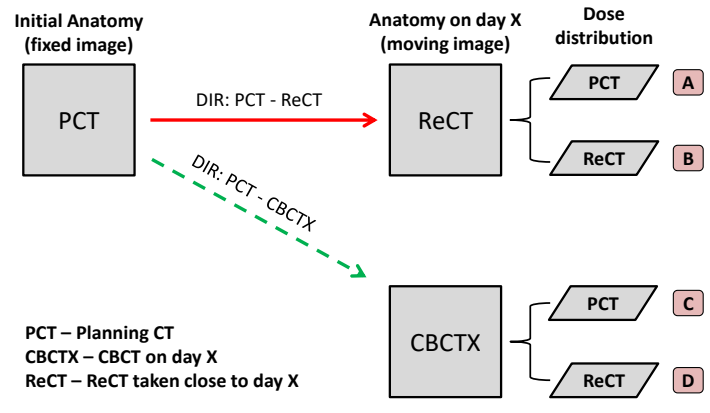

Figure 1: Schematic of different registrations and dose distributions used. (method A is the gold standard)

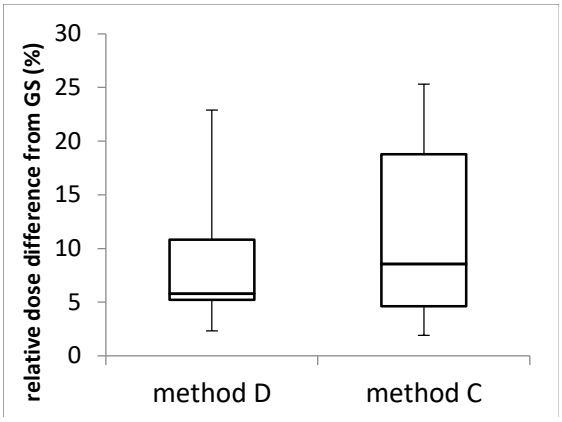

Figure 2: Relative dose difference from gold standard (GS) using DIR to CBCT using either recomputed or planned dose (methods D&C).

Case Report: Hyperpolarized ^{13}C Imaging of a Castration-Resistant Prostate Cancer Patient

Casey Y. Lee[1,2], Benjamin J. Geraghty[1,2], Justin Y. C. Lau[1,2,3], Albert P. Chen[4], William J. Perks[5], Masoom A. Haider[6], Urban Emmenegger[7,8], and Charles H. Cunningham[1,2]

1. Dept. of Medical Biophysics, University of Toronto, Toronto, ON, Canada 2. Physical Sciences, Sunnybrook Research Institute, Toronto 3. Cardiovascular Medicine, Radcliffe Department of Medicine, University of Oxford, United Kingdom 4. GE Healthcare, Toronto 5. Pharmacy, Sunnybrook Research Institute, Toronto 6. Dept. of Medical Imaging, University of Toronto and Ontario Institute of Cancer Research, Toronto 7. Sunnybrook Odette Cancer Centre and Research Institute, Sunnybrook Health Sciences Centre, Toronto 8. Institute of Medical Science, University of Toronto, Toronto

Introduction Hyperpolarized (HP) ^{13}C MRI is a new, non-invasive metabolic imaging approach that has been recently demonstrated in human studies [1,2]. This technique enables the imaging of [1-^{13}C]pyruvate and its metabolic products including [1-^{13}C]lactate and ^{13}C-bicarbonate *in vivo* [3]. It has the potential to be a powerful clinical tool in assessing the risk of metastasis and to monitor response to cancer treatments, based on the known correlation between tumour lactate concentration, metastasis and radiation resistance [4,5]. In this study, the feasibility of imaging ^{13}C-lactate in the region of spinal metastases in a patient with castration-resistant prostate cancer (CPRC) using HP ^{13}C MRI is investigated. Here, we present the data of the first HP ^{13}C imaging study of the vertebral region of this patient.

Methods The ^{13}C volume transmitter and the 8-channel ^{13}C receive array consisting of 2 paddles were installed on a GE MR750 3T MRI (GE Healthcare, Waukesha, WI). The patient was positioned supine with the receive array along the spine and received a 0.1mmol/kg dose of HP [1-^{13}C]pyruvate. The ^{13}C signal was acquired with spectral-spatial excitation of lactate/pyruvate/urea resonances (sequentially) followed by a dual-echo 3D EPI readout (5s TR; sagittal; 2cm isotropic resolution with FOV 256x40x20cm^3) [6]. After each set of metabolite images, a spectrum was acquired from the 4cm-thick axial slab centred over the T8/T9 region for off-resonance shift correction. The final metabolite images were generated by summing the individual time-points to improve SNR. These summed images were overlaid on a standard ^{1}H 3-plane single-shot fast spin echo (SSFSE) localizer images (FOV 48x48 cm^2, 15/6/12cm axial/sagittal/coronal slabs, 7 slices per plane, 5mm slice-thickness) and interpolated to 512x512 matrix to assess the metabolite distributions. ROIs over aorta, kidney, spine, and back muscles were drawn to investigate lactate-to-pyruvate ratio (Lac/Pyr) and mean lactate SNRs for each ROI (Fig.1).

Results and Discussion The resampled ^{13}C images onto the localizer images show notable lactate signals from the aorta, kidney, and skeletal muscle adjacent to the spine. While there was no significantly elevated lactate detected within the spine in this patient (Lac/Pyr = 0.49), strong lactate signals within the skeletal muscle adjacent T10-L5 were observed (Lac/Pyr = 1.68). Since this patient had a remarkable response to his treatment as evidenced by declining prostate specific antigen (PSA) levels prior to HP ^{13}C MRI, which eventually became undetectable 4 months later, the low lactate in the spine is consistent with the patientôs beneficial clinical course. Moreover, the mean lactate SNR from the spine was at 7.65Ñ1.53, which is comparable to that of skeletal muscle adjacent to the spine (12.21Ñ3.62) and aorta (12.84Ñ3.07), suggesting that the coil configuration and pulse sequence used in this study will be adequate in detecting lactate signals from spinal metastases in future studies.

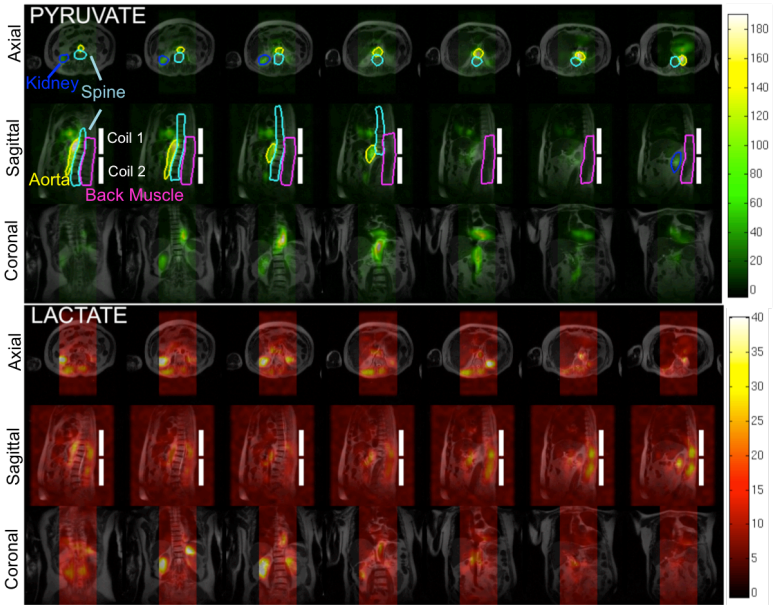

Fig 1. The 13C pyruvate- and lactate-signals are overlaid on the localizer images. The color bars represent the SNR. The Lac/Pyr were 0.49, 1.68, 0.17, and 0.75 and the mean lactate SNRs were 7.65Ñ1.53, 12.21Ñ3.62, 12.84Ñ3.07, and 20.23 Ñ7.65 for spine, back muscle, aorta, and kidney, respectively.

Conclusion In this study, we demonstrated the feasibility of acquisition and reconstruction of large FOV HP ^{13}C pyruvate- and lactate-images of the vertebral region of a CRPC patient with no adverse clinical effects. Recent clinical assessment of this patient suggests that he may have had barely active metastases at the time of the HP ^{13}C study, suggesting that the image presented in this abstract may reflect that of a negative control, providing useful information regarding the background signal that may aid the interpretation in future cases.

Acknowledgements The authors thank Julie Green and Sumeet Sachdeva for coordinating the study and Ruby Endre for MR technical support. Funding support from the Prostate Cancer Canada Movember Discovery Grant (D2013-6). **References** 1) Cunningham CH, *et al*. Circulation research. 2016. 2) Nelson SJ, *et al*. Sci Transl Med. 2013. 3) Ardenkjþr-Larsen JH, *et al*. 2003. 4) Walenta S, *et al*. Cancer Res. 2000. 5) Quennet V, *et al*. Radiother. Oncol. 2006. 6) Geraghty BJ, *et al*. Magn. Res. Med. 2017.

Longitudinal assessment of single-dose radiation-induced tumour vascular changes with functional optical coherence tomography

Valentin Demidov[a,*], Azusa Maeda[a], Mitsuro Sugita[b], Victoria Madge[c], Siddharth Sadanand[d], Costel Flueraru[e], I. Alex Vitkin[a,b,f]

[a]University of Toronto, Department of Medical Biophysics, Toronto, Canada
[b]University Health Network, Princess Margaret Cancer Centre, Toronto, Canada
[c]Carleton University, Department of Systems and Computer Engineering, Ottawa, Canada
[d]University of Toronto, Department of Chemistry, Toronto, Canada
[e]National Research Council Canada, Information Communication Technology, Ottawa, Canada
[f]University of Toronto, Department of Radiation Oncology, Toronto, Canada

Radiation therapy (RT) is widely used to treat many types of cancer either alone or in combination with other therapies. A variety of doses and RT fractionation schemes have been developed to effectively kill cancer cells, and/or to prevent them from growing and dividing. Recent RT advances have revived interest in delivering higher doses of radiation precisely in fewer fractions, which may invoke both cellular and microvascular damage mechanisms. Microvasculature may thus be a potentially sensitive functional biomarker of RT early response [1], but is (1) difficult to measure directly and non-invasively, (2) even if successfully measured and quantified, its time course, dose dependencies, and overall importance in RT remain unclear. This is mostly due to the inability to study the dynamic response longitudinally *in-situ* at the capillary level.

Here we propose a new insight into the response of tumor microvasculature to RT using a novel preclinical experimental platform based on functional optical coherence tomography (OCT). OCT is an emerging label-free non-invasive 3D optical imaging modality for visualizing subsurface tissue details *in-vivo* at resolutions approaching microscopy and blood flow details at the microcirculation level [2]. Early (up to 5-8 weeks post-RT) microvascular response was evaluated for engrafted human-derived pancreatic cancer tumours (BxPC-3 cells) in mouse dorsal skin window chamber model (NRG strain mice, n = 60) subjected to a high-dose small-fields single-fraction radiation treatment of 10, 20, and 30Gy. 3D tumour blood perfusion maps were obtained with a research OCT system [3] in optimized speckle variance mode [4]. After each OCT imaging session, tumour vascular volume density metric was estimated along with two additional vasculature-independent measures: tumour volume (via caliper measurements) and tumour fluorescence (via fluorescence microscopy). Tumor resections for histological staining and evaluation were also performed at selected post-RT stages in several animals to support and validate the *in-vivo* observations.

Developed functional OCT platform enabled rapid and robust *in-vivo* assessment of volumetric tumour vasculature growth and response to radiation. It was able to monitor immediate (minutes to tens of minutes) and early (days to weeks) RT responses of tumour microcirculation. Vascular alterations, as well as changes in tumor volume and fluorescence intensity, were quantified and demonstrated robust and complex temporal dose-dependent behaviors [5]. The findings were also compared with emerging radiobiological models of microvascular radiation response proposed in the literature [6].

References

[1] M. Garcia-Barros et al. *Cancer Res.* 2010; 70: 8179-8186.
[2] J. Fujimoto et al. *Neoplasia* 2000; 2:9–25.
[3] Y. Mao et al. *IEEE Trans. Instrum. Meas*. 2011; 60: 3376-3383.
[4] A. Mariampillai et al. *Opt. Lett.* 2010; 35(8): 1257–1259.
[5] V. Demidov et al. *Sci. Rep.* 2018; 8(38): 1-12.
[6] S. V. Kozin et al. *J Natl. Cancer. Inst.* 2012; 104: 809-905.

Oral Presentation Abstracts

Session 5: Augmented Reality

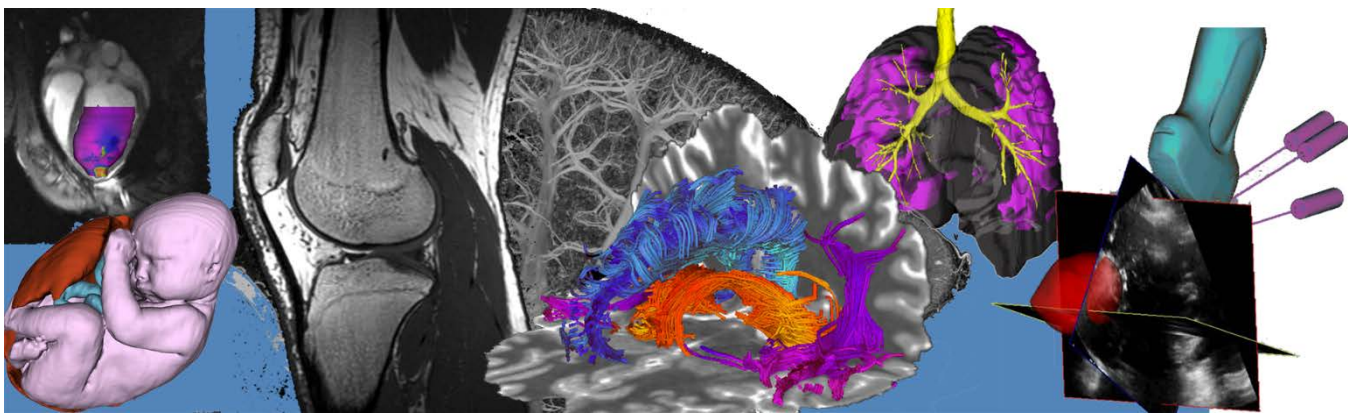

Accuracy of the Microsoft HoloLens for neurosurgical burr hole placement

Emily Rae[1], Andras Lasso[1], Matthew Holden[1], Evelyn Morin[2], Ron Levy[3], Gabor Fichtinger[1,3]
[1]Laboratory for Percutaneous Surgery, School of Computing, Queenôs University, Kingston, Canada
[2]Department of Electrical and Computer Engineering, Queenôs University, Kingston, Canada
[3]Department of Surgery, Queenôs University School of Medicine, Kingston, Canada

Introduction: Tracked navigation systems require large carts of equipment, are operated by specialized technicians, and are generally impractical in bedside neurosurgical procedures. For beside procedures such as a twist-drill crainiostomy for the removal of a subdural hematoma, navigation could optimize the placement of the twist drill in relation to the underlying fluid. Increased accuracy could improve surgical outcomes as incorrect placement of twist drill holes may result in complications such as injury to underlying brain tissue [1]. The Microsoft HoloLens is an optical see-through head-mounted display and is considered the best performing augmented reality technology currently available and the most suitable for clinical use [2]. We use the Microsoft HoloLens to display a hologram floating in the patientôs head to mark a burr hole on the skull. We evaluate the feasibility of using the Microsoft HoloLens to mark a burr hole within a clinically acceptable range of 10 mm.

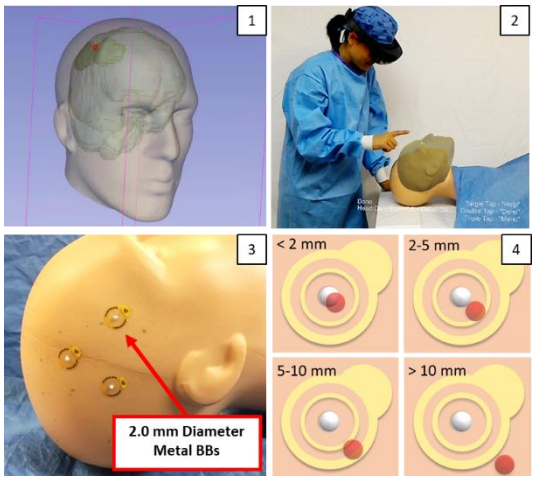

Figure 1: 3D model of the head, hematoma, and brain created from the CT scans (1), a view of the surgeon registering the model (2), the plastic phantom with 2.0mm diameter metal BBs (3), and the different ranges of accuracy using the marks on the base of each BB (4).

Methods: A 3D model of the head, hematoma and burr hole is created from CT images and imported to the HoloLens (Figure 1-1). The hologram is interactively registered to the patient and the burr hole is marked on the skull (Figure 1-2). 3D Slicer, Unity, and Visual Studio were used for software development. The system was tested by 6 inexperienced and 1 experienced users. They each performed 6 registrations on phantoms with fiducial markers placed at 3 plausible burr hole locations on each side of the head (Figure 1-3). Registration accuracy was determined by measuring the distance between the holographic and physical markers (Figure 1-4).

Results: Inexperienced users placed 98% of the markers within the clinically acceptable range of 10 mm (Table 1) in an average time of 4:46 min (range 2:18 ï 9:39 min). The experienced user placed 100% of the markers within the clinically acceptable range (Table 1) in an average time of 2:52 min (range 2:15 ï 3:39 min).

Table 1: Percentage of marker placements within each range and the total percentage of markers within a clinically acceptable range as performed by both inexperienced and experienced users.

Userôs Level of Experience	< 2 mm	2-5 mm	5-10 mm	> 10 mm	Within Acceptable Range (< 10 mm)
Low	35%	24%	39%	2%	98%
High	50%	0%	50%	0%	100%

Conclusion: It is feasible to mark a neurosurgical burr hole location with clinically acceptable accuracy using the Microsoft HoloLens, within an acceptable length of time. This technology may also prove useful for procedures that require higher accuracy of location and drain trajectory such as the placement of external ventricular drains.

References:

[1] Horn et al., ñBedside twist drill craniostomy for chronic subdural hematoma: a comparative study,ò *Surgical Neurology*. 2006 Feb; 65(2):150-3; discussion 153-4.

[2] Qian et al., ñComparison of optical see-through head-mounted displays for surgical interventions with object-anchored 2D-display,ò *International Journal of Computer Assisted Radiology and Surgery*. 2017 Jun;12(6):901-910

Ultrasound-guided needle insertion simulator with tracking- and video-based skill assessment

Sean Xia[1, 2], Zsuzsanna Keri[1], Matthew S. Holden[1], Rebecca Hisey[1], Hillary Lia[1], Tamas Ungi[1], Gabor Fichtinger[1]

[1]Laboratory for Percutaneous Surgery, School of Computing, Queenôs University, Kingston, Canada
[2]School of Medicine, Queenôs University, Kingston, Canada

INTRODUCTION: It has been recognized that several invasive procedures are performed with greater efficiency and minimal risk of complications under ultrasound (US) guidance compared to relying on external or palpable anatomical landmarks[1]. However, inexperienced trainees often struggle with coordinating probe handling and needle insertion[2]. Previously, we demonstrated that using 3D visualization helps learners acquire these skills in a simulated setting[3]. In this study, we aimed to develop and test the efficacy of US Needle Tutor, a training system based on the open-source Perk Tutor platform (www.PerkTutor.org), in teaching in-plane and out-of-plane needle insertion to novice medical trainees.

METHODS: Thirty-eight novice participants were randomly assigned to perform either in-plane or out-of-plane insertions on a Blue Phantom vascular access training phantom. After an instructional video, participants did six US guided needle insertions: one baseline test (no 3D guidance), four practice insertions (with 3D guidance), and one final test (no 3D guidance). For all insertions, performance metrics were computed using electromagnetic trackers attached to the instruments and synchronized videos were also recorded. Five expert operators also performed two in-plane and two out-of-plane insertions to establish performance metric benchmarks.

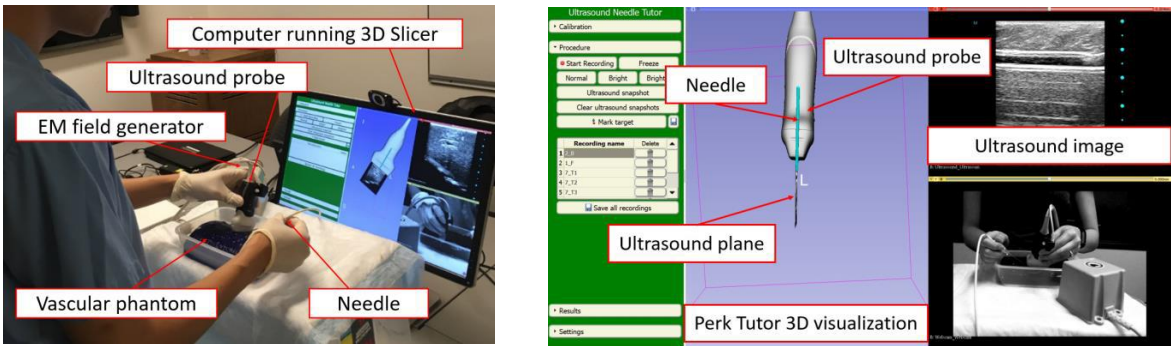

Fig. 1 Training setup with medical trainee performing needle insertion (left) and training platform interface (right).

RESULTS: In-plane novices (n=19) demonstrated significant reductions in needle path inefficiency (45.8 vs. 127.1%, $p<0.05$), needle path length (41.1 vs. 58.0 mm, $p<0.05$), and maximal distance between needle and ultrasound plane (3.1 vs. 5.5 mm, $p<0.05$). They surpassed expert benchmarks in average and maximal rotational error. Out-of-plane novices (n=19) demonstrated significant final reductions in all performance metrics, including needle path inefficiency (54.4 vs. 1102.0%, $p<0.01$), maximum distance of needle past plane (0.0 vs. 7.3 mm, $p<0.01$), and total time of needle past plane (0.0 vs. 3.4 s, $p<0.01$). They surpassed expert benchmarks in maximum distance and time of needle past plane.

CONCLUSION: Results show significant improvement in needle insertion skill after practicing five times with US Needle Tutor. Procedures can be replayed with synchronized video, which will allow us to establish concurrent validity of the performance metrics with expert review.

References: [1] Chapman GA et al. Visualisation of needle position using ultrasonography. Anesthesia. 2006 Feb 1;61(2):148-58. [2] Tielens LK et al. Ultrasound guided needle handling using a guidance positioning system in a phantom. Anesthesia. 2014 Jan 1;69(1):24-31. [3] Ungi T et al, Perk Tutor: an open-source training platform for ultrasound-guided needle insertions. IEEE Transactions on Biomedical Engineering. 2012 Dec;59(12):3475-81.

Comparison of a mixed-reality technology to cadavers for gross anatomy learning

Jeffrey Lao[1*], Stephanie Chevrier[1*], Mustafa Haiderbhai[1], Sheila Esmeralda Gonzalez-Reyna[1], Mina Zeroual[2], Michel D®silets[1], Pascal Fallavollita[1]

[1]Faculty of Health Sciences, University of Ottawa
[2]Faculty of Medicine, University of Ottawa
* *equal first author contribution*

Introduction: Traditional techniques for visualizing human anatomy are limited as a learning method; using textbooks and images makes learning and exploring the human body non-intuitive. Modern technology allows us to utilize virtual and augmented reality interfaces to build a framework that solves these problems. It is also imperative to validate the effectiveness in these technologies in improving the quality of medical education, compared to traditional methods including cadavers and textbooks.

Methods: We developed a mixed-reality application to integrate visual and augmented reality together to allow users to actively visualize human anatomy called Magic Mirror. The application utilizes a Kinect sensor for body tracking along with computer models of human anatomy to create a dual view of the augmented and virtual environments. The application responds to user movement to orient the models in the application to perfectly mirror the user own theoretical anatomy. This allows the user to view the anatomy as if it was their own. Further options in the interface allow the user to manipulate the environment or models to focus in on certain anatomy. Optional labels and quiz features allow users to interactively learn human anatomy. To compare the effectiveness of the Magic Mirror as a learning tool to that of cadavers, a pilot study was conducted. Twenty-two students completed a pre-test in which they had to identify various anatomical structures. Once the pre-test was completed, participants were divided into two groups: one went to the anatomy laboratory where anatomy was taught using cadavers, and the other remained in the histology laboratory where the Magic Mirror was used as the teaching tool. After their learning session, a post-test quiz was taken to assess the impact of both learning tools.

Results & Conclusion: Collected data was analyzed using two-tailed t-Tests by comparing the mean scores of participants who first interacted with the Magic Mirror to those of participants who first interacted with cadavers. This was done for both the pre-test and the post-test, and it was concluded that there was no significant difference between the two teaching methods (pre-test, $p = 0.466$ and post-test, $p = 0.601$). In this initial study, the results demonstrated that students were able to learn gross anatomy just as well when using the Magic Mirror. Due to the cost and limitations of using cadavers, the Magic Mirror could be a possible alternative to cadaver education. Further long-term studies are needed to evaluate the consistent effectiveness of the Magic Mirror as a learning tool compared to cadavers and other learning tools, such as Atlas textbooks, and its possibility to be translated inside anatomy and medical education curricula.

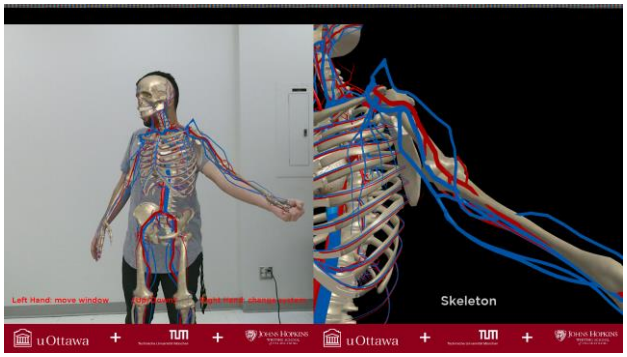

Title: Using augmented-reality for self-directed surgical skills training in competency-based medical education
Authors: Leung, R.,[1,2] Lasso, A.,[1] Holden, M.,[1] Zevin, B.,[3] Fichtinger, G.[1]
[1]Laboratory for Percutaneous Surgery, School of Computing, Queenôs University, Kingston, Canada
[2]School of Medicine, Queenôs University, Kingston, Canada
[3]Department of Surgery, Queenôs University, Kingston, Canada

Introduction:
With the widespread adoption of competency-based medical education (CBME) across Canada, achieving proficiency in technical skills is emphasized over the length of time in training. To achieve proficiency, trainees learn predominantly through apprenticeship under the guidance of a mentor. However, increasingly scarce resources in the healthcare system limits the effectiveness of apprenticeship training and has increased demand for self-directed learning. We propose a new form of self-directed learning where a pair of holographic hands are projected in front of the trainee and guides them through learning hand motions relevant to surgery and medicine. This study looks at the feasibility and effectives of using holographic hands as an augmented-reality skills training modality for learning hand motions compared to the traditional methods of apprenticeship and video-based learning.

Methods:
A pair of holographic hands was created using surface mesh and animation software including MakeHuman, Blender, and Unity. Using the HoloLens, these holographic hands are projected in front of the trainee and used to guide them through learning various hand motions resulting in a ñself-directed apprenticeshipò learning experience. (Figure 1) To evaluate the feasibility and effectiveness of holographic hand learning, 9 participants were recruited and each learned 6 different hand motions from 3 different modalities (video, apprenticeship, HoloLens). Results of successful completion was evaluated by an external assessor. Feedback on effectiveness was also obtained through a questionnaire.

Figure 2. Trainee wearing Hololens learning hand motions (left) and traineeôs view of holographic hands from the HoloLens, with the traineeôs own hands overlaid on the holographic hands for guidance (right). Note: The right image was captured using the HoloLensôoff-axis camera which introduces a slight offset in the position of the holographic hands compared to what the trainee sees.

Results:
Participants had a considerable preference for learning from HoloLens and apprenticeship and a higher success rate compared to video-based learning. Across the 6 different hand motions learned, the highest success rate recorded for video-based learning participants was 33% compared to apprenticeship or HoloLens learning that scored at least a 67%. Furthermore, learning with holographic hands was shown to be comparable to apprenticeship in terms of both effectiveness and success rate. Overall, 78% of participants agreed that HoloLens learning was comparable to learning by apprenticeship. However, more participants still selected apprenticeship as a preferred learning method compared to HoloLens (67% apprenticeship vs 56% HoloLens).

Conclusions:
This initial pilot study has demonstrated the feasibility of learning hand motions from a pair of holographic hands using the HoloLens and its potential to mimic the apprenticeship experience. Although more participants preferred learning by apprenticeship compared to the HoloLens, these differences are expected to decrease over time as AR technology matures and becomes more mainstream. The results are encouraging to suggest a new effective form of self-directed apprenticeship learning that can be used to supplement current skills training methods in achieving proficiency required for CBME. This technology can be further developed and applied to learning a variety of technical skills in medicine and surgery. Work continues toward implementing this technology in knot tying and suture tutoring modules in our undergraduate medical curriculum.

Oral Presentation Abstracts

Session 6: New Contrast Agents

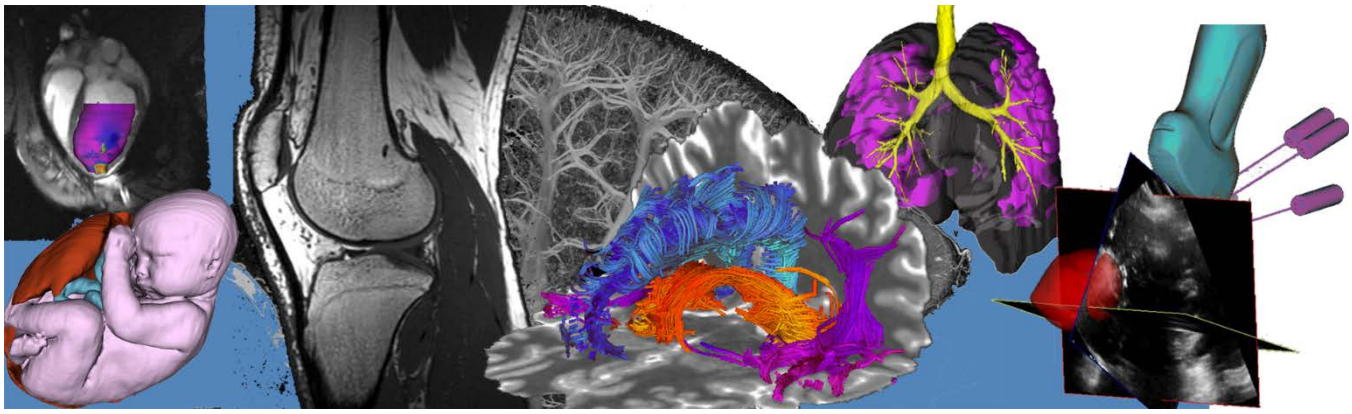

A New Family of Small Manganese(III) Porphyrin Based MRI Contrast Agents and the Analyses of the Binding to Human Serum Albumin

Piryanka Sasidharan[a], Hanlin Liu[a, b] Dr. Xiao-an Zhang[a,b,c*]

[a]Department of Physical and Environmental Sciences, University of Toronto Scarborough [b]Department of Chemistry, University of Toronto. [c]Department of Biological Sciences, University of Toronto Scarborough

Introduction. Magnetic resonance imaging (MRI) relies on the ^{1}H-NMR signal of water existing *in vivo*. Variable proton densities and relaxation properties produce variable signal intensity. In cases of no significant signal difference, a contrast agent (CA) is often employed to allow tissue contrast enhancement. The effectiveness of a CA is referred to as relaxivity (r_1) and is given in $mM^{-1}s^{-1}$. Currently, gadolinium based CAs (GBCA) dominates clinic use but unfortunately GBCAs are associated with Gd-toxicity, such as nephrogenic systemic fibrosis (NSF) in patients with renal dysfunction. Additionally, relaxivity is seen to decrease at magnetic fields of 1-3T, limiting its future application where high field clinical scanners will dominate.[1] To overcome these limitations, we have developed a number of manganese(III) porphyrin (MnP) alternatives to conventional GBCAs. MnPs have been found to display high relaxivity, contains a biocompatible manganese at its core and the porphyrin backbone allows for versatile structural modifications.[2] Here we report a novel family of small, asymmetric MnPs for magnetic resonance angiography (MRA) with high relaxivity and display affinity to human serum albumin (HSA), a prominent protein within the blood plasma.

Methods. MnTPPS has been previously shown to display long *in vivo* retention. This is likely due to the diffused hydrophobicity along the perimeter of the molecule.[3] Additionally, MnTCP has been previously synthesized by our group as an alternate to MnTPPS whereby the four $PhSO_3^-$ arms were replaced with carboxylates as a means of increasing water solubility and polarity. A series of MnPs have been designed herein based upon these two molecules (**Fig 1**) and contain one unique substitution for binding to HSA.

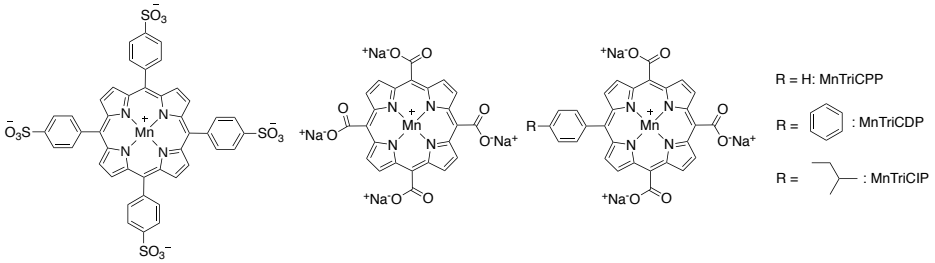

Fig 1. Chemical structure of molecules left: MnTPPS, middle: MnTCP, right: novel MnPs designed herein

The novel MnPs have been synthesized and a series of spectroscopy techniques have been used to confirm its identity and purity. Nuclear magnetic resonance dispersion (NMRD) profiles were acquired with a SMARTracerÊ Fast Field Cycling NMR Relaxometer in combination with a variable high field relaxometer (10ï 120 MHz) HSA binding was followed by relaxivity change.

Results. All novel MnPs were synthesized, purified and characterized by use of NMR, UV-VIS, ESI-MS and HPLC. NMRD profile of MnTriCPP was obtained (**Fig 2**). MnTriCPP was found to display a drastic relaxivity increase upon HSA binding. Moreover, the maximum r_1 was found to be 21.0 $mM^{-1}s^{-1}$ at 31.6 MHz and at high clinical fields an r_1 of 14.8 $mM^{-1}s^{-1}$ was obtained.

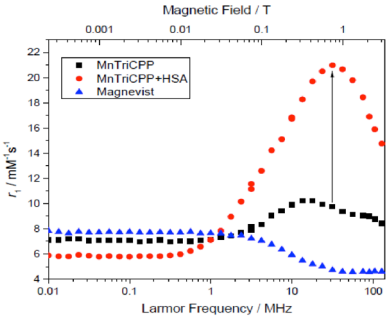

Fig 2. NMRD profile

Conclusion. The new family of MnTriCPP analogs exhibit significant improvement to previously synthesized MnPs and GBCAs, with high sensitivity upon HSA binding, and displays potential for future *in vivo* MRA applications.

References. [1] *J Med Chem*. 2014;57(2):516-520. [2] *J Biol Inorg Chem*. 2014;19(2):229-235. [3] *Magn Reson Med*. 1987;33:24-33.

Engineering non-integrating lentiviral vectors for safe reporter-based imaging of mesenchymal stem cells

Amanda M Hamilton[1], Paula J Foster[1,2] and John A Ronald[1-3]

[1]Imaging Research Laboratories, Robarts Research Institute, London, ON, Canada, [2]Medical Biophysics, University of Western Ontario, London, ON, Canada, [3]Lawson Health Research Institute, London, ON, Canada

Introduction: Cell-based therapies hold great potential for the treatment of a wide variety of ailments and the application of molecular imaging reporter genes can provide invaluable information on the fate of therapeutic cells post-implantation.[1] Viral vectors are one of the most common gene delivery tools used to stably tag cells with reporter genes. However, insertional mutagenesis ï turning a normal cell into a cancer cell - due to random integration of encoded genes into the genome has occurred in the clinic using retroviral vectors[2]. This poses a significant safety concern and barrier to widespread clinical adoption of reporter gene tools. The use of non-integrating lentiviral vectors (NILVs), which lack the integrase necessary for genomic integration, may eliminate any insertional mutagenesis problems. Here we engineered novel integrating lentivirus (ILV) and NILVs expressing fluorescence and bioluminescence imaging (BLI) reporters and compared their ability to longitudinally image human mesenchymal stem cells (hMSC) both *in vitro* and *in vivo* in mice.

Methods: Mutagenesis was performed to create D64V and D116N mutations in the catalytic domain of HIV integrase. Third generation ILVs and NILVs conferring tdTomato (fluorescent) and firefly luciferase BLI genes were produced. Fast dividing (MDA-MB-231) breast cancer cells and slow dividing hMSCs were transduced at known multiplicities of infection and analyzed over time by flow cytometry, fluorescence microscopy and BLI. In an initial *in vivo* study, small numbers of hMSCs ($4x10^4$) transduced with either ILV or NILV were implanted into the hind limb of female nude mice (n=5/group) and BLI was performed on days 0, 3, 6, 10, 14 and 17.

Results: ILV transduced fast dividing MDA-MB-231 cells maintained steady fluorescent and bioluminescent signal over time whereas, as expected, NILV-transduced cells progressively lost signal to 9.9Ñ0.6% within 12 days of cell proliferation ($p<0.0001$). In contrast, initial data with slowly dividing hMSCs showed 50.6% and 10.5% of cells retained tdTomato expression after 12 and 20 days, respectively. The percentage of hMSCs transduced with NILV (79.8Ñ5.2%) and ILV (91.7Ñ2.6%) was not statistically different ($p=0.11$); however, ILV-tagged hMSC were 7.2Ñ2.2 fold brighter by flow cytometry ($p=0.031$). *In vivo*, ILV and NILV-transduced hMSCs were each detectable after implantation in the hind limb of mice using BLI (NILV images seen in Figure 1A) with greater signal detected from ILV-tagged cells (Figure 1B, ~38-fold difference, $p=0.047$). Signal was observed to similarly diminish over time for both ILV and NILV-tagged cell populations, which we attribute to cell death. Despite the reduced signal intensity and the minimal number of cells injected, live NILV-transduced hMSCs were reliably visualized *in vivo* for up to 2 weeks post-implantation.

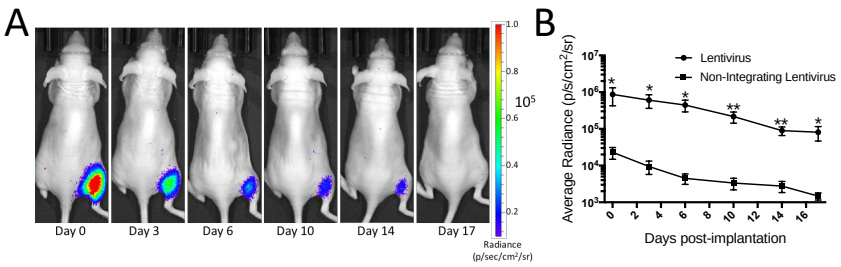

Figure 1: Live NILV-tagged hMSCs can be tracked *in vivo* over time. A) NILV-tagged hMSCs can be detected by BLI for up to 2 weeks. B) Measurements of average radiance (BLI signal) show that despite differences in signal intensity, both cell populations similarly diminish over time.

Discussion: Safety is a major regulatory concern for future clinical applications of reporter gene imaging. Here we present the creation of a NILV platform as a safe means of gene delivery for slowly dividing or non-dividing cells. Using our non-invasive imaging techniques, we successfully and safely tracked the location and viability of the transplanted MSCs cells over time. NILV-tagged cells showed reduced signal intensity which is a known consequence of this technology as it relies on the episomal expression of conferred genes.[3] Future work will look to improve reporter expression, explore clinically relevant reporters (PET, MRI), and apply these novel NILV vectors to other therapeutic cell types. We believe NILVs may have broad clinical applications for expression of imaging reporters and other gene products in numerous cell-based therapies.

References: 1) Cho IK *et al*., Am J Nucl Med Mol Imaging 2016; 2) Howe SJ *et al.,* J Clin Invest 2008; 3) Shaw A and Cornetta K, Biomedicines 2014.

Developing tumour-activatable minicircles as novel reagents for prostate cancer detection

TianDuo Wang[1,2], Yuanxin Chen[1], Gurkamal Deol[1], John. A. Ronald[1,2,3]

1. Robarts Research Institute – Imaging; 2. Department of Medical Biophysics, University of Western Ontario; 3. Lawson Health Research Institute, London, ON, Canada.

INTRODUCTION: Early and accurate detection of prostate cancer (PCa) is critical for a positive patient outcome[1]. Some recent efforts to improve PCa detection have focused on a gene-based approach, developing methods to deliver a foreign gene into cancer cells and force them to produce a unique biomarker that can be detected[2]. Along these lines, we propose a novel non-viral gene vector called tumour-activatable minicircles (TA-MCs), which are shortened plasmids with increased safety and potency[3,4]. These TA-MCs express either secreted embryonic alkaline phosphatase (SEAP), a blood biomarker, or Firefly luciferase (Fluc), which is commonly used for bioluminescence imaging (BLI). SEAP and Fluc expression is mediated by the survivin promoter (pSurv), which is active only in cancers, ensuring TA-MCs are expressed exclusively in tumour cells. Together, these components create a system that is highly specific for PCa. Our goal is to assess the ability of TA-MCs to detect and discern multiple PCa cell lines through a blood test in mice and BLI *in vitro*.

METHODS: We first constructed parental plasmids, precursors to minicircles, that use pSurv to mediate expression of either SEAP or Fluc. SEAP and Fluc TA-MCs were then made from their respective parental plasmid using a previously described production system[5]. Next, we validated these TA-MCs via transfection across PCa cell lines (Du145, LNCaP, PC3, PC3MLN4) of varying aggressiveness and normal prostate epithelial cells. SEAP levels in cell media were quantified using commercially available kits and Fluc expression was quantified via BLI signal using an In Vivo Imaging System (IVIS). We then assessed SEAP TA-MCs in nude mice with subcutaneous PCa tumours (LNCaP, PC3MLN4) of ~200 mm^3. TA-MCs complexed with a polyethylenimine transfection agent was injected intratumourally, then SEAP levels were measured in blood samples collected at 3, 6 and 11 days post-MC injection. At endpoint, tumours were collected and SEAP levels in tumour lysates were measured and compared to survivin expression measured by Western blot.

RESULTS: SEAP and Fluc levels were significantly higher in PCa cell lines than primary prostate epithelium (Fig. 1). Between PCa cell lines, expression of Fluc and SEAP was highest in PC3MLN4 and lowest in LNCaP cells, showing a similar trend to that of survivin expression. Three days after MC-administration, mice with PC3MLN4 tumours had significantly higher blood SEAP levels than mice with LNCaP tumours.

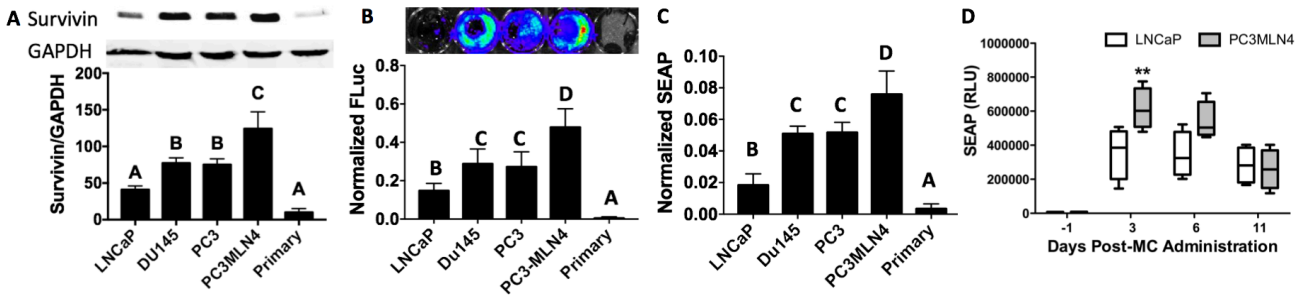

Figure 1. (A) Western Blot analysis of survivin expression relative to GAPDH in tumour lysates (n=4). (B) *In vitro* Fluc and (C) SEAP expression normalized for Renilla luciferase co-expression two days after administration of TA-MCs (n=4). (D) Blood SEAP concentration in mice post-MC administration (n=4). Data are presented as mean ± SD. Letters represent significant differences between groups ($p<0.05$). **, $p<0.01$.

DISCUSSION: The results indicate that TA-MCs can discern PCa cells from healthy tissue via a blood-test or BLI. SEAP levels can also be used to differentiate PCa tumours with varying survivin expression in mice, which can be used as a gauge for tumour aggressiveness. TA-MCs represent a novel diagnostic tool that offers more comprehensive information regarding PCa, which ultimately helps improve patient outcomes. The modular nature of MCs leaves great potential for future implementation of other biomarkers and imaging-based reporter genes.

REFERENCES: [1] Etzioni R. et al., Nat Rev Cancer, 2003, 3(4): 243ï 252. [2] Richter J. et al., Gene Ther, 2014, 21(10): 897ï 902. [3] Chen Z. et al., Mol Ther, 2003, 8(3): 495ï 500. [4] Ronald J. et al., PNAS, 2015, 112(10): 3068ï 3073. [5] Kay M. et al., Nat Biotechnol, 2010, 28(12): 1287ï 1289.

Lanthanide nanoparticles as vascular contrast agents for microcomputed tomography

Charmainne Cruje,[1,2] Joy Dunmore-Buyze,[1,2] David W. Holdsworth,[1,2] Elizabeth R. Gillies,[3,4] and Maria Drangova[1,2]
[1]Robarts Research Institute, [2]Department of Medical Biophysics, [3]Department of Chemistry, and [4]Department of Chemical and Biochemical Engineering, The University of Western Ontario, London, Ontario, Canada

Introduction. Recent advances in nanotechnology have led to the development of blood pool contrast agents in microcomputed tomography (micro-CT). The advantage of using nanoparticles is the ability to achieve high initial contrast element concentrations (100 mg/mL) and prolonged residence times that are suitable for micro-CT, (*i.e.* tens of minutes); this is attained by polymer-coated nanoparticles exceeding 10 nm in size.[1] Although long-circulating nanoparticle-based agents exist for micro-CT, they are predominantly based on iodine, which has a low atomic number. Higher CT contrast can be achieved using elements with higher atomic numbers, such as lanthanides (*e.g.* Erbium or Er) , particularly at higher energies. While lanthanide-based contrast agents are used clinically in MRI, they are composed of small molecules (< 1 nm) that exit the bloodstream of small animals within seconds. Thus, the purpose of this work was to develop polymer-encapsulated lanthanide nanoparticles exceeding 10 nm in size and containing 100 mg/mL of Er as a vascular contrast agent in micro-CT.

Methods. ***Contrast agent preparation and characterization-*** A series of polymers were studied to identify a formulation that remained stable in a mouse blood mimic and had relatively higher Er content than others. This polymer was used to prepare assemblies containing Er nanoparticles[2] by nanoprecipitation.[3] The resulting suspension was filtered, freeze-dried and stored at room temperature. The size and appearance of the nanoparticles were characterized using dynamic light scattering (DLS) and transmission electron microscopy (TEM). The dried formulation was dissolved in normal saline immediately before use at an Er concentration of 100 mg/mL.
In vivo application of the contrast agent- Using 0.2 mL of the contrast agent, male C57BL/6 mice (25-30 g) were injected subcutaneously (n=2) and intravenously (n=3) via tail vein catheterization. The biodistribution of the contrast agent was observed by micro-CT. The animals that were injected subcutaneously were sacrificed for gross examination of subcutaneous tissue a week following injection.
Micro-CT imaging and analysis- Micro-CT images were obtained using the GE Locus Ultra (London, ON), where 1000 views (16 ms per view) were acquired at 80 kVp, 55 mA over 360Áand reconstructed using a cone-beam reconstruction algorithm to a voxel size of (150 Õm)^3. Images were analyzed using MicroView (Parallax Innovations, London, ON) and CT contrast was reported in Hounsfield Units.

Results. ***Physical characterization-*** The polymer assemblies containing Er nanoparticles had an average hydrodynamic diameter of 171 Ñ 3 nm with low size dispersity as measured by DLS and TEM results showed good agreement with the DLS-measured diameters (Figure 1). The optimized formulation was also confirmed to contain 100 mg/mL of Er.
In vivo characterization- After subcutaneous administration, the contrast agent remained at the injection site for up to a week. No signs of irritation or necrosis were observed in the subcutaneous tissue upon gross examination. In the blood pool of the animals that were intravenously injected, contrast enhancements of over 250 HU were observed for up to an hour (Figure 2).

Conclusions. Polymer-encapsulated Er nanoparticles that were larger than 10 nm in size and could encapsulate 100 mg/mL of Er were successfully synthesized. The contrast agent did not irritate subcutaneous mouse tissue for at least a week, and remained stable and inert *in vivo*. In the blood pool, contrast enhancement was observed for at least an hour; this well exceeds *in vivo* micro-CT requirements. This work represents the development of the first nanoparticle-based contrast agent that contains 100 mg/mL of Er and is targeted for *in vivo* micro-imaging.

References. [1] Choi CH et al. Proc. Natl. Acad. Sci. 2011; 108(16): 6656-6661. [2] Zhao G et al. Langmuir 2014; 30(23): 6980-6989. [3] Prashant C et al. Biomaterials 2010; 31(21): 5588-5597.

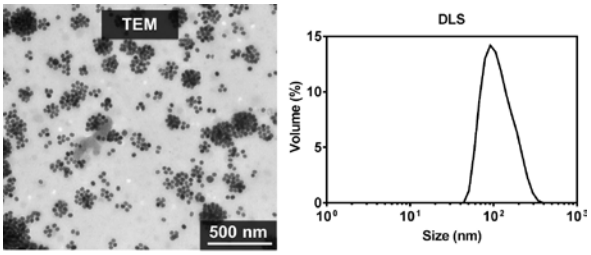

Figure 1. A TEM image and the hydrodynamic volume size distribution of the contrast agent.

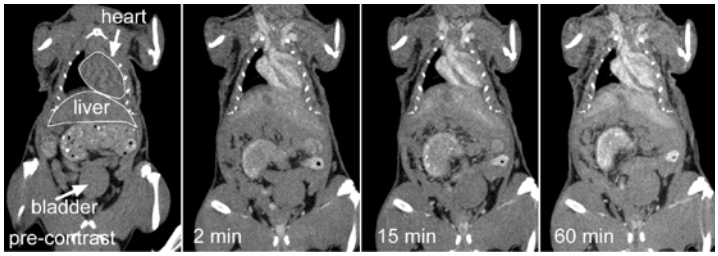

Figure 2. Time-course micro-CT images of a mouse that was intravenously injected with the contrast agent.

Oral Presentation Abstracts

Session 7: Cardiovascular Imaging

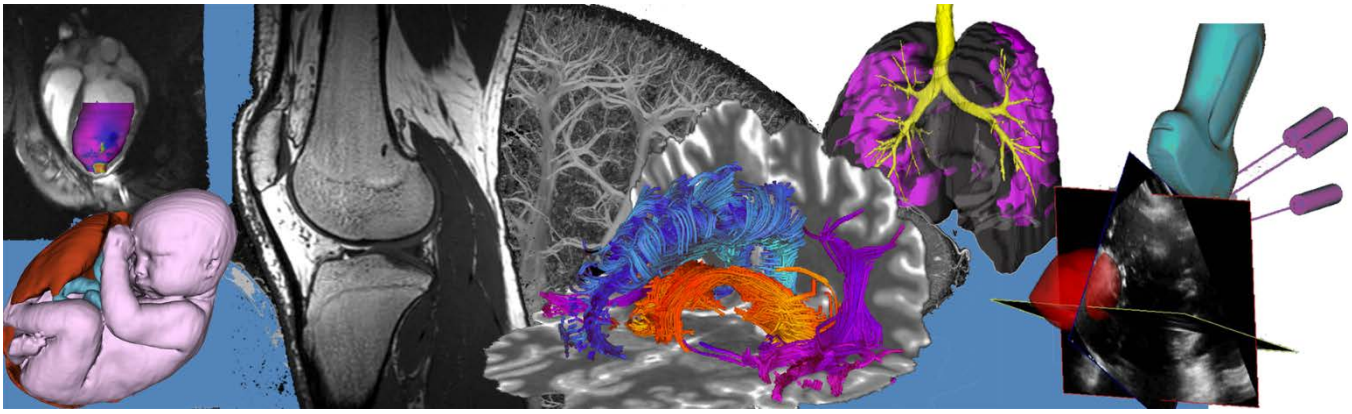

Characterization of T2, T2* relaxation and strain in disease progression post acute myocardial infarction

Dipal Patel[1]; Idan Roifman[2]; Mohammad I. Zia[2]; Bradley H. Strauss[2]; Kim A. Connelly[3]; Graham A. Wright[2,4]; Nilesh R. Ghugre[2,4]
[1] Department of Physics, Ryerson University; [2] Schulich Heart Research Program, Sunnybrook Research Institute; [3] Division of Cardiology, St. Michael's Hospital; [4] Department of Medical Biophysics, University of Toronto, Toronto, ON

Introduction: Microvascular obstruction (MVO) is a common complication in acute myocardial infarction (AMI), which occurs in 50% of the ST-segment elevation of myocardial infarction (STEMI) patient population. Several studies have demonstrated that MVO is an independent predictor of adverse outcomes in AMI. In association with MVO, more recently, hemorrhage has been shown to be an active contributor to myocardial damage and inflammation, elevating the risk even further. The effects of these adverse consequences can be observed by serially assessing regional myocardial systolic function and inflammation in vivo using strain analysis and T2 mapping, respectively. The aim of our study was to longitudinally characterize T2 and strain in STEMI patients with and without MVO to observe the acute to chronic transition during disease progression.

Methods: The study involved patients (n=16) with reperfused STEMI with 3 visits at 48 hours, 4 weeks, and 6 months post-percutaneous coronary intervention (PCI). Imaging was serially performed on 1.5T clinical scanner. Cardiac function was assessed using a cine SSFP sequence. T2 was quantified for the detection of edema using a cardiac-gated free-breathing T2-prepared spiral imaging sequence: TE=2.9-184ms. T2* mapping was utilized for the identification of hemorrhage using a multi-echo gradient-echo acquisition with 8 echos, TE=1.4-12.7ms. Early and Late gadolinium enhancement (EGE, LGE) was employed to identify region of infarction and MVO. Patients were divided into two groups with and without MVO by identifying the hypo-enhanced core in EGE images. Two slices with infarct were chosen for analysis per patient per time point. T2, T2* and radial strain and circumferential strain were analyzed in infarct and remote segments using cvi42 software (Circle Imaging). Statistics were performed using repeated measures 2-way ANOVA.

Results: MVO was identified on EGE images in 8 of the 16 patients (50%). At 48 hrs, the MVO+ group demonstrated low infarct T2* values or greater hemorrhage within the hypoenhanced region that was associated with reduced peak strain compared to the MVO- group. See Fig. 1A for representative images. T2* values were significantly lower in the MVO+ group at 48 hrs and 4 weeks relative to remote indicative of hemorrhage and remained low even at 6 months suggesting persistent hemorrhage. Edema characterized by T2 in infarct myocardium subsided within 4 weeks ($p<0.02$) in both groups, but at 6 months, resolved with significance only in the MVO- group whereas remained elevated in the MVO+ group when compared to week 4. Radial and circumferential strain analysis in infarct regions showed significant recovery over time for only MVO- patients whereas recovery was blunted in MVO+ patients. See associated plots in Fig. 1B. Strain in remote myocardium was not different between the groups and remained unchanged over time.

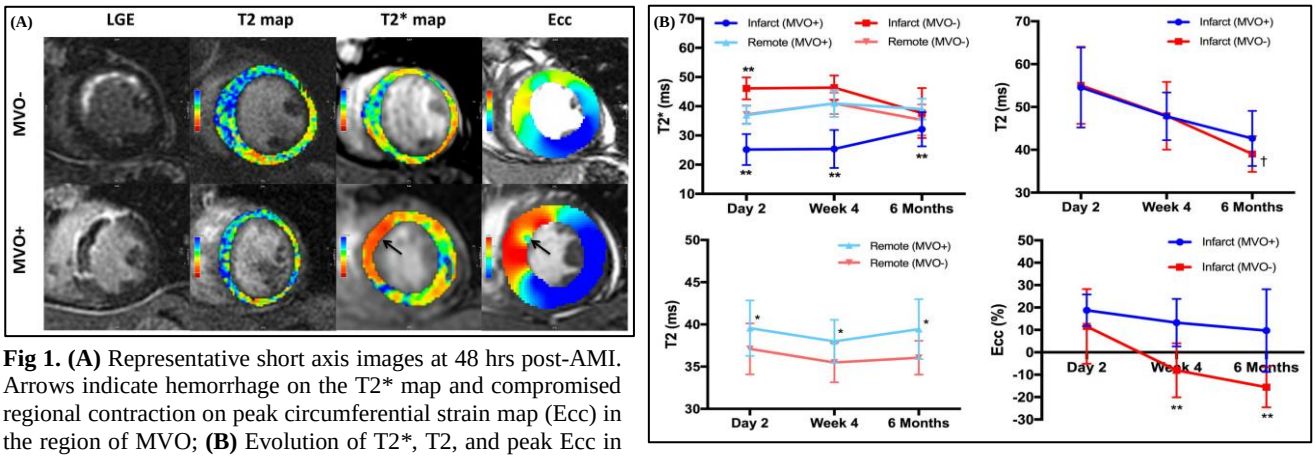

Fig 1. (A) Representative short axis images at 48 hrs post-AMI. Arrows indicate hemorrhage on the T2* map and compromised regional contraction on peak circumferential strain map (Ecc) in the region of MVO; **(B)** Evolution of T2*, T2, and peak Ecc in the infarcted and remote myocardium post-AMI. [**$p<0.001$ compared to remote (T2*) or other group (Ecc); *$p<0.05$ compared to other group. À$p<0.05$ compared to previous time point.]

Conclusions: Edema, hemorrhage and strain progression in the infarct region for patients with microvascular obstruction fails to reach remote levels and has significantly less recovery rate compared to patients without microvascular obstruction. Remote myocardial alterations (T2) may further be an early indicator of adverse remodeling. Thus, our study shows that microvascular obstruction impacts disease progression by hindering the regional myocardial systolic function and edema recovery post-AMI.

Investigating the correlation between cellular iron content and magnetic resonance signal using THP-1 monocytes to model the inflammatory response

P. Dassanayake[1,2,3], O.C. Sehl[1,2], N. Gelman[1,2], R.T. Thompson[1,2], F.S. Prato[1,2,3], D.E. Goldhawk[1,2,3]

[1]Imaging Program, Lawson Health Research Institute; [2]Medical Biophysics and [3]Collaborative Graduate Program in Molecular Imaging, Western University; London, Ontario, Canada

Introduction: Acute myocardial infarction (AMI) is the leading cause of death worldwide [1]. After AMI, inflammatory response(s) stabilize the region of infarction by strengthening the heart muscle. Nevertheless, an unrestricted inflammatory response leads to excessive left ventricular remodeling and, eventually, heart failure. Differentiating between pro- and anti-inflammatory responses may help establish when interventions should be introduced to curb unwanted tissue remodeling [2].

Monocytes are the precursors of M1 (pro-inflammatory) and M2 (anti-inflammatory) macrophages. In each cell type, the iron handling activity is distinct, with M1 macrophages largely displaying an iron storage phenotype while M2 macrophages mainly exhibit an iron recycling phenotype. Hepcidin is a hormone expressed post AMI (unpublished results); is induced by pro-inflammatory signaling; and downregulates ferroportin (FPN), an iron export protein found in monocytes and macrophages. We are investigating the correlation between cellular iron content and transverse relaxation rates in a human monocyte cell line, with the future goal of tracking peripheral blood monocytes as they respond to cardiac inflammation post-AMI. We propose to use MRI to differentiate between pro-inflammatory and anti-inflammatory responses post-AMI [2].

Hypothesis: Changes in monocyte iron regulation during an inflammatory response are partially mediated by hepcidin and influence both cellular iron content and MRI relaxation rates.

Methods: Human THP-1 monocytes were cultured for one week in the absence (-Fe) and presence (+Fe) of iron-supplemented medium, containing 25ÕM ferric nitrate. Upon withdrawal of iron supplement, cells were cultured a further 1 (Fe-1h) and 2 (Fe-2h) hours. At harvest, cells were lysed in RIPA/protease inhibitors (Roche) and sonicated. Expression of iron export protein was assessed by Western blot using rabbit Ŭ-FPN (Invitrogen) as the primary antibody [1]. Transverse relaxation rates (R2* = 1/T2*; R2 = 1/T2) were measured at 3T in MRI phantoms [3], using single-echo spin echo for T2 and multi-echo gradient echo for T2* acquisitions. The irreversible component (R2Nj was calculated (R2* ̧ R2). Cellular iron content was determined by inductively-coupled plasma mass spectrometry (ICPMS, Biotron Analytical Facility).

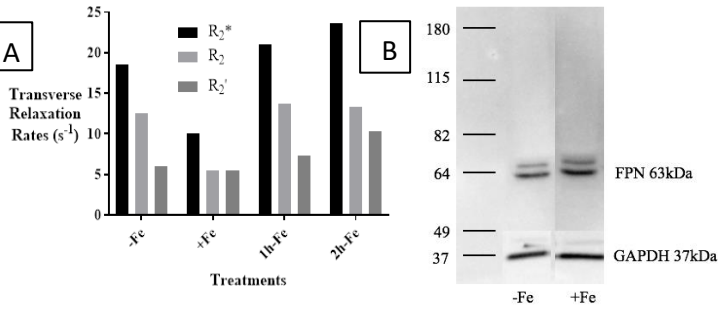

Figure 1. Influence of extracellular iron on THP-1 monocytes. A) To examine the influence of iron export activity on MRI, cells were cultured with (+Fe) or without (-Fe) iron-supplemented medium for 7 days, then harvested and scanned either immediately or 1 (1h-Fe) and 2 (2h-Fe) hours after removal of extracellular iron supplement. B) Regardless of iron supplementation, FPN (63K) was expressed. Molecular weight standards are indicated on the left and glyceraldehyde 3-phosphate dehydrogenase (GAPDH, 37K) was the loading control.

Results: In THP-1 cells, both R2* and R2 decreased in the presence of iron supplementation but returned to baseline non-supplemented values upon withdrawal of extracellular iron. Regardless of the influence of iron on these MR measures, the level of FPN expression is similar +/- Fe, unlike P19 cells [2].

Conclusion: THP-1 monocytes are an iron exporting cell type and, as such, may respond to pro-inflammatory signaling mediated by hepcidin. Since the hepcidin signal is detectable in P19 cells by the change in correlation between cellular iron content and R2 [2], immune cells recruited to sites of inflammation may be subject to similar detection.

References: [1] Goldhawk et al., 2015, MR Insights 8(S1), 9-14; [2] Alizadeh (2017) MSc thesis, Western University; [3] Sengupta et al., 2014, Front Microbiol, 5, article 29.

Analysis of flow and oscillating wall shear stress in the carotid bifurcation using particle image velocimetry: Effects of stenosis severity and waveform pulsatility

Amanda L. DiCarlo*[1] and Tamie L. Poepping[1,2]
[1]Department of Physics & Astronomy and [2]Department of Medical Biophysics, University of Western Ontario, London, Ontario, Canada

Introduction: Hemodynamics and shear forces have been associated with pathological changes in the vascular wall and its function, and the development of atherosclerosis. The carotid artery bifurcation is a common site where these changes occur due to complex flow patterns. More recently, the multidirectional nature of shear stress acting on the endothelial layer has been highlighted as a risk factor for atherogenesis[1,2], emphasizing the need for accurate shear stress magnitude as well as direction measurements. In order to know the direction of shear stress at the vessel wall it is necessary to have information about the wall position *and* orientation. In this in vitro experimental study, a combination of particle image velocimetry (PIV) for obtaining velocity vector fields and micro computed tomography for obtaining vessel geometry information were used to derive 3D three-component wall shear stress vector maps in idealized carotid artery phantoms. Comparisons between time averaged wall-shear stress magnitude (TAWSS), oscillatory shear index (OSI), and transverse wall shear stress (transWSS) were made for models with varying inlet flow waveform pulsatility and increasing eccentric stenosis severity.
Methods: PIV velocity data were collected using a commercial stereoscopic PIV system (LaVision) in conjunction with an in vitro flow system for creating physiological pulsatile flow within optically transparent carotid artery phantom models constructed from PDMS. Three geometries, with 30%, 50% and 70% stenosis of the internal carotid artery were investigated with a healthy inlet carotid artery waveform. For the 50% stenosed geometry, two additional waveforms with decreasing pulsatility were also investigated. 3D three-component velocity vector maps were obtained by stacking individual planes, resulting in a dataset with 100Hz temporal resolution, approximately 0.3 mm in plane spatial resolution, and 0.5 mm resolution in the out-of-plane direction. Micro-CT scans of carotid phantoms were acquired (Locus Ultra, General Electric Healthcare, London, ON, Canada) and the vessel geometry was extracted via level-set segmentation and subsequently registered with the PIV data using an iterative closest point algorithm (VMTK). The wall shear stress tensor was derived from velocity gradients along the inward unit normal vector from the vessel surface at each point: $\vec{\tau} = \mu\dot{\gamma}$ where $\dot{\gamma}$ is the shear rate tensor. The traction vector was calculated from the product of the stress tensor and the normal and the component tangential to the surface denoted the shear stress vector, from which time-averaged shear stress metrics were calculated.
Results: Increasing stenosis severity resulted in an increase in TAWSS (Fig 1A) as well as more surface exposure to high transWSS. Regions of high OSI were found to demarcate recirculation zones, corresponding to a convergence, divergence or recirculation of the mean wall shear stress vector field. (Fig 1B) Surface area exposed to high OSI decreased with decreasing pulsatility and was found to correlate with several waveform shape descriptors (PI, RI, FAI).
Conclusion: We have presented a novel method combining imaging modalities for experimental modeling of 3D vascular wall shear stress patterns, incorporating both magnitude and direction. Both vessel geometry and inlet waveform shape were shown to impact shear metrics which have been used to quantify flow features related to disease risk.

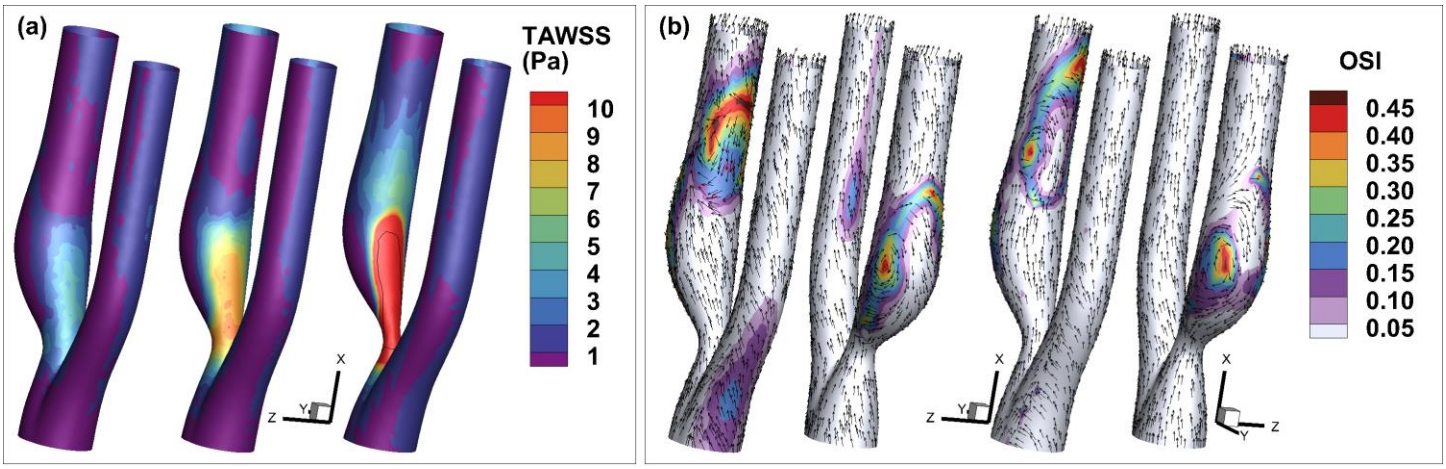

Figure 1. (a) Maps of TAWSS in the 30%, 50%, and 70% geometries from left to right. A single contour line at 20Pa outlines the region of much higher shear for the 70% model. (b) Contour maps of OSI for high pulsatility and low pulsatility cases from left to right, for 50% stenosed geometry. The vessel is shown in two orientations exposing the inner and outer walls of the ICA, and overlayed with surface vectors indicating the direction of the mean wall shear vector.

References:
[1] Peiffer, V. et al. 2013, Journal of Biomechanics, 46(15), pp. 2651-2658.
[2] Wang, C. et al. 2013, Arteriosclerosis Thrombosis and Vascular Biology, 33(9), pp. 2130-2136.

Evaluation of sympathetic function with PET ^{11}C-hydroxyephedrine and ammonia (^{13}N-NH_3) in a canine pacing model of atrial fibrillation

Robert Miner[1,2], John Butler[3], Jane Sykes[3], Jonathan Thiessen[3], Steve Duffett[3], Allan Skanes[3], Pablo Nery[1], Rob Beanlands[1], Frank S. Prato[3], Robert deKemp[1].
[1]Department of Medicine, University of Ottawa Heart Institute, Ottawa, ON
[2]Carleton University, Ottawa, ON
[3]Lawson Health Research Institute, London, ON

Introduction

^{11}C-hydroxyephedrine (HED) is a norepinephrine analog used for positron emission tomography (PET) imaging of the sympathetic nervous system (SNS). HED uptake mechanism is through uptake-1 and to a lesser extent uptake-2, transport into cardiac sympathetic nerve terminals. Pacing the left atrium of a canine heart can produce atrial remodeling and the development of fibrotic tissue caused by atrial fibrillation (Afib). The use of HED and ^{13}N-ammonia (NH_3) allows pre-clinical characterization of the paced left atrium tissue substrate producing Afib.

Purpose

To evaluate sympathetic function in the left atrium of pre- and post-paced canine hearts.

Methods

Ten dogs underwent HED and NH_3 PET baseline scans followed by the surgical placement of pacing wires to induce left atrial fibrosis. After five weeks of rapid atrial pacing (220 to 240 bpm) all dogs underwent HED and NH_3 final scans and then were euthanized. PET perfusion imaging at baseline and after pacing involved the administration of 108 Ñ28.8 MBq NH_3 at the start of a 10-minute dynamic acquisition for baseline and final scans. HED scans were started 50 minutes after the NH_3 injection to allow for a decay of 5 half-lives. PET sympathetic neuronal imaging at baseline and pacing involved the administration of 334 Ñ22 MBq HED at the start of a 50-minute dynamic acquisition for the baseline scan and 30-minute dynamic acquisition after pacing. All scans were performed on a Biograph mMR hybrid PET-MR system.

Regions of interest (ROI) were placed over the left atrium (LA) wall, left ventricle (LV) wall and LV blood cavity. HED and NH_3 peak standardized uptake values (SUV_{peak}) of the LA and LV were measured at baseline and pacing scans. SUVs were measured at 25-30 min after HED, and at 5-10 min after NH_3 injection, and normalized to SUV_{mean} values in the LV blood cavity. Corridor-4DM software was used to calculate ungated left ventricle volumes. Paired t-tests were used to compare baseline values to those after pacing. P-values of less than 0.05 were considered significant.

Results

Ventricular remodeling was demonstrated with LV cavity volumes increased by 1.59Ñ0.27 times after pacing (p=0.006). LA and LV HED SUV_{peak} were consistently increased by 1.50Ñ0.27 (p=0.0002) and 1.13Ñ0.20 (p=0.062) times (respectively) suggesting altered SNS activity. Corresponding NH_3 SUV_{peak} values were not significantly changed in the LA (Ĭ 1.14Ñ0.21) nor the LV (Ĭ 1.03Ñ0.20), confirming that the observed changes in HED uptake were not due to blood flow effects.

Conclusion

Rapid atrial pacing resulted in LV dilatation and altered focal SNS activity in this canine model of Afib. Future studies are needed to correlate these findings with measures of atrial fibrosis.

Research support

Ont. Research Fund (RE07-021) and CANet (NCE-15-P06-001).

Direct Measurement of Blood Flow Reflections by Ultrasound

Luxi Wei[1], Ross Williams[2], Thanasis Loupas[3], Peter N. Burns[1,2]

[1]Department of Medical Biophysics, University of Toronto, Toronto, ON, Canada. [2]Sunnybrook Research Institute, University of Toronto, Toronto, ON, Canada. [3]Philips Ultrasound, Bothell, WA, USA.

Introduction. Pressure and blood flow reflections due to downstream impedance mismatches in arteries are associated with disease and organ damage in the cardiovascular, cerebral, and fetal systems. Increased blood flow reflections in the umbilical artery are an indicator of placental insufficiency, which is a major cause of Intrauterine Growth Restriction (IUGR). The established methods directly analyze pressure and blood flow waveforms, and thus depend on the location of measurement and have low accuracy due to overlapping characteristics of the forward and reflected waves. Current research methods of wave separation analysis allow the complete separation of forward and reflected blood flow in time but require the indirect measurement of pulse wave velocity (PWV), blood vessel cross-sectional area as a surrogate to pressure, blood flow, and involve ECG gating for multi-cardiac cycle synchronization. We propose a new, ultrafast ultrasound imaging method using plane acoustic waves, allowing us to acquire images up to 20,000 frames per second, sufficient to directly capture the pulse wave while making blood flow and cross-sectional area measurements in a single scan, improving the accuracy, robustness, and practicality of the measurement.

Methods. 1) data acquisition; 2) PWV calculation; 3) cross-sectional area calculation; 4) blood flow calculation; 5) reflected blood flow calculation. Data acquisitions were performed using an L12-5 array on a Verasonics scanner. Plane wave ultrasound images were acquired at interleaving 0Áand 15Ásteering angles at a total frame rate of 20 kHz for 1 second (freq: 7.8 MHz). Measurements were obtained with a hand-held transducer positioned parallel to the blood vessel at its diameter. PWV was calculated by applying tissue Doppler on the 0Áimages and tracking the systolic peaks of wall acceleration across the blood vessel (Fig1ab). Cross-sectional area was calculated after integrating wall velocity to obtain vessel diameter (Fig1c). Blood flow could be measured by applying spectral Doppler analysis on the 15Ásteered frames.

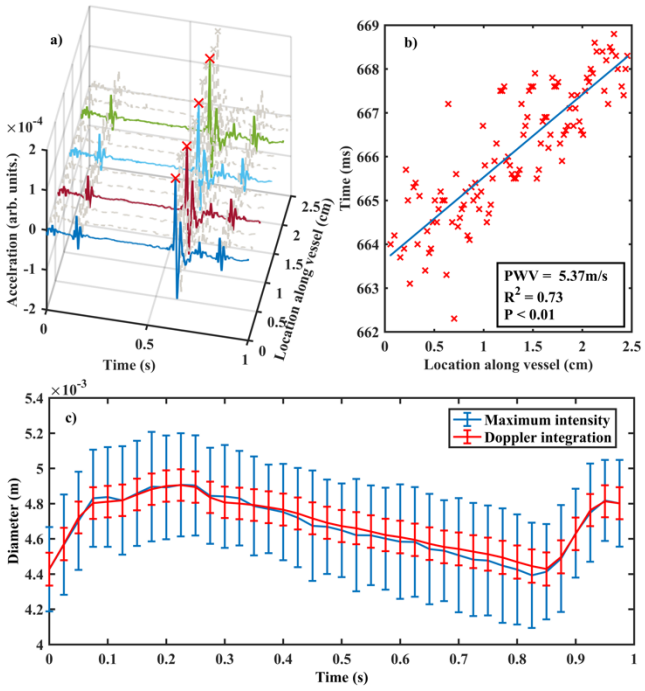

Figure 1: a) Acceleration traces at select locations along the blood vessel wall. Red crosses represent peak systolic acceleration, and are used in b) to obtain PWV. b) Slope of the linear regression line between location and time of the acceleration peaks is PWV. c) Diameter obtained using two methods agree in this example data set. Error bars represent standard deviation of diameter.

Results. Experiments were conducted on the common carotid artery of a healthy volunteer. Currently, we have demonstrated our PWV measurement falls within the range of ~4-6 m/s as expected, and have compared our diameter estimation with M-mode wall tracking. The next step is to derive blood flow velocity, combine all three parameters to find the reflected blood flow and conduct measurements on multiple healthy volunteers to assess the feasibility of the method.

Conclusion. We propose a new and improved method for measuring blood flow reflections in an artery. This method avoids retrospective synchronization across heart cycles, does not require ECG gating, and motion artifacts can be corrected more easily, improving accuracy and robustness. At the temporal resolution of ultrafast imaging, it is possible to visualize the pulse wave moving across the field of view at a speed of more than 6 m/s, as opposed to previously proposed indirect methods. Our method can be used in any large, shallow blood vessel, can be applied easily by hand in a clinical setting, and holds promise for better diagnosis of IUGR and other diseases.

Oral Presentation Abstracts

Session 8: Maternal – Fetal Imaging

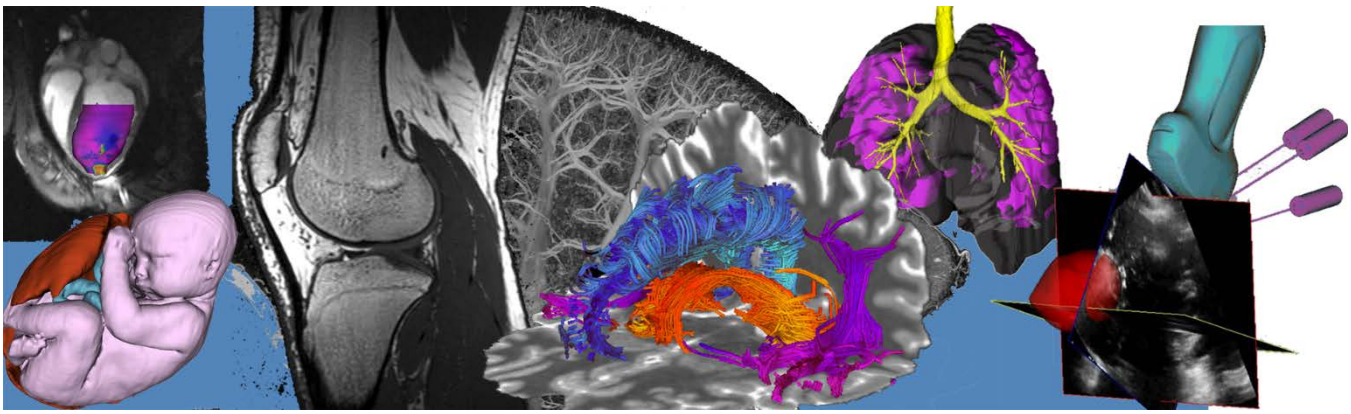

Fetal Cardiac Hemodynamics: Initial Experience using 4D flow MRI

Authors: Eric M. Schrauben[1], Brahmdeep Saini[1], Jack R.T. Darby[2], Jia Yin Soo[2], Mitchell C. Lock[2], Elaine Stirrat[1], Aodhnait S. Fahy[1], Joshua Bradshaw[1], Greg Stortz[1], John G. Sled[1,3], Janna L. Morrison[2], Mike Seed[1,3], Christopher K. Macgowan[1,3]

1. Hospital for Sick Children, Toronto, Canada; 2. University of South Australia, Adelaide, Australia; 3. University of Toronto, Toronto, Canada

Introduction: 4D flow MRI [1] is a comprehensive phase contrast (PC) MRI technique, capable of 3-directional blood flow measurements reconstructed over an entire volume and cardiac dynamics. Motion in fetal imaging ï maternal and fetal breathing and cardiac contraction, and fetal body movement ï causes fetal PC MRI to be limited to fast 2D acquisitions [2, 3]. Extension of these 2D exams to volumetric acquisitions to portray the 3D circulatory patterns within a fetal heart is difficult, and these have not been comprehensively visualized and measured. Here we propose the combination of specialized animal preparation and 4D flow MRI to assess cardiac hemodynamics *in utero*. We present our initial experience, as well as qualitative and quantitative findings from fetal cardiac 4D flow MRI in two mammalian placental animal models of pregnancy.

Table 1. Animal characteristics.

Animal characteristics [Mean ± StDev]		
	Pig (n = 1)	Sheep (n = 5)
Gestational Age (days)	102	129 ± 9
Weight (kg)	0.55	3.01 ± 0.56
Heartrate (bpm)	120	140 ± 12

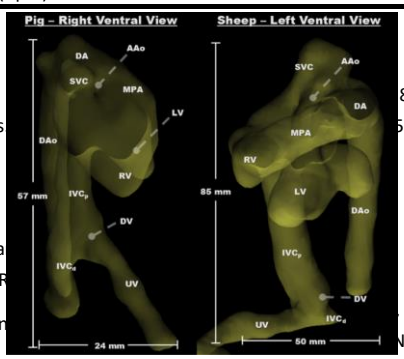

Figure 1. Whole-heart segmentation.

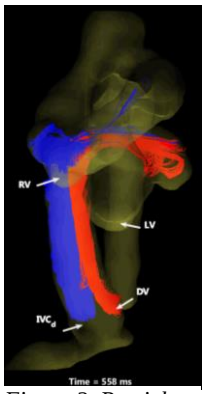

Figure 2. Particle trace time-point in of oxygenated (red) and deoxygenated (blue) blood in a ventral view of fetal sheep heart.

Methods: *Animal Preparation:* This study included a single pregnant Yucatan pig (n=1, 8 fetuses; term, 112 days) and 5 pregnant Merino sheep (n=5, singleton pregnancies; term, 150 days) and was approved by local Animal Ethics Committees. Table 1 lists additional animal characteristics. The surgical procedure was previously described [4] and included appropriate anesthesia, analgesia and antibiotics. A catheter was inserted into the fetus and was exteriorized through the motherôs abdomen, allowing detection of the fetal cardiac cycle. *4D flow MRI:* Data was collected at two sites at 3T (Prisma^{FIT} and Skyra, Siemens), using 60 axial slices of varying thickness with coverage from the liver to the aortic arch. Data were processed using research software (Siemens 4D Flow v2.4) [5]. Whole-heart anatomy was segmented and flow was measured from orthogonal cross-sectional placement and time-resolved contours in all major vessels and flow conduits. Particle traces were emitted to visualize fetal physiological shunts.

Results: Cardiovascular segmentation was achieved in each species, with anatomic locations marked for clarity (Figure 1). Animated particle traces (Figure 2) show *right-to-left* shunting of oxygenated blood while deoxygenated blood can be seen passing through the right heart. Flow values were measured for each species, along with % combined ventricular output (CVO) distribution to major vessels (Table 2).

Conclusion: Here we present the first use of 4D flow MRI for comprehensive evaluation of fetal cardiac hemodynamics in animal models of pregnancy, and present evidence of unmixed streams of oxygenated and deoxygenated blood through the fetal heart. This provides insight into the functional mechanism by which the fetus preferentially supplies oxygen-rich blood to the brain and the heart, and lays a foundation for preclinical studies of fetal cardiovascular physiology. Despite interspecies differences and potential perturbations from anesthesia and experimental handling, % CVO is remarkably similar across species for each measured vessel. Future work should explore the use of 4D flow MRI that measures and compensates respiratory motion and bulk fetal motion.

Table 2. Blood flow measurements across fetal cardiac structures

		CVO	MPA	AAo	SVC	DA	PBF	DAo	UV	FO	IVC_d	IVC_p	DV
Mean Flow (mL/min/kg)	Sheep	383	227	144	174	183	26	245	100	85	87	214	76
	# measurements		2	2	2	2	2	4	5	3	4	5	4
	Pig	129	75	51	37	29	46	81	49	56	46	88	17
			MPA	AAo	SVC	DA	PBF	DAo	UV	FO	IVC_d	IVC_p	DV
Mean Flow (% of CVO)	Sheep		59	38	45	48	7	64	26	22	23	56	20
	Pig		58	39	29	22	36	62	38	43	35	68	13

***Acronyms**: UV: umbilical vein; DV: ductus venosus; IVC_d: distal inferior vena cava; IVC_p: proximal inferior vena cava; SVC: superior vena cava; RV: right ventricle; LV: left ventricle; MPA: main pulmonary artery; DA: ductus arteriosus; AAo: ascending aorta; DAo: descending aorta.*

References: **1**. Markl et al, *JMRI*, 2012. **2**. Prsa et al, *Circ Cardiovasc Imaging*, 2014. **3**. Seed et al, *JCMR*, 2012. **4**. Morrison et al, *Brain Res Dev Brain Res*, 2001. **5**. Gulsun et al, *ISMRM*, 2012.

Imaging Fetal Congenital Heart Disease Using Motion Compensated MRI

Christopher W. Roy, Davide Marini, David F. A. Lloyd, Wadi Mawad, Shi-Joon Yoo,
Edgar Jaeggi, Mike Seed, Christopher K. Macgowan

Background

Recent developments in MRI allow for high resolution imaging of the fetal heart by compensating for the effects of motion and fetal heart rate (1). Here we present our preliminary experience applying a novel framework for fetal MRI to subjects with congenital heart disease (CHD) and compare our MR images to fetal echocardiography (echo).

Methods

Twenty-five pregnant volunteers underwent fetal echo and MRI examination due to suspected CHD on a routine obstetric ultrasound. Golden angle radial MRI data were acquired in each fetal volunteer and real-time images were reconstructed. These real-time images enabled assessment and correction of both stochastic and periodic motion. The corrected data were sorted by cardiac phase and reconstructed to produce motion-robust CINE images of the fetal heart. Quantitative comparison between MRI and echo was performed by two independent reviewers using a binary scoring system of 9 fetal cardiac structures.

Results

Fig. 1 shows images from one representative volunteer indicating an abnormal structure (diverticulum) connected to the right ventricle and a defect in the ventricular septum. Both abnormalities were well visualized by MRI and echo. Quantitative comparison of the two modalities yielded more identified structures by echo (reviewer 1: 7.8 ± 2.3; reviewer2: 7.5 ± 2.4) than MRI (reviewer 1: 7.1 ± 2.1; reviewer 2: 6.7 ± 2.3), however combining information from both modalities enabled identification of additional anatomical features across volunteers (reviewer 1: 8.4 ± 1.3; reviewer 2: 8.4 ± 1.2).

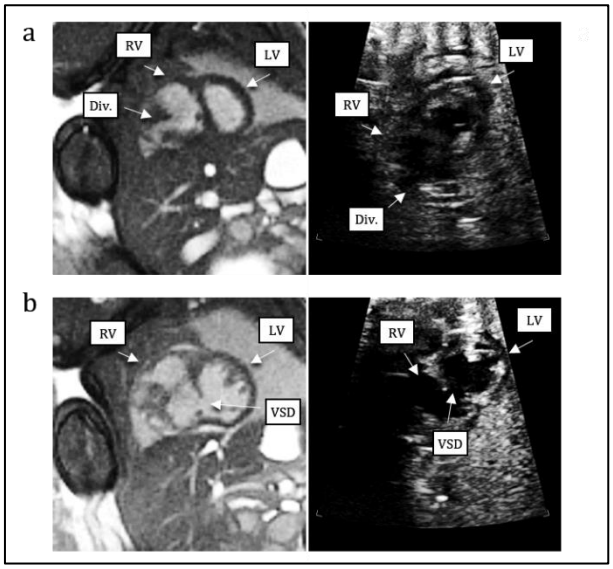

Fig. 1 MRI (left) and echo (right) images demonstrate a) a diverticulum (Div.) attached to the right ventricle (RV) and b) a ventricular septal defect (VSD).

Conclusion

MRI is a promising tool for fetal cardiac examination. This work presents a preliminary comparison between motion compensated fetal MRI and echo across a range of congenital heart defects. We show that fetal MRI provides complimentary diagnostic information to echo during late gestation suggesting its utility in cases with poor acoustic windows such as oligohydramnios, maternal obesity and diaphragmatic hernia.

1. Roy CW *et al.* J Cardiovasc Magn Reson 2017;19(1):29.

A novel optical neuromonitor for simultaneous and real-time quantification of cerebral saturation, perfusion, and metabolism at the bedside

A. Rajaram[a,b], G. Bale[c], M. Kewin[a,b], I. Tachtsidis[c], K. St. Lawrence[a,b], M. Diop[a,b]

[a] *Imaging program, Lawson Health Research Institute, London, Ontario, Canada*
[b] *Department of Medical Biophysics, Western University, Canada*
[c] *Medical Physics & Biomedical Engineering, University College London, United Kingdom*
arajara2@uwo.ca

Introduction: Preterm infants born with very low birth weights are at a high risk of brain injury, in part because the premature brain is believed to be vulnerable to periods of low cerebral blood flow (CBF). Tissue damage is likely to occur if a reduction in CBF is sufficient to impair cerebral energy metabolism for extended periods. There is, therefore, a need for an efficient neuromonitoring method that could alert the neonatal intensive care team to reductions in CBF and cerebral metabolism before injury occurs. In this study, we present the development of a novel optical system for monitoring CBF and the oxidation state of cytochrome c oxidase (CCO) ï a key marker of oxidative metabolism [1].
Methods: The system combines diffuse correlation spectroscopy (DCS) to provide a measure of CBF with broadband near-infrared spectroscopy (NIRS) to quantify changes in the oxidation state of CCO, which has a considerably smaller signal than the hemoglobin signals measured by standard NIRS devices. A custom shutter-based multiplexing method was implemented to prevent crosstalk between the two systems. The ability of the hybrid unit to monitor dynamic changes in cerebral perfusion and metabolism was demonstrated in a piglet model of hypoxia-ischemia (HI).
Results: In 4 subjects, different temporal perfusion and metabolic responses were measured during and immediately after inducing HI; the time course for one piglet is displayed in figure (1). During the insult, CCO fell by 3.0Ñ0.8ε M, with 59Ñ12% of this drop occurring after CBF had reached its nadir. In contrast, hemoglobin changes generally reflected the flow response, including an overshoot in oxyhemoglobin (21Ñ11%) that matched a hyperemic response immediately following the insult (31Ñ8%).
Conclusion: This is the first report of a non-invasive monitor capable of tracking changes in CBF and CCO simultaneously, as demonstrated during hypoxia-ischemia. We believe this system could provide clinicians with greater insight into clinically significant hemodynamic events, enabling them to make adjustments to patient management to avoid brain injury.

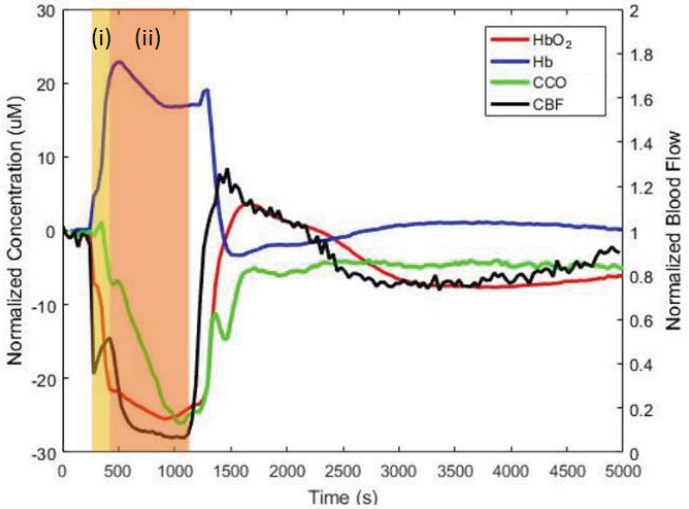

Figure 1: Simultaneous monitoring of changes in Hb, HbO_2, CCO, and CBF in an animal model of hypoxia-ischemia. Protocol was to first clamp both carotids (i), followed by reducing inhaled oxygen to 8% to cause hypoxia-ischemia (ii), insult recovery was achieved by removing clamps and returning oxygen content to baseline values.

[1] G. Bale et al, 2016, J Biomed Opt, 21(9):091307

Generating a 3D ultrasound panorama to monitor neonatal post-hemorrhagic ventricle dilation (PHVD)

A. Harris[1,2], S. de Ribaupierre[2,3], L. Gardi[2], J. Kishimoto[1,2], A. Fenster[1,2]
[1]Department of Medical Biophysics, University of Western Ontario, London, Ontario, Canada;
[2]Robarts Imaging, University of Western Ontario, London, Ontario, Canada;
[3]Department of Clinical Neurological Sciences, University of Western Ontario, London Health Sciences Centre, London, Ontario, Canada

Introduction

Intraventricular Hemorrhage is a common neonatal ailment, occurring in 20-30% of very low birthweight infants. Monitoring of the condition is necessary as 25% of those affected develop post-hemorrhagic ventricle dilation. Methods of monitoring vary, but include tactile examination of the frontal fontanel, 2D ultrasound to estimate ventricle volume (VV), and measurement of the circumference of the baby's skull. Using a volumetric imaging modality (CT, MRI) would allow a more exact VV measurement. However, neonates have poor regulation of their core temperatures and must be kept in an incubator. In seeking a more quantitative, easily replicable imaging modality, our lab previously developed and validated a 3D ultrasound method using a standard 2D ultrasound (2DUS) probe. An atlas-based semi-automated segmentation algorithm was also previously validated by our lab; however, it required capturing the entire ventricular system in a single image. In cases of severe PHVD, dilation can be so extreme that a single image captures too small a volume for this, so multiple partially overlapping images must be acquired. This study aims to automate the blending of multiple volumes such that the semi-automated algorithm can be used in these severe cases of PHVD.

Methods

Following approval by the Research Ethics Board at Western University, patients with confirmed IVH were enrolled in a larger, ongoing study into better monitoring of PHVD. 3DUS images were captured within two days of being imaged in a 1.5 T MRI scanner. The 3DUS device includes a standard 2DUS probe attached to a motor controlled by in-house software. The motor pans through an arc, capturing the probe output every 0.3°. The resulting set of images is organized into a 3D volume. The image registration and stitching pipeline has been assembled in C++ using Insight Toolkit. The Normalized Cross Correlation metric was chosen as a cost function, and because the anatomy being imaged is quite stable in appearance, a rigid 3D transform was used. A Powell optimizer was used to reduce computation time. For validation, it was necessary to calculate a Target Registration Error (TRE) based on homologous anatomical landmarks in the fixed and transformed image. Prior to this, we needed to be sure the user selecting the landmarks was able to select the same ones consistently. This was done by calculating a Fiducial Localization Error (FLE) using the distance between anatomical landmarks selected in separate files, with a 24-hour washout between set selections. Following validation of the user by FLE, 4 homologous anatomical markers were selected in the images. The distance between selected locations for each landmark was calculated and the mean of these differences was taken as the TRE. To be clinically valid, the automatic registration had to accomplish a similar TRE to manual registration, and do so in less time. To validate this, a manual landmark registration was performed on each pair of images and the TRE and times to complete were recorded.

Results

The mean FLE calculated over seven selection occurrences was 2.8 mm. The mean TRE for the successful registrations was 4.25±1.95 mm, with a mean processing time of 38.6±10.8 seconds. The mean TRE for the manual registration was 8.39±4.78 mm, with a mean time of 299.9±70.0 (including landmark selection time). In two of the cases available for study, automated registration failed to register the images prior to stitching.

Conclusions

With validation of the automated pipeline, the option to move to a more quantitative VV calculation becomes accessible to treat even patients with severe PHVD. Future work on this project will include further validation of the pipeline by confirming the linear relationship between 3DUS VV and that of segmented MRI, examining the Dice similarity coefficient between segmented volumes from 3DUS and MRI, and the reduction of the time required for the semi-automated segmentation tool to improve the clinical viability of this technique.

3D Water-Fat MRI Detection of Developmental Maturity in Fetal Adipose Tissue Compartments

Stephanie A Giza[1], Tianna Koreman[2], Barbra de Vrijer[2,3], Charles A. McKenzie[1,3]
[1]Medical Biophysics, Western University, [2]Schulich School of Medicine and Dentistry, Western University, [3]Division of Maternal, Fetal and Newborn Health, Childrenôs Health Research Institute, London, Ontario

Introduction: Fetal adipose tissue development is reflective of the energy balance within the fetus; therefore, assessment of abnormalities in fetal adipose tissue development may provide insight into the metabolic health of the fetus[1]. As adipose cells develop, they grow from water-based fibroblast cells to lipid-based adipocytes[2], a process which can be detected by water-fat MRI using proton density fat fraction (PDFF) quantification[3].
It is also known that fetal adipose tissue starts development in different regions at different gestational ages[4]. Adipose tissue begins to develop in the head first, then extends to the thorax, abdomen and limbs[4]. If these compartments develop at different rates, they will also have different lipid contents at a given gestational age. The objective of this study was to detect differences in the lipid content of the cheeks (adipose in head), thorax, upper arms, forearms, abdomen, perirenal, thighs, and lower legs of individual fetuses using water-fat MRI.
Methods: Volunteers with singleton pregnancies and gestational ages between 29 and 38 weeks were recruited from both low-risk obstetric clinics and specialized high body mass index (BMI) obstetric clinics and imaged in a wide-bore (70 cm) 1.5T MRI (GE MR450w). During an approximately 30 min MRI exam, 3D water-fat MRI (specific implementation: Quantitative IDEAL, TR 9.7-12.7 ms, flip angle 6-7Á Field of View 50 cm, 160Ï 160 pixels, slice thickness 4-6.5 mm, 42-78 slices, ARC acceleration 2x phase 2.5x slice and 32x32 calibration lines, acquisition time 12-24 s) was used to image fetal adipose tissue during maternal breath hold. Fetal adipose tissue compartments including cheeks (high intensity adjacent to mouth), upper arm (shoulders diagonally cut to elbow diagonally cut), lower arm (elbow diagonally cut to wrist), thorax (top of shoulders to bottom of lungs), abdomen (bottom of lungs to where thigh meets body), thighs (along body orthogonal to thigh length to knee diagonally cut), lower leg (knee diagonally cut to ankle), and perirenal (surrounding kidneys) were manually segmented using 3D Slicer (v4.7.0-2016-12-06)[5] (Figure 1). The PDFF was measured after eroding the compartments with a 4-neighbour erosion to reduce partial volume effects. The mean PDFF of the different compartments were compared using a repeated-measures one-way ANOVA with Dunnôs multiple comparisons test in GraphPad Prism (v7.03).
Results: 17 women participated in the study with BMI ranging from 16.6 ï 42.9 kg/m^2 and had their MRI between 29 and 37 weeks GA. The ANOVA showed a significant effect of compartment location on mean PDFF ($p<0.0001$). The results of the multiple comparisons tests are shown in Figure 2, and show that compartments which develop earlier have a higher PDFF. The presence of brown adipose tissue (BAT) serves as a confounding factor in the interpretation of these results. In neonates, BAT has a lower PDFF than white adipose tissue (WAT)[6]. Perirenal adipose tissue is completely BAT and is therefore expected to have a lower PDFF than WAT, which is precisely the result we show here.
Conclusion: Water-fat MRI can be used to detect differences in PDFF of fetal adipose tissue compartments and has the potential to be used to investigate fetal adipose tissue development in pathological pregnancies.

Figure 1. Fetal fat compartments segmentation including cheeks, thorax, abdomen, upper and lower arms, thighs and lower legs.

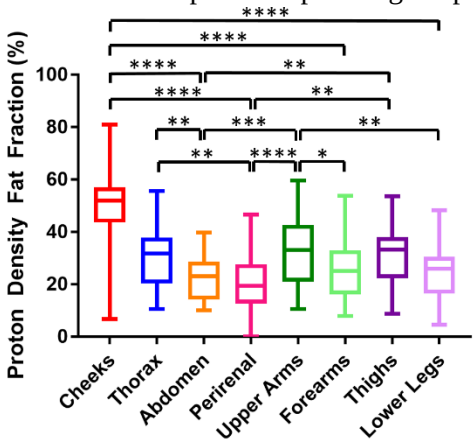

Figure 2. Box and whisker plot of PDFF for different body compartments. * = p Ò0.05, ** = p Ò0.01, *** = p Ò0.001, **** = p Ò0.0001.

References: (1) Toro-Ramos, T., et al. Eur J Clin Nutr 2015; 69(12):1279-1289. (2) Ali A.T., et al. Eur J Cell Biol 2013; 92(6-7):229-236. (3) Giza, S.A., et al. J Magn Reson Imaging 2018, doi: 10.1002/jmri.25929. (4) Poissonnet, C.M., et al. Early Hum Dev 1984; 10(1-2):1-11. (5) Federov, A., et al. Magn Reson Imaging 2013;30(9):1323-1341. (6) Hu, H.H., et al. J Magn Reson Imaging 2012;35(4):938-942.

Oral Presentation Abstracts

Session 9: New MRI Approaches

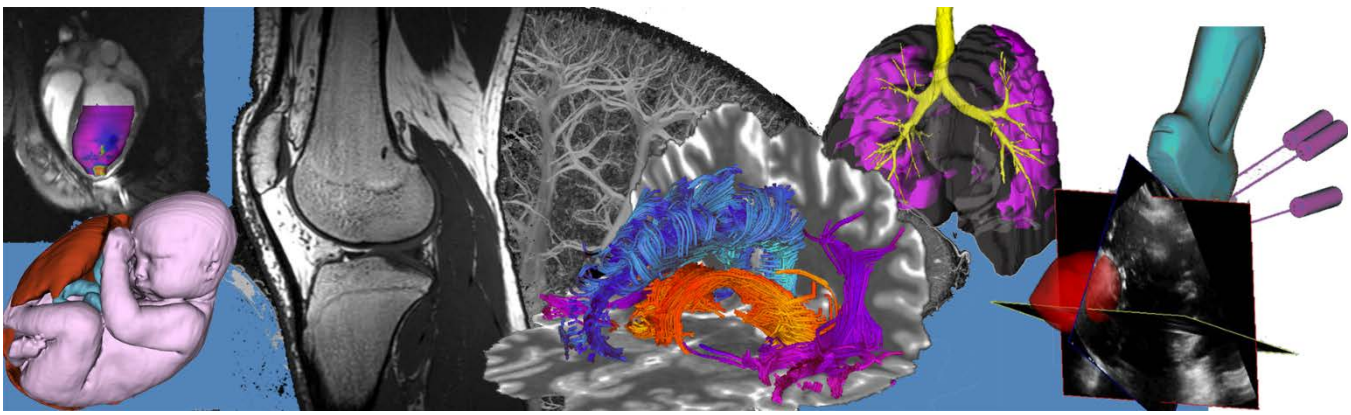

Quantitative MR: Application to Concussion Studies
R. Scott Hinks, PhD
GE Healthcare

MR Imaging is intrinsically sensitive to a wide range of parameters relating to physics, chemistry, and biology of the human body. Parameters such as relaxation times, chemical shift, magnetization transfer, motion, flow, perfusion, and diffusion all contribute to the hope that Quantitative MR (qMR) can radically change diagnosis, treatment, and staging of diseases.

Some key enablers of quantitative MR include:

- Advances in MR system engineering enable MR experiments to more correctly match physics theory.
- Better compute capability improves image quality and the ability to model more complex systems.
- Phantoms for ensuring standardization in qMR are being developed and becoming commercially available.
- Increasing standardization between systems allows improved multi-site trials.
- Modern trends in data analysis including machine learning allow identification of significant patterns in complex data sets.

This talk will build a context of quantitative MR imaging and present initial results from two clinical studies investigating mild traumatic brain injury and amyotrophic lateral sclerosis.

Optimizing signal-to-noise ratio for hyperpolarized carbon-13 MRI using a hybrid flip angle scheme

L.M. Smith[1], T.P. Wade[2], A. Akbari[1,2], C.P. Rockel[1], L.J. Friesen-Waldner[1], C.A. McKenzie[1,2]
[1]*Medical Biophysics, Western University,* [2]*Robarts Research Institute, London, ON, Canada*

Introduction: Hyperpolarized magnetic resonance imaging (MRI) of carbon-13 (^{13}C) allows for real-time quantitative imaging of key biological molecules like pyruvate and their *in vivo* metabolic processes. The hyperpolarized state of pyruvate decays in 20-40 seconds *in vivo*, leading to issues of low spatial resolution and low signal-to noise ratio (SNR) of images. Variable flip angle (VFA) schemes have been used to boost SNR by applying a different flip angle for each excitation. VFA uses the same flip angle for all metabolites, but this limits optimization to one metabolite. Taking advantage of the different chemical shifts of each metabolite, spectrally selective pulses are used to excite lower abundance metabolites with higher flip angles and optimize the SNR for each individual metabolite. Using a spectrally selective VFA could further boost SNR but is not practical for imaging due to the need for unique RF pulses for every readout. We will address the issue of low SNR and practicalities of implementation for imaging by using a hybrid flip angle (HFA) scheme that varies a spectrally selective RF pulse once per image, rather than once per readout.

Methods: The HFA scheme combines the above approaches to produce a different VFA trajectory for each metabolite and each image. This is done by progressively varying both the shape and amplitude of the spectrally selective RF pulse to optimize the signal of each metabolite during the experiment. The pulse shape and amplitude are updated at the beginning of each acquisition of a multi-phase sequence and maintained throughout the acquisition. Spectrally selective RF pulse shapes allow for optimization of the flip angle of each individual metabolite. Bloch simulations were used to determine the optimal flip angles for each metabolite using the HFA scheme. This flip angle strategy was then implemented on a 3T MRI scanner (Discovery MR750, GE Healthcare, Waukesha, WI). Animal experiments were performed on two non-pregnant female adult guinea pigs using a custom built ^{13}C birdcage coil (Morris Instruments, Ottawa, Canada). 3.5mL of the hyperpolarized 80mM [1-C]pyruvate was injected into the hind leg over 12 seconds. Image acquisition began 7.5 seconds after start of bolus injection and images were acquired every 7.5 seconds. Each animal was scanned with either the HFA scheme or spectrally selective constant flip angles (CFA). Regions of interest (ROIs) were drawn around the kidneys on anatomical images and overlaid on ^{13}C images for each metabolite to measure signal intensity.

Results: Figure 1 shows an *in vivo* demonstration of the boost in overall SNR and higher SNR at later time points provided by an HFA acquisition relative to a CFA acquisition. This SNR advantage is quantified in our SNR measurements over each acquisition, shown in Figure 2 using an ROI placed in the left kidney of both animals.

Conclusions: Our *in vivo* data suggest that the spectrally selective HFA pulses produced higher SNR images compared to the CFA scheme. Flip angles were calculated such that the hyperpolarized signal for each metabolite would be preserved sufficiently to acquire images with SNR >5 at time points >30s range. Higher SNR makes it easier to visualize and quantify results from ^{13}C imaging and this is critical for observing metabolism since the steady-state metabolism occurs in the later stages of dynamic imaging, after the pyruvate bolus has arrived from the heart and begun to metabolize. This pulse sequence will be implemented into our ongoing *in vivo* metabolic imaging studies.

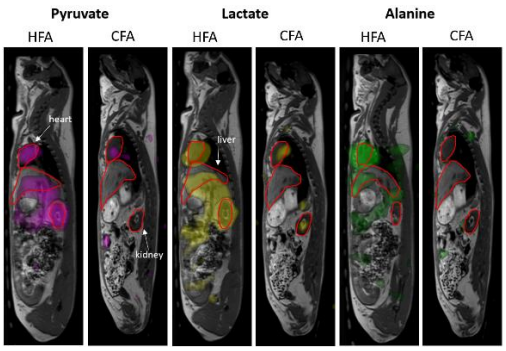

Figure 1: Sagittal T1 slices of the guinea pig with ^{13}C images overlaid. The displayed ^{13}C images were acquired at the 6th timepoint (starting 45s post-injection). Heart, liver, and kidney outlined in red on each image.

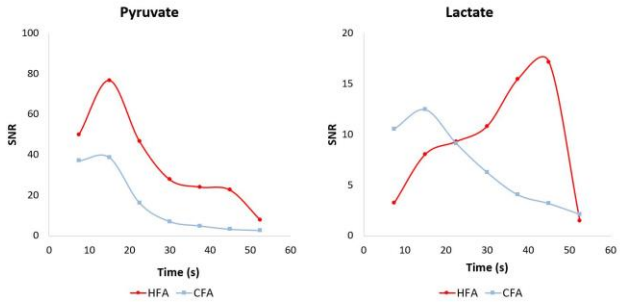

Figure 2: Plots of SNR for pyruvate and lactate calculated from an ROI placed in the left kidney. SNR remains higher for the HFA scheme at the later time points of the scan. Time = 0s is the start of pyruvate injection.

Accelerated 3D Spiral-IDEAL Imaging Approach for Breath-hold Hyperpolarized ^{129}Xe Lung MRI

Brandon Zanette[1,2], Giles Santyr[1,2]

1. Department of Medical Biophysics, University of Toronto, Toronto, ON 2. Translational Medicine, The Hospital for Sick Children, Toronto, ON

Introduction: MRI of hyperpolarized (HP) ^{129}Xe dissolved in lung tissue holds promise for evaluating gas exchange in early functional diseases. Imaging dissolved HP ^{129}Xe is difficult due to low signal, short T_2* (~1ms at 3T), and breath-hold durations achievable by patients (<16s). A technique for rapid imaging of dissolved ^{129}Xe known as spiral-IDEAL[1] has previously been demonstrated by our group in rats[2–4]. Preclinical use of spiral-IDEAL is limited to single-shot spirals and 2D projections at multiple gas exchange times to quantify gas exchange. To address this, clinical translation of spiral-IDEAL has implemented interleaved spirals to keep readout time short and stack-of-spirals encoding for 3D acquisitions. The result is improved image quality and 3D data at the expense of longer acquisition times. Therefore gas exchange timepoints or slice resolution must be sacrificed to meet breath-hold constraints. These constraints are especially problematic for children and patients suffering from pulmonary diseases. Parallel imaging (PI) can accelerate data acquisition and has been explored for gradient-echo imaging of HP gas[5]. To our knowledge, PI approaches have not been applied to spiral-IDEAL acquisitions. In this work we use retrospective undersampling of fully sampled HP ^{129}Xe spiral-IDEAL data acquired from multiple channels reconstructed using PI to investigate the effect of image acceleration factors sufficient for clinical scanning.

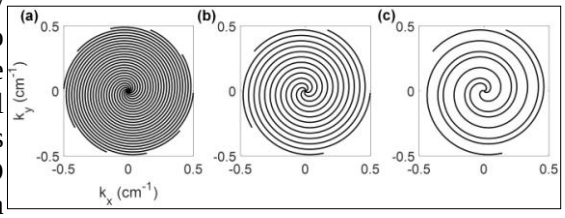

Fig. 1: Interleaved spiral trajectories for **(a)** fully sampled dataset, **(b)** 2x undersampling, **(c)** 3x undersampling.

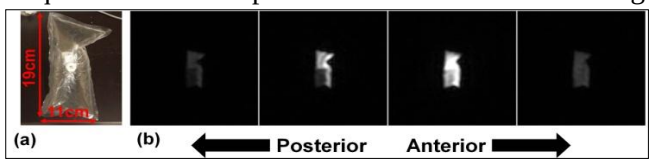

Fig. 2: (a) Photo of HP ^{129}Xe gas phantom with dimensions. **(b)** Fully sampled 3D slices coronal images of the phantom.

Methods: Phantom imaging was performed on a clinical 3T scanner (Skyra, Siemens GmbH, Erlangen Germany) with a coil consisting of an elliptical birdcage transmit coil and an 8-channel surface receive coil (RAPID Biomedical GmbH, Rimpar, Germany). A commercial polarizer (Model 9800, Polarean, Durham, NC) was used to yield polarizations of ~12%. A 300mL Tedlar bag (Jensen Inert Products, Coral Springs, FL) filled with 100% xenon was imaged using a custom designed spiral-IDEAL pulse sequence (FOV=48×48cm^2, resolution=1×1cm^2, slice thickness=3cm, interleaves=10). Reconstruction was performed in MATLAB using the non-uniform fast Fourier transform (NUFFT) algorithm[6] and interpolated to a matrix of 128×128. The fully sampled dataset was retrospectively undersampled by removing appropriate numbers of spiral interleaves to provide acceleration factors of 2 and 3 (Fig. 1). The undersampled data were reconstructed either conventionally or using PI, the latter performed using the SPIRiT algorithm for arbitrary k-space sampling[7].

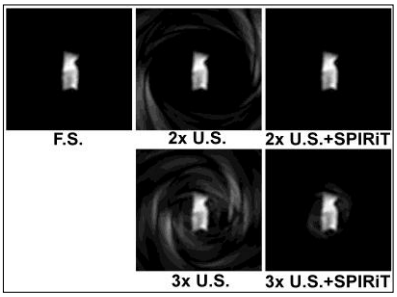

Fig. 3: Reconstructions illustrating fully sampled (F.S.) data, undersampled (U.S.) data, and undersampled data reconstructed with SPIRiT.

Results: Fig.2 shows several slices of the ^{129}Xe phantom in the coronal plane with a photograph of the phantom for comparison. Fig. 3 shows the central slice of the phantom reconstructed: (i) fully, (ii) undersampled, (iii) undersampled + SPIRiT.

Discussion and Conclusion: Fig. 3 confirms that reasonable image quality can be obtained up to an acceleration factor of 3, using retrospective undersampling of multi-channel data from a HP ^{129}Xe gas phantom. Spiral aliasing is present in the 2× undersampled images reconstructed without PI near the edges of the FOV, but because of the small size of the phantom, these artifacts do not significantly interfere with the phantom image due to FOV oversampling. Nevertheless, such artifacts would be expected to affect clinical image quality due to increased size of the lungs with respect to the FOV. These artifacts are significantly reduced when using SPIRiT reconstruction, although some of these artifacts persist with 3× acceleration. Future work will involve testing and optimization of the algorithm in-vivo with fully sampled datasets and retrospective undersampling. Afterwards prospective undersampling by removing sampling interleaves will be investigated. The shortened acquisition can be used to reduce breath-hold duration (2 to 3-fold) or traded for increased number of acquired slices or gas exchange timepoints.

References: 1. Wiesinger F. et al., *Magn Reson Med* (2012). 2. Doganay O. et al., *Magn Reson Med* (2015). 3. Doganay O. et al., *Med Phys* (2016). 4. Zanette B. et al., *Med Phys* (2017). 5. Lee RF et al., *Magn Reson Med* (2006). 6. Fessler J. et al., *IEEE S-TP* (2003). 7. Lustig M. et al., *Magn Reson Med* (2010).

Under-sampling and Reconstruction Effects in 31P-MRSI using flyback-EPSI with Compressed Sensing

Diana Harasym[1], Alejandro Santos-Diaz [1], Michael D Noseworthy [1,2]
[1]School of Biomedical Engineering, McMaster University, Hamilton, ON, Canada.
[2]Electrical and Computing Engineering, McMaster University, Hamilton, ON, Canada.

Introduction

Phosphorus Magnetic Resonance Imaging (^{31}P-MRSI) is able to measure high energy phosphate metabolism in tissues. However, due to its low sensitivity, long acquisition times are necessary to achieve adequate SNR. This has limited the transfer of ^{31}P-MRSI to clinical applications. Rapid MRSI sequences, such as Echo Planar Spectroscopic Imaging with flyback readout (fEPSI) have been implemented to resolve long acquisition times associated with ^{31}P-MRS[1,2]. Compressed sensing (CS) fEPSI has also been implemented to reduce acquisitions times even further[3]. The aim of this study was to compare these acquisition strategies with conventional free induction decay chemical shift imaging (fidCSI).

Methods

Data was acquired using a 3T GE MR750 system and a home designed/built ^{31}P circular quadrature birdcage coil (51.720 MHz/ 30 cm diameter). A custom spherical phantom (1L) was used containing 40 mM of sodium phosphate buffer (Pi) and 20 mM of phosphocreatine disodium salt (PCr). The fEPSI trajectory was created to achieve a 2.5x2.5 cm^2 spatial resolution (8x8 array, 20cm^2 FOV, 1420 Hz BW, 512 spectral points) using an SNR optimized algorithm. Under-sampling was implemented through the inclusion of pseudo-randomly distributed gradient blips in the Ky dimension to achieve acceleration factors of 2x, 2.7x and 4x (TR = 3s, 1024 spectral points, 90^o flip angle, 12 averages, 4cm slice thickness). **Fig 1** shows an example under-sampling scheme. Data processing and CS reconstruction was performed in MATLAB using a modified version of the SparseMRI toolbox[4]. Spectra were fitted using the OXSA MATLAB toolbox[5]. Metabolite ratios (PCr/Pi) were calculated using the normalized amplitudes and compared to fully sampled fEPSI and fidCSI (TR = 5s, 1024 spectral points, 1500Hz BW, 12 averages, 4cm slice thickness).

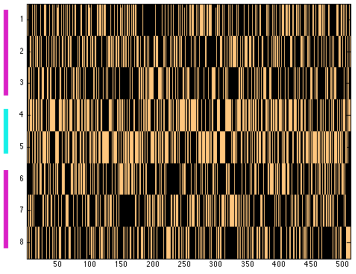

Fig 1: *Under-sampling scheme for CS fEPSI at 2.7x acceleration. The center of k-space (phase encoding 4 and 5) are sampled more than the edges.*

Results

Metabolite ratios of the 3 x 3 center voxels for fidCSI, fEPSI and CS acquisitions are shown in **Table 1**.

PCr/Pi	fidCSI	fEPSI	CS fEPSI 2x	CS fEPSI 2.7x	CS fEPSI 4x
mean	2.486	2.34	2.65	3.22	5.42
SD	0.231	0.221	0.562	0.255	1.39

Table 1: *Mean and standard deviation of PCr/Pi ratio.*

Conclusion

Overall, ratios of fEPSI and CS fEPSI at an acceleration of 2x, show good correspondence with fidCSI ratios. However, at higher acceleration factors (2.7x and 4x) compressed sensing method reduces the Pi amplitude. This is likely due to the under-sampling scheme, which does not sample the center of k-space adequately for higher acceleration factors. Speaking to the importance of sampling center of k-space sufficiently in compressed sensing MRSI. Optimized reconstruction algorithms that do not affect metabolite amplitudes as severely for accelerated sequences could decrease acquisition time even further. It is also evident that fEPSI has lower variance in its measures than fidCSI. Since flyback trajectories do not contain reversed echoes, the spectra are more robust and insensitive to acquisition errors. CS fEPSI gives comparable results to conventional ^{31}P-MRSI methods such as fidCSI, but is able to acquire the data in about half the time.

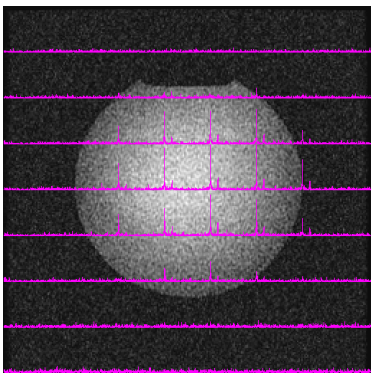

Fig 2: *MRSI of phantom for CS fEPSI at an acceleration of 2x*

References

[1] Obruchkov, S.I., et el., in ESMRMB 2009 congress, 2009, p. eï 76. [2] Santos-Diaz, A., et al., in ISMRM 2016 congress, 2016 [3] Santos-Diaz, A., et al., in ISMRM 2017 congress, 2017 [4] Lustig M., et al., Magnetic Resonance in Medicine, 2007 Dec; 58(6):1182-1195 [5] Purvis, L.A., et al., *PloS one*, 2017, *12*(9), p.e0185356.

Density-Adapted 3-Dimensional Radial Multiple Gradient-Echo Acquisition Scheme for ^{23}Na MRI

Alireza Akbari[1,2], Michael D. Noseworthy[3,4,5] and Timothy J. Scholl[1,2,6]

[1]Medical Biophysics, Western University, London, [2]Robarts Research Institute, Western University, London, [3]School of Biomedical Engineering, McMaster University, Hamilton, [4]Imaging Research Centre, St Joseph's Healthcare, Hamilton, [5]Electrical and Computer Engineering, McMaster University, Hamilton, [6]Ontario Institute for Cancer Research, Toronto

INTRODUCTION Sodium magnetic resonance imaging (MRI) is challenging because of the limited signal-to-noise-ratio (SNR) associated with low *in vivo* concentration. It also suffers from image blurring due to its short biexponential transverse relaxation, T_2. Currently, ultrashort echo time (UTE) sequences employ one gradient lobe per repetition time (TR). The acquisition window is chosen to be relatively long compared to T_2^* to improve SNR. However, the resulting images suffer from blurring due to T_2^*. In this work, we introduce a new method that uses multiple shorter-duration gradient lobes (*i.e.* multiple gradient echoes) that achieve similar SNR to that of a longer single gradient lobe but preserves image resolution by reducing T_2^* blurring (Fig. 1).

METHODS A density-adapted 3-dimentional projection reconstruction (DA-3DPR) sequence **(1)** was implemented on a GE MR750 3T MRI (General Electric Healthcare, Milwaukee WI). Two sodium DA-3DPR acquisition schemes were generated. One scheme employed a series of 6 sequential gradient lobes per radial acquisition, each lobe being 4 ms long corresponding to a total acquisition window of 24 ms. A second scheme used a single gradient lobe with a length of 25 ms. The following additional imaging parameters were used for both gradient strategies: TE/TR = 0.25/100ms, 11310 projections, isotropic resolution/FOV = 3mm/18cm, and 2 averages. Sodium scans were performed on a knee of a healthy volunteer using a home-built 12-rung split design 18-cm-diameter birdcage transmit/receive RF coil tuned for ^{23}Na (33.786 MHz). All images were reconstructed into 60 slices of 540 × 540 (*i.e.* 3-mm in-plane resolution × 3-mm thick slices) using a non-uniform fast Fourier transform (NUFFT) **(2)**. To quantify the extent of blurring, the full-width-at-half-maximum (FWHM) of the line profiles across the patellar, posterior femoral condyle, and femorotibial cartilages were measured for each T_{acq} and SNR was calculated on the aforementioned cartilage sections according to Madelin *et al*. **(3)**.

RESULTS *In vivo* coronal views of the knee using the two acquisition schemes are shown in figure 2. The blurring was reduced in images acquired using DA-3DPR multiple gradient echo scheme by approximately 3 pixels (*i.e.* ~ 1 mm) in femorotibial cartilage as depicted in Figure 3. The SNR measurement in sections of cartilage is shown in figure 4.

CONCLUSIONS Our new proposed sodium MR acquisition scheme (DA-3DPR multiple gradient echo) is capable of achieving similar SNR to that of conventional single-lobed DA-3DPR while reducing T_2^* blurring for preserved image resolution.

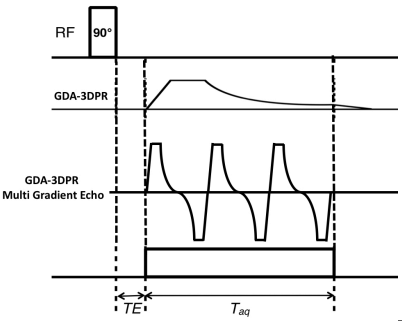

Figure 1. DA3-PR conventional single-lobe and proposed multiple gradient echo schemes. The proposed method matched the conventional acquisition window length to preserve the SNR while short gradient lobes makes imaging more immune to blurring.

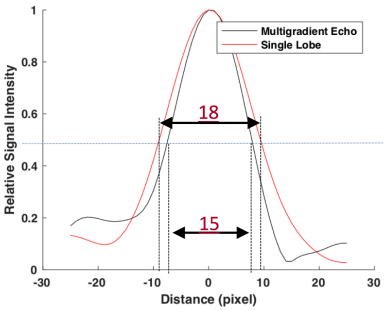

Figure 3. Line profile through femorotibial cartilage. Multiple gradient echo shows less blurring (narrower cartilage cross-section) as compared to conventional DA-3DPR.

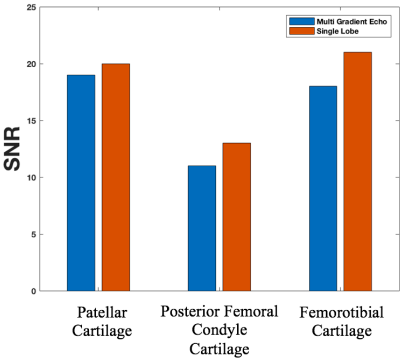

Figure 4. SNR measurements for different sections of articular cartilage. Multigradient echo achieved similar SNR as conventional DA-3DPR.

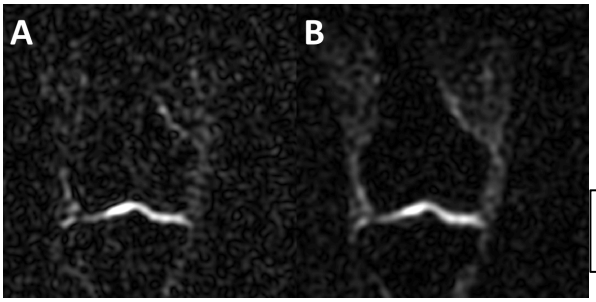

Figure 2. Coronal views of ^{23}Na MR images of the knee using (A) multiple gradient echo and (B) conventional DA-3DPR.

REFERENCES 1. Nagel AM, er al. Magn Reson Med. 2009;62(6):1565-1573. 2. Fessler J a. J Magn Reson. 2007;188(2):191-195. 3. Madelin G, et al. Magn Reson Med. 2012;68(3):841-849. 8. Madelin G, et al. Prog Nucl Magn Reson Spectrosc. 2014;79:14-47.

Oral Presentation Abstracts

Session 10: Neuroimaging

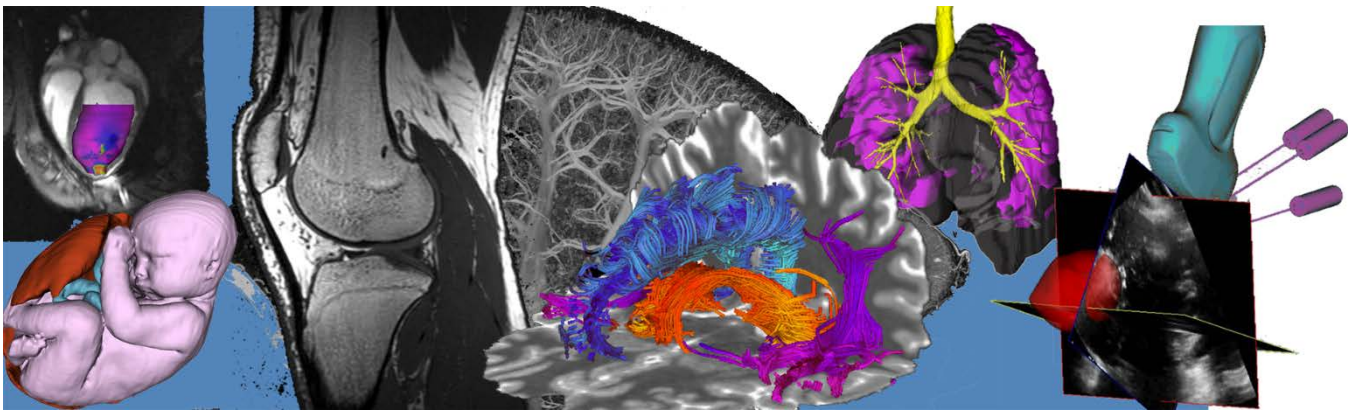

Effect of scan duration on CT Perfusion-derived Hemodynamic Parameters and Infarct Volume

E Wright[1]*, C. dôEsterre[2], L Hur[1], C McDougall[3], M Horn[3], M Goyal[2,3], A Demchuk[2], B Menon[2,3], T-Y Lee[1]

Theme: Perfusion, Metabolic, and Hypoxia Imaging

[1]Medical Biophysics, University of Western Ontario, London, Ontario. [2]Radiology and [3]Clinical Neurosciences, Foothills Medical Center, University of Calgary, Calgary, Alberta.

Introduction: Applying thresholds to cerebral blood flow (CBF), time-to-maximum (T_{max}) and other parameter maps from CT Perfusion (CTP) allows quantification of the volume of irreversibly damaged infarct core and salvageable penumbra in an acute ischemic stroke patient (1). These infarct and penumbra volumes are important for determining patient eligibility for endovascular therapy and other aspects of triaging (2). However, CTP scan durations in clinical studies range from 40-120s (3) despite the possibility of truncation artifacts from delayed wash-in and wash-out of contrast agent affecting the accuracy of CTP parameter calculations for ischemic tissue, and by extension, the accuracy of infarct or penumbra volumes used for triaging. The purpose of this study was to investigate the relationship between scan duration and CTP parameters and threshold-derived infarct and penumbra volumes.

Methods: 66 acute ischemic stroke patients underwent admission CTP with a scan duration of 150s, and follow-up non-contrast CT (NCCT) 24-48 hr post symptom onset. Images were progressively removed from the end of the acquisition to simulate scan durations of 120, 90, 60, and 40s, and maps were computed for each scan duration. The follow-up NCCT was co-registered with CTP maps and used to delineate 3 regions of interest (ROIs), namely infarct (CBF<7 mLÃmin^{-1}Ã100g^{-1}, T_{max}>16 or 21s) ipsilateral penumbra (CBF<13 mLÃmin^{-1}Ã100g^{-1}or T_{max}>9s excluding infarct) and autologous contralateral tissue. Median cerebral blood volume (CBV), CBF, and T_{max} were measured from all ROIs for each scan duration, and the volumes of tissue quantified from the above thresholds were also recorded for each scan duration. 1-way repeated measures ANOVA and post-hoc paired t-test with Bonferroni correction were used to assess the effect of scan duration on median parameter values and the threshold-derived volumes.

Results: Scan duration did not have a significant effect on median CBF but had significant effects on median CBV ($p<0.001$) and median T_{max} ($p<0.001$) in all 3 ROIs. Decreasing scan duration from 150 to 40s changed median CBF, CBV, and T_{max} in the infarct ROI by 2, -44, and -44% respectively, relative to the 150s duration. Scan duration had a significant effect on tissue volumes derived using both CBF thresholds ($p<0.05$), and all three T_{max} thresholds ($p<0.001$). Maximum percentage change of threshold-derived volumes, relative to the 150s duration, occurred at a scan duration of 40s for all thresholds. Average volumes of tissue with CBF<7 and 13mLÃmin^{-1}Ã100g^{-1} decreased by 3 and 4% respectively, and volumes of tissue with T_{max}>9, 16, and 21s decreased by 38, 62, and 75% respectively (see figure).

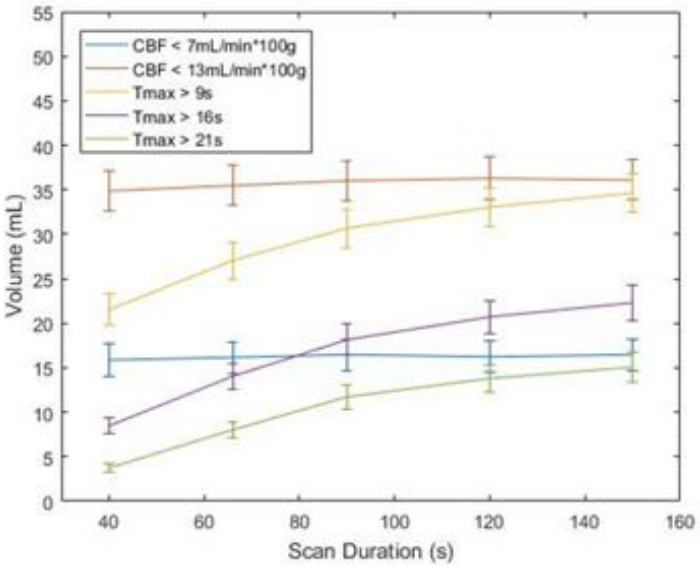

Figure 1: Average volume derived by CBF and T_{max} thresholds vs. scan duration. Volumes derived by T_{max} thresholds decrease greatly at short scan durations whereas CBF-derived volumes are relatively unaffected.

Conclusions: CBV and T_{max} are strongly dependent on scan duration, and likely underestimated when shorter scan durations are used. CBF is relatively independent of scan duration, and infarct/penumbra volumes derived by CBF thresholds remain within ~3.5% agreement over a range of scan durations from 40-150s.

References: [1] Jovin et al. *Int J Stroke.* 2017: 12(6): 641-652. [2] Campbell et al. *N Engl J Med* 2015: 372(11): 1009-1018. [3] Borst et al. *PLoS ONE.* 2015: 10(3): e0119409.

Design and evaluation of a diffusion MRI fibre phantom using 3D printing

Uzair Hussain[a,b], Serene O. Abu-Sardanah[a], John Moore[a], Corey Baron[a,b], Terry Peters[a,b] and Ali R. Khan[a,b]
[a]Robarts Research Institute, [b]Departments of Medical Biophysics and Medical Imaging Western University, London, ON, Canada

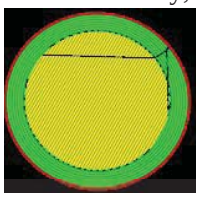

Figure 1: Phantom model

Introduction: Interpretation of diffusion magnetic resonance imaging (dMRI) data relies heavily on the mathematical models used for fitting. In-vivo studies cannot describe the effectiveness of such models. One approach is to fabricate carefully designed phantoms which provide a ground truth to test the accuracy of the models. In this study we use 3D printing technology to efficiently construct various fibrous phantoms and then scan them under a typical dMRI protocol. We use the resulting data to test the accuracy and effectiveness of dMRI mathematical models.

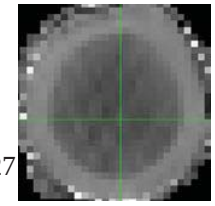

Figure 2: Fractional anisotropy

Methods: To 3D print the fibers we utilize a commercially available material, Gel-Lay, which is composed of Polyvinyl Alcohol (PVA) and a rubber elastomeric polymer. When immersed in water the PVA dissolves leaving a porous fibrous material. The 3D printer used is the Ultimaker 3 Extended 3D. We print phantoms in the shape of flat disks with a 27 mm diameter and a height of 5 mm. The disk is composed of an exterior cylindrical rim 4.8 mm thick (Figure 1). The rim is made by printing a family of concentric circles. The interior of this rim is printed in layers such that the fibers in each consecutive layer make an angle with the fibres in the previous layer and fibers in each alternate layer are parallel. Three disks were printed with angles 30, 60 and 90 degrees. To generate the diffusion weighted images the disks were scanned in a 7T Siemens Magnetom (30 b=1000 directions, 90 b=2000 directions and 6 b=0 directions). Our scanning protocol also included T1 and T2 relaxation time maps. Mean T1 and T2 values were calculated from data taken from regions in the geometric center of each disk. After the scanning we also performed optical microscopy to verify the relative angles. We fit the dMRI data with a tensor model (FSL DTIFIT), and a compartmental ball & stick model (FSL BEDPOSTX)[1]. We also construct a distribution of the relative angle between the first two sticks from BEDPOSTX (Figure 4), this is done by using the mean orientation angles of each stick in a one voxel thick ñbest sliceò, i.e., where the sticks showed the most coherence.

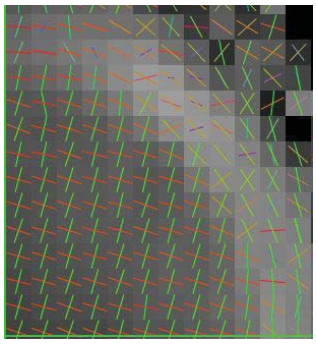

Figure 3: 90 degree "sticks"

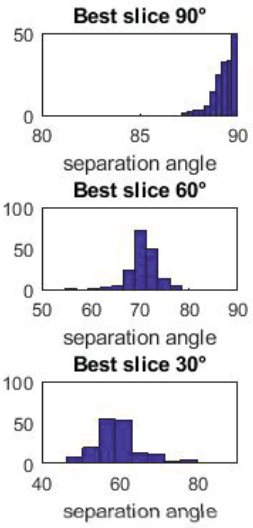

Figure 4: Distribution of relative angle

Results: In Figure 2 we see the mean fractional anisotropy (FA) of the 60 degree disk, note the higher values around the cylindrical rim. The sticks in one of the quadrants from the BEDPOSTX model are shown in Figure 3. We can qualitatively see the 90 degree pattern in the infill and a circular pattern at the boundary. Figure 4 shows the distributions of the relative angle of all three phantoms. Notice how the 90 degree phantom leads to the best results. For the 60 degree phantom we see an offset of approximately 12 degrees from the ground truth value. Lastly, for the 30 degree phantom we see a wider spread and an even larger offset. From the T1 and T2 maps we found mean T1=1536.9 Ñ34.7 ms and mean T2= 78.3 Ñ1.1 ms.

Conclusion: In this study we have used novel 3D printing methods and materials to construct dMRI phantoms. We then used these phantoms to check the effectiveness and accuracy of dMRI fitting models. We find that the FA map accurately captures the outer rim and even some of the crossing fibers (Figure 2). For the compartmental model with two sticks, we see a peculiar shift in the 60 and 30 degree angles which warrants further exploration. However, the 90 degree sticks show excellent results in line with the ground truth (Figueres 3 & 4). From the T1 map we calculated a mean T1 of 1536.9 Ñ 34.7 ms which falls close to white matter (1063 ms) and grey matter (2144 ms) values at 7T [2]. In future studies we plan to further explore various printing parameters and geometries which will enable us to test and develop fitting models.

References: [1] M. Jenkinson, C.F. Beckmann, T.E. Behrens, M.W. Woolrich, S.M. Smith. FSL. NeuroImage, 62:782-90, 2012 [2] Ansorge, Richard and Graves, Martin, The Physics and Mathematics of MRI, Morgan & Claypool Publishers, 2016

Between- and within-site MRI scanner stability investigated using EPI fMRI phantom scans

M Kayvanrad[1], A Chemparathy[1], SR Arnott[1], F Dong[1], M Zamyadi[1], T Gee1, R Bartha[2,3], CJM Scott[4], SE Black[4], SP Symons[4] , the ONDRI investigators, G MacQueen[5], J Harris[5], A Davis[6], G Hall[6], S Hassel[5,7], SC Strother[1,8]

[1]Rotman Research Institute, Baycrest, [2]Centre for Functional and Metabolic Mapping, Robarts Research Institute, [3]Department of Medical Biophysics, Western University, [4]Sunnybrook Research Institute, [5]The Mathis Centre for Mental Health Research and Education, University of Calgary, [6]Department of Psychology, Behaviour and Neuroscience, McMaster University, [7]School of Life and Health Sciences, Aston University, UK, [8]Department of Medical Biophysics, University of Toronto

Introduction The Ontario Neurodegenerative Disease Research Initiative (ONDRI) (1) and the Canadian Biomarker Integration Network in Depression (CAN-BIND) (2) are multisite longitudinal studies that employ 12 MRI scanners across Canada (6 in CAN-BIND) to collect neuroimaging data. To ensure comparability of neuroimaging data collected at different sites, fBIRN (functional Biomedical Informatics Research Network) phantoms have been scanned approximately monthly at each site for more than two years to obtain quality assurance (QA) measures from the fBIRN pipeline.These measures have been used to assess inter- and intra-scanner variability.

Methods fBIRN phantoms were scanned using fMRI EPI sequences using 3T MRIs. 16 fBIRN QA parameters from 353 scans were analysed using principal component analysis (PCA). To reduce inter-scanner variance caused by differences in imaging resolution, all scans were smoothed to FWHM=7mm using AFNI (3). The fBIRN QA pipeline was rerun and QA measures analysed using PCA.

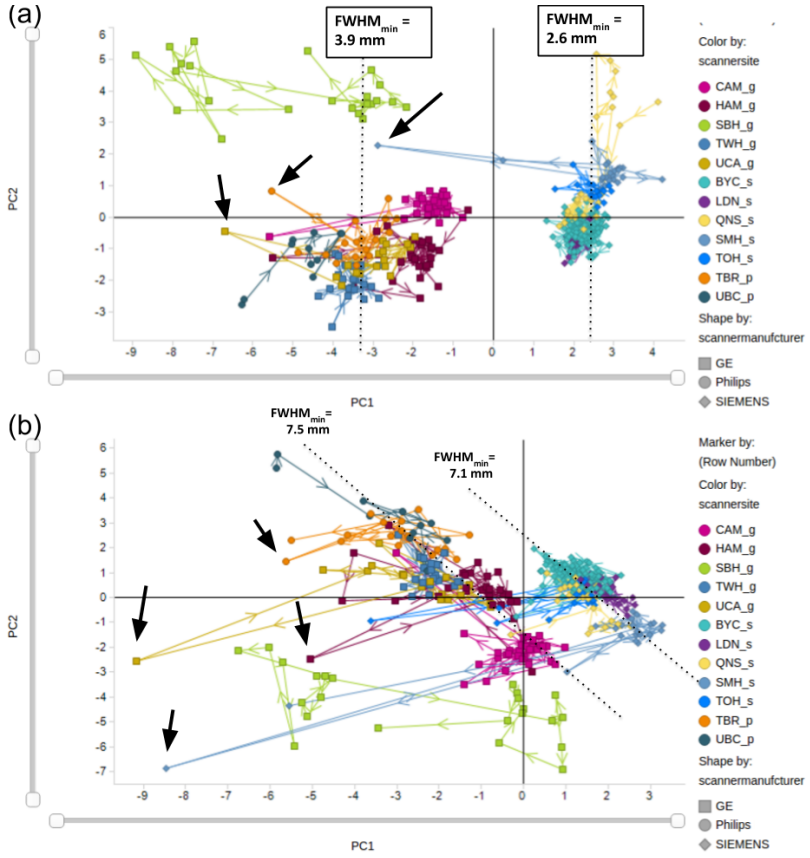

Figure 1- PCA analysis of fBIRN QA measures of unfiltered (a) and smoothed (b) images. 353 scans are plotted in terms of the first two PCs. Arrowheads highlight examples of prominent within-site outliers.

Results The results of PCA analysis of unfiltered images are shown in Figure 1(a). PC loadings show that PC1 is primarily driven by measures of FWHM and radius of decorrelation (RDC), while ghosting and drift are the primary factors driving PC2. There is a prominent inter-scanner separation along PC1. While within-site variance is generally smaller than between-site variance, several sites show prominent within-site outlier sessions. After spatial smoothing (Figure 1(b)), vendor-based inter-scanner separation is observed, though to a lesser extent, along both PC1 and PC2.

Conclusion Scanner vendor (i.e., GE, Siemens, Philips) appears to be a major source of inter-scanner variance, primarily due to FWHM differences attributed to different image reconstruction techniques employed by different vendors. While spatial smoothing reduces inter-scanner differences, within-site outlier sessions are exacerbated by spatial smoothing (Compare Figure 1(b) and Figure 2(b)). These non-uniformities presumably account for a significant proportion of the variability in fMRI time series. We are currently investigating these instabilities, their origin, and their impact on human resting-state scans, as well as improved preprocessing pipelines that further reduce scanner variability.

Reference 1. Farhan, et al. Can J Neurol Sci 2017; 44:196ï 202. 2. Lam et al. BMC Psychiatry 2016; 16:105. 3. Cox, Comput Biomed Res 1996; 29:162ï 173.

RELATING HIPPOCAMPAL GLUTAMATE TO STRUCTURAL CHANGES AND COGNITIVE PERFORMANCE IN ALZHEIMERÕS DISEASE: A 7T MRI STUDY

Dickson Wong[1], Samir Atiya[2], Jennifer Fogarty[3], Manuel Montero-Odasso[3,4], Stephen Pasternak[2,3,4], Chris Brymer[4], Michael Borrie[3,4], Robert Bartha[1,2]

[1]Medical Biophysics, Western University, [2]Robarts Research Institute, Western University, [3]Parkwood Institute Research Program, Lawson Health Research Institute, [4]Geriatric Medicine, Western University

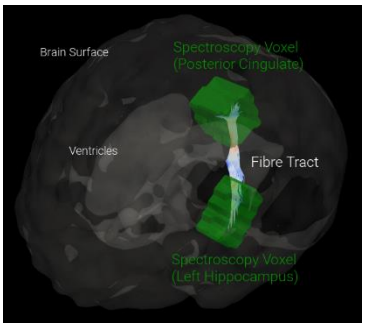

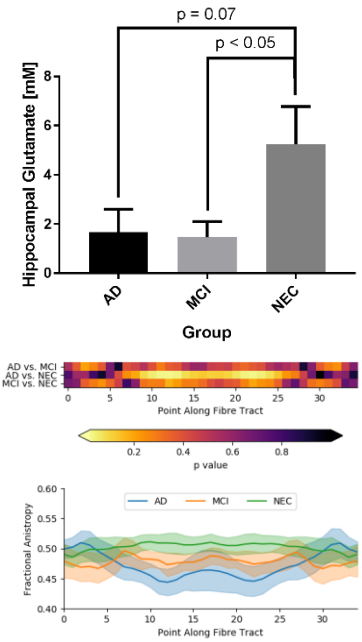

Introduction: Alzheimerõs disease (AD) is a type of dementia that causes problems with memory, thinking, and behaviour. Diagnosis and prognosis in AD remains a challenge, but MRI biomarkers could help meet this need. Using high-field proton magnetic resonance spectroscopy (^{1}H-MRS) at 4T, we previously reported decreased hippocampal glutamate (Glu) levels in participants with AD compared to normal elderly control participants [1] and proposed hippocampal glutamate levels as a biomarker of AD. In this study, we aimed to further investigate Gluõs potential as an AD biomarker by measuring Glu levels at ultra-high field (7T) and relating them to measures of neurodegeneration and cognitive performance.

Methods: We have recruited normal elderly controls (NECs, n=13, 74Ñ7.3 years), individuals with mild cognitive impairment (MCIs, n=6, 75 Ñ 10 years), and individuals with prodromal AD (ADs, n=7, 79Ñ7.9 years). Recruitment will continue until there are 15 participants in each group. ^{1}H-MRS data were acquired using the semi-LASER sequence (TE=60 ms, TR=7500 ms, 64 averages) from single voxels in the left hippocampus (23x12x12 mm^3) and in the posterior cingulate cortex (PCC, 16x20x18 mm^3). Spectroscopy data were analysed using in-house software and absolute glutamate levels were compared between groups using a one-way analysis of variance (ANOVA) with post-hoc adjustment for false discovery rate (FDR). Diffusion weighted imaging was performed using a multi-shot diffusion-weighted spin-echo EPI sequence (b=1000 s/mm^2, TR=5100 ms, TE=50.2 ms, 64 directions, 2 mm isotropic resolution). Using Camino [2], whole-brain fractional anisotropy (FA) maps were obtained. Bayesian probabilistic streamline tractography was performed on the FA maps to find fibres passing through both spectroscopy voxels. Fibres were grouped by geometric similarity using k-means clustering, allowing for the isolation of the main hippocampal-PCC white matter tract connecting the two spectroscopy voxels (*Top Figure*). Tract-based measurements of FA (*Bottom Figure*) were also obtained and compared between groups using a two-way ANOVA with post-hoc FDR adjustment. Cognitive performance was assessed using the National Alzheimerõs Coordinating Center Neuropsychological Battery, Version 3.0 [3]. Relationships between glutamate levels, tract FA, and cognitive measurements were assessed using the Spearman correlation coefficient (ρ).

Results: In the left hippocampus, a statistically significant trend towards decreased Glu in ADs compared to NECs was observed (p=0.07). Hippocampal Glu levels were significantly lower in MCIs compared to NECs (p<0.05, *Middle Figure*). In the hippocampal-PCC tract, ADs had significantly lower tract FA values than NECs (*Bottom Figure*). Higher hippocampal Glu level was associated with higher average tract FA (ρ=0.59, p<0.05). Hippocampal Glu levels were positively correlated with several cognitive measurements including figure copy performance (ρ=0.48, p<0.05), a measure of spatial planning and working memory. Better figure copy performance was also associated with higher average tract FA (ρ=0.48, p<0.05). No significant differences in Glu levels were observed in the PCC. PCC Glu levels were not related to tract FA or cognitive measurements.

Conclusions: ^{1}H-MRS results in this preliminary study agreed with our previous findings at 4T. Lower FA values in the hippocampal-PCC tract of AD participants indicates less restricted diffusion and may reflect a loss of neuronal density in AD. Lower hippocampal Glu was associated with lower FA and lower cognitive performance, suggesting that hippocampal Glu could be a biomarker of neuronal loss and cognitive performance in AD.

References: [1] Rupsingh et. al, Neurobiol Aging. 2011 May;32(5):802-10. [2] Cook et. Al, ISMRM, Seattle, WA, USA, p. 2759, May 2006. [3] Weintraub et. al, Alzheimer Dis Assoc Disord. 2009;23(2):91-101.

Magnetic Resonance Spectroscopy in a Rodent Concussion Model

Amy Schranz*, BMSc, Kathy Xu, Patrick Mccunn, BSc, Arthur Brown, PhD, Robert Bartha, PhD
Robarts Research Institute, The University of Western Ontario

Introduction: A concussion is a brain injury induced by rapid rotational and translational accelerations to the brain [1]. Athletes participating in contact sports have a high risk of sustaining a concussion, which can lead to structural and metabolic changes in the brain. Biomarkers are urgently required to monitor the effect of concussion on the brain. In concussion, diffuse axonal injury and a secondary chemical cascade can result in mitochondrial dysfunction and altered metabolism [2] that can manifest as changes in brain metabolite levels measurable *in-vivo* by magnetic resonance spectroscopy (MRS). Our group has previously measured changes in human prefrontal white matter metabolite levels using MRS. Specifically, we have shown reduced choline levels in male adolescent hockey players [3], and reduced glutamine levels in female varsity rugby players [4]. Development of a rodent concussion model that reproduces these changes would allow careful evaluation of the biological mechanisms causing these changes and aid in the evaluation of therapeutics. The purpose of the current study was to demonstrate the feasibility of measuring metabolite changes in mice post-concussion. It was hypothesized that the metabolite changes previously characterized could be replicated in concussed mice.

Methods: Sixty C57BL/6 male mice were used in the current study. Mice were divided into five groups, sham control (n=12), 48 hours post-concussion (n=12), 1 week post-concussion (n=12), 4 weeks post-concussion (n=12), and 10 weeks post-concussion (n=12). Concussed mice were anaesthetized and positioned under a traumatic brain injury device (TBI 0310, Precision Systems and Instrumentation, LLC). Following a midline incision, the animal received a mild controlled cortical impact centred at the midline bregma, with a custom-made silicone tip. Mice received 5 impacts at 24-hour intervals. The concussed mice were then imaged at either 48 hrs, 1 week, 4 weeks, or 10 weeks after the final impact. Sham control mice received no surgery or impacts. All imaging was performed on a 9.4 Tesla small-bore MRI scanner at the Robarts Research Institute. Magnetic resonance spectra were localized by adiabatic selective refocusing (LASER; TR/TE=3250/20ms, 128 averages). Acquisition of the full spectrum was interleaved with a metabolite nulled (using a single-inversion recovery) macromolecule only spectrum. Spectra were lineshape corrected by combined QUALITY and eddy current correction (QUECC), macromolecule subtracted, then fitted in the time domain using a Levenberg-Marquardt minimization routine. The analysis software (fitMAN) created in our laboratory in the IDL programming language was used to model the *in vivo* spectra using prior knowledge of metabolite lineshapes. A one-way ANOVA was used to assess statistical significance (α=0.05) across time points.

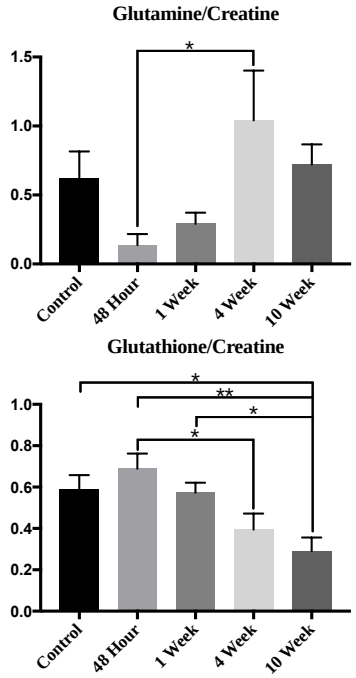

Figure 1. Bar graphs showing the mean Glutamine/Creatine (Top) and Glutathione/ Creatine (Bottom) ratio. Standard error of the mean is represented by vertical bars. Glutamine/ Creatine changed between 48 hours and 4 weeks (F=3.27, P=0.019). Glutathione/Creatine significantly dropped by the 10 week time point (F=5.73, P=0.0008).

Results and Discussion: Preliminary findings show a similar pattern of changes in the glutamine/creatine ratio as that observed in our previous human studies [3,4], with a significant difference between the 48 hour and 4 week time points (Figure 1, top). In addition, the glutathione/creatine ratio was also reduced 10 weeks after injury (Figure 1, bottom). These changes may be indicative of altered oxidative metabolism [5] and oxidative stress [6], respectively. Future work includes examination of sex differences in metabolite responses and refinement of the fitting procedure to measure absolute metabolite levels and increase the reproducibility of the measurements.

References: [1] McCrory et al. *J Athl Train*, *48*(4), 554ï 75, 2012. [2] Giza et al. *J Athl Train*, *36*(3), 228ï 235, 2001. [3] Manning et al. *Neurology, 89*(21), 2157-2166, 2017. [4] Schranz et al. *Hum Brain Mapp,* 2017. [5] Bartnik et al. *J Neurotrauma, 24*(7), 1079-1092, 2007. [6] Rae et al. *Anal Biochem,* 529, 127-143, 2017.

Oral Presentation Abstracts

Session 11: Tissue Characterization

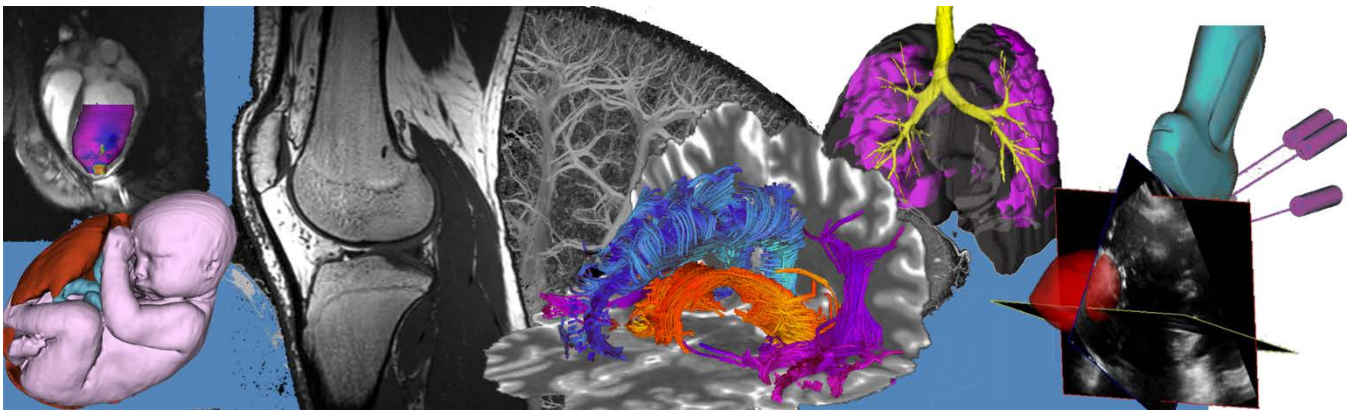

Magnetic resonance imaging of the microbiome using MagA-expressing bacteria

[1,2,3]* Donnelly, SC; [1,4] Thompson, RT; [1,3,4] Prato, FS; [1,4] Gelman, N; [2,5,6] Burton, JP; [1,3,4] Goldhawk, DE
* Trainee, Supervisors
[1] Imaging Program, Lawson Health Research Institute; [2] Microbiology & Immunology, [3] Collaborative Graduate Program in Molecular Imaging, [4] Medical Biophysics, [5] Surgery, Western University; [6] Human Microbiome & Probiotics Research Program, St. Josephôs Health Care; London, Ontario, Canada

Introduction: Magnetic resonance imaging (MRI) is a non-invasive imaging modality with superb resolution at any tissue depth, ideal for examining the soft tissues of the intestinal mucosa. Currently, to identify microbes and explore their properties, samples are removed and propagated *ex vivo*, risking changes in behaviour, or even contamination[1]. Although *in vivo* microbiome analyses are challenging[2], imaging may provide an alternative to *ex vivo* microbial analyses, especially through the use of contrast agents. For example, gene-based contrast agents, using genes from magnetotactic bacteria, have been developed to provide long-term labelling for MRI. Magnetic resonance (MR) contrast has been previously demonstrated in mammalian cells using single genes like *magA*[3] and *mms6*[4]. To explore microbial behaviour, growth and dispersion *in vivo*, in the gut microbiome where commensal relationships exist between host and bacteria, we hypothesize that MagA expression in *Escherichia coli* will increase cellular iron content and impart magnetic properties for cellular detection using MRI at clinical field strength. Here, we examine MR relaxation rates in a bacterial model using a gelatin phantom previously validated in mammalian systems using MagA expression[5].

Methods: *E. coli* BL21(DE3) cells were cultured overnight in lysogeny broth (LB) and pelleted from LB or washed with phosphate-buffered saline (PBS). 8-20 x 10^9 cells were loaded into Ultem wells by centrifuging at 4500 x g and mounted in gelatin phantoms in a protocol adapted from previous mammalian cell work[5] to measure MR contrast at 3 Tesla. Images were evaluated using MATLAB software, using longitudinal (R1 = 1/T1) and transverse (R2* = 1/T2*; R2 = 1/T2) relaxation rates as measures of iron contrast where R2* = R2 + R2N̊j T1 was acquired with inversion-recovery spin-echo (SE); for T2, a single-echo SE sequence was used with varying echo times; and T2* was collected with multi-echo gradient echo, as previously reported[5]. Cells were also assessed after transformation with an epitope-tagged *magA* fusion construct: pcDNA3.1MycHisA$^+$/HA-magA[6]. Expression of HA-MagA-Myc driven by the T7 promoter was examined by Western blot using commercial antibodies (Clontech) to verify HA- and Myc-tagged protein. Statistical analyses were done using GraphPad Prism 7.03 software.

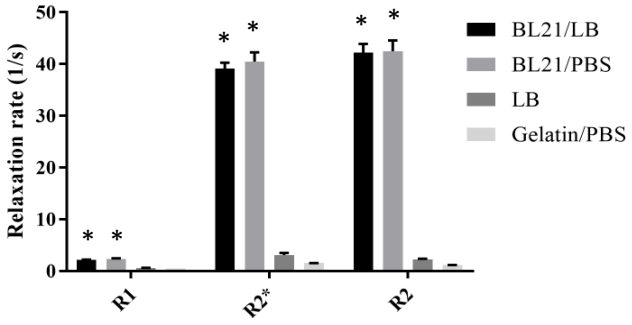

Figure 1. MR relaxation rates in *Escherichia coli*. In the absence of iron supplement, untransformed BL21(DE3) display substantial transverse relaxivity. Bars graphs show mean +/- standard error of the mean (n=4). One-way analysis of variance and Tukeyôs test indicate that bacterial R1, R2* and R2 are significantly higher than background (LB or PBS), (* p<0.0001).

Results: Longitudinal and transverse relaxation rates in untransformed BL21(DE3) are significantly higher (12-36x larger) than the background signal from LB or gelatin (Fig. 1). However, the R1 signal is only 3-4x higher than background and may not be a useful MR measure in these bacteria for future work. The irreversible R2 component accounts for virtually the entire transverse relaxation rate (R2*), with little or no contribution from the reversible R2N̊j component (R2* - R2 ~ 0).

Conclusions: This is the first report providing transverse and longitudinal relaxation rates in a model gut bacterium. Untransformed *E. coli* provide detectable MR contrast, with relaxation rates much higher than those of previously studied mammalian cells[5]. Next, we will examine whether a contrast agent (*magA*) is necessary for imaging *E. coli* as we show that the baseline signal is high, indicating that bacteria alone may be suitable. MRI of the gut provides a large MR signal[7], possibly due to extensive contribution from bacteria. In the future, MRI may be useful for non-invasively imaging bacteria of the microbiome within the host, to diagnose dysbiosis (microbial imbalances, species diversity and abundance) and microbial behaviour that leads to disease.

References: [**1**] Bao et al (2016) Annals of Translational Medicine 5, 33. [**2**] Bron et al (2012) Nat Rev Microbiol 10, 66. [**3**] Goldhawk et al (2009) Mol Imaging 8, 129. [**4**] Zhang et al (2014) Mol Imaging 13, 1. [**5**] Sengupta et al (2014) Frontiers in Microbiology 5, article 29. [**6**] Quiaoit (2015) MSc Thesis, Western University. [**7**] Rohani et al (2014) Mol Imaging Biol 16, 63.

An Investigation into the Biosynthesis Pathway of Serotonin using CEST MRI

Ryan T. Oglesby[1,2], Wilfred W. Lam[1], and Greg J. Stanisz[1,2]
[1]*Physical Sciences, Sunnybrook Research Institute, Toronto, Ontario, Canada,*
[2]*Medical Biophysics, University of Toronto, Toronto, Ontario, Canada*

Purpose: Serotonin (5-HT) is a small molecule neurotransmitter produced in the brain and intestines of the human body. Serotonin plays a role in a variety of biological functions including but not limited to: bowel function, mood, clotting, nausea, bone density, and sexual function. In humans serotonin is synthesized from the amino acid tryptophan in a short metabolic pathway consisting of 3 enzymes and 4 metabolites[1]. The research objectives of this investigation are to characterize the Z-spectrum of each of the 4 metabolites using CEST MRI. With the in-vitro CEST MRI data acquired we may increase the specificity of the in-vivo Z-spectrum interpretations.

Methods: Four metabolites were prepared: Tryptophan, 5-HTP, 5-HT, and 5-HIAA at a concentration of 30 mM and pH of 7.4 Ñ 0.3. Samples were scanned at 7T (BioSpec 70/30 USR, Bruker BioSpin, Billerica, MA) using a temperature controlled phantom holder stabilized at 37.2 Ñ 0.5 ÁC. Single slice images were acquired using magnetization transfer (block saturation pulse, t_{sat} = 490 ms per line of k-space) prepared FLASH (TR = 500 ms, TE = 3 ms, matrix = 64 Ĭ 64, and FA = 30Á). Rician noise bias, B_0, and B_1 corrections were applied.[2,3] Fitting was done in MATLAB using a two-pool and three-pool Bloch-McConnell equation with least squares fit to the Z-spectra acquired with peak saturation amplitudes B_1 of 0.1 (WASSR[3]), 0.5, 1.0, 1.5 and 3.0 ÕT and a T_1 map calculated from inversion recovery RARE scans (TR = 10,000 ms and TI = 30, 110, 390, 1400, 5000 ms). At a saturation B_1 of 0.1 ÕT, data was acquired at frequency offsets between Ñ0.5 ppm in 0.01 ppm steps (water = 0 ppm). For all other saturation B_1, data was collected between Ñ7.0 ppm in 0.033 ppm steps.

Results: Serotonin biosynthesis molecules were characterized according to their peak location φ_{0C}, exchange rate R_C, and CEST pool size M_0 (Figure 1). It was found that the peak locations and amplitudes of these metabolites can be distinguished from one another within experimental uncertainty. The Z-spectra for each metabolite at a saturation B_1 of 1.5 ÕT are shown in Figure 2.

Molecule Name	R_C (s^{-1})	M_{0C} (mM)	φ_{0C} (ppm)
L-Tryptophan	103 ± 26	7.04 ± 1.38	5.46 ± 0.02
5-HTP	70 ± 46	6.44 ± 3.63	5.26 ± 0.02
5-HT	131 ± 31	6.82 ± 1.38	5.27 ± 0.01
5-HIAA	> 300*	< 1.5*	5.10 ± 0.04

Figure 1: Estimated parameters for the two-pool Bloch-McConnell exchange model using the metabolites involved in the biosynthesis pathway of serotonin (5-HT). *Note that due to fast exchange rate of 5-HIAA and small CEST effect, it was not possible to accurately report exchange rate R_C and CEST pool size M_0. Additionally there is a strong correlation between these two parameters.

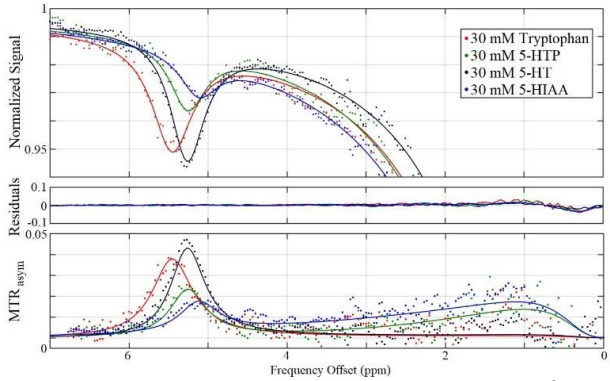

Figure 2: Molecular comparison of Z-spectra at 1.5 ÕT saturation B_1 for the metabolites involved in the biosynthesis pathway of serotonin (5-HT) using a two-pool and three-pool Bloch-McConnell exchange model.

Conclusions: The results of this in vitro phantom study lead us to believe that we will be able to more accurately interpret the results of an in vivo CEST investigation focused on the detection of serotonin. The next stages of this investigation involve the manipulation and observation of brain serotonin in rats to determine whether or not it is possible to detect serotonin in vivo using CEST MRI.

References:

1. Martinez A., Knappskog P.M., and Haavik J. A Structural Approach into Human Tryptophan Hydroxylase and Implications for the Regulation of Serotonin Biosynthesis. Current Med Chem. 2001:8:1077-1091.
2. Henkelman R.M. Measurement of signal intensities in the presence of noise in MR images. Med Phys. 1985:12(2):232-233.
3. Kim M., Gillen J., Landman B.A., Zhou J., van Zijl P.C.M. Magn Reson Med. 2009:61(6):1441-1450.

Acknowledgements: We thank the Canadian Institutes for Health Research (PJT148660) for financial support.

The growth hormone secretagogue receptor, ghrelin, and biochemical signaling processes in human heart failure

Rebecca Sullivan[1], Varinder Randhawa[6], Anne Stokes[2], Derek Wu[1], Sophia Yijia Liu[1], Carlie Charron[3], Tyler Lalonde [3], Leonard Luyt[3,5], Bob Kiaii[6], Gerald Wisenberg[4,7], and Savita Dhanvantari[1,4,7,8]

1. Pathology and Laboratory Medicine, Western University, London, Ontario, Canada; 2. Medical Sciences, University of Ottawa, Ottawa, Ontario, Canada; 3. Chemistry, Western University, London, Ontario, Canada; 4. Imaging Program, Lawson Health Research Institute, London, Ontario, Canada; 5. Department of Oncology, London Regional Cancer Program, Western University, London, Ontario, Canada; 6. Cardiac Surgery Unit, London Health Science Centre, London, Ontario, Canada; 7. Medical Biophysics, Western University, London, Ontario, Canada; 8. Metabolism and Diabetes, Lawson Health Research Institute, London, Ontario, Canada

Background

The leading cause of mortality in Canada is heart disease (HD) which impacts nearly 1.6 million people with over 500,000 affected by heart failure (HF). HF is a specific condition that occurs when the heart is unable to provide enough blood flow and oxygen to organs across the body. Currently, a diagnosis of HF is made using a combination of clinical features, cardiac imaging, and detection of circulating biomarkers, notably B-type natriuretic peptide (BNP). However, a biomarker specific to cardiac tissue and that reflects the heartôs contractile state is lacking. Our group is characterizing the growth hormone secretagogue receptor (GHSR) and its ligand ghrelin as possible cardiac-specific biomarkers for HF. We have previously developed a fluorescent analog of ghrelin, Ghrelin(1-18, Lys^{18}(Cy5), to detect GHSR in cardiac tissue *in situ*. We hypothesize that GHSR and ghrelin are biomarkers for the early detection of HF.

Methods

We obtained samples of cardiac tissue from 10 cardiac transplant patients at the time of organ harvesting and serial post-transplant biopsies. Samples from the LV and RA of the explanted hearts, and biopsies from the newly-transplanted hearts (weekly for 4 weeks, monthly for 6 months, and 1 year post-Tx). GHSR levels were measured using Ghrelin(1-18, Lys^{18}(Cy5) and ghrelin and BNP were measured using fluorescent antibodies. Fluorescent antibodies were also used to measure sarcoplasmic reticulum ATPase pump (SERCA2a) and phosphorylated extracellular signal-related kinase (pERK) for contractility and cell metabolism respectively. All samples were quantified using fluorescence microscopy. Fibrotic tissue was detected using Massonôs trichrome stain. Levels of all markers were compared between the explanted heart and the healthy biopsies using two-tailed t-test, one-way ANOVA and Tukeyôs test and Pearsonôs correlation ($p<0.05$).

Results

GHSR and fibrosis levels increased and were highly variable in explanted hearts when compared to the healthy biopsies, which had lower levels of variability. Levels of ghrelin and BNP showed similar trends to GHSR with less variability. SERCA2a and pERK showed significantly elevated expression in end stage heart failure tissues compared to the implanted heart ($p<0.05$). Regression analysis showed a strong positive correlation between both ghrelin and GHSR ($r=0.7817$, $p<0.0001$) and ghrelin and BNP ($r=0.6782$, $p<0.0001$). There were strong and significant positive correlations between ghrelin and SERCA2a ($r=0.7171$, $p<0.0001$), ghrelin and pERK ($r=0.5719$, $p<0.0001$) and SERCA and pERK ($r=0.6866$, $p<0.0001$). There were weaker, but significant, positive correlations between SERCA2a and BNP ($r=0.4838$, $p<0.0001$), and pERK and BNP ($r=0.2745$, $p<0.0196$).

Discussion

Similar trends of GHSR and ghrelin are seen with higher expression in end stage heart failure. The correlation between GHSR and ghrelin suggest an independent GHSR/ghrelin system in the myocardium, and this unit may be acting as an integrated biomarker in HF. Significant correlation between ghrelin and both SERCA2a and pERK indicate the combined GHSR/ghrelin unit is activating cellular signaling processes known to be affected in HF. The increases in expression of SERCA2a and pERK in end stage heart failure could be due to a compensatory signaling mechanism through GHSR/ghrelin. Ghrelin and BNP showed a strong correlation indicating ghrelin may be a good marker of HF while BNP showed weaker correlation to the biochemical signaling processes, indicating that ghrelin may be a more sensitive biomarker of downstream signaling events involved in HF progression. These results indicate the potential use of the GHSR/ghrelin unit as a new cardiac-specific biomarker for the detection of HF. GHSR is currently being characterized as a marker of HF using noninvasive imaging with hybrid positron emission tomography/ magnetic resonance imaging.

MRI of Magnetically Labeled Alveolar-Like Macrophages in Rat Lungs Using Hyperpolarized ^{129}Xe: Confirmation with Histology

*Vlora Riberdy[1,2], Michael Litvack[1], Elaine Stirrat[1], Marcus Couch[1,2], Martin Post[1], Giles Santyr[1,2]
[1]Translational Medicine Program, Peter Gilgan Center for Research and Learning, The Hospital for Sick Children, Toronto, ON, Canada. [2]Department of Medical Biophysics, University of Toronto, Toronto, ON, Canada.

Introduction: Stem cells are a potentially useful treatment for chronic lung diseases, such as asthma, chronic obstructive pulmonary disease (COPD) and bronchopulmonary dysplasia (BPD). It has been shown that the major innate immune cells in the lungs, alveolar macrophages, can be derived from pluripotent embryonic stem cells and these alveolar-like macrophages (ALMs) promote repair of lung disease in animal models[1]. Translation of this approach to the clinic will benefit from imaging methods that can detect and monitor ALMs *in vivo* following instillation in the lungs. It has been demonstrated that superparamagnetic iron oxide nanoparticles (SPIONs) can enable proton MRI of cells in the lung[2]. Hyperpolarized (HP) MRI provides further improvement in detection sensitivity of SPION-labeled cells in the lung[3]. In this work, we use histology to confirm the location of SPION-labeled ALMs observed using HP ^{129}Xe MRI in the rat lung.

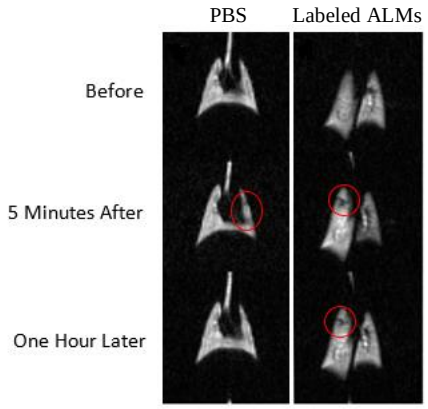

Figure 1: Images before, five minutes after and one hour after instillation of (a) PBS, (b) 2 million ALMSs labeled with 4% SPIONs.

Methods: ALMs were produced following the method of Litvack et al[2] and loaded with varying concentrations of green fluorescent-labeled SPIONs (Molday ION EverGreenÊ). As a preliminary step, the effects of localized instillation of (i) phosphate buffer saline (PBS) and (ii) SPION-labeled ALMs on HP ^{129}Xe signal acquired from the lungs of two separate healthy Sprague Dawley rats *in vivo* were investigated. ALMs were incubated with a 4% SPION solution (v/v) for four hours and approximately two million ALMs were resuspended in 100 ÕL of PBS. Imaging was performed in anesthetized mechanically ventilated rats during a ten second breath-hold using a 3D gradient-recalled echo (GRE) sequence. Solutions of 100 ÕL of PBS and ALMs were delivered via a tracheostomy to the right or left lung using a 24-gauge catheter. Imaging was performed approximately five minutes after instillation and one hour later. To confirm the location of the SPIONs, the excised lungs from the animal receiving ALMs were harvested, fixed and stained with Prussian blue, which detects the presence of iron. Eosin was used as a counterstain to identify the cytoplasm of different cells.

Results: Figure 1 shows representative coronal ^{129}Xe images before and following instillation of (a) PBS and (b) labeled ALMs. Localized ^{129}Xe image signal hypo-intensities (shown by red circles) were observed five minutes following both instillations. The signal hypo-intensities associated with SPION-labeled ALMs persisted one hour following instillation, unlike those observed following instillation of PBS, which resolved after one hour. Figure 2 shows the detection of iron (red circles) in the upper lobe of the right lung, the same region where signal hypo-intensities were observed.

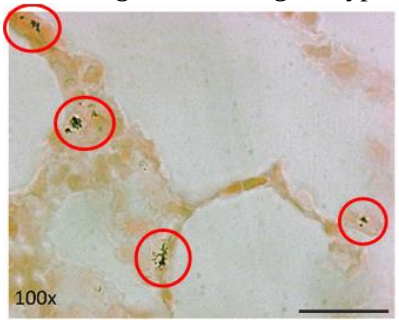

Figure 2: Tissue of the upper lobe of the right lung stained with Prussian blue and eosin. The presence of SPIONs is noted by the red circles. Scale bar is 20 Õm.

Conclusion: After instillation of SPION-labeled ALMs, the lungs appear to retain hypo-intensities associated with the SPION-labeled ALMs for at least one hour following instillation, unlike the signal hypo-intensities observed after instillation of PBS. This is likely due to retention of the SPION-labeled ALMs and clearance of the PBS by ventilation. Prussian blue staining of excised tissue confirmed the presence of iron in the area where hypo-intensities were observed. These preliminary results suggest that this method could potentially be used to detect and monitor ALMs in the lungs *in vivo*, regionally and longitudinally. Further experiments will be conducted with a larger number of ALMs instilled in multiple rats. Histology will be used to confirm the location of ALMs after the one-hour imaging time point.

References: [1] Litvack, M.L. et al. AJRCCM. 2016. [2] Faraj A. et al. BMC Med. 2015. [3] Branca, R.T. et al. PNAS. 2010. **Acknowledgments:** The authors would like to thank the Ontario Institute for Regenerative Medicine and Medicine by Design for the New Ideas grant. VR is funded by an NSERC CGS Masterôs scholarship and a Restracomp scholarship from the Hospital for Sick Children. Special thanks to members of the Santyr lab for their help with imaging and to the Post lab members for their help with cell work.

Blood clot hematocrit and age differentiation in vitro using R2* and quantitative susceptibility mapping

Spencer D. Christiansen,[*,1,2] Junmin Liu,[1] Michael B. Boffa,[3] and Maria Drangova[1,2]
[1]Robarts Research Institute, [2]Dept. of Medical Biophysics, [3]Dept. of Biochemistry
The University of Western Ontario, London, Ontario, Canada

Introduction: Knowledge of thrombus composition and age may aid treatment of common ischemic conditions including stroke, heart attack and pulmonary embolism, such as predicting the efficacy of thrombolytic agents[1] and mechanical thrombectomy procedures,[2] and possibly determining thrombus etiology.[3] Current MR-based thrombus characterization methods rely on a ñsusceptibility vessel signò obtained from late-echo gradient echo (GRE) images, a qualitative metric sensitive to deoxygenated red blood cells (RBCs), but unable to distinguish between the effects of RBC concentration (hematocrit) and deoxygenation (associated with thrombus ageing).[4] Quantitative methods that can distinguish between these factors are required for more accurate thrombus characterization. This work evaluates the ability of R2* (=1/T2*) and quantitative susceptibility (QS) maps, derived simultaneously from multi-echo GRE, to distinguish between clots of varied hematocrit and age *in vitro*.

Methods: ***Phantom-*** Arterial porcine blood was used to create duplicate 5 mL blood samples of 10 ï 60% hematocrit. Samples were clotted using calcium chloride and thromboplastin inside 1 cm diameter polystyrene tubes, placed within an agar phantom and kept at 37ÁC except while scanning. The phantom was scanned without repositioning every 15 minutes up to 6 hours post clotting, and then intermittently for up to 6 days.
Imaging- Scans were performed at 3T with a 32-channel receive head-coil using a custom dual echo-train 3D GRE sequence (TE1/æTE/TE5 = 3.20/1.46/9.04 ms, TE6/æTE/TE10 = 16.75/7.15/45.35 ms, TR: 47.6 ms, resolution: 0.94x0.94x1 mm^3, matrix: 192x192x40, BW: 142.86 kHz, flip angle: 10Á). Total scan time for the acquisition was 6 minutes 10 seconds; no acceleration was performed.
Image post-processing- Channel-combined complex data were processed using the non-iterative B0-NICE algorithm[5] to calculate R2* maps and the MEDI QS algorithm[6] to calculate QS maps.
Data analysis- Segmentation of clot samples was performed in Matlab. A circular ROI was drawn across each tube at the central coronal slice and used to calculate mean clot R2* and QS values.

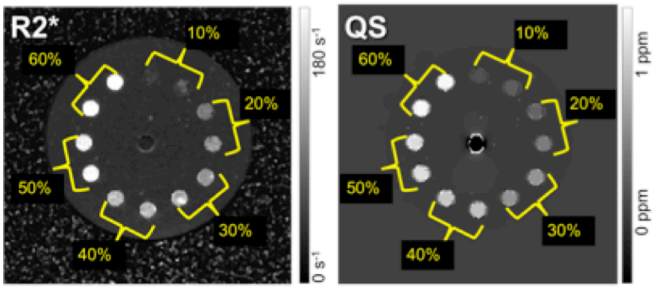

Fig. 1: R2* and QS maps of clots of varying hematocrit within the phantom at 72 hours post clotting.

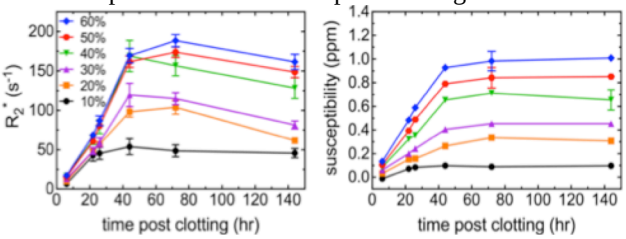

Fig. 2: Variation of R2* and QS with time post clotting for clots of varying hematocrit.

Results/Discussion: Only results from scans Ó6 hours post clotting are shown. Figure 1 shows a representative slice from the R2* and QS maps of the phantom at 72 hours post clotting. Mean clot R2* and QS values from 6 to 144 hours post clotting are plotted in Fig. 2, showing both parameters increase and plateau after ~40 hours to a value proportional to clot hematocrit. This result was expected given that both R2* and QS are sensitive to the progressive clot deoxygenation that accompanies clot ageing. These increases also imply that R2* or QS values alone would be unable to accurately infer hematocrit in clinical thrombi of unknown age. Figure 3 shows the same R2* values plotted against QS values; demonstrating that clot hematocrit and age may be inferred when both values are considered simultaneously.

Conclusions: Fresh blood clots (< 6 hours after formation) of up to 60% hematocrit can be differentiated on the basis of R2* or QS alone (data not shown). Aged blood clots (up to 6 days after formation) of up to 60% hematocrit may be differentiated by measuring R2* and QS values simultaneously. This method shows promise for inferring the hematocrit and age of clinical thrombi *in vivo*.

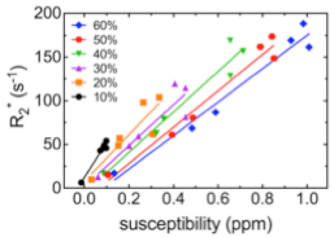

Fig. 3: R2* vs. QS for different hematocrit clots at all times post clotting.

References: [1] Niessen, F., et al. Stroke, 2003. [2] Yuki, I., et al. Am J Neuroradiol, 2012. [3] Boeckh-Behrens, T., et al. Clin Neuroradiol, 2016. [4] Rovira, A., et al. Radiology, 2004. [5] Liu, J. and M. Drangova. Magn Reson Med, 2015. [6] Liu, J., et al. NeuroImage, 2012.

Oral Presentation Abstracts

Session 12: Instrumentation and Technology Development

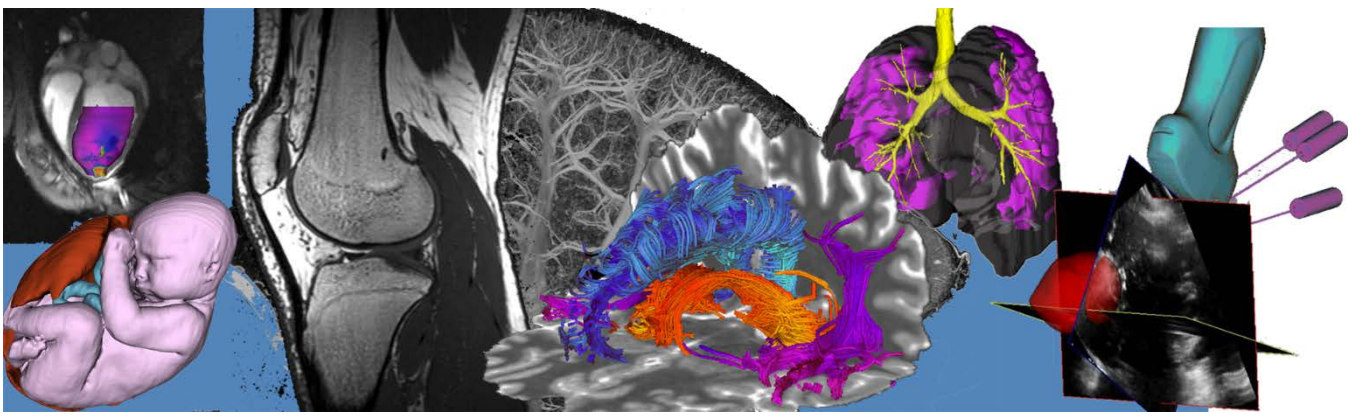

Apodized-Aperture Pixel: A novel x-ray detector design to improve cancer detection in mammography

Tomi F. Nano, BSc, and Ian A. Cunningham, PhD, FCCPM, FAAPM
Imaging Research Laboratories, Robarts Research Institute, Dept. of Medical Biophysics, Western University

Introduction: Breast cancer is one of the most prevalent cancers and the second leading cause of mortality amongst Canadian women [1]. Recent studies from the Ontario Breast Screening Program have shown that women who are screened have up to 40% reduced risk of death. However, not all digital mammography technologies result in the same cancer detection rates [2] and significantly higher detection rates were attributed to higher x-ray detector performance [3]. The ability of an x-ray detector to produce high signal-to-noise ratio (SNR) in an image for a given amount of radiation is quantified by the detective quantum efficiency (DQE), which is a Fourier-based metric where low frequencies pertain more to large features and high frequencies to small features. While DQE of digital detectors vary, current clinical detectors can have high DQE (60-80%) at low frequencies, but high frequency DQE is much lower (<30%) [4]. We are developing a novel x-ray detector design, called the apodized-aperture pixel (AAP) [5], that can have greater DQE at high frequencies than current detectors. This would result in images with higher SNR and better visualization of small structures, such as micro-calcifications, which are crucial for early detection of breast cancer in screening programs.

Rationale: DQE at high frequencies can be reduced by noise aliasing [6]. Aliasing is an image artifact due to discretization of frequencies beyond the digital image sampling rate, and noise aliasing is undesirable because it increases total image noise. The AAP design aims to reduce noise aliasing by making a separation between physical sensor elements from image pixels. It uses a micro-element sensor (0.01-0.025mm) and an anti-aliasing filter to synthesize desired clinical images of current pixel size (0.05-0.1mm).

Methods: A cascaded-system analysis was used to compare image signal and noise of conventional and AAP designs. Analysis included x-ray interactions (including reabsorption) in the converter material which liberate secondary quanta, relocation of secondary quanta due to converter material blur, coupling efficiency of secondary quanta to sensor array, collection of secondary quanta, electronic readout noise and digital sampling. The modulation transfer function (MTF), Wiener noise power spectra (NPS) and DQE were used to evaluate system performance. For proof-of-concept demonstration, current cesium iodide (CsI) and selenium (Se) detectors were used to synthesize conventional and AAP images of the same pixel size to allow for validation of theoretical model. MTF, NPS and DQE was measured with a DQE-testing instrument (DQE Instruments Inc.).

Results: Excellent agreement was found between theoretical and empirical results. For both CsI and Se detector types, the AAP design has 1.5x greater MTF near the image cut-off frequency than conventional design and attenuates all frequencies above the cut-off. High frequency DQE of the AAP design was greater than conventional by different amounts for CsI and Se detectors. DQE of the AAP design with CsI was only slightly greater than conventional CsI design, while DQE of the AAP design with Se was 2.4x greater at high frequency.

Discussion and Conclusions: The AAP design achieves greater MTF and DQE at high frequencies (near the image cut-off frequency) than conventional design. Higher MTF with the AAP design is due to use of a micro-element sensor and is independent of x-ray converter material type. Greater DQE with the AAP design is due to reduction in noise aliasing, which depends on the x-ray converter material. Noise aliasing reduces DQE and is highest in converter materials that have no x-ray reabsorption of scattered or emitted photons from x-ray interactions, negligible blur from converter layer and no secondary quantum sinks. These same properties are also necessary for high MTF, which is why the DQE performance of a conventional design is fundamentally limited by noise aliasing. The AAP design is a novel approach that eliminates noise aliasing and can acquire high SNR images for better visualization of fine detail to improve cancer detection in breast screening programs.

[1] Canadian Cancer Statistics 2017, Toronto, ON. [2] Chiarelli et al., Radiology, 268(3), 2013. [3] Yaffe et al., Med. Phys., 40(12), 2013. [4] Escartin et. al., Proc. of SPIE: MI, 9783, 2016. [5] Nano et al., Med. Phys., 44(4), 2017. [6] Cunningham et. al., Proc. of SPIE: MI, 4682, 2002

3D Verification of Flow in Microfluidic Devices Using Micro-PIV

Kayla Soon[1] and Tamie L. Poepping[2]
[1] Dept. of Electrical and Computer Engineering, Ryerson University, Toronto
[2] Dept. of Physics & Astronomy, University of Western Ontario, London

Introduction: As the development of microfluidic devices becomes more complex in geometry, there is also an increasing need to be able to characterize the flow pattern accurately. Micro-particle image velocimetry (micro-PIV) provides instantaneous velocities on the micron scale. Using an inverted epifluorescent microscope and fluorescent particles seeded into the fluid, a series of laser pulses illuminate sub-micron tracer particles as they follow the motion of the flow [1]. To determine the velocity of the flow, each frame is subdivided into interrogation windows. Using cross-correlation analysis, the interrogation window of one frame is mapped onto the next frame to determine the distance those particles have moved between frames. To improve the accuracy of the velocity calculation, the interrogation window should be sufficiently large to include at least 10 particles per window, while small enough to ensure all particles move uniformly [2]. Here, we demonstrate the accuracy and precision to measure laminar flow in a straight microfluidic channel to construct a 3D velocity profile by stacking the 2D velocity fields.

Methods: The microfluidic device was manufactured using polydimethylsiloxane (PDMS) to create a channel with a cross-sectional dimension of 300x500 εm^2. The inlet was connected to a gravity feed containing distilled water seeded with 0.5-εm diameter fluorescent polymer microspheres (R500, Thermo Fisher Scientific) to achieve roughly 30 particles per 100x100 εm^2. The micro-PIV was used to image a 1792x500 εm^2 window (1 pixel $\cong$1 εm), with a frame rate of 2.541 kHz (inter-frame time of 0.4 ms). This process was repeated with vertical increments of 50 εm to image subsequent horizontal profiles. All data acquisition and cross-correlation analysis were performed using commercial PIV software (DaVis 8.3, LaVision, Inc.). To evaluate the data, an initial interrogation window of 96x96 pixels was applied with a 50% overlap between cross-correlations, and reduced to a final window of 32x32 pixels with a 75% overlap, leading to velocity vectors spaced 8 εm apart.

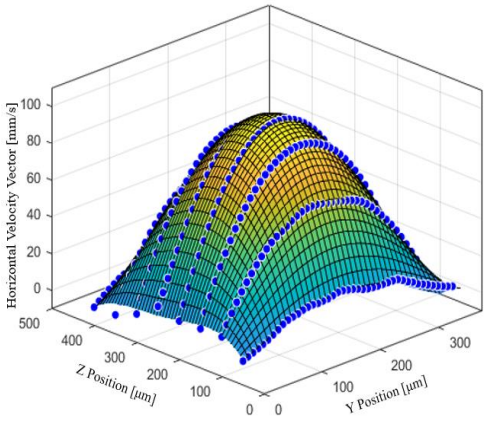

Figure 1: Plot of 3D velocity profile constructed from eight 2D velocity profile averages and computed surface of best fit.

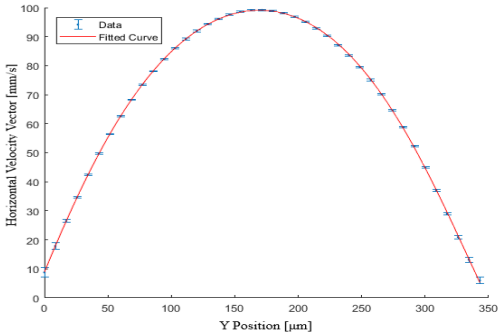

Figure 2: Plot of velocity profile at central plan, with error bars representing the standard deviation in 100 velocity vectors at each location.

Results: The resulting 100 velocity profiles imaged over 40 ms were averaged to yield a 3D velocity profile (Fig. 1). The 8 planes of measured velocities were fitted with a 4th-degree polynomial in both dimensions (R^2=0.997). The measured peak velocity was 99.2Ñ0.23 mm/s at the center of the channel. Fig. 2 is the velocity vector profile along the central plane near the center of the imaged channel. This demonstrates the expected parabolic trend of laminar flow, with measured velocities spanning approximately 0.1 mm/s near the wall to 100 mm/s at the center for a flow rate of 0.58 mL/min. The standard deviation in velocity magnitude for the middle 80% of the channel is less than 0.35 mm/s for all velocities and less than 1.0 mm/s when approaching the channel walls.

Conclusion: Micro-PIV measurements provide accurate instantaneous velocities in flow channels on a micron scale and enable 3D velocity profiles, built up from 2D profiles, to determine trends in the flow.

Reference: [1] Lindken, R., Rossi, M., GroÇe, S. and Westerweel, J. (2009). Micro-Particle Image Velocimetry (ÕPIV): Recent developments, applications, and guidelines. *Lab on a Chip*, 9(17), p.2551.
[2] Rossi, M., Segura, R., Cierpka, C. and K^{a}hler, C. (2011). On the effect of particle image intensity and image preprocessing on the depth of correlation in micro-PIV. *Experiments in Fluids*, 52(4), pp.1063-1075.

Transmit Coil impedance measurements to estimate radiofrequency induced currents on wires in MRI

Brandon J Coles[1], Kevan J Anderson[2], Greig Scott[3], Christopher Ellenor[3], Graham A Wright[1,2]
[1]Medical Biophysics, University of Toronto, Toronto, Ontario, Canada
[2]Sunnybrook Research Institute, Toronto, Ontario, Canada
[3] Electrical Engineering Department, Stanford University, Stanford, CA, United States

Introduction: MRI can provide images with information relevant to the success of image guided cardiac interventions, such as Radio Frequency (RF) ablations to treat ventricular tachycardia [1]. However, use of MRI introduces a potential safety issue from the RF field coupling to the devices, inducing a current that can lead to dangerous temperature increases near the tip [2]. Parallel RF transmission has been shown to reduce this effect for stationary devices [3] however, cardiac interventions require the device to change positions; that can still result in heating. Without a way to detect coupling changes caused by device displacement, it would be difficult to ensure safety. Throughout the procedure a fast estimate of coupling between the device and individual transmit coils could be used to detect these changes. This could also provide information on how to readjust the transmit field to a safe configuration, previously investigated by Ellenor [4].

Figure 1: Experimental setup. The signal is created by the Medusa (1) and fed into a 500W RF amplifier (2). This is output to the coil under the phantom (3). The device is inside the phantom, and the current is measured via the current sensor (4) and fed into a spectrum analyzer (5) for recording.

Methods: To study the ability to predict current induction on a wire from coil impedance measurements, a wire was moved near a coil, and induced current and coil impedances were measured. A coupling coefficient is estimated between a transmit coil and wire by measuring the impedance change of the coil due to the wire, using a modified version of the reflection coefficient (1):

$$\Gamma = \frac{Z_C - Z_U}{Z_C + Z_U} \quad (1),$$

where Z_C is the coil impedance with a coupled wire, and Z_U the coil impedance with no wire. A 17x12cm rectangular loop coil was built with 1cm copper tape, and tuned to have an S_{11} value of -33.3 dB. The coil was centered 2.5cm below a body mimicking, 9x42x65 cm phantom containing Poly-Acrylic Acid. A 26cm length (approximately the half wavelength at 1.5T) of guidewire (Radifocus Glidewire, Tokyo, Japan) was submerged in the phantom, and moved in 1 cm increments across the coil (fig 2). At each location, the coil transmits a series of RF pulses, produced via the Medusa console [5], then amplified by a 500W RF amplifier (Procyon Engineering). While transmitting, the peak induced current on the wire is measured with an optical current sensor [6]. The impedances of the coil were measured separately using a Network Analyzer. Simulations using FEKO (Altair, MI, USA) were conducted to compare with the measurements.

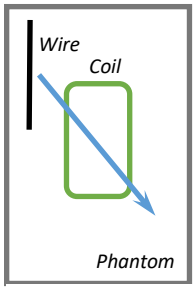

Figure 2: Experiment and simulation configuration.

Results: When fitting a model to predict peak induced current from the reflection coefficient, it was noticed taking the square root of the magnitude of the reflection coefficient resulted in a strongly predictive linear relationship between reflection coefficient and peak current (figure 3).

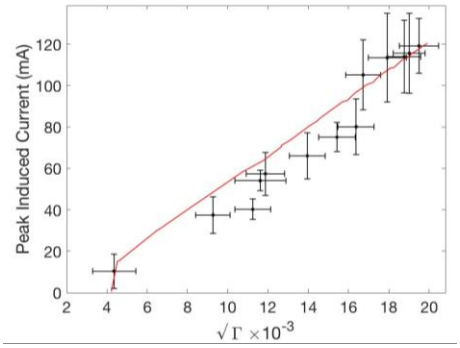

Figure 3: The relationship between peak current, and the square root of the magnitude of the reflection coefficient. Error bars show standard deviation, each measurement has 6 samples. Red line shows simulated relationship.

Conclusions: A fast method to estimate a coupling coefficient between a transmit coil and a wire is presented in the form of a modified reflection coefficient. Future work aims to implement a transmit coil array, and use each individual coilôs modified reflection coefficient to calculate an RF field to suppress the induced current on a wire, while maintaining an acceptable B_1 field for imaging.

References: [1] Halperin H.RMMJ 2010;1(2):e0015. **[2]** Mattei E. BioMed Eng 7:11(2008). **[3]** Etezadi-Amoli M. MRM 74:1790ï 1802 (2015). **[4]** Ellenor C. MRM 73:1328ï 1339 (2015). **[5]** Stang P. IEEE 2012;31(2)370-379. **[6]** Zanchi MG. IEEE Trans Med Imaging 2010;29:169ï 178.

Parametric Modeling and Metal 3D Printing of Anti-Scatter Grids for Cone-beam CT

Santiago F Cobos,[1] Hristo N Nikolov,[2] Steven I Pollmann,[2] and David W Holdsworth,[1,2,3]
Development of Novel Therapies for Bone and Joint Diseases Consortium
[1]Department of Medical Biophysics, Western University, [2]Robarts Research Institute, [3]Department of Surgery, Western University, London, Ontario, Canada

Introduction: Cone-beam CT (CBCT) takes advantage of efficient acquisition geometry to acquire high-resolution volumetric data rapidly. At the same time, this volume acquisition geometry increases the scatter fraction in CBCT, leading to image artifacts, increased noise, and errors in quantitative imaging. While the effects of scatter can be ameliorated to some extent in post-processing, scatter remains a problem in current clinical CBCT systems. Advances in 3D design and additive manufacturing (*i.e.* 3D printing) have now made it possible to produce complex metal objects using selective laser melting, and this approach is ideal for producing highly focused anti-scatter grids (ASGs) for CBCT.

Methods: Computer-aided design (CAD) of the ASG prototypes was achieved using open-source design software (Blender 2.78). Parametric design of a node tree allowed an operator to input specified parameters (*i.e.* cell width, septal thickness, grid thickness, and focal spot location). The software then automatically produced corresponding stereolithographic (STL) format files for 3D printing. Recent advances in 3D metal printing have made it possible to produce devices with very small feature size (*i.e.* <200 Õm) in solid metal,[1] including dense metals such as tungsten. We have taken advantage of this new fabrication technology to fabricate two-dimensionally focused ASGs with grid ratio of 10 and nominal septal thickness of 0.1 mm, giving an overall geometric transmission efficiency of 83%. Prototype ASGs have been fabricated in metal using powder-bed selective laser melting (AM400, Renishaw plc). Preliminary prototypes have been built in cobalt-chromium alloy; this technology can also be used to fabricate in denser metals, including tungsten. For test purposes, a cylindrical collimator (40 mm diameter; 10 mm thick) was fabricated with 1 mm cell spacing and 0.1 mm thick septa (nominally). In addition, a focused collimator was designed with the following parameters: 75 mm diameter, 15 mm thick, 10 mm cell spacing, 0.1 mm septal thickness, 230 mm focal distance.

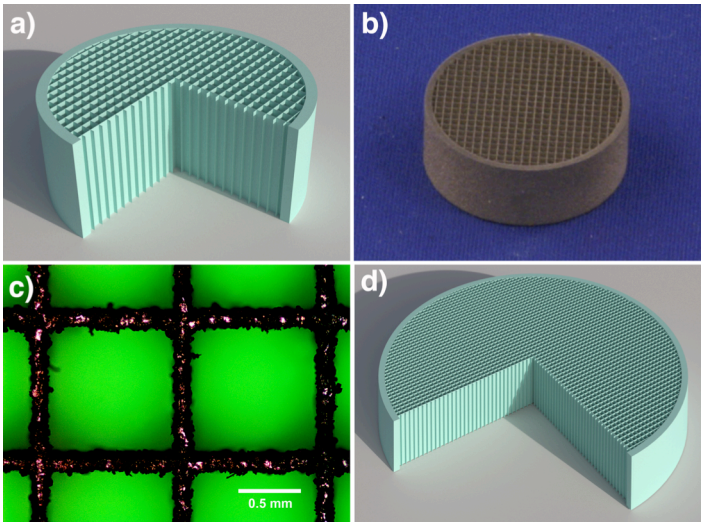

Fig. 1: (a) CAD design and (b) fabricated prototype of cylindrical ASG with 0.1 mm septa. (c) optical micrograph of thin-walled ASG. (d) CAD design of focused ASG.

Results: Septal thickness in the prototype cobalt-chrome alloy collimator was verified with a measuring microscope (Olympus STM6). Septal thickness averaged 100.6 Õm, with no significant difference in the x- and y-directions (Fig. 1c). Geometric accuracy and mechanical stability was maintained, with calculated radiographic transmission efficiency greater that 80%. Parametric design software produced optimized STL files that were compatible with a commercial 3D printing interface (Renishaw QuantAM).

Conclusions: Custom-designed 2D focused ASGs are possible using conventional additive manufacturing in metal, resulting in highly efficient grids capable of effective scatter rejection in CBCT imaging geometries. Efficiency is maintained through the use of very thin septa, which require no additional filler material for structural support. This approach may lead to nearly complete scatter rejection for CBCT, potentially improving the performance of quantitative cone-beam imaging systems.

References: 1. M. G. Teeter et al., "Metrology test object for dimensional verification in additive manufacturing of metals for biomedical applications," Journal of Engineering in Medicine **229**, 20-27 (2015).
2. C. Altunbas et al., ñTransmission characteristics of a 2D antiscatter grid prototype for CBCT,ò Med. Phys. **44**, 3952-3964 (2017).

Array-Based Dual Frequency Acoustic Angiography

Jing Yang[1], Emmanuel Chérin[2], Jianhua Yin[2], Stuart Foster[1,2], and Christine Démoré[1,2]
[1]Department of Medical Biophysics, University of Toronto;
[2]Physical Sciences Platform, Sunnybrook Research Institute

Introduction: Acoustic angiography using dual frequency (DF) ultrasound systems enables high resolution and high contrast imaging of the microvasculature within tissue while suppressing clutter from background tissues. This could aid the monitoring of diseases and evaluation of treatment outcomes. DF ultrasound imaging uses conventional frequency ultrasound transducers (~2-4 MHz, LF) on transmit (Tx), and high frequency (HF) transducers on receive (Rx) to detect higher order harmonics (~10-20MHz) from microbubble contrast agents. Current DF imaging systems for acoustic angiography use single-element transducers and has been tested on rat tumour models (Fig 1a)[1]. However, the useful field of view (FOV) is limited by the fixed focus of single-element transducers, while 2D and 3D image frame rates are limited by mechanical scanning. A DF array-based imaging system with electronic focusing and beam steering is needed for extending the focal region and increasing frame rates towards real-time 2D acoustic angiography. The focus of this project is the development of a DF array beamformer and imaging approaches suitable for acoustic angiography. As a first step towards this goal, we investigate plane wave beamforming techniques that can acquire a full 2D image frame for each transmit event, for frame rates in the range 100 - 18000 frame/s. This is significantly faster than conventional line-by-line beamforming with linear arrays. Here, we demonstrate proposed plane wave beamforming algorithms in simulation; these will be implemented with combined high- and low-frequency imaging systems.
Methods: To investigate beamforming schemes, plane wave imaging of point reflectors in a field (Fig 1b) was simulated with a *Verasonics* programmable ultrasound system. The dash lines define the imaging field directly in front of the transducer aperture, and the solid lines, with an angle of 36° to y-axis, define a sector FOV. A single-frequency linear array was used for Tx and Rx for these initial simulations with f_0=7.8MHz, a 32-element aperture and a pitch size of 0.99λ. Beamforming schemes with single axial plane wave transmission and with both Tx beam steering (angles: ±18°, ±12°, ±6° and 0°) and compounding were implemented.
Results: Raw RF data were obtained and beamformed offline and images reconstructed (Fig 1c, 1d). Coherent compounding was applied for Fig 1d, demonstrating improved image quality with compounding. The reconstructed images show an estimated image lateral resolution (-6dB width) of 2-3 mm for both scenarios. However, sidelobes in the beam steering and compounding case (-40dB) were reduced to significantly compared to non-steering case (-20dB). The compounded image could be acquired in 200 μs, whereas conventional linear array imaging would require 100 ms per frame.
Conclusion: The plane wave beamforming schemes can achieve comparable image quality to those produced by a conventional linear array imaging schemes, but at significantly higher rates. The resolution results are expected to scale with the imaging wavelength, and both resolution and contrast improve further with a complete 256-element 20 MHz Rx array. These results indicate a strong potential for real-time DF imaging of microbubble contrast agents. The beamforming algorithms will be used for compound plane wave imaging with combined LF and HF ultrasound arrays and systems.

Reference: [1] S. E. Shelton, et al. *Ultrasound Med. Biol.*, vol. 42, no. 3, pp. 769–781, Mar. 2016.

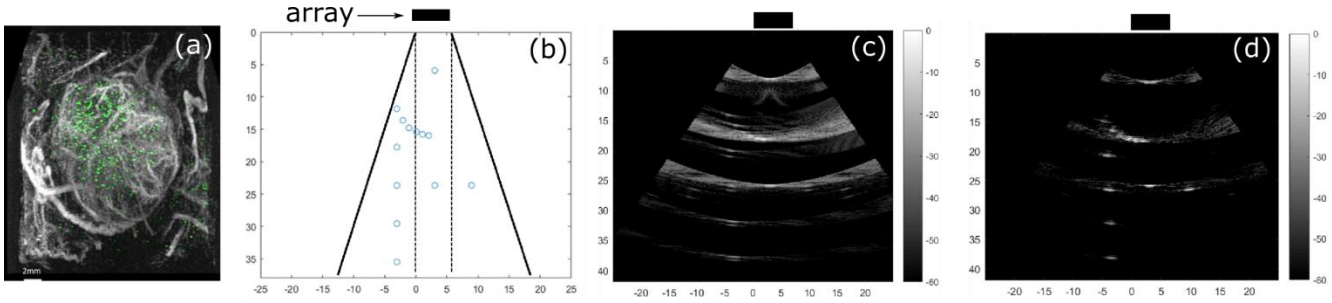

Figure 1: (a) Fused image of a rat tumour model using DF acoustic angiography and molecular imaging (microvasculature is in gray-scale and targeted protein in green)[1]; (b) Pre-defined sector FOV and point scatterers in simulation; (c) beamformed image without beam steering; (d) beamformed image with beam steering and compounding. X-axis: lateral distance (mm); y-axis: depth (mm)

Poster Presentations Abstracts (in order of presentation)

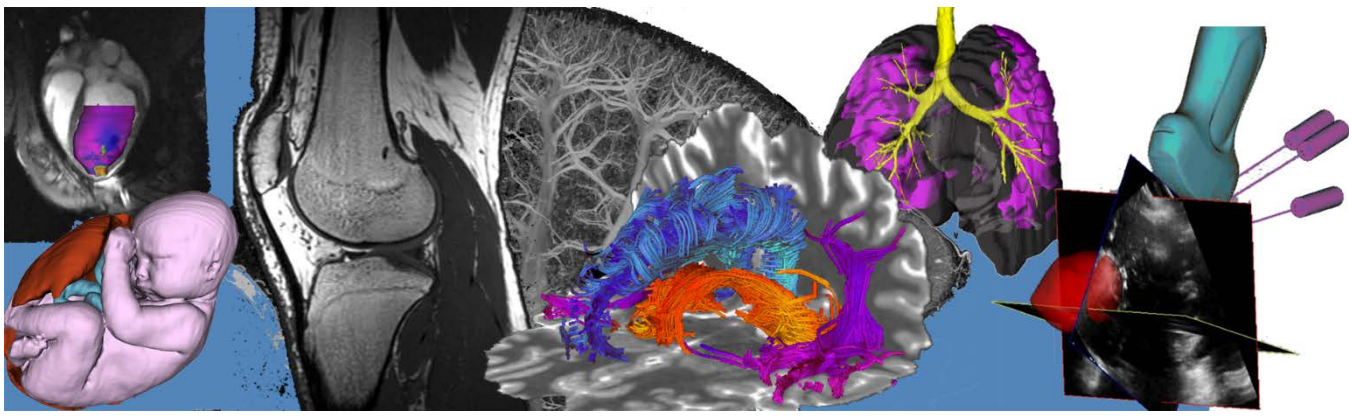

Poster Presentation Abstracts

Session 1: Image Guided Intervention

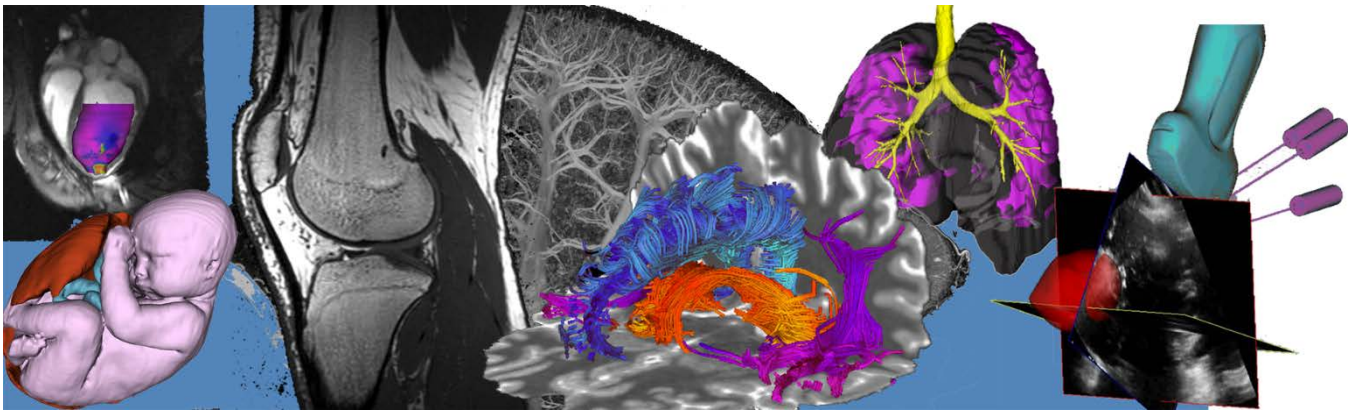

Basic suturing training using Microsoft HoloLens

Hillary Lia[1], Gregory Paulin[2], Caitlin T. Yeo[3], Jessica Andrews[3], Nelson Yi[1], Hassan Haq[1], Steve Emmanuel[1], Kristian Ludig[1], Zsuzsanna Keri[1], Andras Lasso[1], Gabor Fichtinger[1]

1. Laboratory of Percutaneous Surgery, School of Computing, Queenôs University, Kingston, Canada
2. School of Medicine, Queenôs University, Kingston, Canada
3. Department of Surgery, Kingston Health Sciences Centre, Queenôs University, Kingston, Canada

INTRODUCTION: Suturing is an essential skill across specialties. The most common method of teaching basic suturing is workshop format with a faculty instructor. However, many medical students do not reach proficiency due to lack of exposure[1]. It can be expensive and time-consuming to supply these sessions with a sufficient number of faculty-experts, thus there has been increased interest in self-directed learning. This often entails the use of computer-based video instruction. A video-tutorial based curriculum for suturing training has been shown to be effective for training to proficiency[2]. Furthermore, augmented reality is an emerging tool for effective medical education. This involves the projection of virtual instructional material in the userôs real environment. The usage of a voice-commanded headset with projected virtual content can help traineeôs maintain their flow of practice when interacting with instructional content. Our aim was to combine augmented reality with video-based instruction using Microsoft HoloLens to determine if the two methods combined would be accepted as an educational tool and if it is an effective method of training.

METHODS: Suture Tutor was developed using Unity for use on the HoloLens. This module includes four videos, outlining the steps of the running locking suturing skill. Voice commands are used to play, pause, skip, and slow videos. Thirty six participants in their second year of medicine were split into two groups, the HoloLens group or the control group. The HoloLens group practiced the suturing technique using the Suture Tutor module while the control group used the same four videos on a laptop (Figure 1). Each participantôs first and final attempts at the technique were video recorded and assessed by experts using a previously validated global rating scale[3]. The participants were given seven minutes to practice between the first and last attempts. The time spent interacting with the video during practice was recorded. At the end of the session, the HoloLens group was given a survey evaluating the usability and realism of Suture Tutor.

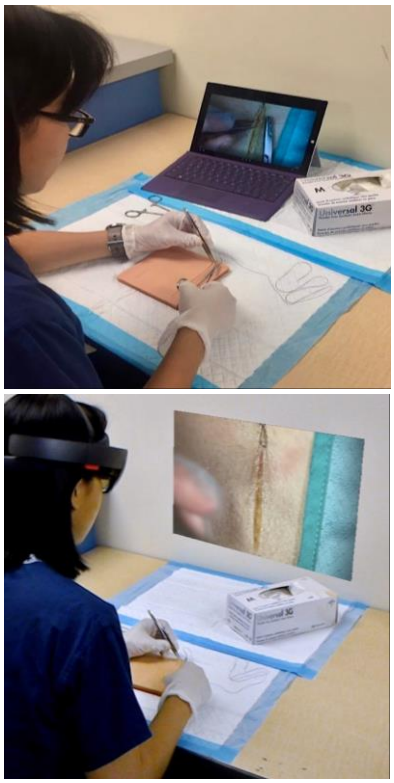

Fig 1. Setup of the control group (top) and the HoloLens group (bottom).

RESULTS: 85% of the participants who used Suture Tutor agreed or strongly agreed that it is useful in the training of medical students. Furthermore, 95% of respondents agreed or strongly agreed that the instructional material used was realistic. We were unable to determine the effectiveness of Suture Tutor. However, the HoloLens group watched the instructional videos significantly more than the control group (7 [5.75 ï 9.25] *views* vs 4.5 [3.75 ï 6] *views*, P = 0.0175).

CONCLUSION: Participants found the Suture Tutor to be a user friendly and helpful adjunct. The study suggests that Suture Tutor improved accessibility of training material.

REFERENCES: [1] Wongkietkachorn *et al., J Surg Educ.*, 2016.
[2] Mashaud *et al., J Surg Educ.*, 2013.
[3] Moorthy *et al., BMJ*, 2003.

Assessment of the use of webcam based workflow detection for providing real-time feedback in central venous catheterization training

Rebecca Hisey[1], Tamas Ungi[1], Matthew Holden[1], Zachary Baum[1], Zsuzsanna Keri[1], Caitlin McCallum[2], Daniel W. Howes[2], Gabor Fichtinger[1]

[1]Laboratory for Percutaneous Surgery, School of Computing, Queen's University, Kingston, Canada

[2]Department of Critical Care Medicine, Kingston General Hospital, Kingston, Canada

Introduction: Central venous catheterization is an important skill used in several different medical disciplines. The procedure is complex, and requires many steps and multiple different tools. Research has shown that novice residents have complication rates as high as 35% for this procedure [1]. This complication rate can be reduced through the use of simulators. It has been shown that students who first train on simulators show superior performance when compared to those trained using traditional methods [2]. Central Line Tutor creates a realistic training environment that provides residents with real-time instruction and feedback in order to gain competency without risking patient safety. In this work we evaluate the effectiveness of the workflow detection method used.

Methods: Central Line Tutor (Fig.1) provides real-time instruction and feedback by assessing which task is being completed at a given time. Tasks that require precise positional information, such as those involved in locating and inserting the needle into the vessel, use electromagnetic (EM) tracking. EM sensors are placed on the phantom, needle and the ultrasound probe. The remaining tasks are detected through the live webcam video using coloured object recognition. The EM tracker, ultrasound machine along with the webcam are connected to a computer which shows the user the ultrasound and webcam videos as well as a 3D model of the setup. While performing the procedure, Central Line Tutor records the positional information from the EM tracker, the ultrasound and webcam videos as well as the timestamps of when key transition points occur. For this study, five trials of the procedure were recorded using Central Line Tutor. Using these recordings five reviewers were asked to identify the same transition points as Central Line Tutor. The times identified by the reviewers were then compared to those identified by Central Line Tutor and were used to calculate the average transitional delay. A negative transitional delay indicates that Central Line Tutor identified the transition point earlier than the reviewers.

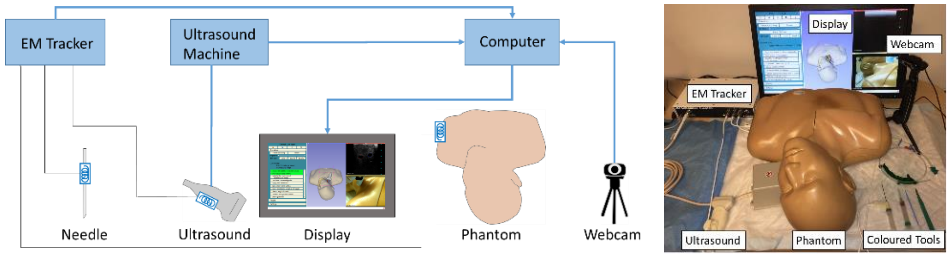

Figure 1: Central Line Tutor setup

Results: The Central Line tutor correctly identified 100% of all 19 transition points in the procedure. The average transitional delay between Central Line Tutor and the reviewers was 1.5 ± 0.8s. The average transitional delay of tasks detected using the webcam video and those using EM tracking were 2.5 ± 3.6s and 0.3 ± 2.5s respectively.

Conclusions: Central Line Tutor was able to identify all transition points in the procedure with minimal delay. This shows that Central Line Tutor is able to detect all tasks in the procedure's workflow. As the average transitional delay is shorter than the minimum amount of time required for any task, this indicates that Central Line Tutor may be used to provide residents with real-time instruction and feedback.

[1] Kumar A, Chuan A. Ultrasound guided vascular access: efficacy and safety. Best Pract Res Clin Anaesthesiol. 2009 Sep;23(3):299-311.

[2] McGaghie WC, Issenberg SB, Cohen ER, Barsuk JH, Wayne DB. Does simulation-based medical education with deliberate practice yield better results than traditional clinical education? A meta-analytic comparative review of the evidence. Acad Med. 2011 Jun;86(6):706-11.

Applicator Segmentation in Three-dimensional Ultrasound for Interventional Liver Therapies

Derek J Gillies[1,2], Joseph Awad[3], Jessica R Rodgers[2,4], Chandima Edirisinghe[2], Nirmal Kakani[5], Aaron Fenster[1-5]

[1]Department of Medical Biophysics, [2]Robarts Research Institute, [4]Biomedical Engineering Graduate Program, [5]Department of Medical Imaging, Western University; [3]Centre for Imaging Technology Commercialization; London, Ontario, Canada

Introduction: Liver cancer is the second and sixth most frequent cause of cancer mortality worldwide in men and women, respectively. Transplantation and resection are curative therapies, with 5-year survival rates of about 40%; however, these open surgery procedures are often followed by long patient recovery times and serious problems, including organ rejection and bile duct complications. Minimally invasive percutaneous techniques, such as radiofrequency ablation, are quickly becoming primary treatment options for early-stage liver cancer due to lower complication rates and shorter recovery times. Unfortunately, these procedures have higher local recurrence rates than resection due to insufficient or inaccurate local tumour ablation. The standard of care for percutaneous techniques uses x-ray computed tomography (CT) images for planning and two dimensional (2D) ultrasound (US) for intraoperative guidance of oblique applicator insertion(s) into the tumour. Poor ablation coverage has been associated with 2D US guidance, leading to variability in applicator targeting accuracy, which has led to the introduction of intraoperative three dimensional (3D) US imaging for improved verification of applicator placement. Thus, we have developed a semi-automated 3D US applicator segmentation algorithm with the aim of improving the efficiency of applicator localization. This tool could be used intraoperatively to provide verification and follow-up long-term tracking of applicators during liver-based interventional therapies when used in conjunction with a 3D US guidance system.

Methods: The algorithm is based on intensity thresholding to compute clusters of candidate applicator voxels. After creating a spherical search space of line segments around a manually chosen seed point, the most probable trajectory is chosen by maximizing the quantity and intensity of voxels along a line that exceed a signal-to-background intensity threshold of 1.5. Once the trajectory is chosen, it is extended to compute a second (more sensitive) intensity threshold using Otsuôs method to further eliminate voxels and determine the tip location. This algorithm was tested on 10 applicators obliquely inserted and 3D US imaged in a homogeneous agar phantom followed by a triple-user study on 17 clinical 3D US images of patients with liver cancer undergoing percutaneous therapies. Each applicator in the agar phantom images was segmented using three different manual seed points to assess variability in the algorithm. Tip and trajectory errors were computed based on manually segmented ñgold standardò segmentations. Tip and trajectory errors were assessed independently and considered failures if the differences between segmentations were greater than 10 mm or 6Á respectively.

Results: Tip and trajectory identification, respectively, were 87% and 100% successful during phantom trials. The mean tip error was 3.0 Ñ2.2 mm and the trajectory error was 1.8 Ñ1.1Á The tip identification rate for the novice, intermediate, and expert US users were 76%, 76%, and 88%, respectively, with corresponding trajectory identification rates of 94%, 76%, and 94% for the clinical images. Tip errors were 3.6 Ñ2.4 mm, 2.9 Ñ1.6 mm, and 1.9 Ñ1.2 mm for the novice, intermediate, and expert users, respectively. Trajectory errors were 2.4 Ñ1.8Á 2.3 Ñ1.1Á and 2.0 Ñ1.2Áfor the novice, intermediate, and expert users, respectively.

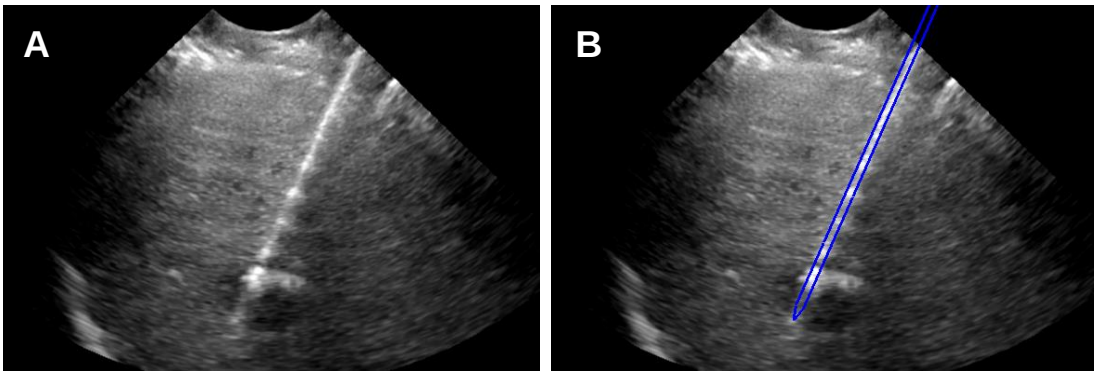

Figure 1. Example input (A) and segmented (B) image planes of applicators in 3D US patient images.

Conclusions: Applicator segmentations on clinical 3D US images were closest to the expert segmentations with tip and trajectory errors of 1.9 Ñ 1.2 mm and 2.0 Ñ 1.2Á respectively. Future work will focus on increasing segmentation success rates and investigation of curved applicator segmentations.

Ultrasound Calibration: A Method for the Common User

Leah Groves*[1, 2], E. Chen[1, 2], Terry Peters[1, 2]
*First author, [1] Robarts Research Institute, London, Canada; [2]Biomedical Engineering Program, Western University, London, Canada;

INTRODUCTION: Ultrasound (US) is commonly used for image-guided interventions, as it is a low cost and real time imaging modality that does not expose the patient to harmful ionizing radiation. Navigated image guided interventions require all tracked components to be in a common coordinate system in order to properly visualize the tracked US probe and other tools within the US image. Probe calibration is the method to solve for the geometries between the tracked US probe and the US image. One common method of probe calibration is based on point-to-point registration, where the transformation between some tracked object and the tracked US probe is known through a common tracker [1]. Thus, the transformation that registers the US probe and US image as the only unknown [1]. The other method to solve for this unknown transform is to use a tracked phantom consisting of rods that connect Z pattern wires (Z-Phantom) as the tracked object [2]. The ultrasound scanner scans the Z-Phantom and the resulting image contains three collinear ellipses that correspond to the reflections from the three wires in the phantom [2]. The locations of the centroids of the elliptical reflections can be found through automatic or manual segmentation and used to find the location of the center of the oblique wire with respect to its end points [3]. Since the location of the wire is known with respect to the probe and the location of the reflection within the image is known, the transformation connecting the image to the probe can be solved for [3]. During the US calibration process fiducial localization error (FLE) is introduced due to error in tracking segmentation, and calibration of other tracked objects. To reduce the effect of the compound FLE and to achieve the minimal target registration error is the aims of our research.

METHODS: To implement the point to line registration the Z-Phantom is replaced by a magnetically tracked needle made out of a suitable echogenic material, to provide a symmetric elliptical appearance in a B-mode US image. The tracked straw is specified by the two end points in tracked space. Through the tracking of the straw the coordinates that form the line, as well as the orientation of the line is known. The US fiducial that is required to solve for the transform can be easily segmented with a cross hair cursor that the user aligns with the center of the elliptical reflection in the US image. Utilizing the information of this pixel location selected by the cross hair and the line obtained through the tracked straw an iterative closest point (ICP) calibration technique can be implemented to solve for the transformation. Our approach minimizes the target registration error (TRE) through decreasing the number of transforms required. This algorithm was then implemented as a 3D slicer open source module to allow for easy distribution of the method to other researchers after a user study to validate the method has been performed. This study will involve 30 users testing the algorithm through this module.

PRELIMINARY RESULTS: The results of one user testing this algorithm showed that with 12 or more measurements the calibration stabilizes with a minimized TRE of approximately three pixels. Figure 1 depicts the result a post-calibrated tracked tool within an image.

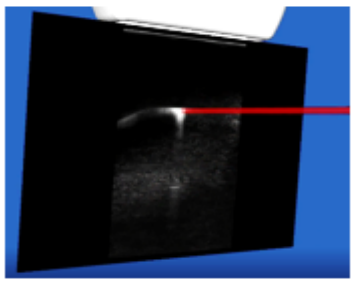

Fig 1. Result of tracking a needle after applying this novel algorithm

CONCLUSIONS: These preliminary results highlight the ability to minimize the TRE without restricting the transform to isotropic scaling. The minimization of error at 12 measurements is indicative of the ease of usability of the method and insures that the calibration time can be minimized through the optimization of number of measurements taken. It is imperative at this time that this method is further validated through a user study to quantify the average number of measurements required to minimize the TRE to a usable quantity. This study will also provide insights into the accuracy and robustness of the algorithm. This algorithm is currently being created as an open source 3D Slicer module and upon validation through the user study will be made publically available.

REFERENCES: [1] Muratore et al. Ultrasound Med Biol (2001). [2] Cormeau et al. SPIE (1998). [3] Horn, Berthold K.P. J. Opt. Soc. Am (1987).

Histology to Ultra-High Field MRI Registration of a Human Cadaveric Subcortex: Workflow Model

John P. Demarco[1,2], Jonathan C. Lau[2,4], Ali R. Khan[2,3]

[1]Department of Anatomy and Cell Biology, Schulich School of Medicine and Dentistry, Western University, London, Ontario, Canada
[2]Imaging Research Laboratories, Robarts Research Institute, Western University, London, Ontario, Canada
[3]Department of Medical Biophysics, Western University, London, Ontario, Canada
[4]Department of Clinical Neurological Sciences, Western University, London, Ontario, Canada

Introduction/ Objectives: Deep Brain Stimulation (DBS) is an effective neurosurgical intervention that is used for the treatment of Parkinson's Disease (PD) and other movement disorders. Through the development of higher resolution templates and atlases, DBS targeting can be performed with higher accuracy, and structures, such as the Subthalamic Nucleus (STN) and Globus Pallidus Interna (GPi), can be clearly delineated (Yelnik et al. 2007; Bardinet et al. 2009; Lau et al. 2017). Below we discuss the workflow for the creation of a subcortical 3D histological atlas using Ultra-High Field MRI Registration.

Method: The steps taken to develop the model begin with a 7 Tesla (T) Magnetic Resonance Image (MRI) of a cadaveric brain *in-situ* using a T2 SPC sequence at 500µm resolution. The brain was then extracted and fixed in 10% formalin before being imaged *ex-vivo* with 7T MRI. The cortex was then dissected and the subcortical hemispheres were isolated and imaged individually at 7T using a multi-echo gradient echo sequence at 300µm resolution. Each subcortex was then histologically processed into 8um thick sections and stained with hematoxylin and eosin. The Histology-to-MRI registration will allow for the mapping and reconstruction of histological sections back into the MRI space.

Results: We predict that registration of the histological sections back into the 3D MRI space will allow for better visualization and delineation of subcortical nuclei boundaries.

Conclusion: We hope that further development of this model can be applied to visualization of clinically significant anatomical structures, such as the STN and GPi, in order to assist in the planning of DBS surgery.

Support or Funding Information: Canadian Institutes of Health Research, Natural Sciences and Engineering Research Council, BrainsCAN, Brain Canada Foundation

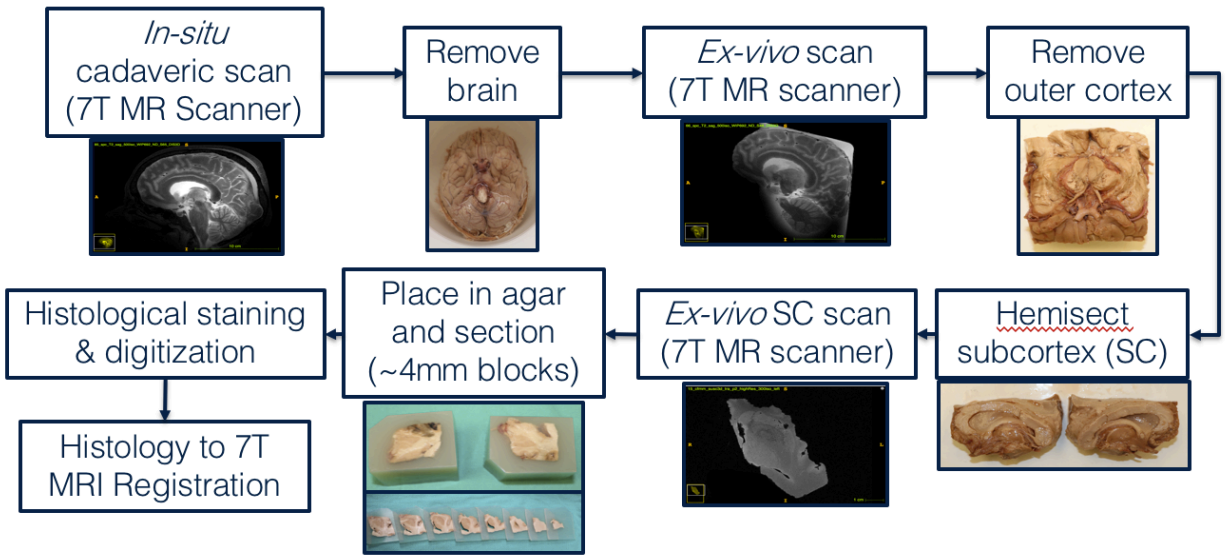

Adam Rankin
Dr. Terry Peters

Augmented Reality in Image Guided Therapy

January 18, 2018

INTRODUCTION: Recent advances in computing power and head-mounted display (HMD) technology have produced a marked increase in the availability and capabilities of consumer-grade virtual (VR) and augmented reality (AR) products. The academic community has seen a surge publications related to integrating AR and VR techniques that provide visualization platforms for image-guided therapy (IGT). This work provides a preview of our efforts towards developing an open-source platform for IGT applications using the Windows Mixed Reality ecosystem of devices. Additionally, we discuss the recent fruition of efforts towards enabling the OpenVR ecosystem of devices for visualization of the virtual scene in 3D Slicer.

WINDOWS MIXED REALITY: We have developed an image-guidance system using C++/CX and the Windows Mixed Reality (WMR) API focusing primarily on the use of the Microsoft HoloLens as our display and computing platform. Our system supports rendering of 2D and 3D objects, volume rendering of 3D anatomical datasets, gesture and voice interaction, interaction with spatial mapping of the usersô surroundings, automatic and semi-automatic registration to external magnetic and optical trackers, integrated webcam capture and analysis via OpenCV, and support for real-time 2D and 3D ultrasound visualization via the OpenIGTLink protocol as implemented by the Plus server.

Our current efforts are centered on performing a thorough assessment of our platform via a number of user studies. We are recruiting novice and expert clinical users to perform a series of simulated surgical tasks including navigating and positioning a needle to a specific pose and identifying physical characteristics of a phantom via in-situ ultrasound. In addition to user-based assessment, we will also be quantifying the performance characteristics of the platform during various task phases and system loads in order to ensure stable performance during a critical IGT procedure

SLICEROPENVR: Recent efforts by the Laboratory for Virtual Augmentation and Simulation for Surgery and Therapy, the Laboratory for Percutaneous Surgery, Kitware Inc., and other contributors have succeeded in enabling a VR view of the 3D Slicer virtual scene. Using consumer VR devices that support the OpenVR platform, any existing 3D Slicer based application can now be visualized and interacted with in a VR environment with no change to existing code required.

Other industries have begun to experiment with interaction models in VR, but no clear set of best practices has been identified. SlicerOpenVR can now provide a platform for researchers to experiment with various interaction and visualization methods to further this promising addition to image-guided interventions.

RESULTS & CONCLUSIONS: Experiments for quantification of performance and usability of the WMR platform are on-going and as a consequence on results are available yet. Figure 1 presents some preliminary qualitative results of our WMR platform as captured by a webcam angled through the left eye of the HoloLens.

Figure 1: stylus inserted into chest phantom

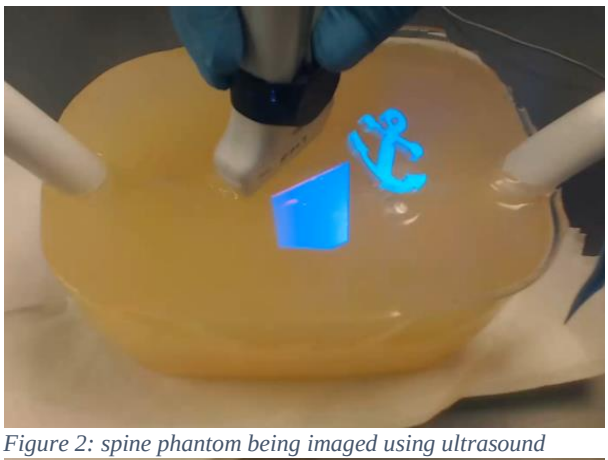

Figure 2: spine phantom being imaged using ultrasound

Development and evaluation of a navigation workflow for radiofrequency ablation of spinal metastases

D Jafari[1, 2], M Hadisty[1], N Robert[1], AJ Yee[2, 3], CM Whyne[1, 2]

1. Orthopaedic Biomechanics Laboratory, Sunnybrook Research Institute, Toronto, ON; 2. Institute of Biomaterials and Biomedical Engineering, University of Toronto, Toronto, ON; 3. Division of Orthopedics Surgery, Sunnybrook Health Sciences Center, Toronto, ON

Introduction: Bone metastases present in more than 85% of cancer patients at the time of death, with the spine being the most common site. The presence of spinal metastatic disease may lead to instability resulting in pain, fracture, and spinal cord or nerve root compression, causing severe pain, weakness, and reduction in quality life of cancer patients [1]. The early targeted treatment of these tumours may prevent or reduce negative skeletal related events. New improvements in radiofrequency ablation (RFA, Osteocool, Medtronic) has adapted this technology for local control of spinal metastases [2]. However currently, manual treatment planning and execution is dependent on operator experience and without quantitative evaluation of outcome. There is a need to develop and evaluate treatment planning and navigation in the spinal RFA.

Methods: A navigation workflow has been developed for vertebral RFA within the 3D Slicer platform integrating RFA treatment plans based on pre-procedural CT imaging data with intra-procedural 3D imaging (Cone Beam CT images, O-Arm, Medtronic). The software solution utilizes StealthLink to connect the navigation and imaging information with the Plus Server platform to enable software developed within 3D Slicer framework to provide real time navigation. Image registration is performed by initial manual landmark registration of the vertebrae of the interest, followed by creation of a region of interest mask on the CT images based on predefined threshold voxel values of bone. Automatic 3D-to-3D intensity based rigid registration algorithms are then used to align the pre-procedural and intra-procedural CT scans. The RFA probe poses (position and orientation) are then tracked optically using a StealthStation S7 navigation system (Medtronic) to ensure that the final Osteocool probe positioning matches the prescribed pose. Since the optical navigation system provides the tacking data of the origin of the optical markers attached to the probes, pivot and spin calibrations are performed in order to obtain the poses of the probe tips with respect to the tracking markersô origins. Treatment visualization throughout the procedure provides the guidance necessary to place the probe according to the plan and monitor the ablation. To evaluate the system accuracy and reproducibility, the pre-procedural scans and sample RFA treatment plans, developed in ex vivo specimens for testing purposes, are input to the software. The software transforms the data from pre-procedural coordinates to intra-procedural coordinates using a reference frame. A 3D CT image is obtained after the probe is placed at the treatment pose to verify final positional accuracy of the RFA device.

Results: The technologies involved in this project, O-arm CBCT scanner, StealthStation navigation system, SureTrak optical trackers, Osteocool RFA system, the developed RFA navigation software (3D Slicer and Plus Server) have successfully been integrated. Introducer needles and RFA probes equipped with optical markers have successfully been tracked on 3D triangulated surface models of the vertebra. By utilizing the existing image registration algorithms in the Elastix toolbox, the pre-procedural and intra-procedural CT scans are registered and the desired tool pose can be tracked in real time within the intraprocedural reference frame.

Conclusions: Thus far, the workflow shows promise for use in navigation of vertebral RFA procedures. Future post-procedural MRI imaging (T1-weighted (TR/TE:557/16.4) and T2-weighted (TR/TE:5513/125.4)) will be evaluated to delineate the generated vertebral ablation volumes. Comparison of the MRI segmented RFA volumes and the planned CT ablation volumes (via linear regression) can assess performance and yield an estimate of the acceptable margin of error on the RFA probe pose which can provide adequate thermal damage to the ROI. Ultimately, more accurate and targeted RFA treatment is expected to improve the safety and efficacy of this procedure, and enhance the quality of life for patients with spinal metastases. Ongoing collaboration with Medtronic, the commercial partner, will allow for rapid commercialization and clinical translation of this research.

References: [1] Sutcliffe, P.; Connock M.; Shyangdan D.; Court R.; Kandala N.B.; Clarke A. A systematic review of evidence on malignant spinal metastases: natural history and technologies for identifying patients at high risk of vertebral fracture and spinal cord compression. Health Technol Assess, 2013. 17(42): p. 1-274. [2] Pezeshki, P.S.; Woo, J.; Akens, M.K.; Davies, J.E.; Gofeld, M.; Whyne, C.M.; Yee, A.J. Evaluation of a bipolar cooled radiofrequency device for ablation of bone metastases: preclinical assessment in porcine vertebrae. Spine J, 2014. 14(2) p. 361-70.

Specular highlight removal for endoscopic images

Wenyao Xia[12], Elvis Chen[12], Terry Peters[12]

1: Robarts Research Institute and **2**: Medical Biophysics, Western University, London, Canada

Introduction: Stereoscopic endoscopes have been used increasingly in minimally invasive surgery to visualize the organ surface and manipulate various surgical tools. However, due to the glossiness of the organ surfaces and the closeness of the light source, the endoscopic images are always corrupted by high amount of specular highlight. The presence of specular highlight would severely occlude the organ surface and affect other computer-assisted algorithm such as stereoscopic surface reconstruction. To address this problem, we propose a specular highlight removal algorithm based on dichromatic model to recover and interpolate the specular highlight corrupted image regions.

Methods: The proposed method is mainly consisted of two parts. In the first part, the true color of the pixel is estimated using non-local means method, where the non-local weight function is determined by distance, hue similarity, and minimum intensity of pixel color channel. In the second part, the magnitude of the highlight-free image is obtained via convex optimization with total variation regularization. A dual formulation is also proposed to solve the optimization problem with good efficiency. The experimental results are validated through visual inspection, improve signal to noise ratio (PSNR), and 3D surface reconstruction accuracy.

Results: The proposed method is tested on benchmark natural images for specular highlight removal as well as stereoscopic endoscopy image dataset (TMI dataset) created by Lena Maier-Hein in 2014. Qualitatively, the proposed algorithm has achieved a great improvement in terms of visual inspection, as shown in Figure 1. As we can see, the specular highlights are completely removed from the original image with good color and texture preservation. Quantitatively, the proposed method yields higher PSNR values (38 dB in average) for benchmark natural images compared with state-of-the-art method (37 dB in average). The root mean square distance (RMSD) for surface reconstruction on TMI dataset is 0.69mm after highlight removal, which shows significant improvements compared with RMSD of 1.10mm obtained before highlight removal.

Discussion: The proposed specular highlight removal algorithm is able to effectively remove large amount of specular highlight from both natural and endoscopic images. Through visual inspection, not only the proposed method is able to obtain higher quality results, it is also able to preserve image details, such as texture and color. Experimental results also demonstrate that the proposed highlight removal method can improve the accuracy of 3D surface reconstruction and enable more accurate surgical planning and guidance.

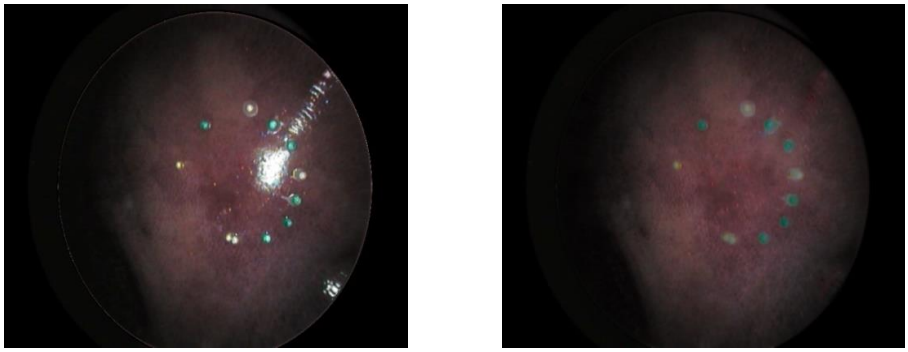

(a) (b)

Figure 1. (a) Input image with specular highlight (b) Output diffusive image without specular highlight.

Poster Presentation Abstracts

Session 2: Image Analysis

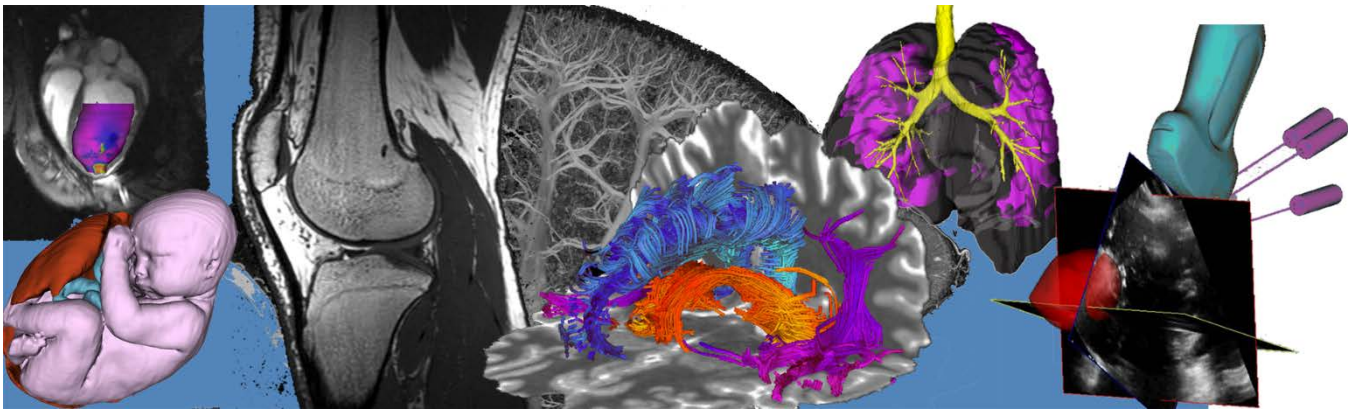

Retrospective comparison of analysis methods for hyperpolarized ^{129}Xe lung MRI in stable CF

Nikhil Kanhere[1], Marcus Couch[1], Raymond Hu[1], Felix Ratjen[1] and Giles Santyr[1]
[1]Translational Medicine Program, The Hospital for Sick Children, Toronto, ON, Canada,

Introduction- Hyperpolarized (HP) gas Magnetic Resonance Imaging (MRI) has been demonstrated to be a sensitive measure of functional changes in early cystic fibrosis (CF) lung disease (1). HP gas MRI has excellent potential as an outcome measure for management of early CF and testing novel therapeutics (e.g. CFTR modulators). However, before HP gas measures can be adopted clinically, multi-centre prospective clinical trials will be required, which will likely involve different MRI platforms and coil hardware. Therefore, standardized operating procedures will need to be developed to acquire and analyze the data consistently. As a preliminary step in the pathway to clinical translation, we retrospectively compared the image analysis method used at The Hospital for Sick Children (SickKids) to another approach used in the community (1). Specifically, in stable CF, we measured the ventilation defect percent (VDP) from ^{129}Xe MRI using the two analysis methods, and compared VDP results to the lung clearance index (LCI), which is a measure of ventilation heterogeneity.

Methods- Ten stable CF and five healthy participants, age: 8-17 yos were recruited at SickKids, Toronto. LCI was measured from N_2 multiple breath washout. Most participants had two repeated HP ^{129}Xe scans within a few minutes of each other. We cross-analyzed VDP from ^{129}Xe images using two analysis methods: the SickKids method used a k-means based segmentation (2,3) to identify defects, while the Cincinnati Children's Hospital method used a mean-anchored histogram to set defect thresholds (1). For both methods, the final VDP was calculated as the total volume of unventilated lung obtained from the ^{129}Xe images divided by the total lung volume obtained from the proton image masks.

Results- As shown in Fig. 1(a), both SickKids and Cincinnati methods yield VDP results that are moderately correlated. The Cincinnati method showed stronger correlation with LCI compared with the SickKids method as shown in Fig. 1(b). Fig. 1(c) shows a comparison of ventilation (green) and defect (purple) masks obtained in a CF subject, where the larger purple areas with the Cincinnati method indicate a greater VDP.

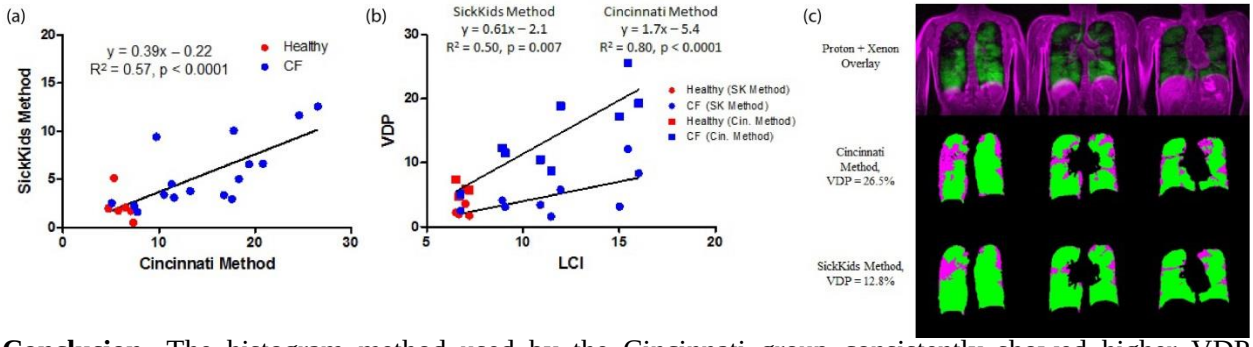

Conclusion- The histogram method used by the Cincinnati group consistently showed higher VDP values, as the chosen thresholds caused more voxels to be classified as defects compared with the k-means clustering approach used by the SickKids method. VDP from the Cincinnati method appears to have a stronger correlation to LCI than the SickKids method; however, these numbers are likely influenced by other factors, such as the number of slices included and the expertise of the observer. The comparison of the two methods shows only a moderate correlation for VDP suggesting that it might not be appropriate to use the two methods interchangeably. Future work will involve modifying the VDP calculation or developing a new hybrid method to improve the correlation with pulmonary function measurements.

References- [1] Thomen RP et al. J Cyst Fibros 2016; 16(2):275-282. [2] Kirby M et al. Acad Radiol 2012;19:141–152. [3] Kanhere N et al. Am J Respir Crit Care Med 2017; 196(8):1073-1075.

Acknowledgements- Thanks to Robby Thomen and Jason Woods for help with the histogram-based VDP calculation.

Differentiating Bracytherapy and Gold Fiducial Markers with Varying Off-Resonant Frequency Offsets

Evan McNabb[1], Raimond Wong[2], Michael D Noseworthy[1,3]

[1]School of Biomedical Engineering, McMaster University, Hamilton ON; [2]Juravinski Cancer Centre, Hamilton ON; Department of [3]Electrical and Computer Engineering, McMaster University.

Purpose: Magnetic Resonance Imaging is increasingly used in the integration of image guided radiation therapy planning [1]. Two current issues in MR-only workflows are identifying implanted gold fiducial markers (FMs) with positive contrast, and differentiating the FMs from brachytherapy seeds in patients undergoing external beam boost [2]. An MR pulse sequence, developed for visualizing low-dose rate brachytherapy seeds with positive contrast, centre-out radial sampling with off-resonance reception (co-RASOR) [3], is proposed here to differentiate the two seeds as they have different magnetic susceptibilities, with gold being diamagnetic ($\chi_m < 0$) and the platinum layer of the brachytherapy seed being paramagnetic ($\chi_m > 0$).

Materials and Methods: Two seeds were placed between in a gel phantom parallel to the B0-magnetic field (Figure 1). The left seed is a ^{125}I LDR brachytherapy seed (4.5x0.8 mm) containing a paramagnetic outer layer. The right seed is a gold fiducial marker (3.0x1.2 mm). The MR acquisition protocol used a GE 3T Discovery 750 and a 32-channel head coil and consisted of the following scans: a negative contrast 3D axial bSSFP followed by 2D dual-plane co-RASOR (TE/TR=2.8/25ms; FOV=16.0cm; thickness=3.0mm; matrix=256x804; bandwidth=250 Hz/pixel, flip=30, scan time=40s). Each co-RASOR acquisition was reconstructed with off-resonant frequencies from +/- 1.25 kHz in 50 Hz steps resulting in 51 offsets. A projection using all the frequency offsets is used to view both seeds in axial and coronal planes. A smaller positive frequency range, centred about 500 Hz +/ 50 Hz, was used to rewind signal pileups from the gold fiducial marker, whereas negative frequency range, centred at -600 Hz, was used for the brachytherapy seed.

Results and Discussion: Applying a smaller range of frequency offsets centred about -600 and +500 Hz, each seed can be individually identified (Figure 2a,b). The MR signal vs frequency offset of a small ROI placed in the centre of the brachytherapy seed and gold FM shows the signal maxima for each seed (Figure 2c). The dual-plane co-RASOR sequence is able to differentiate the two seeds based on their susceptibility difference, as this causes the signal pileups to have unique patterns around the seeds, seen in the on-resonant images. Different frequency offsets are able to bring into focus the hyperintensities at the geometric centre for a single marker. When reconstructed at -600 Hz, the brachytherapy seed has a much higher local signal intensity (red arrow Fig 2a) and can be isolated by thresholding, whereas at 500 Hz, the gold FM has the highest local signal and is also isolated by thresholding. The signal vs frequency plot reveals that each seed has a signal maxima which is used to tune the off-resonant frequency offsets. One limitation is that the hyperintensities must have distinct patterns. In the axial plane, the hyperintensities show a ring pattern around the signal voids and rewind at nearly equally with similar frequency offsets, however this does not apply equally to the dipole pattern observed in the coronal plane.

Conclusion: The dual-plane co-RASOR sequence is able to differentiate between a LDR brachytherapy seed and gold FM by exploiting signal pileups and rewinding them radially inwards using different off-resonant frequency offsets.

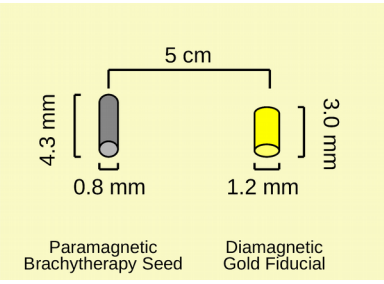

***Figure 1**: Gel phantom schematic of the seed sizes (left – LDR brachytherapy; right- GFM)*

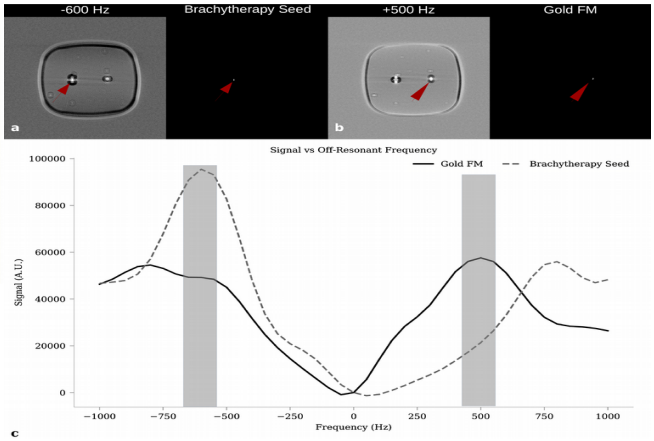

Figure 2: Off-resonant reconstructions centred at -600 Hz (a) and 500 Hz (b). Signal vs frequency plot (c) with shaded regions to demonstrate the signal maxima of each seed is localized to positive and negative frequency bands.

An ultrasound imaging study of the posterior skull without hair removal for registration

Grace Underwood[1], Tamas Ungi[1], Andras Lasso[1], Gernot Kronreif[2], and Gabor Fichtinger[1]

[1]Laboratory for Percutaneous Surgery, Queenôs University, Kingston, ON, Canada

[2]Austrian Center for Medical Innovation and Technology, Wiener Neustadt, Austria

Introduction: Neurosurgical registration using optical tracking in prone position is problematic due to a lack of anatomical landmarks on the posterior skull and difficulty maintaining line of sight to commonly used registration points on the anterior skull. Obtaining full access to the posterior skull would require patient hair removal, which is not favored by patients as it can cause an increased risk of surgical site infection and a less aesthetic outcome [1]. Ultrasound may provide access to bone surfaces along the posterior skull that were previously inaccessible by a tracked pointer and are sufficient for surface registration. We performed human ultrasound scanning to determine if bone surfaces on the posterior skull could be identified in ultrasound without hair removal. This would provide insight into designing a realistic and favorable ultrasound scanning protocol for registration of patients in the prone position.

Methods: This analysis was performed using 3D Slicer (www.slicer.org), the Plus Server application (www.plustoolkit.org), a Telemed MicrUs ultrasound (Telemed Ultrasound Medical Systems, Vilnius, Lithuania), a Telemed L12-5L40S-3 linear ultrasound probe, a Telemed C5-2R60S-3 curvilinear ultrasound probe, water, and ultrasound transmission gel. Participants were scanned around each mastoid process, and the occipital base of the skull. Ultrasound scans were recorded using the Sequences extension in 3D Slicer [2]. The linear and curvilinear probes, at their maximum and minimum frequencies, were used to conduct ultrasound scanning. The linear probe was operated at 12MHz and 5MHz. The curvilinear probe was operated at 5MHz and 2MHz. Each scan was evaluated to determine if bone regions were clearly identifiable, not identifiable or if there was uncertainty about bone surfaces. Ultrasoundôs inability to penetrate bone meant that in areas containing bone surfaces bright white surface was visible with notable shadowing.

Figure 1. Phantom and human participants

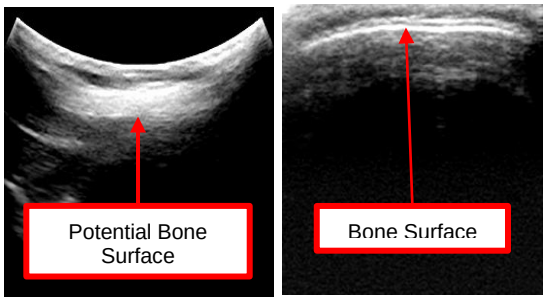

Figure 2A) Scan using a curvilinear probe on the occipital base, B) Scan using a linear probe on the occipital base

Results: A phantom skull and five human participants were scanned with ultrasound (Figure 1). The participants varied in gender, hair length, and hair thickness. The ability to identify bone surfaces in ultrasound was evaluated and recorded. The linear probe at 12MHZ frequency consistently provided clearly identifiable regions and the curvilinear probe at both frequencies consistently did not provide sufficient identifiable bone surfaces (Figure 2).

Conclusion: Tracked ultrasound may be used as a non-invasive method of registration for patients undergoing neurosurgery in prone position. The linear ultrasound probe at a high frequency provided clearly identifiable bone surfaces in all areas without requiring hair removal. A higher resolution would decrease the width of bone surfaces in the ultrasound image and could improve the placement of surface.

References

[1] Winston K., ñHair and Neurosurgeryò, Neurosurgery, vol. 31, no. 2, 1992.

[2] T Kapur et al., "Increasing the Impact of Medical Image Computing using Community-based Open-access Hackathons: The NA-MIC and 3D Slicer Experience," Medical Image Analysis, vol. 33, 2016.

Development of a Biometric Hand Size Measurement Software Tool for use in Acromegaly Screening

J.S. Milner[1], S. De Brabandere[2], A. Azzola[2], S. Van Uum[2], D.W. Holdsworth[1]

[1]Robarts Research Institute, Western University, London, Canada
[2]Division of Endocrinology and Metabolism, St. Joseph's Health Care, London, Canada

Introduction: Acromegaly is a rare and chronic progressive disease characterized by the overproduction of growth hormone (GH) and insulin-like growth factor 1 (IGF-1) and is most commonly caused by a pituitary adenoma. There is usually a delay of 5 to 10 years between the onset of symptoms and the diagnosis of acromegaly. Earlier diagnosis would potentially decrease acromegaly-related morbidity and healthcare costs. A relatively early finding in this disease is increased hand and ring size. Herein we describe the development of a fast, low-cost, easy-to-use image acquisition and analysis system requiring no specialized hardware for producing and analyzing 2D images of the hands that can be used as a potential screening tool for earlier diagnosis of acromegaly.

Methods: Hand digitization is performed using a consumer-grade, desktop flatbed document scanner (Canon LiDE 220). Subjects place their hand on the scanner and the lid is closed and draped with black cloth to prevent entry of stray light. Acquisition time is less than 15 seconds and produces 8-bit greyscale images at a resolution of 150 DPI (0.169 mm/pixel). Output image format is JPEG and EXIF image data is recorded in order to encapsulate acquisition parameters. A customized, cross-platform software application is used to automatically compute specific biometric measurements of the hand thought to be potential indicators of acromegaly. Implementation of the software was carried out using C++, VTK, and Qt. Computed measurements include: length, width, and aspect ratio of each finger and of the palm surface; palm surface area; and maximum incircle diameter of the palm. Digitized hand images from the acquisition step are loaded into the software where the operator interactively identifies 14 well-defined landmarks. Automatic boundary detection is used to minimize inter- and intra-operator variability by constraining landmarks to locations on the computed hand periphery. Biometric measurements are automatically calculated upon completion of the landmark initialization. Computation time is negligible. Graphical results are overlaid on the digitized hand image and numeric results presented via a pop-out window. Subject information is recorded and results are exported into a format conducive to data analysis in spreadsheet applications.

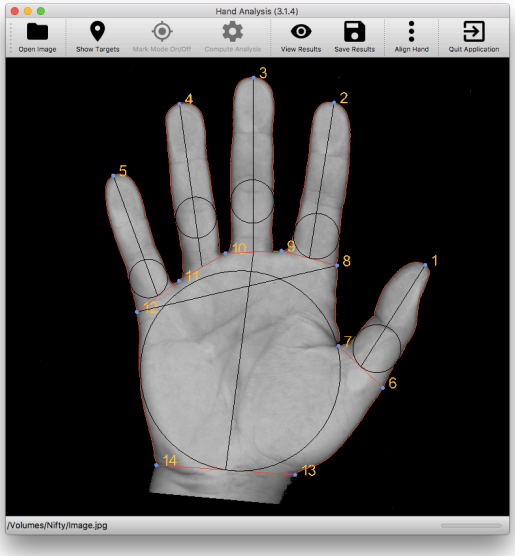

Figure 1. Completed biometric hand size measurements

Results: As an initial test of the acquisition and measurement system a pilot study examining the hand sizes in 20 individuals: 10 (5 male and 5 female) with acromegaly (ACRO) and 10 (5 male and 5 female) with non-functioning pituitary adenoma (NFPA, acromegaly excluded via normal a IGF-1) was undertaken. Group results compared using ANOVA showed significant differences between the ACRO and NFPA groups for male patients in both left palm area ($P < 0.01$) and left palm maximum incircle diameter ($P < 0.001$) and as well between the ACRO and NFPA groups for female patients in both left palm area ($P < 0.01$) and left palm maximum incircle diameter ($P < 0.01$). Similar results were observed for the right-hand measurements.

Conclusions: We have demonstrated the feasibility of a low-cost, easy-to-use system for biometric hand size measurement. Biometric hand size measurement is considerably cheaper and more easily accessible than biochemical tests. Further studies are needed to determine if biometric hand size measurement may be a potential screening tool for earlier diagnosis of acromegaly.

Performance evaluation of a peripheral cone-beam CT scanner with weight-bearing capabilities

Rudy Baronette[1,2,3], Xunhua Yuan[2], Steven I Pollmann[2], Matthew G Teeter[1,3,4,5], David W Holdsworth[1,2,3,4]
[1]Western Bone and Joint Institute
[2]Imaging Research Laboratories, Robarts Research Institute
Depts. of Medical Biophysics[3] and Surgery,[4] Western University
[5]Lawson Health Research Institute, London ON, Canada

Introduction: Weight-bearing imaging of the lower extremity is limited to supine positioning by scanner design in conventional clinical CT scanners. Due to recent advances in cone beam computed tomography (CBCT), true 3D weight-bearing CT is now available for clinical evaluations of patients in a health care setting.[1,2] The Verity CT scanner (Planmed Oy) is a CBCT imaging system optimized for upper and lower extremities. The system acquires high-resolution volumetric images of the target and includes a motorized gantry that allows for weight-bearing CBCT imaging of lower extremities. The purpose of this study was to perform a quantitative evaluation with four reconstruction algorithms to test the imaging performance of this peripheral CBCT scanner.

Methods: Performance of the Verity CBCT system (Fig. 1a) was evaluated using a small and a large custom-built image quality phantom, with diameters similar to the average-sized elbow (diameter = 70 mm) and knee (diameter = 150 mm). These phantoms were used to assess the noise, resolution, and uniformity, as previously described.[3] Upon completion of the scans, performance results were evaluated with custom image analysis software and MicroView (Parallax, London, ON). Both phantoms were tested using scan parameters prescribed by the manufacturer. Resulting image volumes (11 cm length, 16 cm diameter) were reconstructed at an isotropic resolution of 0.2 mm.

Results: Analysis of the slanted-edge image, using the current reconstruction algorithm, (Fig. 1b) indicated limiting resolution of 1.41 lp/mm, compared with 1.70 lp/mm obtained with the beta algorithm. Noise was evaluated as the standard deviation within a uniform region, over a range of exposures (Fig. 1c). Minimum standard deviations of 65 HU and 96 HU were observed for the current and beta algorithms, in the large phantom, at the highest exposure setting with an adaptive noise optimization algorithm. The system uniformity (calculated as the average difference in signal intensity values between the peripheral and central regions) was 66.4 HU and 3.9 HU for the large and small phantoms, respectively.

Conclusion: The performance evaluation of the peripheral CBCT scanner shows the Verity meets the manufacturerôs specifications for high-resolution scans. Analysis of the resolution yielded a limiting spatial resolution exceeding 1.25 lp/mm. The noise characteristics were well within the manufacturerôs guidelines, where the HU standard deviation is less than 100 HU. Uniformity performance was excellent over the central region and within the limits of 50 HU set by the manufacturer. The uniformity test displayed a large difference in average HU from the centre to the periphery, which can be attributed to beam hardening and scatter.

References: **1.** Tuominen, E. K., et al. (2013). AJR Am J Roentgenol 200(1): 146-148. **2.** Zbijewski, W.E., Et al. (2011) Med. Phys 38(8): 4700-4713. Du L., et al. (2007) Phys. Med. Biol 52: 7087-7108.

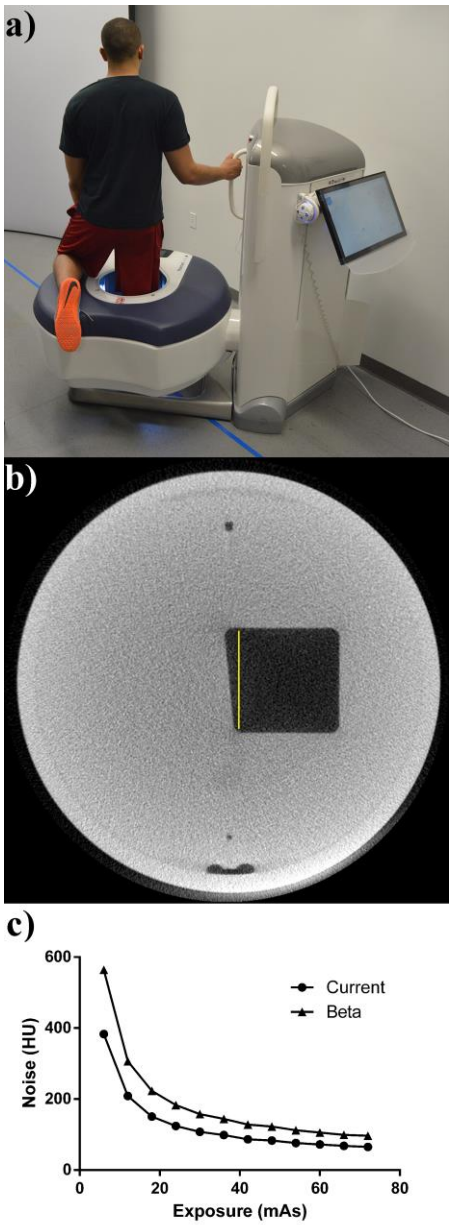

Fig. 1: (a) photo of the Planmed Verity peripheral CT scanner; (b) transverse image of a slanted edge from large phantom, used to calculate MTF; and (c) noise (SD) in HU *vs* exposure.

Brain Extraction Methods for Neurological FLAIR MRI

Justin DiGregorio*, Alan R. Moody**, April Khademi*
*Image Analysis in Medicine Laboratory (IAMLAB), Faculty of Engineering, Ryerson University,
**Department of Medical Imaging, University of Toronto

Introduction: Fluid-Attenuated Inversion Recovery (FLAIR) MRI is a common MRI technique for diagnosing neurodegenerative diseases [1]. FLAIR images are particularly good at visualizing white matter lesions (WML) when compared to images generated by T1- and T2-weighted MRI [1]. Quantification of WML commonly requires manual segmentation of the lesions, which is tedious and subject to observer variability. Automatic WML segmentation frameworks have been developed to offer an alternative to manual analysis [1]. Brain extraction (BE), a pre-processing step in which any non-brain tissue is removed from the images, is critical to these algorithms. BE algorithms exist for T1- and T2-weighted MRI images [2]. However, these methods may not be adequate for FLAIR images due to differences in the contrast mechanisms. This work assesses if there is a need for brain extraction methods designed exclusively for FLAIR and proposes techniques to develop these methods.

Methods: Two commonly used open-source brain extraction tools for MRI were tested on FLAIR MRI volumes. The ROBEX algorithm described in [2] uses a machine learning approach that has been trained on T1-weighted data. ROBEX is designed for use on T1-weighted images and is fully automatic with no parameter settings. The FSL brain extraction tool (BET) uses a deformable model that is initialized at the center of the brain volume and expands until it reaches a significant threshold typically represented by the skull [3]. FSL BET is designed for use with T1- and T2-weighted images and allows users to configure parameters. In addition to these two commonly used methods, a FLAIR intensity standardization method described in [4] was utilized to enable automated whole-volume brain extraction in FLAIR. This method, utilizes histogram-matching to overcome intensity non-standardness; a common issue in MRI. Segmentation was then performed by using the same thresholds and morphological operations across all the data. The metric used to compare these BE methodologies was the Dice Similarity Coefficient (DSC), which evaluates overlap between manual and automatic brain segmentations.

Results: 432 FLAIR images (9 volumes) from the Canadian Atherosclerosis Imaging Network (CAIN) along with 280 FLAIR images (8 volumes) from the Alzheimerôs Disease Neuroimage Initiative (ADNI) were used to test each brain extraction schema. The DSC is shown as an average for all images in Table 1 and sample segmentations of an image from the CAIN dataset are shown in Figure 1. The low DSC for the FSL BET is likely linked to cerebrospinal flow or lesions (i.e. bright spots common in FLAIR) which caused the threshold to be prematurely crossed. ROBEX performed second best with an average DSC of 0.606 across both datasets. The proposed method, consisting of intensity standardization followed by thresholding, performed best with an average DSC of 0.778 across both datasets. These results highlight the need for FLAIR specific BE tools.

Method	CAIN DSC	ADNI DSC
FSL BET	0.4529	0.2258
ROBEX	0.6306	0.5814
Thresholding	0.8152	0.7414

Table 1 Average DSC for each BE method

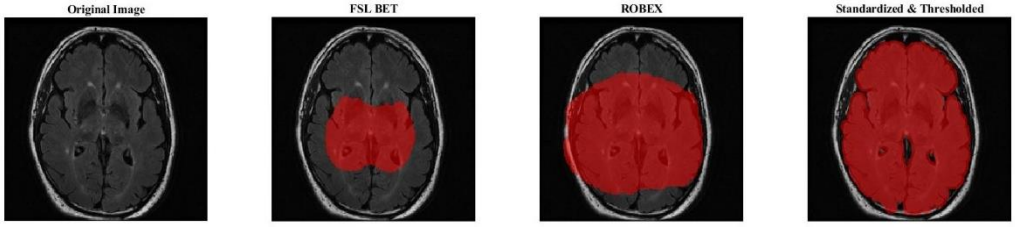

Figure 1 Sample brain extractions for each BE method on a CAIN dataset image

Conclusions: This work demonstrates that algorithms designed for T1- and T2-weighted images are not optimal for FLAIR due to tissue intensity variation across modalities. Thus, the development of tools to process FLAIR images is crucial. However, intra-modality intensity non-standardness makes the development of these algorithms difficult. This work also highlights that utilizing intensity standardization can be used to overcome this obstacle.

References: [1] Khademi, A., Venetsanopoulos, A., & Moody, A. R. (2012). Robust white matter lesion segmentation in FLAIR MRI. *IEEE Transactions on biomedical engineering*, *59*(3), 860-871. [2] Iglesias, J. E., Liu, C. Y., Thompson, P. M., & Tu, Z. (2011). Robust brain extraction across datasets and comparison with publicly available methods. *IEEE transactions on medical imaging*, *30*(9), 1617-1634. [3] S.M. Smith. Fast robust automated brain extraction. *Human Brain Mapping,* 17(3):143-155, November 2002. [4] Reiche, B., Moody, A. R., & Khademi, A. (2015). Effect of image standardization on FLAIR MRI for brain extraction. *Signal, Image and Video Processing*, *9*(1), 11-16.

Development and Validation of a Platform for High Throughput Quantitative Digital Pathology, using Machine Learning for Tissue Cytometric Analysis on Immunostained Slides

Authors: Trevor D. McKee[1*], Naz Chaudary, Jade Bilkey, Mark Zaidi, Michael Milosevic, David A. Jaffray

Affiliations: STTARR Innovation Centre, Princess Margaret Cancer Centre, University Health Network, Toronto ON.

Purpose: The goal of precision medicine is to increase therapeutic efficacy by more precise targeting. The advent of molecular therapeutics targeting specific proteins in cancer cells or the tumor microenvironment, holds promise to improve therapy. These therapies require proper selection of patients with specific mutations or microenvironmental differences to be effective. The development of robust biomarkers has been hampered by the time consuming process of inter-group analysis collaborations and limited pathologist time.

Methods: Our goal is to enhance this development process by making a cloud based, open source image analysis pipeline available. This pipeline allows rapid analysis development using a set of building block analysis tools, and incorporates advances in machine learning to assist in pathological identification of regions of interest. This service will assist clinical pathologists with their workflows and ease the pathway to validation for new biomarkers in drug development and basic science.

Results: We have developed a GPU-accelerated analytical pipeline for brightfield image separation, cellular segmentation, and customized marker algorithm development. Our approach is to work closely with UHN Pathologists on a quantification procedure appropriate to the tissue and marker of interest, perform stain separation and cellular segmentation in a semi-automated fashion, and define quantitative readouts appropriate for the marker and tissue being investigated. Initial pilot projects using machine learning from pathologist annotations have produced results that match with pathologist quantitative estimations, but that run in a semi-automated fashion, increasing quantitative analysis throughput by several fold over manual scoring methods. We have also applied similar approaches to quantification of multi-colour immunofluorescence, imaging mass cytometry, and DESI imaging mass spectrometry data.

Conclusions: An image analysis pipeline for semi-automated analysis of digital pathology images stained for specific markers has been built, providing quantitative readouts for staining intensity and distribution within the tumor microenvironment. We continue to work closely with UHN Pathologists to build appropriate validation steps into this analytical pipeline, including collaborative tools for image annotation and review, in order to improve the robustness of this process, and ultimately to provide useful tools to augment the clinical pathologistôs toolbox.

Exploring regional CSF volume differences in patients from the Sunnybrook Dementia Study.

Emmanuel Edward Ntiri, Joel Ramirez, Maged Goubran, Fuqiang Gao, Sandra E. Black
Sunnybrook Research Institute, Hurvitz Brain Sciences Program, Toronto, ON, Canada

Introduction: Alzheimerôs disease (AD), frontotemporal dementia (FTD), and Lewy body dementia (DLB) exhibit regional atrophy that are both unique and overlapping between these diseases. Regional differences in ventricular (vCSF) and sulcal cerebrospinal fluid (sCSF) volumes measured on structural MRI may be useful imaging markers to establish differences between these complex dementias.
Methods: Data were acquired from 632 participants recruited from the Sunnybrook Dementia study (AD=347; FTD=121; DLB=52; NC=112). Structural MRI was acquired using a 1.5 Tesla GE scanner. Each patientôs T1 was divided into 13 regions using SABRE [1], a technique that involved generating an individualized Talairach grid through registration. Volumes for sCSF and vCSF were previously segmented from T1[2]. The regions of interest (ROIs) were then established by using the anterior commissure (AC), posterior commissure (PC), and other SABRE-defined landmarks. The left and right anterior ventricle ROIs were defined as vCSF that was anterior to the AC, while the left and right posterior ventricles ROIs consisted of vCSF that was posterior to the PC. The interhemispheric fissure (IHF) was defined as sCSF within the medial superior and medial frontal regions, as delineated by the SABRE parcellation. Each ROI (see Fig.1) was then divided by the total intracranial volume to account for individual differences in head size. All analyses accounted for age, education, and disease severity estimated by the Mini-Mental State Examination score.
Results: An analysis of covariance accounting for the aforementioned covariates (see Table 1) found that patient group had a significant effect across all ROIs ($p < 0.001$). A post hoc comparison using the Tukey HSD test found that the FTD group had significantly larger left anterior ventricles (FTD=6.8 vs AD=5.8, $p<0.01$), while AD had significantly larger right posterior ventricles (AD=11.1 vs. FTD=9.0, $p<0.01$?). The differences in the interhemispheric fissure were not significant. All groups had significantly larger ROI volumes ($P<0.01$) compared to NC.
Discussion: Dividing ventricles into regions can provide for better regional atrophy characterization of these complex dementias. Future studies should measure the progression of regional atrophy to explore differences in the rate of atrophy, as well as potential atrophic patterns.

References:
[1] Dade LA, Gao FQ, Kovacevic N, Roy P, Rockel C, OõToole CM, Lobaugh NJ, Feinstein A, Levine B, Black SE. Semiautomatic brain region extraction: a method of parcellating brain regions from structural magnetic resonance images. Neuroimage. 2004;22: 1492-502. [2] Kovacevic, N, Lobaugh NJ, Bronskill MJ, Levine B, Feinstein A, Black SE. (2002). A robust method for extraction and automatic segmentation of brain images. *Neuroimage* 17, 1087ï 1100.

Table 1: Demographic and volumetric summaries for study patients

Demographics[a]	**AD**	**FTD**	**DLB**	**NC**
n	347	121	52	112
Age, y	72.2 (9.2)	66.5 (9.1)	70.1 (10.5)	68.8 (8.6)
Gender, *n* (%) male	154 (44.4)	58 (47.9)	52 (65.4)	46 (41.1)
Education, y	13.7 (3.8)	14.2 (3.9)	14.1 (3.0)	15.6 (3.3)
MMSE/30, y	23.0 (4.7)	23.1 (6.2)	22.0 (5.7)	28.8 (1.2)
Volumetrics[b]				
Interhemispheric fissure	29.5 (8.7)	31.1 (8.8)	29.4 (8.5)	24.6 (6.7)
Left anterior ventricle	5.8 (3.0)	6.8 (4.1)	6.0 (3.3)	4.2 (2.2)
Left posterior ventricle	11.7 (7.4)	10.2 (5.9)	12.2 (6.8)	6.8 (3.8)
Right anterior ventricle	5.8 (3.3)	6.3 (3.4)	5.9 (3.2)	4.2 (2.3)
Right posterior ventricle	11.1 (7.2)	9.0 (5.5)	11.6 (6.3)	6.6 (3.5)

[a]Values reported are mean (SD), unless otherwise stated. [b]Values reported are in mean (SD) mL

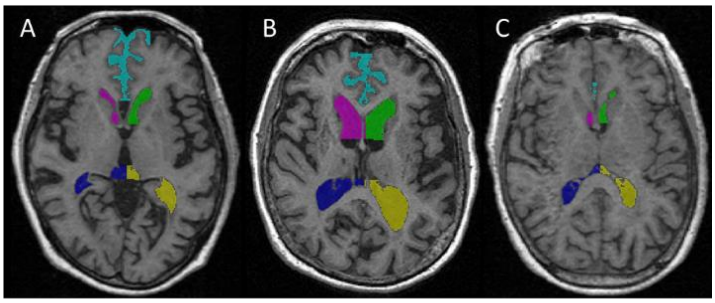

Fig 1. Image showing segmentation of interhemispheric fissure (light blue), left (green) and right (purple) anterior ventricles, and left (yellow) and right (blue) posterior ventricles for (A) AD, (B) FTD, (C) NC.

An Automatic Radiology-Pathology Fusion Resource in Pathology Image Informatics Platform (PIIP)

Rushin Shojaii[1], Mihaela Pop[1,2], Azadeh Yazdanpanah[1], Anne L. Martel[1,2]
[1]Sunnybrook Research Institute, 2075 Bayview Avenue, Toronto, ON, Canada M4N 3M5
[2]Department of Medical Biophysics, University of Toronto, Toronto

Introduction: Correlation of medical images with histology has an important role in validation studies, where the effect of underlying pathology on the imaging signal is investigated. Accurate registration of the images is the key point in the validity of the conclusions obtained from these studies. Due to tissue deformation and distortion, which occur during histopathological processes, manual registration of the images is a difficult task. Contrast and resolution differences between images obtained from different modalities also add to the level of difficulty of the image registration. This abstract presents an automatic image registration plugin[1], which is developed and embedded in a freely available pathology image viewer, Sedeen, from PathCore Inc.[2]. The image registration plugin is a part of Pathology Image Informatics Platform (PIIP) project [3], which is sponsored by NCI/NIH for digital pathology.

Methods: Currently the image registration plugin has the capability of performing a 2D to 2D rigid registration of a source image to a target image. The algorithm, which has been previously validated[1], finds the registration parameters by minimizing the Euclidean distance between the dense SIFT features of the images. Sedeen Software Development Kit (SDK) was used to implement the image registration plugin in the form of a DLL file. To test the plugin, a pair of contrast enhanced MR image of a swine heart and its corresponding histology image, stained with Masson's trichrome, were registered. Masson's trichrome is a collagen-specific stain and is used to detect the extent of tissue fibrosis. The overlapping of the regions of the post-infarction scar tissue detected on both images was observed to evaluate the registration. Two regions of interests outlining the Infarct Core (IC) and Gray Zone (GZ) in MRI[4] were transferred to the histology image by using the ExportTransformedROI plugin. The percentage of stain positivity in these regions calculated by StainAnalysis plugin was used to confirm that the transferred regions lie in the IC and GZ in the histology image as well.

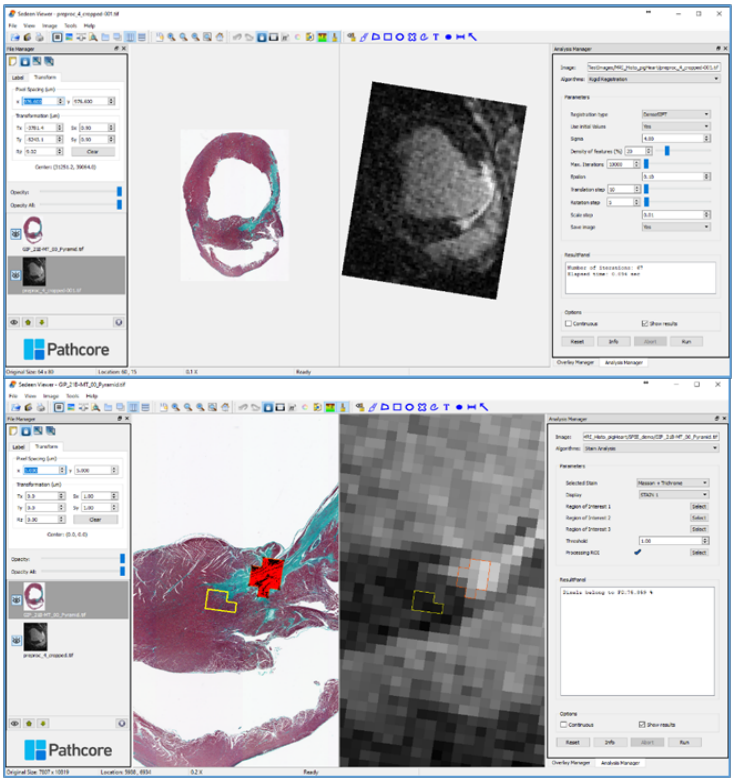

Figure 1: snapshots of the image registration plugin in Sedeen viewer (top) and transferred annotations with stain analysis (bottom).

Results: The side by side view of the registered MR and histology images in Sedeen viewer is shown in figure 1. Although the tissue is quite deformed in histology with respect to MR and only rigid registration has been used, the images in figure 1 show that the regions of scar tissue in both images are aligned. The stain positivity of the transferred infarct regions from MRI to histology also shows that the regions overlap the same infarct zones in the histology image. The percentage of the stain positivity complies with literature[4]. Currently the rigid registration plugin considers an isotropic scale factor for registration. In future the scale factor will be anisotropic to compensate for different shrinkage or expansion rates in x and y directions.

Conclusion: An automatic 2D to 2D rigid image registration algorithm has been developed for radiology-pathology fusion, which is fast and does not require down sampling of the histology images.

Acknowledgement: The authors would like to thank NCI/NIH for funding and Pathcore for supporting this project.

1. Shojaii R, Martel AL. *SPIE J Med Imaging*. 2016; doi: 10.1117/1.JMI.3.4.047501.
2. PathCore. Sedeen Viewer. http://www.pathcore.ca/products/visualizations. Published 2016.
3. Martel AL, Hosseinzadeh D, Senaras C, et al. *Cancer Res*. 2017;77(21):e83-e86. doi:10.1158/0008-5472.CAN-17-0323.
4. Pop M, Ramanan V, Yang F, et al. 2014;61(12):2930-2938. doi:10.1109/TBME.2014.2336593..

Automated Detection of DCIS in Whole Slide Images

Nikhil Seth[1,2], Shazia Akbar[1,2], Sharon Nofech-Mozes[1], Sherine Salama[1], Anne L. Martel[1,2]

[1]Sunnybrook Research Institute, Toronto, ON, Canada, [2]Department of Medical Biophysics, University of Toronto

Introduction: Ductal carcinoma in situ (DCIS) is a common early form of breast cancer, accounting for approximately 2,500 new cases per year in Canada [1]. Most patients diagnosed with DCIS undergo breast conserving surgery. To reduce the risk of developing local recurrences, some patients undergo post-surgery radiotherapy. Determining which patients have very low risk of recurrence and thus do not require radiotherapy is challenging with traditional histopathological techniques, due to variabilities in microenvironment and molecular subtype. However, it has been shown that these variabilities can manifest themselves at the cellular level as morphological subtleties [2]. That is, quantitative features can be extracted from histology images of DCIS and used to predict the risk of local recurrence. To do this efficiently, relevant regions must be localized within the whole slide image (WSI). Thus, there is a need for an accurate and reliable DCIS segmentation routine.

Methods: Several convolutional neural network (CNN) based segmentation methods have been developed and compared. The dataset used to train these networks consists of 183 women who were diagnosed with DCIS and underwent breast conserving surgery. Their tumors were sectioned and stained with H&E, before being imaged in a slide scanner. An expert pathologist reviewed each whole slide image and marked annotations around the ducts containing DCIS, which were used as ground truth segmentations for training the CNNs. The whole slide images were split 60/40 into training and testing sets, and the training set was further split 90/10 into training and validation sets. Patches were extracted from tissue regions at each of the available resolutions (20x, 10x, 5x) to create image datasets. A U-Net [3] was trained on each dataset separately to compare the effects of using patches at different resolutions. Finally, a custom multiresolution U-Net architecture was created to take three inputs, and was trained using images from all three resolutions. We hypothesise that this network can combine information contained at different resolutions to achieve a greater segmentation accuracy.

Results: The performance of these networks was evaluated by making predictions on an independant test set. The 10x network performed the best of the single input U-Nets, achieving 82.72% accuracy and an AUC of 0.903. The multiresolution U-Net achieved a test accuracy of 83.59% and an AUC of 0.894.

Conclusion: Since the U-Net outputs images with dimensions identical to the input, predictive power remains constant across varying input sizes. Thus, it is interesting that the 10x U-Net had the best test performance, rather than the high resolution (20x) network. Additionally, the multiresolution network shows comparable performance to the highest performance single input U-Net. This indicates the network is not fully taking advantage of the additional inputs. We believe this could be improved by varying the field of view of patches entering the multiresolution network. Further investigation into this hypothesis is needed.

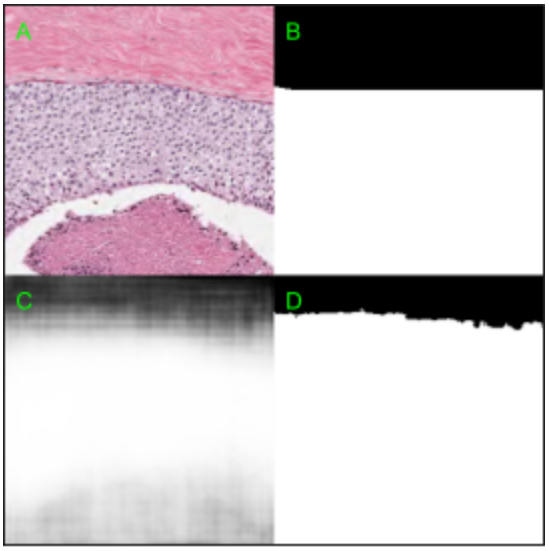

Figure 1: Example images from the 10x resolution U-Net. A: input patch. B: ground truth labelling of DCIS. C: probability map output from the U-Net. D: thresholded probability map (threshold = 0.5).

References: [1] Canadian Cancer Societyôs Advisory Committee on Cancer Statistics. Canadian Cancer Statistics 2017. [2] A. H. Beck *et al.*, ñSystematic Analysis of Breast Cancer Morphology Uncovers Stromal Features Associated with Survival,ò *Sci. Transl. Med.* Nov. 2011. [3] O. Ronneberger, P. Fischer, and T. Brox, ñU-Net: Convolutional Networks for Biomedical Image Segmentation,ò *Miccai 2015*.

Groupwise Registration and Diffusion Tensor Reorientation in Cardiac MRI: Application to Explanted Porcine Hearts

Mia Mojica[(*)], Mihaela Pop[(**)], Maxime Sermesant[(***)], and Mehran Ebrahimi[(*)]
[(*)] Faculty of Science, University of Ontario Institute of Technology, Oshawa, ON, Canada
[(**)] Department of Medical Biophysics, University of Toronto, Sunnybrook Research Inst., Toronto, ON, Canada
[(***)] Asclepios Team, INRIA Sophia Antipolis, France

Introduction: Cardiovascular diseases (CVDs) are the leading cause of mortality worldwide, accounting annually for over 15 million deaths. Image-based models and statistical atlases of the cardiac anatomy and physiology can aid in better diagnosis and treatment planning of CVD. In this abstract, we propose a framework for constructing a myocardial statistical atlas from *ex vivo* diffusion tensor images (DTI) of porcine hearts (with size comparable to human hearts), by first computing an average geometry and then obtaining directional information of diffusion linked to the reference frame of the transformed subjects.

Methods: All high resolution DT MR images were acquired on a 1.5T GE Signa Excite scanner in freshly explanted healthy pig hearts (N = 4) at sub-millimetric resolution, by using the following MR parameters: TE = 35 ms, TR = 700 ms, echo train length = 2, b-value = 0 for the unweighted MR images and b = 500 s/mm^2 for the seven diffusion gradients, respectively [2]. Notably, the total MR imaging time is ~10 hours/heart, which is not feasible for *in vivo* patient studies. An average geometry was computed by performing groupwise registration on the 3D anatomical images. At every iteration, the reference geometry was updated using an averaging technique that takes into account all the transformations aligning each subject to the current reference geometry. The said transformations were obtained through multilevel affine and nonparametric registration. This scheme normalizes the cardiac geometries of the anatomical MR images despite a high variability in their measurements. Once the transformations aligning the subjects to the average geometry are known, the diffusion tensors then need to be reoriented according to the modification of the reference frame [1]. To this end, we used the Finite Strain method, wherein the rotation components of the transformations were used to reorient the tensor at each voxel.

Results and Conclusions: The subjects overlaid on top of each other and the average geometry obtained from our experiments are shown in Figure 1(a) and (b), respectively. The method needed only 5 to 7 iterations until it converged to a stable average geometry. In Figure 1(c), we display the convergence of the groupwise framework measured in terms of the change in intensity values between successive reference geometries. Note that the values dropped by about 82% after the 7th iteration. In Figure 2, we present the results of the Finite Strain reorientation method. Observe that the geometric features of the diffusion tensor fields were preserved. This makes Finite Strain an ideal method for inter-subject DT-MRI registration [1]. Future work will focus on including more datasets in the atlas.

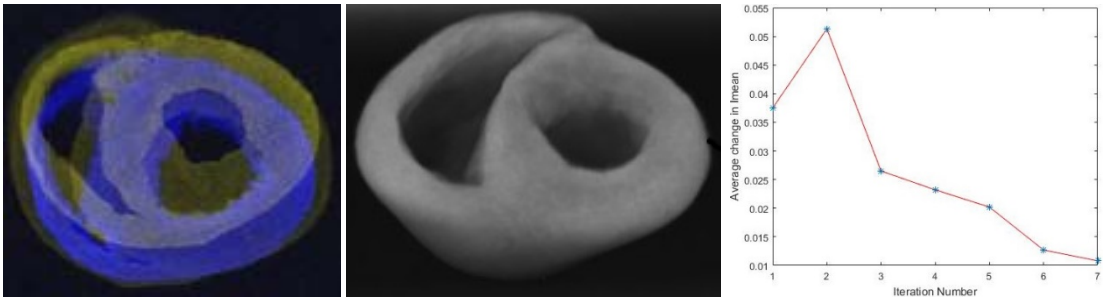

Figure 1[a,b,c]. (a) Axial view of the four subjects overlaid on top of each other, (b) the computed average geometry, and (c) the average change in I^n_{mean} after each iteration.

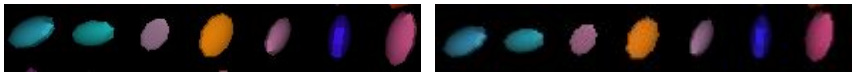

Figure 2[a,b]. The (a) original and (b) transformed tensors of one of the subjects in the data set.

References: [1] Peyrat, J.M., Sermesant, M., et al., IEEE Trans. Med. Imag. 26, 1500-14 (2007), [2] Pop, M., et al., Physics in Medicine and Biology. 58 (15), 5009-28 (2013)

Convolutional Neural Network based Brain Metastasis Segmentation

Andrei Mouraviev[1], Mark Ruschin[3], Young Lee[3], Irene Karam[3], Arjun Sahgal[3], Chris Heyn[3], Anne L. Martel[1,2]
[1]Dept. Medical Biophysics, University of Toronto, Toronto, Canada
[2]Physical Sciences, Sunnybrook Research Institute, Toronto, Canada
[3]Odette Cancer Center, Sunnybrook Health Science Centre, Toronto, Canada

Introduction. Brain metastases are secondary cancer sites that spread to the brain from a primary malignant tumor. This is a common complication which occurs in 20ï 40% of all cancer patients, often originating from lung, breast, melanoma, renal cell, and colo-rectal cancers. Accurate segmentation of the diseased regions on contrast enhanced MRI (T1c) is necessary for Stereotactic Radiosurgery treatment planning and longitudinal studies aiming to assess disease progression. In this study we implemented a convolutional neural network (CNN) for automated segmentation of brain metastases.

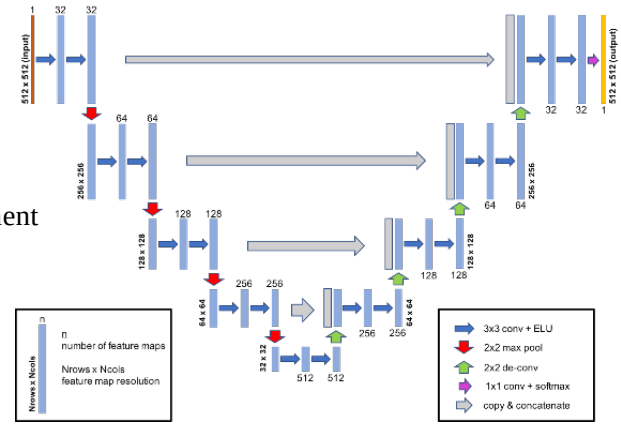

Figure 1. U-NET architecture.

Methods. The CNN model was trained and validated on 133 skull-stripped T1c axial FSPGR brain scans via 5-fold cross validation. Ground truth consisted of researcher annotated binary masks encompassing the tumor borders as they appear on T1c scans. The CNN architecture was based on U-NET [1], which is commonly used for medical image segmentation. This model architecture has the advantage of learning more global features by taking whole axial slices as input compared to traditional patch based CNNs. Its skip connections (figure 1) allow for local image features to be maintained throughout the network. The output consists of a probability map which provides the predicted likelihood of each input voxel belonging to the tumor class as opposed to the non-tumor/background class (figure 3 ï b,d). In order to learn basic features relevant for segmentation without overfitting to the primary training data we implemented transfer learning by pre-training on the open source BraTS 2015 [2] dataset followed by fine tuning on our brain metastasis data.

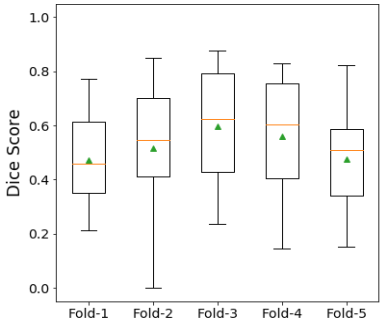

Figure 2. Mean dice score across each fold. Yellow line denotes median, while green triangle denotes the mean.

Results. Average volume-wise segmentation performance across all validation folds shows an average DICE coefficient of 0.52 (0.05 s.d.), and AUC ROC of 0.96 (0.01).

Conclusions. Segmentation performance is comparable to modern state of the art brain metastases segmentation [3] in AUC. The two main sources of error of our method come from noisy ground truth, and under-segmentation of lesions due to class imbalance (figure 3 ï c,d). Future work will address these issues by acquiring expert annotated data, and accounting for the imbalance of tumor to background voxels in the training procedure.

Acknowledgments. We acknowledge the support of the Natural Sciences and Engineering Research Council of Canada (NSERC).

References. [1] Ronneberger, Olaf, Philipp Fischer, and Thomas Brox. "U-net: Convolutional networks for biomedical image segmentation." *International Conference on Medical Image Computing and Computer-Assisted Intervention*. Springer, Cham, 2015. [2] Kistler, Michael, et al. "The virtual skeleton database: an open access repository for biomedical research and collaboration." *Journal of medical Internet research* 15.11 (2013). [3] Liu, Yan, et al. "A deep convolutional neural network-based automatic delineation strategy for multiple brain metastases stereotactic radiosurgery." *PloS one* 12.10 (2017): e0185844.

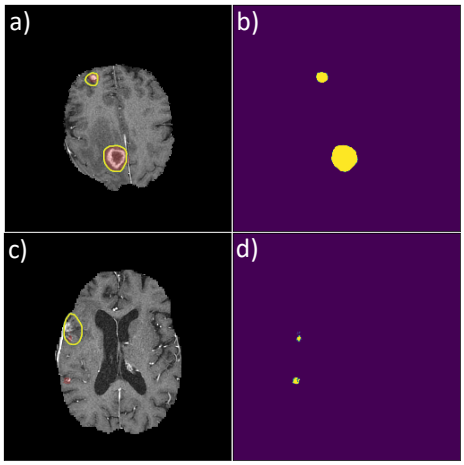

Figure 3. a,c ï T1c axial slice with ground truth annotations (yellow contour), and model prediction (red highlight). b,d ï Predicted probability corresponding to input.
a,b (c,d) image shows a successful (unsuccessful) segmentation corresponding to a DICE score of 0.77 (0.35).

Detecting myocardial hemorrhage with R2* maps

Khalid Abdalla[1,2,3], Jonathan D. Thiessen [1,2,3], Frank S. Prato[1,2,3], R. Terry Thompson[1,2]
Donna E. Goldhawk[1,2,3] and Neil Gelman[1, 2]
[1]Imaging Program, Lawson Health Research Institute, London, ON; [2]Department of Medical Biophysics
& [3]Collaborative Graduate Program in Molecular Imaging, Western University, London, ON

Hemorrhage within the myocardium often occurs following myocardial infarction (MI). The specificity of MRI for detecting hemorrhage has been validated in experimental studies[1]. Visualization of hemorrhage is possible because of the degradation of erythrocytes which leads to iron deposition that can be detected by T2*-weighted magnetic resonance (MR) images[2], and quantitatively assessed by image based measurements of R2* (1/T2*). In this study, we aimed to follow R2*-based measures post MI to determine if we can detect changes in these measures possibly associated with the evolution of acute hemorrhage to chronic iron deposition.

Methods: Analysis was performed on canine images (n=4) acquired at baseline (0 day) and several time points (3 to 43 days) post MI following experimentally induced MI[3]. The images consisted of 10 to 13 short-axis slices (slice thickness=6mm) covering the whole left ventricle (LV) obtained with a multi-gradient echo (eight echo times (TE) covering 3-23 ms). For baseline experiments only single slice images (two-chamber) were available. The images were processed to generate R2* (1/T2*) maps by applying exponential curve fitting to the signal on a pixel by pixel basis. The endocardial and epicardial borders were manually drawn on the shortest echo time image of each slice, and then applied to the R2* maps. For the post MI images, we determined the volume of tissue, relative to the LV volume, with R2* greater than the 99th percentile R2* value of the baseline image for that animal. This measure will be referred to as the percentage of LV volume with high R2* (%LVHR2*). We also determined the mean values of R2* for these abnormal R2* regions (Figure2).

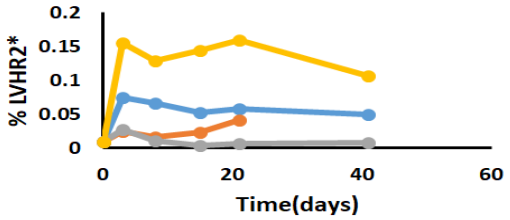

Figure 1. Temporal evolution of the extent of (%LVHR2*) over time post MI.

Results and Discussion: The plots of %LVHR2* (Fig. 1) show a high degree of variability between animals. These volumes may represent an approximation of the volumes of hemorrhage and/or chronic iron containing regions. For the two animals with the largest abnormal R2* regions (yellow and blue lines), the %LVHR2* do not return to baseline by day 43 post MI. However, in one case (gray line) of a small %LVHR2* there may be a return close to baseline. The mean values of R2* within the abnormal R2* regions (Fig. 2) seem to be relatively stable with time following MI, suggesting that any changes reflecting the evolution of acute hemorrhage to chronic iron may be difficult to detect with R2* mapping. Future work should involve assessing the post MI evolution of other relaxation parameters, such as T1.

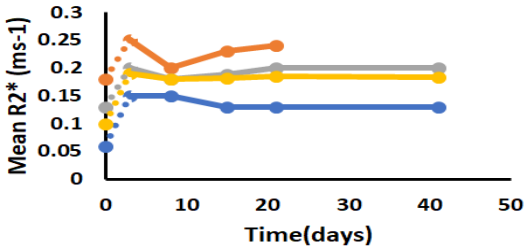

Figure 2. The mean values curves of abnormal regions over time post MI with respect to the mean values of entire LV at baseline (0 day).

Conclusion: Detecting the evolution of acute hemorrhage to chronic iron may be difficult with R2*

Reference. [1] Payne *et al.* Cardiovasc. Imaging 4, 738ï 745 (2011). [2] Ghugre *et al.* Magn.Reson. Med.70, 1095-1105(2013). [3] Prato *et al*. J Nucl Med 56: 299-304 (2015)

Effect of Reduced Contrast Agent on Kinetic Analysis of early stage breast cancer patients

Matthew Mouawad*, Heather Biernaski, Muriel Brackstone, Michael Lock, Anat Kornecki, Olga Shmuilovich, Ilanit Ben Nachum, George Hajdok, Frank S. Prato, R. Terry Thompson, Stewart Gaede, Neil Gelman
Western University, Lawson Health Research Institute, London Health Sciences Center

Introduction: Dynamic contrast enhanced (DCE) MRI is a widely applied technique that uses delivery of a contrast agent (CA) to investigate microvasculature function in disease sites such as cancer. However, recent studies have found residual signal intensity in brain and bone associated with gadolinium deposition for linear agents, as well as measurable quantities of gadolinium CA in post-mortum studies of patients who received either linear or macrocyclic CAs ï long after a patient underwent their contrast enhanced MRI (Gulani *et al.,* Lancet Neurol, 2017). While no pathological risks have been identified, it is prudent to reduce the exposure of CA to patients as much as possible, especially in the context of research studies that may have no inherent benefit to the patient. One possible method to reduce the risk would be to reduce the dose of CA used. As such, the objective of this study is to determine the effect of a reduced dose of gadolinium based contrast agent on kinetic modelling in early stage breast cancer patients.

Methods: DCE-MRI breast images were acquired on a 3T-PET/MRI system (Siemens Biograph mMR) in 22 patients as part of the SIGNAL trial being conducted at the London Regional Cancer Program [Guidolin *et al.* J Radiat Oncol, 2015]. Three-Dimensional fat suppressed fast low angle shot (FLASH) images were acquired (spatial/time resolution of 1.0x2.1x1.2mm/18s) which included one pre- and 28 post-contrast images. Thirteen patients received the full clinical dose (0.1 mMol/kg) of Gadovist with an injection time of 3.5s. Following the findings mentioned above, the next nine patients enrolled in the SIGNAL trial received half the clinical dose (0.05 mMol/kg) with an injection time of 4.76s. Motion was corrected using deformable registration [Mouawad *et al. ISMRM* 2017]. Otsuôs segmentation method was used to segment the tumour and the Tofts kinetic model was applied, voxel-by-voxel, to the segmented volume using a population derived AIF (parker *et al*. 2007). Three of the constants (A1, A2, alpha) in the AIF were reduced by a factor of two to account for the reduced concentration. The root-mean-square-error (RMSE) about the fitted curve normalized by the maximum concentration, best-fit values, and relative uncertainty (standard error divided by parameter value - $\mathring{u}K^{trans}$, $\mathring{u}k_{ep}$) of the model parameters (K^{trans}, k_{ep}) were extracted. The median and 90th percentile were calculated from the parametric maps. From experience, k_{ep} is difficult to estimate for ñpersistent wash-inò kinetic curves. As such, the signal enhancement ratio was used to exclude voxels that were continuously enhancing when evaluating k_{ep} and $\mathring{u}k_{ep}$ (Wu *et al.,* SPIE Medical Imaging, 2015). The median and 90th percentile were compared using a two-tailed unpaired t-test.

Results: Table 1 shows a summary of the statistical analysis where bolded values indicate significance between the full versus half CA dose. Between the two groups, there was a significant increase in the relative uncertainty value for both K^{trans} and k_{ep} when using half the dose i.e., greater uncertainty in the recovered estimates. There was also a significant increase in the normalized RMSE indicating higher variability of data points around the fit. There was no significant difference in the median or 90th percentile of K^{trans} or k_{ep}.

Conclusion: Reducing contrast dose increased the uncertainty in fit parameters, especially for $k_{ep,}$ in which case the increase was quite large, particularly for some voxels. It is important to reduce the exposure of contrast to patients, but care should be taken to ensure it does not affect analysis. Further work is needed to see what other aspects DCE-MRI analysis are affected by using a reduced dose.

	Median		90th Percentile	
	Full	Half	Full	Half
K^{trans} (min $^{-1}$)	0.072 Ñ0.032	0.052 Ñ0.018	0.13 Ñ0.054	0.10 Ñ0.041
$\mathring{u}K^{trans}$ (%)	**4.8 Ñ1.5**	**10 Ñ6.6**	**7.4 Ñ3.4**	**20 Ñ15**
K_{ep} (min^{-1})	0.17 Ñ0.070	0.12 Ñ0.058	0.31 Ñ0.13	0.24 Ñ0.12
$\mathring{u}k_{ep}$ (%)	**8.5 Ñ2.6**	**21 Ñ13**	**14 Ñ5.7**	**55 Ñ59**
Norm RMSE (%)	**7.4 Ñ1.8**	**12 Ñ6.1**	**10 Ñ2.4**	**18 Ñ2.9**

Table 1 ï Summary of statistical analysis comparing parameters extracted from the kinetic fit for patients who received the full versus half the clinical CA dose. Values represent the mean Ñ standard deviation and bolded values represent significance.

A Framework for Reproducible Evaluation of Geometric Inhomogeneity in Magnetic Resonance Images

Patrick J. Park[a], Terry M. Peters[a,b], Ali R. Khan[a,b,c,d], Jonathan C. Lau[a,d]

[a]Robarts Research Institute, [b]Department of Medical Biophysics, Schulich School of Medicine and Dentistry, [c]Brain and Mind Institute London, Ontario, Canada, [d]Co-senior authors: contributed equally to the supervision of this study

Introduction: Geometric inhomogeneity in magnetic resonance images (MRI) results from scanner and patient-specific factors that affect the anatomical accuracy of image acquisitions. These inherent spatial uncertainties should be accounted for in neuroimaging studies and clinical applications like stereotactic neurosurgery. We recently described a workflow for characterizing geometric distortion in ultra-high field (>= 7 Tesla (T)) MRI, permitting the identification of regions of both increased susceptibility and gradient distortion[1]. However, these findings were scanner and acquisition dependent and thus not generalizable to other sites or scanners. There remains a lack of standardization regarding the processing steps necessary to produce geometrically optimal MR images. One solution is to use standard physical phantoms; however, these fail to account for subject-specific factors. Here, we have implemented our framework using an open, extensible format[2] to facilitate morphometric evaluations between images. To illustrate the utility of this workflow, we quantify the impact of vendor-provided gradient distortion correction on a prospective series of 7T images.

Methods: The framework begins by converting DICOM data into BIDS format[3]. The dataset consists of raw and vendor-corrected 7T T1w scans for 28 normal healthy controls (MP2RAGE sequence: TE=2.73 ms, TR=6000ms, TI=800ms/2700ms, flip=4/5o, PAT=3, resolution=0.7mm3). The vendor-provided method uses an in-slice (2D) gradient inhomogeneity correction method to produce a more anatomically accurate image. The deformable registration algorithm requires reference and floating images from each subject as input. In the registration steps, the reference image and floating image are iteratively aligned using the NiftyReg linear and nonlinear registration algorithms[4]. The distortion between corresponding points in these images are calculated as the per-voxel Euclidean distance derived from the deformation field. An ROI analysis was conducted on the final displacement maps resampled to 1 mm using a cortical/subcortical[5] and cerebellar atlas[6]. The nonparametric Wilcoxon rank sum test was used to evaluate the null hypothesis of no geometric distortion more than one voxel (0.7 mm) using a false discovery rate of 5%[7]. Statistical analysis was performed using R.

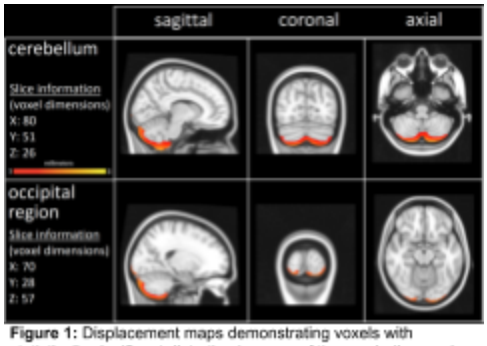

Figure 1: Displacement maps demonstrating voxels with statistically significant distortion in areas of the cerebellum and occipital cortex (FDR *q*-value < 0.05)

Results: ROI analysis failed to reveal any significant regions of distortion in the cortical/subcortical regions or cerebellum proper. Using a more detailed cerebellar ROI atlas revealed statistically significant displacements in specific lobules (bilateral II, VII, VIII, and IX) also visible on voxel-wise analysis (Figure 1; top row). Distortions were highest in lobule VIIIb at 1.03 +/- 0.39 mm and 1.15 +/- 0.58 mm on the left and right sides respectively. Subtle areas of increased distortions were also observed at the inferior cortical surface of the occipital lobes not identified using ROI analysis (Figure 1; bottom row).

Conclusions: We present a software framework for evaluating geometric inhomogeneity in MRI that can be easily deployed on different datasets including human and MRI phantom data[8]. Given two sets of images from the same subject, the framework is capable of capturing subtle regions of distortion on the scale of a single voxel in size. Future work includes integration with preprocessing steps such as image quality control, and validation of different MRI sequences, deformable registration methods, and correction algorithms. This framework will enable robust inter-site morphometric evaluation on both the individual and group levels in an open and reproducible software environment.

References:

[1]Lau, JC et al. NeuroImage. 2017.
[2]Gorgolewski KJ et al. Front. Neuroinform, 2011.
[3]Gorgolewski KJ et al. Sci. Data, 2016.
[4]Genovese CR et al., Neuroimage, 2002.
[5]Desikan RS et al., Neuroimage, 2006.
[6]Diedrichsen J et al., Neuroimage, 2009.
[7]Genovese CR et al., Neuroimage, 2002.
[8]Fonov VS et al., Lect. Notes Comput. Sci., 2010.

Investigating quantitative and structural differences in short association, U-shaped fibres in temporal lobe epilepsy

Jason Kai[1], Loxlan W. Kasa[2], Terry M. Peters[1,2,3], Ali R. Khan[1,2,3]

[1]Dept. of Medical Biophysics, [2]Biomedical Engineering Program, and [3]Robarts Research Institute, Western University, London, Ontario, Canada

Introduction: The brain can be considered a network, comprising of many regions interacting and communicating via white matter fibres[1]. Abnormalities to regions or fibres[1,2] can lead to network disorders, such as epilepsy which is associated with multiple seizures. Other groups have studied these pathological changes at both the microscopic scale (histology) and macroscopic scale (structural and functional networks). Despite this, little is known about short association, u-shaped fibres, joining adjacent brain regions (local connectivity)[3] which have exhibited lesser fibre counts in epilepsy[4]. Diffusion MRI (dMRI) is one technique capable of providing data to model and group white matter fibres via tractography and clustering techniques to identify structural pathways (tracts). We hypothesize that short association tracts would exhibit quantitative MRI characteristics that differentiate local pathways in patients with epilepsy from healthy individuals.

Methods: We acquired dMRI data from healthy individuals (N=20) and patients diagnosed with temporal lobe epilepsy (N=19) on a 3T Siemens Prisma MRI. The data was acquired with a multiband echo-planar sequence (2mm resolution, b-value=1300, 2600 s/mm^2, 140 diffusion-encoding directions, acquired with alternating phase encoding directions). Whole-brain tractography was performed using MRTrix[5] following data processing to correct for image distortion. An algorithm was implemented into our tractography tool to identify candidate U-shaped fibres (figure 2). Quantitative diffusion measurements and fibre geometry metrics were computed. Comparison of computed measurements between control and patient groups were performed for each identified tract using two-tailed t-tests, corrected for false discovery rates (example in figure 3).

Results: Candidate U-shaped fibres were identified and extracted using the implemented filter. Comparisons of quantitative diffusion measurements in identified pathways did not find significant differences between control and patients with epilepsy. Similar comparisons performed for geometric measures also failed to identify significant differences.

Conclusion: The ability to identify pathways can reaffirm connections of coupled brain regions and help explain activity in functional networks. While no significant differences were found for quantitative diffusion data or geometric structure of U-shaped fibres in this preliminary investigation of individual tracts, differences may be present at the network level. Future work includes investigating differences in specific classifications of epilepsy (e.g. left vs right temporal lobe epilepsy) and probing local connectivity at a network level.

References: [1] Kramer and Cash, 2002. [2] Liu and Zhou, 2013. [3] Nieuwenhuys, 1978 [4] OôHalloran, 2017. [5] Tournier et al, 2012.

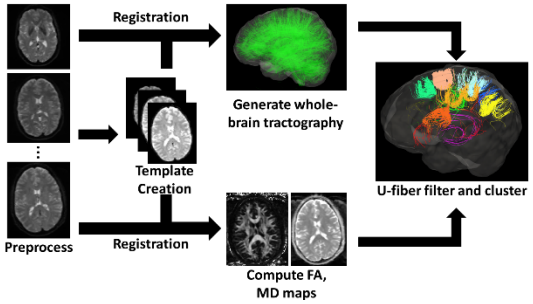

Figure 1: Short association fibre investigation workflow.

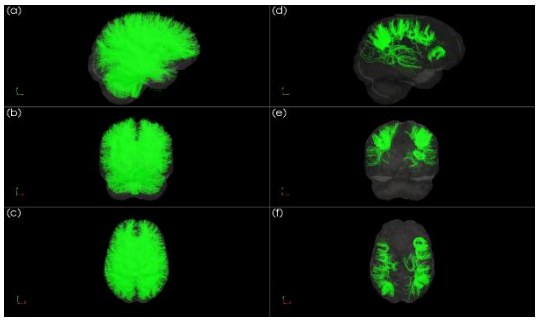

Figure 2: View before (a)-(c) and after (d)-(f) application of U-shaped fibre filter.

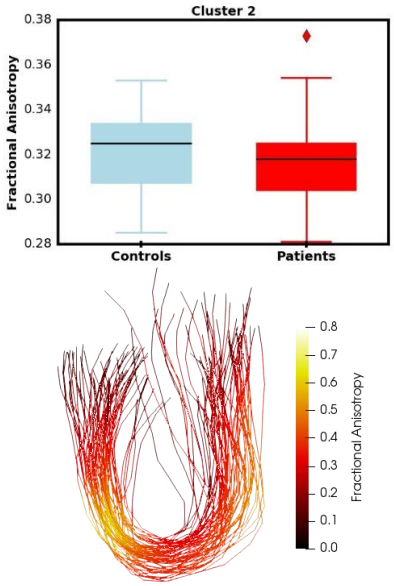

Figure 3: Example comparison for identified cluster (top) of fractional anisotropy (FA), a quantitative dMRI metric, and corresponding extraction with FA overlay (bottom)

Poster Presentation Abstracts

Session 3: Bone and Joint Imaging

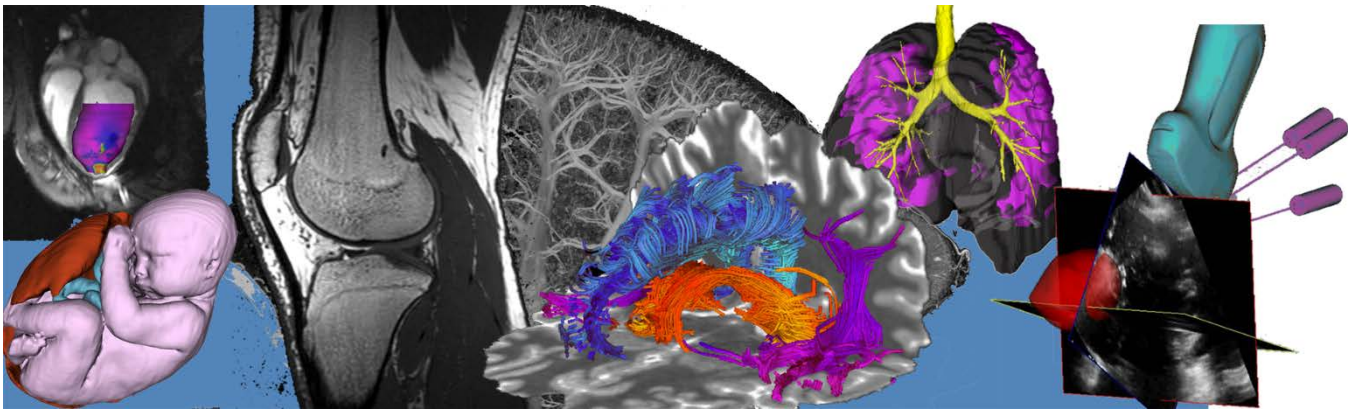

Tomographic and Histological Analyses of Ectopic Calcification Associated with Diffuse Idiopathic Skeletal Hyperostosis (DISH)

Dale E. Fournier[1], Chris J. D. Norley[2], Steven I. Pollmann[2], Ryan J. Beach[3], Christopher S. Bailey[4], Katherine E. Willmore[1], David W. Holdsworth[2,4], S. Jeffrey Dixon[3], and Cheryle A. Séguin[3]

[1]Anatomy and Cell Biology, [2]Robarts Imaging Research Laboratories, [3]Physiology and Pharmacology, [4]Surgery; Schulich School of Medicine & Dentistry, Bone and Joint Institute, The University of Western Ontario

Introduction: Diffuse idiopathic skeletal hyperostosis (DISH) is a non-inflammatory spondyloarthropathy characterized by ectopic calcification of spinal ligaments and intervertebral discs (IVDs). The diagnosis of DISH is based on Resnickôs radiographic criteria: i) flowing calcifications along at least four contiguous vertebral bodies; ii) preservation of IVD height; and iii) absence of bony ankylosis within facets and sacroiliac joints (vs. *ankylosis spondylitis*). The estimated prevalence of DISH is 15-25% in North Americans over the age of 50 years with a predominance in males (2:1). Despite this prevalence, the pathophysiology of DISH is poorly understood and there are no disease-modifying treatments. The present study aimed to characterize the pathological features associated with ectopic calcification in human spine tissues that met the radiographic criteria for DISH.

Materials and Methods: A cohort of 19 embalmed cadavers (6 females, 13 males; mean age 81 years, range 65-94) were accessed from the HEART Lab at Western University, in accordance with the Anatomy Act of Ontario and Westernôs Committee for Cadaveric Use in Research. Intact vertebral columns (cervical to thoracic) were dissected and scanned by micro-computed tomography (ÕCT, eXplore Ultra, GE Medical) with 154 Õm isotropic voxel spacing. Imaging outputs were generated to: i) identify DISH using the current radiographic criteria; and ii) characterize ectopic calcification in these specimens. Histological and physical analyses were used to elucidate the tissue-specific changes associated with DISH.

Results: Ten specimens (53%: 3 females, 7 males; mean age 81 years, range 72-94) met the radiographic criteria for DISH. Analyses of spines associated with DISH identified remarkable heterogeneity in the presentation of ectopic calcification falling into three broad categories: i) incomplete-patchy calcifications; ii) continuous vertical bands resembling cortical bone (bridging angle >90Ü; and iii) large horizontal prominences of cortical and trabecular bone associated with IVDs (bridging angle <90Ü [**Figure 1**]. Each presentation was differentiated by the relative volume of ectopic calcification (contoured as: i) anterior to the IVD, and ii) superior-inferior by the subchondral vertebral bone) and the internal lesion composition (calcified tissue = 400-2750 ADU). Interestingly, discrete regions of hypercalcified tissue exceeding normal cortical bone (i.e., >2750 ADU) were identified within lesions (~1% of lesion volume). Analysis of calcified material by EDX showed high levels of calcium and phosphorus in a ratio of ~1.5, slightly less than the stoichiometric ratio for hydroxyapatite. Histological examination of DISH specimens revealed features of both mature trabecular bone (outermost tissue) and irregular amorphous calcified material (within the annulus fibrosis of IVDs).

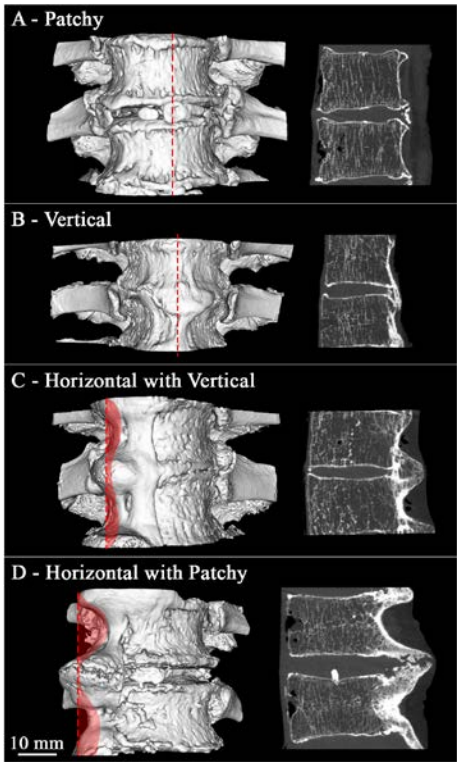

Figure 1. The categorizations of DISH positive spines. Each presentation is displayed as a 3-dimensional isosurfaced rendering (left) with a representative sagittal/oblique ÕCT section (right) denoted by red dotted line. (**A**) Patchy calcifications, T8-9 from a 72 year-old male; (**B**) continuous vertical bands of calcification, T3-4 from an 87 year-old male; (**C, D**) horizontal outgrowths in conjunction with patchy and vertical, T7-8 from a 78 year-old male and T10-11 from an 86 year-old male, respectively.

Discussion and Significance: The current radiographic criteria for DISH appear to capture a heterogeneous subset of features associated with ectopic spine calcification. In this study, ÕCT imaging allowed for the identification of spinal tissues affected by DISH, as well as the quantification of features of ectopic calcification. Moreover, physical and histological analysis of affected tissues contributes to the characterization of ectopic calcification. It is currently unknown whether DISH is naturally heterogenous with numerous presentations, or if the variability captured in this study reflects different stages of disease progression or pathological processes distinct from DISH.

Recent reports have highlighted the need for improved diagnostic criteria for DISH to include early detection. Thus, findings from this study will contribute to better classifying ectopic spinal calcifications as well as understanding their pathology.

Ultrasound-based vertebral landmark localization using deformable spine models

Zachary Baum[1], T. Ungi[1], A. Lasso[1], B. Church[1], C. Schlenger[2], G. Fichtinger[1]

1. Laboratory for Percutaneous Surgery, Queenôs University, Kingston, Canada
2. Premier Chiropractic, Stockton, California, USA

PURPOSE: Identifying vertebral landmarks in ultrasound (US) is non-trivial. Landmarks may be hidden or difficult to identify in patients with diseased spines [1]. We propose to assist the user in discerning spinal geometry through overlay of a visual aid in the US image space during landmark identification.

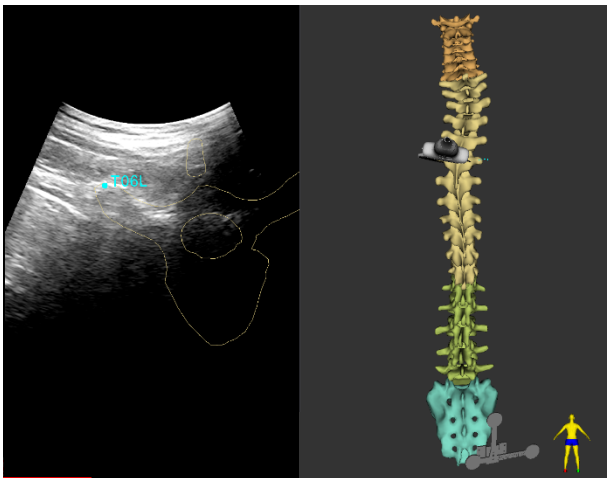

Figure 1. US image with overlay of T6 vertebrae.

METHODS: Users identify several prominent landmarks to create deformably registered generic healthy spine model in the US space with Church *et al.*ôs method [2]. This model is overlaid on the images to provide visual aid to the operator for remaining landmarks (Fig. 1). With each identified landmark, the registration is re-computed. A tracked US system was developed using the open-source 3D Slicer application platform and the PLUS toolkit [3, 4] (Fig. 2). Six operators identified vertebral landmarks using US images, and using visualizations and US images. A one tailed Studentôs t-Test for independent unpaired samples compared the mean landmark identification rate between all operators. Analysis of time to task completion is also presented. Software usability was assessed through a questionnaire following the study.

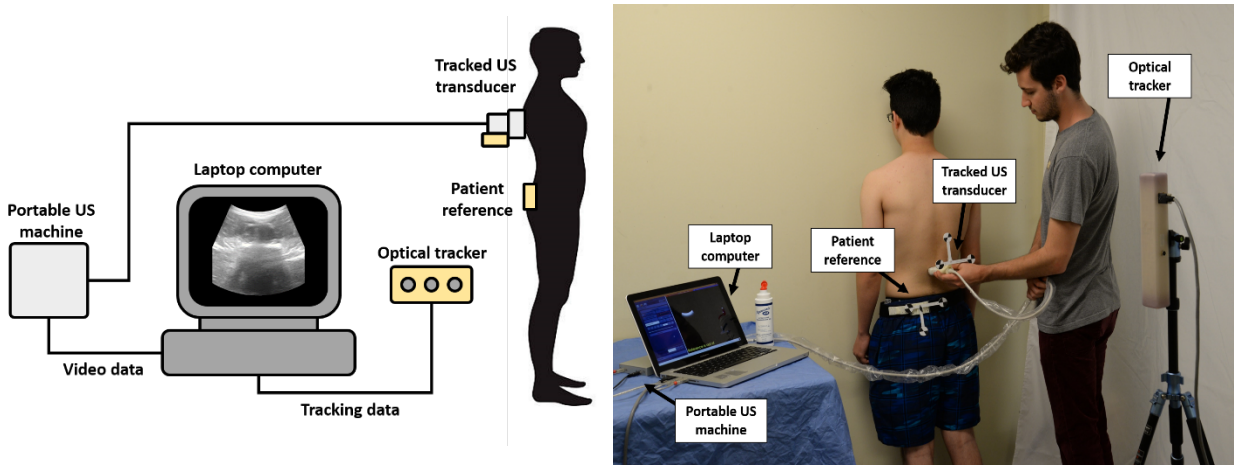

Figure 2. *Left*: Schematic diagram of the tracked US imaging system. *Right*: The tracked US imaging system in use.

RESULTS: The mean landmark identification rate of operators using visualizations and US was significantly higher than US only (82 [72 ï 94] % *vs* 51 [37 ï 67] %, respectively; $p = 0.001$). Additionally, time to completion was higher using visualizations and US than US only (842 [448 ï 1136] s *vs* 612 [434 ï 785] s, respectively; $p = 0.047$). Operators found visualizations helpful in landmark identification, and in visualizing the spine.

CONCLUSION: A three-dimensional visual aid was developed to assist in vertebral landmark identification in a tracked US system by deformably registering and visualizing a healthy spine model in US space. Operators found visual aids useful and they were able to identify significantly more vertebral landmarks than without it.

REFERENCES: [1] Ungi *et al.*, "Spinal curvature measurement by tracked ultrasound snapshots," *Ultrasound in Medicine & Biology*, 2014. [2] Church *et al.*, ñVisualization of scoliotic spine using ultrasound-accessible skeletal landmarks,ò SPIE Medical Imaging, 2017. [3] Kapur *et al.*, "Increasing the Impact of Medical Image Computing using Community-based Open-access Hackathons: The NA-MIC and 3D Slicer Experience," *Medical Image Analysis*, 2016. [4] Lasso *et al.*, "PLUS: open-source toolkit for ultrasound-guided intervention systems," *IEEE Transactions on Biomedical Engineering*, 2014.

Real-time transverse process delineation in tracked ultrasound for scoliosis measurement

Csaba Pinter[1], Bryan Travers[1], Zachary Baum[1], Shahrokh Kamali[2], Tamas Ungi[1], Andras Lasso[1], Ben Church[1] and Gabor Fichtinger[1]

[1] Laboratory for Percutaneous Surgery, Queenôs University, Kingston, ON, [2] Dalhousie University, Halifax, NS

PURPOSE: Ultrasound (US) is a safe, radiation-free imaging modality for visualizing the spine and measuring scoliosis. Poor bone visibility in US, however, poses a major challenge in measurement of spinal curvature. We propose an algorithm and its implementation for real-time automatic delineation of the posterior surface patches.

METHODS: The algorithm operates in the image space, so scan-lines are first converted to a linear image. Pre-processing follows to prepare the image for bone detection using thresholding, Gaussian smoothing, edge detection, island removal, and morphological opening. Potential transverse processes are then marked based on the presence of a shadow; bones cast shadows in US images, so the area on their far side becomes darker (*i.e.* of lower intensity). A subsequent filtering step ensures viable position and size for the detected patches. Further shadow analysis follows, which looks for sufficient non-shadow areas to both sides of the potential bony areas. Finally, the image is converted back to its original geometry, which is an essential step in case of curvilinear probes. The algorithm was developed as part of the PLUS toolkit [1]. All image processing and analysis parameters used can be changed in the PLUS configuration file.

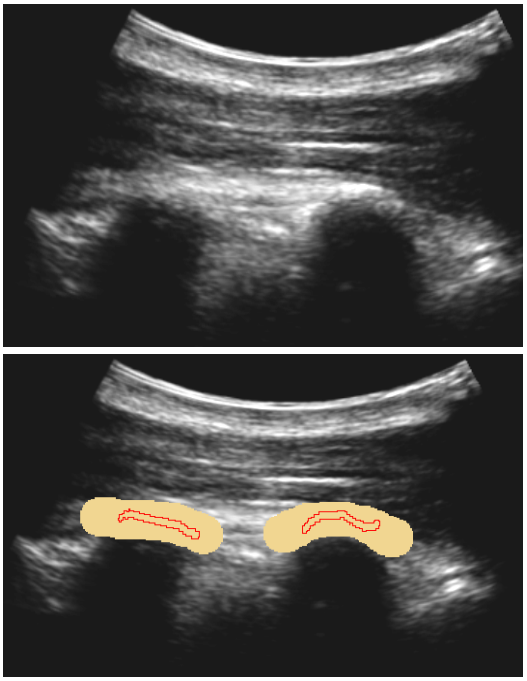

Fig. 1. Top: Frame produced by a SonixTouch US machine (Analogic Corp., Peabody, MA, USA) using an Ultrasonix C5-2 probe. Bottom: Output (red) compared to ground truth with added tolerance margin

Utilizing the pose data from a 3D trakSTAR (NDI, Waterloo, ON, Canada) electromagnetic tracker also acquired with the scan, a 3D volume is reconstructed from the output. By matching the reconstruction to a spine model using deformable registration, a qualitatively accurate patient-specific spine visualization can be achieved, allowing for accurate measurement of the curvature.

RESULTS: An expert provided manual segmentation of the posterior surface of the transverse processes in four US sweeps in two steps: ground truth regions that definitely contained bone, and tolerance margins encompassing possible accepted regions as well. Accuracy was evaluated by comparing the output to the two marked regions (Fig. 1). The mean of the average Hausdorff distance between tolerance margin and output was 5.13mm, with mean false positive ratio of 0.19%. Same metrics for the ground truth segmentation was 3.02mm and 1.22%, respectively. Each frame took on average 0.016s to process, yielding 62 frames per second. Future plans include enhancing the edge detection step and thorough evaluation of the method against CT data.

Fig. 2. Left: Reconstructed output bone patches. Right: Registered to spine model.

CONCLUSION: An algorithm has been presented for automatic detection of transverse processes in tracked US images. The result can be reconstructed in 3D and matched to a spine model by deformable registration. Both detection and reconstruction happen real-time, allowing the sonographer to improve results by returning to inadequately processed regions. The proposed method aims to facilitate quantitative spine curvature measurement under ultrasound modality.

REFERENCES: [1] Lasso, A., Heffter, T., Rankin, A., Pinter, C., Ungi, T., & Fichtinger, G. (2014). PLUS: open-source toolkit for ultrasound-guided intervention systems. *IEEE Transactions on Biomedical Engineering*, *61*(10), 2527-2537.

Quantifying Femoral- and Tibial-Subchondral Bone and Microvessel Changes in Rats with Surgically-Induced Osteoarthritis using Dual-Energy Micro-Computed Tomography

Justin J Tse,[1,3] Vasek Pitelka,[2] Joy Dunmore-Buyze,[1,3] Maria Drangova,[1,3] and David W Holdsworth[1,3,4]
[1]Robarts Research Institute, [2]Department of Physiology and Pharmacology, [3]Department of Medical Biophysics, [4]Department of Surgery
Western University, London, Ontario, Canada

Introduction: Osteoarthritis (OA), characterized by the degeneration of bone and cartilage, has been hypothesized to result from changes in the jointsô microvascular environment (*i.e.* negative impact on nutrient and oxygen flow). Cartilage, an avascular tissue, receives its nutrition from the highly-vascularized neighbouring synovium; however, the nutritional supply from the underlying subchondral bone microvessels is not well-understood. The study of these microvessels has been difficult due to their (1) small size (*i.e.* < 10 Õm, capillaries), (2) lack of contrast against surrounding tissues, and (3) proximity to dense bone. Combining an *ex vivo* Er-based vascular perfusion contrast agent[1] and optimized dual-energy micro-CT (DECT)[2] with a surgically-induced rat hindlimb model of OA, we investigated the vascularized bony regions underlying the cartilage of the knee joint (*i.e.* distal femoral epiphysis and proximal tibial epiphysis) during the initiation and progression of OA.

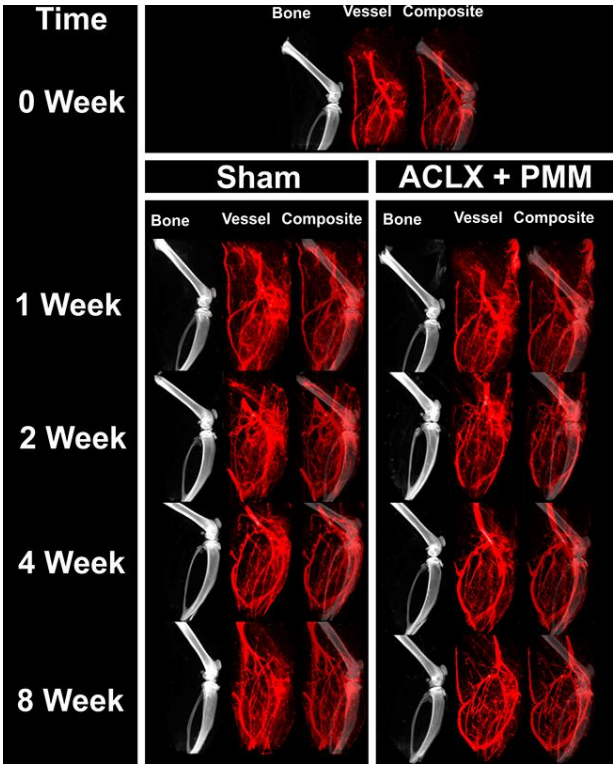

Figure 1. DECT-decomposition of representative hindlimbs from both surgery groups and each experimental time-point.

Methods: Sprague Dawley rats (N=54) were separated into sham and surgery-induced OA (*i.e.* anterior cruciate ligament transection (ACLX) and partial medial meniscectomy (PMM)) groups. Rats were further divided into time-points (*i.e.* 0 (pre-surgery), 1, 2, 4, and 8-weeks post-surgery). Surgeries were performed on the right (ipsilateral) hindlimb, allowing the left (contralateral) hindlimb to serve as an internal control. At each end-point, rats were perfused with an Er-based contrast agent, DECT-scanned, and decomposed into individually segmented and quantitative volumes of soft tissue, bone, and microvessels. Means values from custom volumes-of-interests of the distal femoral and proximal tibial epiphysis from each hindlimb were recorded from each decomposed volume. Statistical analysis was performed, and significance was achieved if $p < 0.05$.

Results: Quantitative results from the successful DECT decompositions of perfused rat hindlimbs (Fig. 1) revealed a significant increase ($p = 0.0472$) in microvessel density 1-week post-operatively within the tibia of the operated ACLX + PMM hindlimb when compared to the non-operated hindlimb. No further significant microvessel differences were observed for the remaining time-points. Additionally, no significant differences ($p > 0.05$) in soft tissue or bone, between the ipsilateral and contralateral hindlimb within either surgery group (*i.e.* sham or ACLX + PMM) were observed at any time-point.

Discussion: The 1-week post-operative vascularity increase is most likely due to an inflammatory response to the ACLX + PMM surgery; as 2-weeks post-operatively the microvascular density returned to baseline levels. Using a combination of an Er-based contrast agent, DECT, and ACLX + PMM model of OA, we visually segmented and quantified the soft tissue, subchondral bone, and microvessels within the distal femoral epiphysis and proximal tibial epiphysis. The ability to automatically segment various tissues is not limited to OA and could facilitate the study a variety of other vascular-related disease (*i.e.* musculoskeletal, cardiac, neurological, and oncological).

References: **1**. J. J. Tse, P. J. Dunmore-Buyze, M. Drangova, D. W. Holdsworth, Erbium-Based Perfusion Contrast Agent for Small-Animal Microvessel Imaging. *Contrast Media & Molecular Imaging* **2017**, 10 (2017). **2** J. J. Tse, J. Dunmore-Buyze, M. Drangova, D. W. Holdsworth, Dual-Energy Computed Tomography for a Gantry-Based Pre-Clinical Cone Beam Micro-CT Scanner. *SPIE Medical Imaging* **Submitted**, (2017).

Micro-CT of Developing and Aging Mice: Measurement of Wholebody and Long Bone Lengths

Joseph U. Umoh[1], P. Moon[2], M. Sun[2], K. Tyml[2], E. Tutunea-Fatan[3], R. Gros[3], M. Drangova[1,3,4], F. Beier[2], and D.W. Holdsworth[1,3,4,5]

Development of Novel Therapies for Bone and Joint Diseases Consortium

[1]Preclinical Imaging Research Centre, Robarts Research Institute, [2]Dept. of Physiology and Pharmacology,[3]Robarts Research Institute, [4]Depts. of Medical Biophysics and [5]Surgery, Western University, London, ON, Canada

Introduction: Mice have been extensively utilized to study skeletal development and model diseases affecting skeletal growth such as achondroplasia[1]. Bone length has been measured using different methods, including calipers, and micro-computed tomography (micro-CT) images; the latter method had been shown to be more accurate[2]. The measurement of the mouse bone lengths has been done at different time points of the mouse age[3]. The objectives of this study are to measure mouse bone lengths during the life span of a typical normal mouse, and to establish an empirical relationship among them.

Methods: Forty-one male C57BL/6J mice were used in this study. Micro-CT imaging was used to acquire wholebody image data of the mice. Only wild-type male mice were used because this study focuses on describing the changes in normal male mice as they age. The animals were imaged at age 0.5, 1.5, 3, 6, 8, 12, 18, 22, and 24 months. The number of mice used at those time points was 5, 5, 5, 5, 3, 5, 3, 5, and 5 respectively. All animals were imaged on the same micro-CT scanner (GE Locus Ultra), with the same scan protocol (x-ray tube voltage 80 kV, tube current 55 mA, 1000 projections, exposure time 16 s) and the same reconstruction parameters (154 Õm 3D image voxels). To measure the length of the bones (wholebody, vertebrae, skull, humerus, femur and tibia), each of the bones was first segmented, re-oriented to lie parallel to the z-axis, then the y-component of the Maximum Intensity Projection (ymip) was taken. The lengths of the long bones were measured in GE MicroView while those of the wholebody, skull and vertebrae were measured using the Point Picker tool in Parallax MicroView.

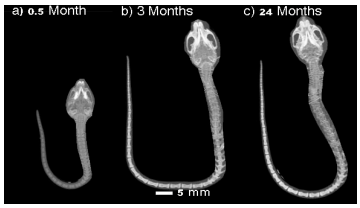

Figure 1: Micro-CT image showing a maximum intensity projection rendering of the mouse wholebody-length of (a) a developing, (b) a mature, and (c) an aging mouse.

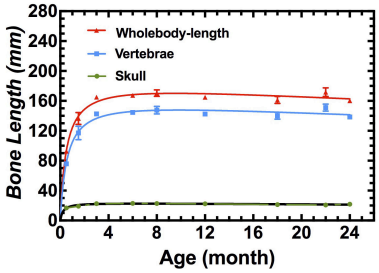

Figure 2: Plots of mean and standard deviation of the mice wholebody-length, vertebrae, and skull with age showing the fitted curve (solid line).

Results: The mouse wholebody-length (WBL) relates with age (Age) as follows: $WBL = K_o\ Age/(K_1 + Age(1+ Age/K_2))$, where $K_0=188.5$, $K_1=0.51$, $K_2 = 175.2$, and $R^2=0.95$. The same functional relationship is obtained for the vertebrae, and $K_0=164.9$, $K_1=0.57$, $K_2=169.5$ (Fig.2). Mouse bones develop rapidly in the first three months. Between age 0.5 month and age 3 month, the growth rates for humerus, femur, and tibia are 1.66, 3.09, and 3.14 mm/month, respectively (Fig. 3). For the vertebrae and wholebody-length, the growth rates are 26.72 and 28.95 mm/month, respectively. The skull has the lowest growth rate of 2.24 mm/month. Between age 3 month and age 24 month, the following relation among the bones is obtained:
Humerus:Femur:Tibia:Skull:Vertebrae:Wholebody=1:1.33:1.50:1.79: 11.69:13.49. Their standard deviations are 0:0.01:0.02:0.06:0.29:0.27, respectively.

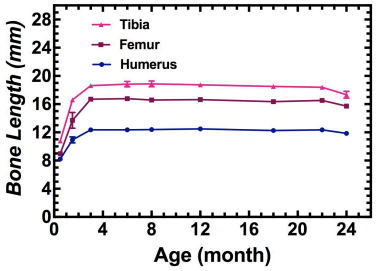

Figure 3: Plots of mean and SD of the mice tibia, femur, and humerus with age.

Conclusions: This study provides accurate measurement and ratios of the length of the axial skeleton (vertebrae and skull), humerus, femur and tibia in male mice during aging. A relationship between bone length and mouse age is established and used to develop an algorithm to approximate wholebody and long bone length as a function of animal age. These data can then be used as a reference of normal skeletal growth during aging while allowing researchers to quickly identify abnormalities in global skeletal development or more subtle differences in limb development of male C57BL/6J mice.

References: [1] Moon *et al. J. Mol. Med* 2015; 93: 845-856. [2] Citardi *et al. Skull Base* 2001; 11: 5-11. [3] Beaucage, *et al.* and Holdsworth, D.W. *Bone Reports* 2016; 70-80.

Arm activity and implant migration analysis following reverse total shoulder arthroplasty

Madeleine Van de Kleut[1,2,5], George S. Athwal[4,5], Xunhua Yuan[1], Matthew G. Teeter[1,3,4,5]
[1]Robarts Research Institute, The University of Western Ontario, London, Canada
[2]Graduate Program in Biomedical Engineering, The University of Western Ontario, London, Canada
Depts. [3]Medical Biophysics and [4]Surgery, The University of Western Ontario, London, Canada
[5]Lawson Health Research Institute, London, Canada

Introduction: Reverse total shoulder arthroplasty (RTSA) is a relatively new surgical procedure for patients with advanced osteoarthritis of the shoulder suffering from pain and reduced joint function, with few studies investigating early migration of implant components. Implant migration on the order of 1 mm or greater within the first two years postoperatively has been associated with implant loosening leading to revision within 5-10 years postoperatively. As early stability is key to long-term success, we seek to identify whether arm activity during early healing influences implant migration. Further, we will determine whether implant fixation ï cemented or cementless ï is a contributing factor to migration. It is hypothesized that cementless stems will migrate more during early healing than their cemented counterparts, but that both will stabilize within the first year postoperatively. On an individual patient level, it is hypothesized that increased arm activity will be associated with greater implant migration.

Methods: Forty patients will be enrolled in this prospective randomized clinical trial. The data from three participants is presented: two cemented and one cementless humeral stem. Patients were imaged using a validated, calibrated dual-source x-ray technique at six weeks (baseline following removal of sling) and at three months to measure implant migration within this six-week period (Fig. 1). At three months, patients also wore a tight-fitting shirt embedded with inertial sensors to measure arm activity in terms of elevation angle (Fig. 2). Frequency of arm elevation above 20 degrees per hour for each patient was compared to their migration data. Preliminary results are presented, with results from 14 patients expected by time of presentation.

Results: Cemented humeral stem migration was measured to be 0.100 and 0.382 mm, with arm elevation frequencies of 164 and 61 motions per hour, respectively. The migration measured for the cementless humeral stem was 0.559 mm, with 205 motions per hour.

Conclusion: Presently, there is not enough data to provide conclusive evidence relating arm activity and humeral stem migration, though it is our expectation that cementless humeral stems will migrate more than their cemented counterparts during this early post-operative phase, and that excessive arm motion may be a contributing factor. Results from this study may provide insight into rehabilitation practices following RTSA.

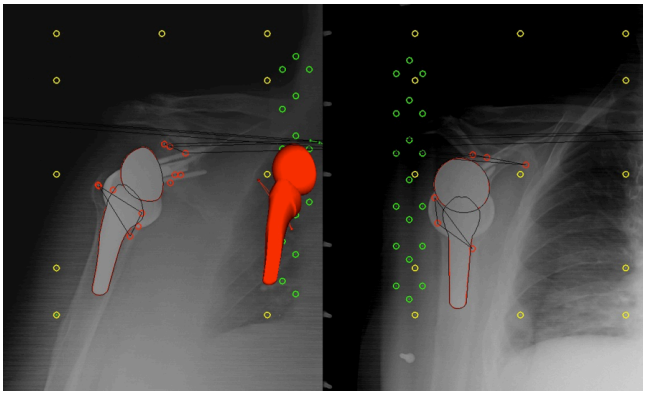

Fig. 1 Stereo x-rays are used to determine implant position and orientation within the bone. Migration is measured between time points.

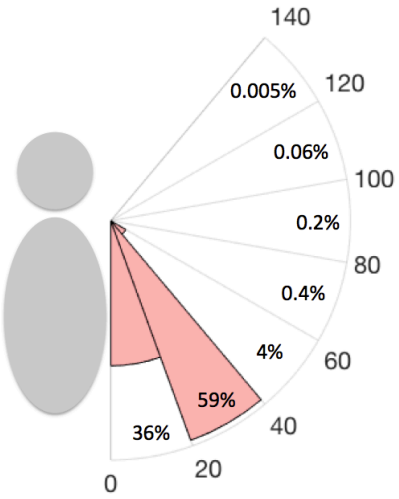

Fig. 2 Example of patient arm elevation angle throughout the day (10h). Though the majority of time is spent with the arm near the side, elevation angles up to 129 degrees were reached on occasion.

Acute qMRI Response of Tibiofemoral Articular Cartilage in Knees at Risk for Osteoarthritis after Challenged Walking

Authors: Atkinson, H.F.[1,2], Birmingham, T.B.[1,2], Moyer, R.F.[2,3], Milner, J.S[4], Thiessen, J.D.[5,6], Thompson, R.T.[5,6], Holdsworth, D.W.[2,4,5] & Giffin, J.R.[1,2]

Development of Novel Therapies for Bone and Joint Diseases Consortium

[1]Wolf Orthopaedic Biomechanics Lab, Western University, [2]Bone & Joint Institute, Western University, [3]Faculty of Health, Dalhousie University, [4]Robarts Research Institute, Western University, [5]Department of Medical Biophysics, Western University, [6]Imaging Program, Lawson Health Research Institute

Introduction: Articular cartilage degeneration is the hallmark of osteoarthritis (OA), and induces aberrant knee joint loading, leading to the functional decline of the joint. Quantitative MRI measures such as T1rho and T2 relaxation time are proposed to be sensitive to acute and long-term changes in knee articular cartilage structures such as collagen and proteoglycan. The purpose of this study is to explore the changes in T1rho and T2 relaxation time immediately following a functional loading stimulus in participants at risk for knee OA.

Methods: Participants include those at risk for knee OA according to the criteria of the Osteoarthritis Initiative Incidence Cohort (frequent knee symptoms, overweight, history of serious knee injury or surgery, family history of knee OA, occupational risk for OA) and/or frequent knee pain with an OARSI joint space narrowing grade of Ò1. Participants undergo a baseline MRI using a 3T Siemens Magnetom Trio magnet, and a 15-channel Siemens PRISMA knee coil. Pulse sequences consist of a 3D Dual-Echo Steady State (DESS) sequence, Sagittal Multi-Echo Spin Echo T2 Mapping sequence, and a 16-shot Gradient Echo T1rho Mapping sequence. Participants are seated for 30 minutes prior to the initial scan to reduce effects of earlier loading on qMRI values. Following the baseline MRI, all participants complete the same standardized loading stimulus, which consists of 25 minutes of challenged walking on an instrumented, dual-belt treadmill capable of moving with six degrees of freedom. During walking, participants are subjected to changes in speed, inclines and declines, lateral sways, and random pre-specified perturbations in the form of rapid belt slips, sagittal plane pitches, and frontal plane sways. Immediately following challenged walking, participants undergo a post-loading MRI with the same sequences as the baseline scan. T1rho and T2 relaxation maps are generated using software developed in-house by fitting image intensities of the T1rho and T2 weighted images pixel-by-pixel to the equation $S(TE) \propto \exp(-TE/T2)$ using a Levenberg-Marquardt mono-exponential fitting algorithm implemented in ITK. Superficial and deep load-bearing regions of medial and lateral articular cartilage of the femur and tibia are manually segmented and analyzed using 3D Slicer software. The reader is blinded to scan order. The individual and group mean T1rho and T2 relaxation times before and after challenged walking were compared using paired t-tests.

Results: Six participants at risk for knee OA have completed the protocol to date. Following loading, T2 relaxation time of the superficial medial tibia, superficial lateral femur, and superficial lateral tibia were all significantly shorter ($p=0.03$) compared to baseline, and T1rho relaxation time of the superficial lateral femur and superficial lateral tibia were significantly shorter ($p=0.04$) compared to baseline.

Conclusions: T1rho and T2 relaxation time shortened in several superficial load-bearing regions after challenged walking, suggesting a decrease in water content in articular cartilage after the functional loading stimulus. These results support the use of the standardized challenging walking test to evoke acute changes in knee articular cartilage.

Magnetic Resonance Imaging to Assess Muscle Quality and Quantity in Patients with Chronic Inflammatory Demyelinating Polyneuropathy

Jacob Fanous[1], Kevin J. Gilmore[2], Kurt Kimpinski[2,3], Charles L. Rice[1,3]

[1]Department of Anatomy and Cell Biology, Schulich School of Medicine and Dentistry, Western University, London, ON, Canada
[2]School of Kinesiology, Faculty of Health Sciences, Western University, London, ON, Canada
[3]Department of Clinical Neurological Sciences, Schulich School of Medicine and Dentistry, Western University, London, ON, Canada

Introduction: Chronic inflammatory demyelinating polyneuropathy (CIDP) is an autoimmune disease characterized primarily by demyelination of peripheral nerves. Patients typically present with symmetrical motor deficits such as diffused muscle weakness, as well as sensory impairments. Studies to date have mainly focused on the neuropathic aspects of CIDP and its involvement in paresis. Impairments in skeletal muscle quality and quantity may be a consequence of motor nerve deficits, but these aspects have not been investigated comprehensively. The purpose of this study was to use magnetic resonance imaging (MRI) to compare anatomical and functional differences in the triceps surae complex between a group with CIDP and a healthy control group.
Methods: To date, five patients with CIDP and five healthy control subjects were matched on anthropomorphic characteristics. Both groups underwent isometric plantar flexion strength measurements on a custom dynamometer. On separate days, MRI (T1 and T2) of the leg musculature was acquired via serial axial plane scans in a 3.0- Tesla magnet. All MRI scans were analyzed using OsiriX imaging processing software. Total muscle volume was computed using the T1 weighted anatomical images with a 3D FLASH sequence: (9.57-ms repetition time (TR); 2.46-ms echo time (TE); 320 x 240 matrix; 243 x 325-mm field of view; 0.9mm slice thickness with slice separation of 1mm ranging from 280 to 400 slices). T2 weighted relaxation times were determined from images with a spin-echo sequence (5.0mm slice thickness; 3500-ms TR; 16 echoes (TE=13.2ms) between 13.2-211.2ms; 10 slices). Both total volume (T1) and relaxation times (T2) were calculated separately for the three components of the triceps surae: soleus, medial gastrocnemius (MG), and lateral gastrocnemius (LG).
Results: Patients with CIDP had ~35% less plantar flexion strength compared with controls. Patients also had significantly smaller total muscle volumes with the soleus being ~23% smaller, the MG ~36% and the LG ~44% smaller when compared with controls. When strength was normalized to total triceps surae volume the strength difference disappeared. Furthermore, the soleus, MG, and LG showed ~39%, ~33%, and ~31% longer T2 relaxation times, respectively.
Conclusion: Patients with CIDP were significantly weaker compared to control subjects. Total muscle volume was significantly reduced pointing to a decrease in muscle quantity. Additionally, the significantly increased T2 relaxation times may reflect an increase in intramuscular fat infiltration in the group with CIDP. This suggests that the patients have lower intrinsic muscle quality which may reflect the decrease in strength. These results further support the utilization of MRI as a tool for muscle analysis and provide a better understanding of the impact of neuronal changes in CIDP on muscular characteristics.

Supported by NSERC

An Image-Based 3D Metal-Printed Implant System for a Small Animal Model of Partial Hip Replacement

Adam. D.M. Paish[1,2], Hristo N. Nikolov[1,2], Tomasz Chmiel[3], Alexander O. El Warrak[2], Ian D. Welch[4], Matthew G. Teeter[1,2,5], Douglas D. Naudie[2,5], David W. Holdsworth[1,2,5]
[1]*Robarts Research Institute, London, ON,* [2]*Western University, London, ON,* [3]*ADEISS Canada, London, ON*
[4]*University of British Columbia, Vancouver, BC,* [5]*London Health Sciences Centre, London, ON*

Introduction: As new innovations are developed to improve the longevity of joint replacement components, preclinical testing is necessary in the early stages of research into areas such as osseointegration, metal-cartilage wear and infection. Large-animal studies that test load-bearing components are expensive though, requiring that animals be housed in special facilities, not available at all institutions. Comparably, a small animal model, such as the rat, has several advantages, namely lower cost. However, load-bearing implants are difficult to manufacture via traditional methods in the sizes required for small-animal testing. Fortunately this barrier can be overcome due to recent advances in additive manufacturing (3D metal-printing). Thus, our objective is to create and optimize an image-based 3D-printed rat hip hemi-arthroplasty system that will allow *in vivo* testing of functional implant properties in a rat model.

Methods: A database of n=25 previously-acquired, 154Õm micro-CT volumes (*eXplore Locus Ultra*, GE Medical) of male Sprague-Dawley rats (390-610g) were analyzed to obtain spatial and angular relationships between several anatomical features of the proximal rat femora. Mean measurements were used to guide the creation a femoral implant template in computer-aided design software (*Solidworks*, Dassault Systemes). Several different variations were created, including collared and collarless designs, in a range of sizes to accommodate rats of various weights. Initial prototypes were 3D-printed 316L stainless steel with subsequent iterations printed in Ti6Al4V titanium and F75 cobalt-chrome (*AM 125, AM 400*, Renishaw plc). Implants were post-processed via sandblasting, hand-polishing (ball), ultrasonic bath, and sterilization in an autoclave. Innate surface texturing was left on stems to promote osseointegration. Surgical implantation was performed in n=3 live Sprague-Dawley rats (900g, 500g, 750g) with preservation muscle attachments to the greater trochanter. Micro-CT imaging and X-ray fluoroscopy were performed post-operatively on each animal to and at 3, 6, 9 and 12 weeks to evaluate gait, and component positioning within the bone.

Results: Installation of components was successful and each animal was observed to ambulate on its affected limb immediately following recovery from surgery. The 900g rat, given a 316L component, was kept for 11 months post-implantation, before succumbing to old age. Micro-CT and fluoroscopic findings revealed no evidence of implant subsidence. The 500g animal, also given an uncollared 316L implant, showed evidence of implant subsidence at three weeks, with full subsidence and hip dislocation at 12 weeks. The 750g rat, given a collared F75 implant, showed no evidence of failure up to 6 weeks, but experienced implant rotation at 9 weeks.

Conclusions: We report the first hip hemi-arthroplasty in a rat using a 3D-printed metal implant. This model aims to provide a low-cost platform for investigating osseointegration, metal-cartilage interactions, and infection using a functional, loaded implant. Efforts to further optimize the surgical approach will be made to reduce early implant loosening. A study with larger sample sizes is needed to determine if implants can be installed repeatedly, without complications, before the utility of this approach can be validated. Future works will include surface preparations on implant stems, with micro-CT to longitudinally track changes at the bone-metal interface, and gait analysis on a radiolucent treadmill to quantify post-operative kinematics.

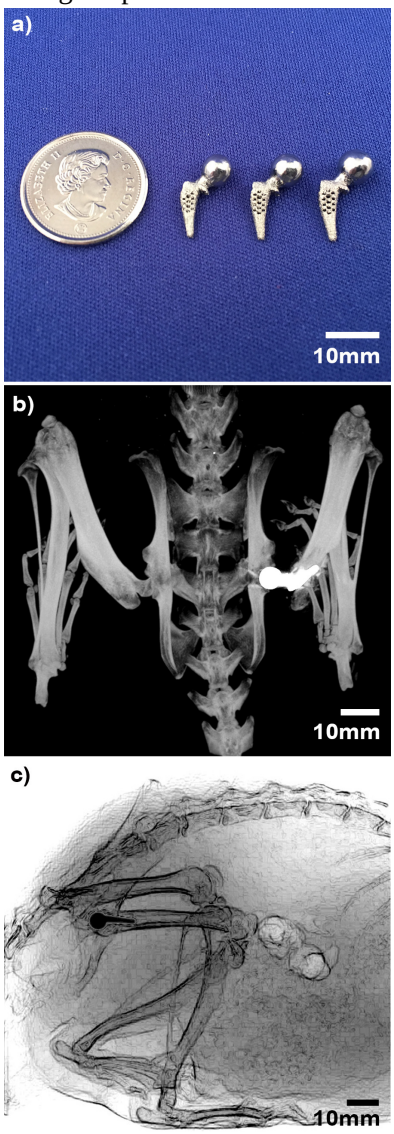

Fig 1: (a) 3D-metal printed implant set in F75 cobalt-chrome; (b) maximum intensity projection of a rat (male, 750g) at 3 weeks post-implantation, and; (c) fluoroscopic image of a rat with an implant *in situ.*

Image Based Comparison between the Bilateral Symmetry of the Distal Radii through Established Measures

Robert J. Gray[a]*, Mitchell Thom[a], Michael Riddle[a], Dr. Nina Suh[b], Dr. Timothy Burkhart[a], Dr. Emily Lalone[a]

[a]Department of Mechanical and Materials Engineering, University of Western Ontario, 1511 Richmond Street, London, ON, CA. [b]Roth|McFarlane Hand & Upper Limb Centre, St. Joseph's Hospital, University of Western Ontario, 268 Grosvenor St, London, ON N6A 4V2

Introduction

Assessment of bone geometry has important implications for fracture fixation, finite element modeling and the design of medical devices. Clinical measurements of the distal radius are often still taken with two-dimensional (2D) X-Ray radiography. The availability of three-dimensional computed tomography (3DCT) allows researchers and clinicians to take measurements. The purpose of this study was to use 3DCT data to introduce new measurements and collect established clinical measurements with the hope of gaining greater insight into the anatomic symmetry between the left and right distal radius.

Methods

Computed Tomography of 37 paired fresh frozen healthy cadaveric male upper limbs (75.4 Ñ8.3 years) were collected. Three-dimensional reconstructed models were created using semi-automatic segmentation (MIMICS, Materialise, Belgium). Established clinical measures such as radial inclination, volar inclination, radial height among other measures were taken. A single rater (primary researcher) completed all measures considered for this study and inter-rater reliability was completed. All quantitative measures were compared between the left and right radius and tested using Principal Component Analysis (PCA) and paired t-test. Statistical significance was set at $p < 0.05$.

Results

Analysis of the data indicated that there was no statistically significant difference between the bilateral symmetry of the distal radius for all quantitative measures. All measurements were found to be reliable across multiple raters. It was found that moving laterally across the volar ridge of the radius, Volar Cortical Angle (VCA) increases. Principal components for both the left and right radii exhibited strong similarities within components When looking at the Transverse Sigmoid Notch Type, the C-type was the most common and the S-type being the least common.

Measurement	Left		Right		Mean Difference	95% Confidence Interval of the Difference		p-value
	Mean	SD (Ñ)	Mean	SD (Ñ)		Lower	Upper	
RH (mm)	12.81	1.74	12.88	1.72	-0.06	-0.48	0.36	0.763
VT (ę)	10.74	3.74	10.77	3.19	-0.02	-1.03	0.98	0.960
RI (ę)	24.05	2.63	24.18	3.41	-0.13	-1.08	0.83	0.787
MeVCA (ę)	137.54	7.03	136.43	7.15	1.08	-0.62	2.84	0.202
MiVCA (ę)	140.82	7.27	140.69	7.25	0.13	-1.27	1.53	0.850
LVCA (ę)	144.48	8.20	143.19	8.26	1.25	-0.92	3.48	0.245

Table 1: Average values and reliability for all measurements (left and right)

Conclusions

When designing implants, fracture fixation devices, or studying the distal radius in general; differences between the left and right radius must be taken into consideration. Through all measures tested it can safely be assumed that there is no significant difference between the left and right distal radius. Recognizing the strong bilateral symmetry of the distal radius aids in the design of implants, fracture fixation devices and the study of the distal radius in general.

Effect of patient-specific instrumentation on postoperative tibiofemoral contact kinematics in total knee replacement

Jordan S. Broberg[1-3], J.L. Howard[4], E.M. Vasarhelyi[4], X. Yuan[2], R.W. McCalden[4], D.D.R. Naudie[4], and M.G. Teeter[1-4]

[1]*Department of Medical Biophysics, Schulich School of Medicine & Dentistry, Western University, London, Canada;* [2]*Robarts Research Institute, London Canada;* [3]*Lawson Health Research Institute, London, Canada;* [4]*Department of Surgery, Schulich School of Medicine & Dentistry, Western University, London, Canada*

Introduction: Currently, the only treatment for end stage arthritis in the knee is total knee replacement (TKR). Even though TKR has improved over the years, with implants having greater longevity, patient satisfaction following TKR has not improved, with approximately 20% of patients recording dissatisfaction with their new knee joint.[1] It is unclear why many patients feel this way, but it may relate in part to surgical techniques that do not respect individual patient anatomy. Manufacturers have attempted to solve this issue with patient-specific instrumentation (PSI), custom surgical guides designed preoperatively using MRI or CT scans, allowing surgeons to account for a patientôs unique anatomy when making bony resections. However no consensus has been reached on the effectiveness of PSI.[2,3] With the use of radiostereometric analysis (RSA), a highly accurate X-ray measurement technique,[4] tibiofemoral contact kinematics can be measured, providing insight on TKR performance. Since a departure from normal kinematics can lead to potential early implant failure,[5] the current study aims to analyze the contact kinematics when PSI is used to determine whether PSI provides an improvement to TKR.

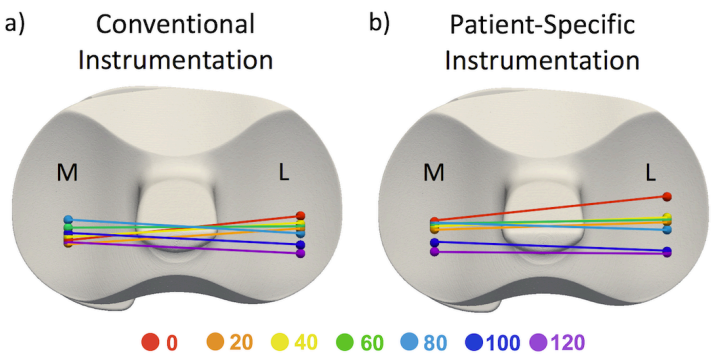

Figure 1. A map of the average tibiofemoral contact locations on the medial (M) and lateral (L) condyles for patients in the (a) conventional instrumentation group and the (b) patient-specific instrumentation group from 0Áof flexion to 120Áof flexion. Both show typical patterns for TKR patients, with the patient-specific instrumentation group displaying a greater magnitude of excursion medially and laterally.

Methods: A cohort of patients undergoing TKR were recruited to the study and randomized evenly to either PSI (Visionaire, Smith & Nephew, TN, USA) or conventional instruments. All patients received the same implant (Legion, Smith & Nephew) and postoperative care. At the 2-year follow-up, a series of RSA images were acquired at different knee flexion angles, ranging in 20Áincrements from 0Áto 120Á Model-based RSA software (RSACore, Leiden, Netherlands) was used to obtain the 3D positions and orientations of the femoral and tibial implant components. Results from the model-based RSA software were used to attain kinematic measures of condylar separation (between the femoral component and tibial insert), contact location, and magnitude of excursion on each condyle. Statistical analyses were performed for comparisons between PSI and conventional instrumentation.

Results: Preliminary results from 12 patients (6 PSI, 6 conventional instrumentation) suggest that there is no significant difference between PSI and conventional instrumentation with respect to contact locations for all angles of flexion ($p = 0.18$ to 0.91) and magnitude of excursion on both medial ($p = 0.25$) and lateral ($p = 0.46$) condyles. However, Figure 1 shows a visible difference in the contact locations between groups. While both groups present a typical pattern for contact locations throughout flexion, the PSI group appears to have a greater mean area of anterior-posterior contact than the conventional group on both condyles. There were no instances of condylar separation present in either group.

Conclusions: Early results suggest that PSI provides no advantage for TKR surgery with respect to kinematic measures. However, data from the full patient cohort ($n = 50$) is required in order to make conclusions on the significance of differences between the two instrumentation techniques. Given the greater cost associated with PSI, a lack of improvement in kinematics with the technique would suggest it should not be routinely utilized.

References: [1]Bourne et al. (2010). *Clin. Orthop. Relat. Res.* 468, 57-63. [2]Ast et al. (2012). *Orthop Clin N Am.* 43, e17-e22. [3]Mattei et al. (2016). *Ann. Transl. Med.* 4, 126. [4]Kª rrholm et al. (1989). *Acta Orthop. Scand.* 60, 491ï 503. [5]Dennis et al. (2001). *J. Bone Joint Surg. Br.* 83, 33ï 39.

The influence of soft tissue balancing performed during total knee arthroplasty on postoperative tibiofemoral contact kinematics

Jared S. Webster[1,2], James L. Howard[5], Dianne Bryant[2,3], Matthew G. Teeter[2,4,6,7], Brent A. Lanting[2,5]
[1]School of Kinesiology, Faculty of Health Sciences, Collaborative Training Program in Musculoskeletal Health Research,
[2]Bone and Joint Institute, Western University
Depts. of [3]Physical Therapy, [4]Medical Biophysics and [5]Surgery, Western University, London, Canada
[6]Robarts Research Institute, Western University, London, Canada
[7]Lawson Health Research Institute, London, Canada

Introduction: Total knee arthroplasty (TKA) aims to produce a functional and stable knee for patients suffering from debilitating arthritis. Soft tissue balancing is an essential aspect of TKA that serves to optimize joint kinematics and stability, which cannot be accomplished through bone cuts and implant design alone. The selected soft tissue balancing performed intraoperatively, whether conservative or extensive, depends primarily on the preoperative knee condition of the patient and intraoperative judgements made by the surgeon. Previous literature has shown soft tissue balancing accurately produces a mechanically balanced knee when measured intraoperatively, however, little is known of the postoperative kinematic implications. The purpose of this study was to evaluate weight-bearing kinematic data in postoperative TKA patients that received varying levels of soft tissue dissection.

Methods: Thirty-four patients who received a primary single radius, posterior-stabilized TKA underwent weight-bearing radiostereometric analysis (RSA) imaging at one-year post-operation. RSA images were taken in 20Áincrements of flexion starting at 0Áto the maximum attainable flexion angle of 100-120Á Kinematic measures of condylar liftoff, contact location, and magnitude of excursion on each condyle were collected using model-based RSA software. Patients were divided in to mild (n = 22), moderate (n = 6), and severe (n = 6) groups depending on the extent of soft tissue modification completed intraoperatively. The mild group received mid-coronal plane and osteophyte corrections. The moderate group received deep MCL, posterior capsule, and/or semimembranosus/posterior oblique ligament corrections. The severe group received tibial reduction osteotomy, superficial MCL, and/or medial epicondyle osteotomy corrections.

Figure 1. RSA trial with participant in full extension (Top) in 20^{o} flexion (Bottom).

Results: Demographic data was similar between groups. No patients in the moderate group experienced condylar liftoff, however three patients in the mild group and two patients in the severe group did experience liftoff. Anterior-posterior (AP) excursion of the medial condyle ranged from 0.4 ï 13.9 mm in the mild group, 3.5 ï 5.8 mm in the moderate group, and 2.3 ï 5.6 mm in the severe group. AP excursion of the lateral condyle ranged from 1.0 ï 13.1 mm in the mild group, 2.5 ï 8.1 mm in the moderate group, and 2.3 ï 9.9 mm in the severe group.

Conclusions: It was expected that with increasing medial soft tissue dissections, patients would experience increased AP excursion and condylar liftoff due to surgically increased laxity of the passive stabilizers. Our interim data demonstrated a greater range of AP excursion in the mild group compared to the moderate or severe groups, however, this may be a result of the number of participants in this group. A higher percentage of patients experienced condylar liftoff in the severe group, which aligns with our hypothesis that those with extensive soft tissue releases may be more susceptible to instability. As the number of participants in the moderate and severe groups continue to rise, we will use more robust measures beyond AP excursion and liftoff to characterize the postoperative kinematics by the varying levels of soft tissue modifications.

Poster Presentation Abstracts

Session 4: Cancer Imaging

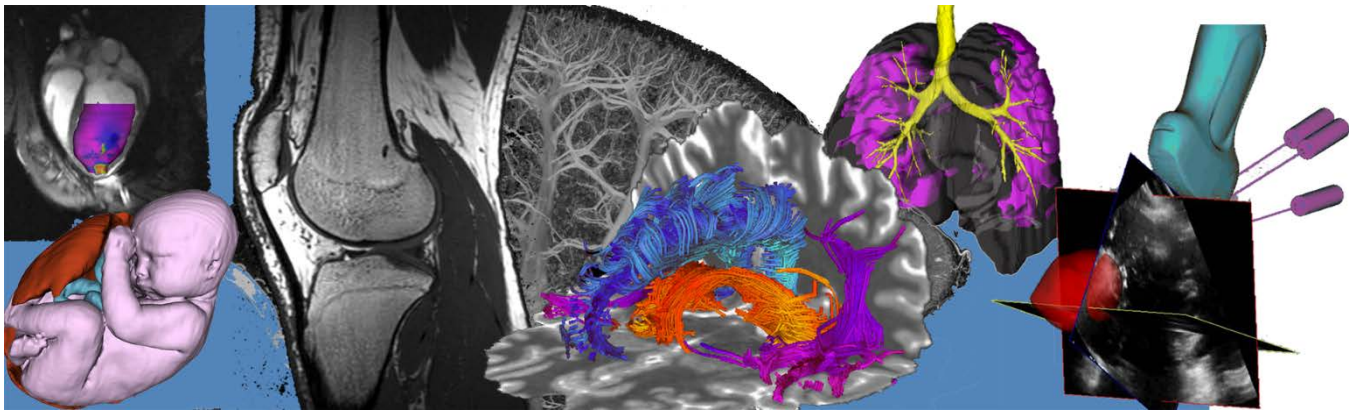

3D Surface Scanning for Tumour Localization in Non-Melanoma Skin Cancer

Anna Ilina[1*], Csaba Pinter[1], Andras Lasso[1], Ingrid Lai[2], Chandra Joshi[2], Kevin Alexander[2], L. John Schreiner[2], Timothy Hanna[2], Gabor Fichtinger[1]

[1] Laboratory for Percutaneous Surgery, Queenôs University, Kingston, Canada

[2] Department of Physics, Engineering Physics, and Astrophysics, Queenôs University, Kingston, Canada

Introduction. Non-melanoma skin cancer (NMSC) is characterized by a tumour present on the surface of the skin. When the tumour presents in the head and neck region, surgical excision of the tumour can cause poor cosmetic outcome. Orthovoltage radiation therapy (ORT) is a non-invasive treatment commonly used to treat such superficial tumours, providing better cosmetic results than surgical removal [1]. Presently, there is no treatment planning system commercially available for ORT. As the first step of the treatment planning process, the tumour must be localized in a CT scan [2]. We propose localizing the tumour using optical 3D surface scanning, to acquire a colored textured image of the patient, since NMSC tumours are not visible in CT. The tumour is then segmented from the surface scan image, and its contour overlaid onto the patientôs CT images for dosimetry planning.

Methods. A male plastic head and neck mannequin was used as a phantom, with a red sticker placed on the face representing a skin lesion. The phantom was segmented from CT using thresholding based on image intensity. The Artec Eva 3D Surface Scanner (Artec 3D, Luxembourg) was used to scan the surface of the phantomôs face, resulting in a full-coloured textured 3D mesh (Figure 1). Five fiducials were manually placed on the nose tip, inner corners of eyes and front of ears to pre-register the model segmented from CT and the surface scan model. The Iterative Closest Points (ICP) algorithm was used after pre-registration to align the two models more precisely and yield the final registration (Figure 2). The tumour was localized by manually segmenting it to a depth of approximately 1cm, mimicking the depth of superficial NMSCs. The segmented tumour was saved with the CT scan to DICOM-RT, for use in treatment planning. Segmentation and registration was done in 3D Slicer, an open-source software platform for medical image visualization and analysis [3].

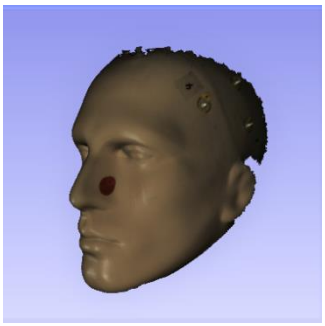

Figure 1: 3D surface scan model of head and lesion on nose.

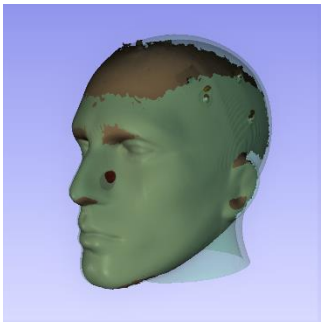

Figure 2: Surface scan model is registered to head model segmented from CT.

Results. The workflow of 3D surface scanning, segmenting head and neck from CT, registering the surface scan model to the segmented phantom model and segmenting the tumour required approximately 7 minutes. The red sticker representing a skin lesion was clearly visible on the textured mesh created using the 3D surface scannerôs software, and could be easily segmented following the contour of the lesion. Following pre-registration using fiducials, the ICP algorithm yielded the final registration, with a mean distance after registration of 0.25mm. Mean distance was computed between the points of the surface scan model and the nearest corresponding points on the surface of the model segmented from CT.

Conclusion. Using 3D surface scanning allows for a quick workflow for localizing a tumour at the surface of the skin, eliminating the need for more complex procedures. This project is the first step towards a free open-source treatment planning system for ORT. This method of localizing the tumour using surface scanning may be extended beyond non-melanoma skin cancers, to any superficial tumours which are visible at the skinôs surface.

Acknowledgements. This work was funded in part by CANARIEôs Research Software Program.

References. [1] Kharofa J, Currey A, Wilson J (2013) Patient-Reported Outcomes in Patients with Nonmelanomous Skin Cancers of the Face Treated with Orthovoltage Radiation Therapy: A Cross-Sectional Survey. International Journal of Radiation Oncology [2] Burnet N, Thomas S, Burton K, Jefferies S (2004) Defining the tumour and target volumes for radiotherapy. Cancer Imaging 4(2):153-161 [3] Fedorov A et al. (2012) 3D slicer as an image computing platform for the quantitative imaging network. Magnetic Resonance Imaging 30(9):1323-41

Breast volume computation for planning and monitoring fat grafting

House, R[1]. Lasso, A[1]. Kunz, M[2]. Rudan, J[1]. Martou, G[1]. Fichtinger, G[1,2].
[1]Laboratory for Percutaneous Surgery, School of Computing, Queen's University
[2]Department of Surgery, Queen's University

INTRODUCTION: Breast Cancer is the most frequently occurring cancer in Canadian women. The majority of these patients are candidates for breast-conserving therapy consisting of partial mastectomy and radiation therapy. Following partial mastectomy, up to one-third of the patients experience significant breast deformity, requiring surgical reconstruction. Fat grafting has been emerging as a safe and suitable modality in breast reconstruction of such deformities. The fat, harvested from donor areas of the same patient, is injected into the breast in several fractions, typically 100-150 cc each time. There is always a percentage of fat resorption and more than one surgery is frequently required. Therefore, it becomes imperative to accurately monitor the changes of volume, in order to plan and execute the optimal fat grafting regimen. Currently, there is no available cost-effective, widely available tool for the reconstructive surgeon.

OBJECTIVE: We aimed to provide a system and clinical workflow to accurately compute volume changes of the breast, in a safe and convenient manner during a clinic visit.

METHODS: A 3D surface scan, using the Artec Eva (**Fig. 1 A**) of the patientôs upper body is obtained, in a non-contact manner, in a standing pose with hands rested on the hip. The surface scan (**Fig. 1 B**) is imported into 3D Slicer for processing and visual rendering. The breast is separated from the chest (**Fig. 1 C)** along anatomical landmarks, and the volume of the breast region is computed. To assist in planning the total graft volume, volume differences between the two breasts are computed by mirroring the healthy breast onto the reconstructed side. To monitor the retention of graft volume between fat grafting sessions, the volume difference between two consecutive scans of the same breast is computed. Three-dimensional distribution of the volume differences over the breast is visualized on the computer display using semi-transparent surfaces and surface-to-surface distance maps **(Fig. 1 D**).

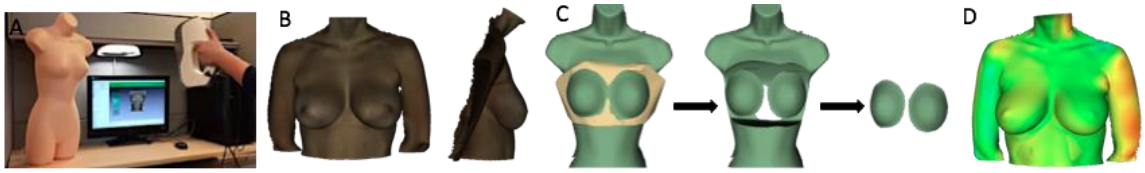

Figure 1. A) Mannequin being scanned by Artec Eva. **B)** 3D surface scan of a volunteer. **C)** Isolation of mannequin breasts from upper body surface scan. **D)** Surface-to-surface distance map of two scans after alignment.

RESULTS: We demonstrated the ability to measure volume differences in the breast in three (3) female volunteers. Each volunteer was scanned three (3) times. Between each scan, the volunteer was asked to relax a few seconds and reposition herself for the next scan. The average difference between three consecutive measurements of the same breast was 1.1 cc. In addition, we also demonstrated the ability to measure the absolute volume of the breast. To this end, a mannequinôs breast volume was first measured by water displacement and compared to the volume measured by our system. Having repeated each measurement five (5) times, the average difference between the measurements was 4.1 cc. The difference in the breast volume using water displacement can be attributed to inaccuracies in the technique.

CONCLUSION: Considering the typical volume of a graft injection fraction (100-150cc), our accuracy in measuring breast volume changes (1.1 cc) is highly promising for clinical use. Research Ethics Board approval has been sought to commence clinical evaluation in 25 post breast-conserving therapy patients.

Cranial irradiation increases the propensity of tumor growth in experimental breast cancer brain metastasis

Amanda M Hamilton[1], Suzanne M Wong[1], Eugene Wong[2], and Paula J Foster[1,2]

[1]Imaging Research Laboratories, Robarts Research Institute, London, ON, Canada, [2]Medical Biophysics, University of Western Ontario, London, ON, Canada

Introduction: Whole brain radiotherapy (RT) is the standard of care for breast cancer patients with multiple brain metastases. While this treatment has been shown essential to the management of existing brain tumors, RT is known to have multiple negative consequences in normal brain tissue including radio-necrosis, cognitive deficits and both short and long-term inflammation [1]. Several studies have also suggested that RT of normal tissues may promote the invasiveness of cancer cells. For example, Bouchard et al. showed that RT of normal mouse mammary tissue induced migration from a contralateral mammary tumor, increased the number of circulating cancer cells and the incidence of lung metastases [2]. In our study, we built on these findings to investigate the influence that RT-induced inflammation in the healthy brain has on the arrest and growth of metastatic breast cancer cells in a model of breast cancer brain metastasis.

Methods: Seven days before cell delivery (day -7) our experimental (RT) female BALB/c mice (n=8) received 10Gy WBRT in one fraction. Control mice (n=7) were not irradiated. Murine 4T1-BR5 mammary carcinoma cells were labeled with 25Õg Fe/mL MPIO beads and injected into the left ventricle of anesthetized mice by ultrasound guidance. All animals were imaged on a 3T GE Discovery MR750 whole-body clinical MR scanner using a custom-built high-performance gradient coil with a solenoid radio-frequency mouse head coil and a 3D balanced steady-state free precession (bSSFP) sequence. Mice were imaged for proof of cell delivery on day 0 and for tumor assessment on day 13. Images were analyzed using OsiriX image software and assessed for tumor number, total tumor burden and average tumor volume per mouse brain. After end point imaging mice were sacrificed, perfusion fixed and brains were excised for histological assessment.

Results: Imaging mice on the day of MPIO-labeled cell injection using our validated single-cell protocol [3] permitted the quantification of cell delivery to the brain. There was no significant difference in the number of detected signal voids in the control mice compared to RT mice. At endpoint (day 13), metastases appeared in bSSFP images as high signal intensity regions compared to normal brain parenchyma (Figure 1A&B). Image analysis revealed a significant difference in the observed number (Figure 1C, p=0.001) of detectable brain tumors in pre-irradiated (RT) mouse brains compared to never-irradiated controls, with 32.0Ñ2.5 and 18.5Ñ2.1 metastases detected, respectively. The RT group also displayed a significantly greater average tumor volume (0.28Ñ0.03 mm^3) compared the control mouse brains (0.20Ñ0.01 mm^3, Figure 1D, p=0.01). Subsequently these two distinct differences in tumor progression resulted in a very significant difference (Figure 1E, p=0.0002) in total tumor burden between experimental groups (control = 2.93Ñ0.21 mm^3, RT = 5.16Ñ0.99 mm^3).

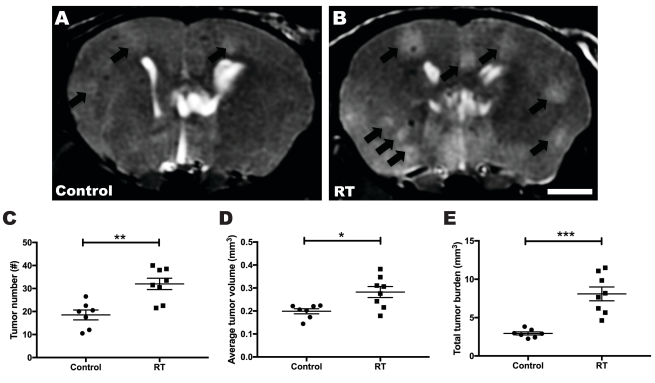

Discussion: Elucidating the impact of RT on normal neural tissue could have implications in the management of patient treatment. We observed no significant difference in the number of signal voids detected in the brains of each mouse group, therefore there was no evidence that irradiation of normal tissue has any effect on cancer cell arrest. End point data, however, clearly showed that neural tissue that had been irradiated but was otherwise healthy had an increased propensity to support metastatic tumor growth. This was evident by the increased number, average volume and total burden of tumors in the irradiated mouse brain thereby demonstrating that as a result of whole brain RT cancer cells were able to form tumors with greater efficiency (increased number) and at a greater rate (increased volume and total burden) than in normal neural tissue. This preclinical data suggests that there may be an increased risk of recurrence particularly in patients with residual systemic disease or with residual radio-resistant brain cancer.

References: 1) Moravan MJ, et al. Radiat Res. 2011;176(4):459-473. 2) Bouchard G, et al. Br J Cancer. 2013;109:1829-1838. 3) Heyn C, et al. Magn Reson Med. 2006;55(1):23-29.

Assessment of Tumour Response after Stereotactic Ablative Radiation Therapy for Lung Cancer: Quantitative Hybrid ^{18}F-FDG PET and CT Perfusion Study

Dae-Myoung Yang[1,2,3], David Palma[1,4], and Ting-Yim Lee[1,2,3]

[1]Medical Biophysics, [2]Robarts Research Institute, The University of Western Ontario, London, Ontario, Canada [3]Lawson Health Research Institute and [4]London Regional Cancer Program, London Health Sciences Centre, London, Ontario, Canada

Introduction. A phase II trial (MISSILE-NSCLC study) is currently assessing the efficacy of neoadjuvant stereotactic ablative radiotherapy (SABR) followed by surgery to treat early-stage non-small cell lung cancer (NSCLC). SABR is a promising treatment option for patients with early-stage NSCLC who are non-surgical candidates. Studies have shown that SABR had a 3-year ~90% local control. Because of its ability to decrease the positive tumour margins, to sterilize tumours to avoid seeding of circulating tumour cells during surgery, and to reduce the mass of required resection, SABR is being evaluated as neoadjuvant therapy to surgery for T1T2aN0 NSCLC, and hybrid ^{18}F-fluorodeoxyglucose (FDG) PET/CT imaging is a clinical imaging modality used for post-SABR monitoring. Despite the promising results reported with SABR, radiation-induced lung injury (RILI) is difficult to differentiate from recurrence after treatment because it can have similar size, morphology and hypermetabolic activity to a recurrent tumour due to inflammatory response following treatment with SABR. Since the intense radiation used in SABR destroys blood vessels and suppressed tumour proliferation; therofere, we hypothesized that using dynamic ^{18}F-FDG PET and CT Perfusion (CTP) is more sensitive to SABR than simple tumour size and SUV as perfusion, blood volume, vessel permeability surface product and glucose metabolic rate in NSCLC would significantly decrease following SABR treatment.

Methods. After Research Ethics Board approval was obtained, 31 patients with histologically confirmed early stage T1 or T2a N0 NSCLC underwent ^{18}F-FDG -PET and CTP pre- and post-SABR. The post-scan was acquired 8 weeks after SABR. Dynamic ^{18}F-FDG-PET measured SUV_{max}, SUV_{mean}, K_1 (influx rate), k_2 (efflux rate constant), k_3 (binding rate constant), k_4 (dissociation rate constant) and K_i (net uptake rate from plasma) using Johnson-Wilson-Lee kinetic model (fig. 1) while CTP quantitatively mapped blood flow (BF), blood volume (BV), mean transit time (MTT), vessel permeability surface product (PS) and largest diameter (LD) in tumours. Since free-breathing was allowed during CTP scanning, non-rigid image registration of CT images was applied to minimize misregistration among the images from breathing motion before the BF, BV, MTT and PS functional maps were generated. Lobectomy was performed 10 weeks after SABR, to allow sufficient time for reactive response to SABR to subside. Differences between pre- and post-SABR ^{18}F-FDG metabolic and CTP parameters were compared using Wilcoxon signed rank test.

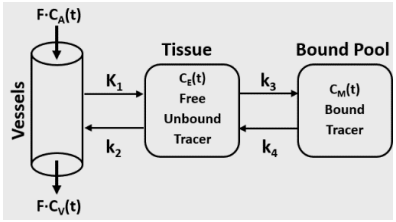

Figure 1. *Schematic of JWL kinetic model*

Results. Metabolic ^{18}F-FDG-PET and hemodynamic CTP studies showed significant changes in SUV_{max}, SUV_{mean}, k_3, k_4, and K_i following SABR. There were decrease in SUV_{max} (-56.7%, P<0.001), decrease in SUV_{mean} (-39.8%, P<0.001), decrease in LD (-13.7%, P=0.01), decrease in k_3 (-39.8%, P=0.002), increase in k_4 (347.7%, P<0.001), and decrease in K_i (-17.2%, P=0.03) before and after SABR.

Conclusions. Hybrid ^{18}F-FDG-PET/CTP can quantify and assess the response of NSCLC to SABR. Kinetic analysis of ^{18}F-FDG-uptake along with perfusion analysis indicated that SUV_{max}, SUV_{mean}, k_3, k_4 and K_i are potential imaging biomarkers to predict the response to SABR and may be used to evaluate primary NSCLC after treatment. As the next step, we will correlate imaging results pre- and post-SABR with histopathology of an explanted tumour to identify perfusion and metabolic parameters for differentiating RILI from tumour recurrence.

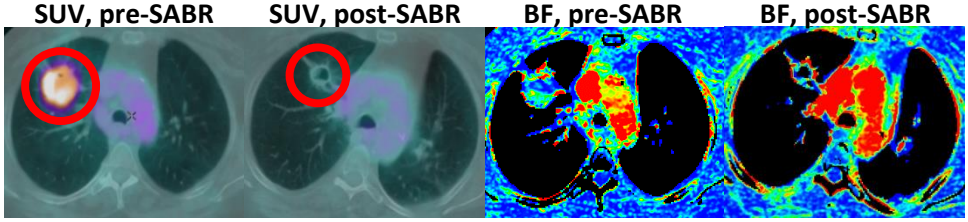

Figure 2. *SUV and BF maps of a patient pre- and post-SABR study. The tumour (red circle) was in the left lobe of the lung.*

Multimodality cellular and molecular imaging of the impact of a primary tumor on metastatic growth in a syngeneic mouse model of breast cancer brain metastasis

Katie M. Parkins*[1,2], Veronica P. Dubois [1,2], Amanda M. Hamilton[1], Ashley V. Makela[1,2], John A. Ronald[1,2,3], Paula J. Foster[1,2]

[1]Robarts Research Institute, The University of Western Ontario, London, Ontario, Canada
[2]The Department of Medical Biophysics, The University of Western Ontario, London, Ontario, Canada
[3]Lawson Health Research Institute, London, Ontario, Canada

Introduction: Metastasis is responsible for the majority of cancer-related deaths and mechanisms that control metastasis are poorly understood. One mechanism of interest called concomitant tumor resistance (CTR) refers to the ability of the primary tumor to restrict the growth of distant metastases[1,2]. Removal of a primary tumor can be followed by abrupt acceleration of residual metastatic disease, and has been observed in both animal models of breast cancer[3] and patients[4]. Conversely, a primary tumor can likewise increase metastatic outgrowth, a phenomenon coined concomitant tumor enhancement (CTE). CTE has been reported in the clinic, with most cases being related to suspected regressions of hepatic or pulmonary metastases following nephrectomy for renal cell carcinoma[5-8]. While imaging has been used to describe CTR/CTE effects in patients[9], the majority of studies evaluating CTR/CTE in preclinical models have relied on histological evaluation of tumor burden[10,11]. The application of cellular and molecular imaging tools capable of visualizing metastatic progression *in vivo* will yield a better understanding of the mechanism(s) by which CTR/CTE effects occur and under what conditions. In turn, this may lead to new therapeutic approaches to halt metastatic outgrowth. Here we apply iron-oxide-based cellular MRI and bioluminescence imaging (BLI) to study the effects of a primary tumor and its size on metastatic growth of breast cancer cells in a novel syngeneic mouse model.

Methods: BALB/c mice (n=24) received an injection of vehicle (Control) or $3x10^5$ parental 4T1 cells in the mammary fat pad (MFP) either 7 days (small MFP) or 14 days (large MFP) prior to intracardiac injection of $2x10^4$ luciferase-expressing, iron-labeled brain-seeking 4T1BR5 cells. Cellular MRI and BLI were performed over the next 2 weeks to measure brain and whole-body cancer cell viability (BLI), whole-brain single cell arrest (iron-induced MR signal voids), and the number and volume of metastases at endpoint (MRI). Whole body MRI was performed on large MFP and control mice on days 9 and 14. BLI was performed on an optical imaging scanner and MRI was performed on a 3T scanner using customized gradient and solenoidal RF coils using the iron-sensitive bSSFP sequence.

Results: Iron labeled cells were visualized in brain MR images as discrete signal voids on day 0 (arrested cells) which was not significantly different between Control and MFP mice. Brain BLI signal at day 0 was also not significantly different. At day 14, both small and large MFP mouse groups had significantly more brain metastases ($p<0.05$) and brain tumor burden ($p<0.05$) than Control mice. Whole-body and brain BLI signal at endpoint were not significantly different between small MFP mice and Control mice, but were significantly higher for the large MFP group compared to Control mice. Lung metastases were detectable at day 14 with whole body MRI in mice with a large MFP primary tumor but not Control mice.

Discussion: The mechanisms of CTR and CTE remain unclear. These findings are in contrast to our previous study in immune compromised mice where we found the presence of a human MDA-MB-231 breast tumor significantly inhibited the growth of MDA-MB-231BR brain metastases. Other groups have suggested the immune system can play a crucial role in CTR/CTE effects[12]. Furthermore, previous studies have shown that the size of the primary tumor can play a key role in whether a CTE or CTR effect is observed[13]. For the present study, we injected our metastatic cell line at an early time point (day 7) when the primary tumor was relatively small and a late time point (day 14) when the primary tumor was large. We found the presence of a primary tumor enhances the growth of brain and body metastases and secondly, this effect could be amplified by increasing the size of the primary tumor at the time of secondary injection. Using *in vivo* BLI/MRI we could determine this was not related to differences in initial arrest or clearance of viable cells in the brain, which suggests that the presence of a primary tumor can increase the proliferative growth of brain metastases in this syngeneic model.

Conclusion: For the first time, we have applied cellular and molecular imaging tools to evaluate the effect of a primary breast tumor on the growth of brain metastases in an immune competent model. Our work highlights new insights into the effects a primary tumor can have on metastasis. Understanding the molecular mechanisms behind stimulation (CTE) versus inhibition (CTR) of metastatic growth could lead to new targets for therapy that could prevent recurrence and improve patient outcome.

Automatic Selection of Hues for Stain Deconvolution in Digital Histopathology Image Analysis

Justin Pontalba*, April Khademi*
*Image Analysis in Medicine Lab (IAMLAB), Faculty of Engineering, Ryerson University, Toronto, Ontario

Introduction: Colour inconsistency in digital histopathology images, due to the lack of standardization in histopathology practices and different stain and scanner vendors [1], impacts the accuracy of digital pathology algorithms. Colour normalization methodologies are useful to solve this problem by correcting for the variability automatically. The first critical step in colour normalization is stain deconvolution, which separates a histopathology image into its constituent stain components based on stain vectors that represent each of the constituent pure stains. Existing methods estimate stain vectors using manual, semi-automated and, ideally, fully-automated approaches. Some automated stain vector estimation methods rely on estimating hue components of each vector by fitting distributions to the hue histogram (and its variants) [2]. Hematoxylin and eosin (H&E) hue histograms can appear to be unimodal or bimodal, in which the bimodal variant can exhibit skewed-left or skewed-right characteristics based on the amount of each respective stain in the sample. Unpredictable proportions of stained content make fitting a specific distribution to a histogram difficult. The proposed method overcomes this issue by not relying on fitting a distribution to automatically estimate stain vectors. Instead, we propose an automatic method that partitions the saturation-weighted hue histogram (SWHH) into stain regions using the median and adaptive outlier detection algorithm to select the hue of each stain robustly, even for skewed distributions. To demonstrate the benefits of the proposed method, we compare it to two other methods that estimate histogram centrality based on the mean and Otsuôs threshold.

Table 1: Normalized energy of the third-channel

Image	Method 1	Method 2	Proposed
1	0.1124	0.1119	0.1115
2	0.1119	0.1115	0.1113
3	0.1134	0.1124	0.1117
4	0.1115	0.1113	0.1112
5	0.1137	0.1127	0.1118
6	0.1118	0.1112	0.1112
7	0.1111	0.1111	0.1111
8	0.1113	0.1111	0.1111

Methods: The query image is converted from the red, green, blue (RGB) to the hue, saturation and value (HSV) colour space. Subsequently, the SWHH is generated; this representation of hue minimizes the impact of noisy hue values in nearly white pixels [1]. A very small threshold (0.01*max) is applied to capture the region in which most pixels occur. The hues of the hematoxylin and eosin stains are then estimated using the $\sigma_{median} \pm interquantile\ range$ (IQR). In doing so, we assume symmetry around the median, which effectively ignores skewed-right or skewed-left distributions. The other two methods we compare use the mean and Otsuôs histogram threshold to estimate histogram centrality, in addition to the IQR to estimate stain hues. The remaining HSV vectors are transformed back to the RGB space and using the automatically found stain vectors, the hematoxylin, eosin, and background or no-stain (ns) images are produced through stain deconvolution. **Results:** To quantify the effectiveness of the proposed method, the normalized energy of the ns-channel was calculated (Table 1) for three methods of hue estimation. If the vectors estimated by the proposed methods are accurate, the image information is fully represented in the H&E channels. If there is error in the approximated H&E vectors, the ns-channel would contain colour not represented by the estimated stain vectors. Method 1 and 2 partitioned the stain regions using mean and Otsuôs threshold respectively. The proposed method produced the lowest energy in the ns-channel and qualitatively demonstrated that it is effective in separating the stains. The decomposed images of the eosin channel in methods 1 and 2 (Figure 1) exhibit blurred edges in areas where nuclei have been. This indicates that more colour was needed to estimate these low eosin concentration areas. **Conclusions:** This work introduced an automatic stain deconvolution method for digital histopathology images. Our results demonstrate the ability of our method to adapt to histogram skewness, while accurately estimating stain vectors in H&E images. This demonstrates the potential for developing more reliable and efficient standardization systems. **References:** [1] Khademi et al., CRC Press, 2017. [2] Li et al., IEEE Trans. Bio. Med. Eng., vol. 62, no. 7, pp. 1862-73, Feb 2015. [3] Neeraj et al., IEEE Trans. Med. Eng., vol. 36, no. 7, pp. 1550-1560, 2017.

Figure 1: Stain separation using our method, 2nd ï 4th row: Left - Hematoxylin, Right- Eosin

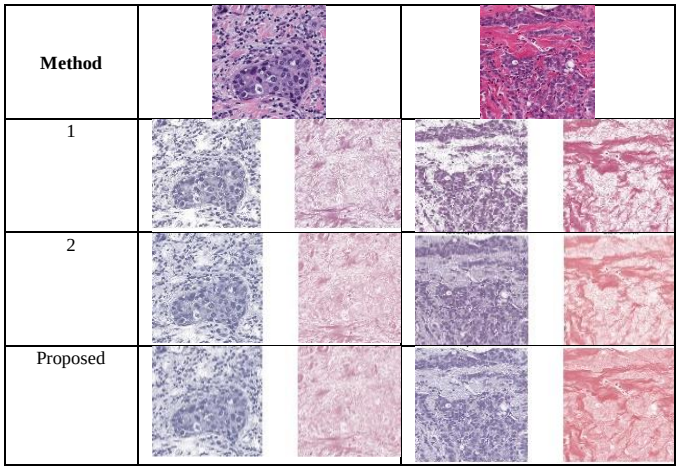

Automation of H&E Staining of Whole Mount Slides

Tyna Hope[1], David Hunter[1], Gordon Mawdsley[1], Mohammed Kazem[1], Taha Rashed[1], Rachel Peters[1], Adebayo Adeeko[1], Mayan Murray[1] & Martin Yaffe[1, 2]

Ontario Institute for Cancer Research - Imaging Translation Program

1 Biomarker Imaging Research Laboratory (BIRL), Physical Sciences, Sunnybrook Research Institute, Toronto. 2 Departments of Medical Biophysics and Medical Imaging, University of Toronto.

Introduction: Whole mount slides are cross-sections of complete tissue specimens (e.g. breast lumpectomy, mastectomy, prostate) that can be viewed microscopically or scanned and processed as digital images. Haematoxylin and eosin (H&E) stained whole mount slides are a valuable research tool and show potential as a clinical tool [Hong, N.J. Look et al. Current Oncology 23.Suppl 1 (2016)] as they provide spatial context not available from the small sampled sections that are created by standard 1x3 slides [Clarke, GM et al. Comput Med Imaging Graph. 2011 Oct-Dec;35(7-8)]. While they are informative, whole mount slides have been considered prohibitively expensive by some researchers, due in part to the manual staining process requiring the constant attention of the technologist. Manual staining has been required as the slides are too large (up to 5ò x 7ò) to be processed by standard H&E autostainers. **Methods:** We have developed a software-controlled robotic system to H&E stain whole mount slides, which is automatic after the unstained slides are loaded. This automation allows the user to walk away during staining and perform other tasks, such as specimen preparation, loading staining or scanning equipment, and report writing. The overall system program is a QT application built in C/C++ which operates on a standard desktop computer running the Ubuntu operating system. The system transports a slide holder to the tanks and submerges the slides in the required solutions, according to the coded H&E staining protocol (Figure 1). The motion is performed using 3 single-axis linear actuators formed by rails and 4 motors run by Phidgets controllers (Calgary, AB) and companion software which interface with the QT application. The tanks are held in place by a guide and their location hardcoded within the software. The Graphical user interface is suitable for use by pathology laboratory personnel. The H&E staining protocol is adjustable to suit any tissue and can be modified by non-developer personnel, via the simple text commands (e.g. T12 means ñgo to tank 12ò) that are provided to the system via an ASCII text file. **Results:** While the automatic system requires 110 minutes to stain one to eight slides, as opposed to 90 minutes by the manual process, it is a walk away system that frees the operator to perform other tasks in the laboratory. Staining results are equivalent to those from manual staining and are acceptable for research studies and has potential use for clinical diagnosis. The system has been used successfully for breast and cardiac tissue (Figure 2). **Conclusion:** Automation removes the need for continual expert supervision during H&E staining of whole mount slides. The subsequent cost reduction may make whole mount technology more accessible to researchers.

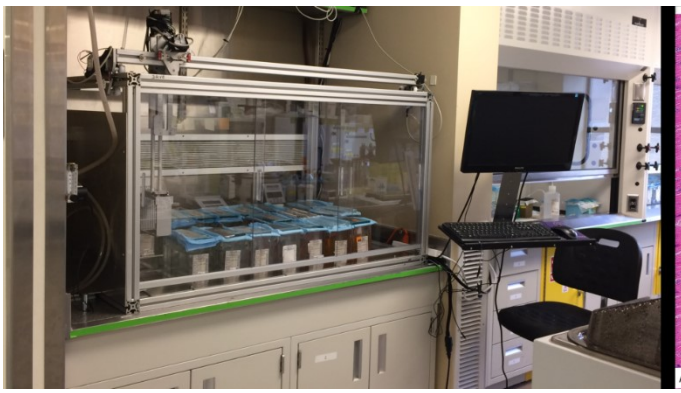

Figure 1 Autostainer robotics and controls within the BIRL laboratory.

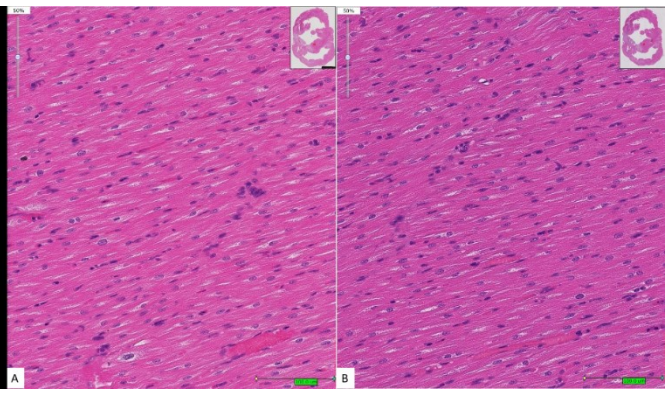

Figure 2. Representative micrographs of H&E stained cardiac muscle tissue scanned using a 20x objective on Leica slide scanning system (Leica SCN400). A: Autostainer, B: Manual staining

Multiple Instance Batch Learning as a Means for Dealing with Imprecise Labels

Shazia Akbar, Sunnybrook Research Institute, University of Toronto, Toronto
Anne L. Martel, Sunnybrook Research Institute, University of Toronto, Toronto

In the past decade, machine learning algorithms have been embedded in a whole host of medical applications from registration of MR images to robotics in surgical implements. There are two main families of machine learning applications, namely, "supervised" learning which infers mapping between input and output from labeled data, and "unsupervised" learning which models the underlying structure from raw data alone. Due to the complexity of medical applications and the need for expertise to interpret biological material, supervised learning approaches are often employed in practice. However one of the main bottlenecks of supervised learning is the need for detailed annotated data samples to train a system, which is costly and time consuming. Furthemore, with the growing uses of deep learning, the demand for more annotated samples has arisen to train large networks with millions of parameters.

Here, we explore the use of multiple instance learning (MIL) in a deep learning framework to minimize detailed annotations required to train a deep neural network. Instead, we opt to collect coarse labels for a large number of training samples and *infer* detailed segmentations from these. The problem we tackle is segmentation of lymph node metastasis in breast H&E stained tissue sections acquired from three different institution [1]. Each tissue slide is digitized and scanned at x20 objective resulting in high dimensional images with dimensions around 200,000 x 100,000 pixels. Traditionally in MIL [2], a single label is associated with a bag of instances; in our case patches from each digital slide. Therefore our dataset consisted of a single label (tumor or healthy) assigned to a bag of patches extracted from a single slide. No segmentations of metastatic lymph nodes were provided during training, therefore the task of the learning framework was to distinguish between patches with true or false labels. We trained a deep convolutional neural neural with 10 layers to output predictions per patch indicating the presence of tumor (Figure 1).

We propose an adaptation of the commonly-used binary cross entropy loss function, which measures the error rate between predictions from the model in its current state and labels provided during training. We add a second loss term used in combination with cross entropy, which measures similarities between patch instances. Similarities are based on image features learned in an unsupervised manner (autoencoder) and were used to compensate for negative labels assigned to patches. Tumor predictions produced using this adapted loss function on a digital slide in an independent test set is shown in Figure 1. Preliminary results show that even with coarse labels we can precisely locate the metastatic regions amongst other complex textures and patterns. Notice how the manual annotation is not accurate to the pixel-level and without guidance, our automated method was able to eliminate large areas containing lumen and fat (red arrow). This holds great promise for reducing annotation loads in machine learning for medical applications and learn from image data directly.

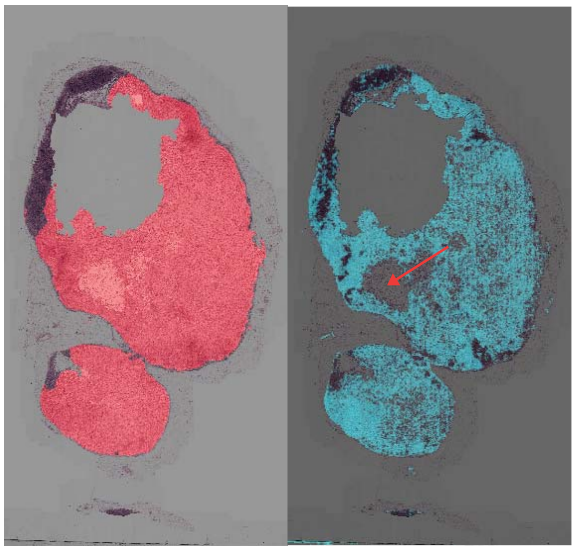

Figure 1: Digital slide with manual annotation overlay (left) and predictions thresholded at 0.5 generated from multiple instance batch learning framework (left)

[1] Camelyon16: ISBI challenge on cancer metastases detection in lymph nodes. https://camelyon16.grand-challenge.org/, 2016.
[2] T. G. Dietterich, R. H. Lathrop, and T. Lozano-Pérez. Solving the multiple instance problem with axis-parallel rectangles. Artificial Intelligence, 89:31–71, 1997.

Cellular heterogeneity in breast cancer evaluated using immunofluorescence biomarker multiplexing

Alison Cheung[1], Dan Wang[1], Tyna Hope[1], Kela Liu[1], Yulia Yerofeyeva[1], Sireesha Kaanumalle[2], Fiona Ginty[2], Sharon Nofech-Mozes[3] & Martin Yaffe[1]

[1]*Biomarker Imaging Research Lab (BIRL), Sunnybrook Research Institute;* [2]*Biosciences, General Electric Global Research Centre;* [3]*Sunnybrook Health Sciences Centre*

Background: Breast cancer is a heterogeneous disease with multiple subtypes. These subtypes are classified either by the expressions of protein markers studied using immunohistochemistry (IHC), or by gene expression using molecular sequencing techniques. Although these classifications are often used to provide diagnoses of the cancer, they are determined based on the observation of a sub-population of the cancer cell mass, and the identities of individual cells are rarely studied due to technical limitations of the methods used. Being able to accurately assess the composition of breast cancer is essential for assigning the most effective treatment to the patient. Using protein marker multiplexing, we studied the simultaneous expressions of eight protein markers on single cancer cells in a spectrum of breast cancer cases. We evaluated the heterogeneity of the characteristics of breast cancer cells and compared our findings to clinical annotations from pathological evaluation. ***Methods:*** The Immunofluorescence multiplex (MxIF) system was developed by the General Electric Global Research Centre (GE GRC, Niskuyuna, NY). It uses a sequential-(fluorescein) stain-image-bleach (SSB) method of multiplex biomarker IHC on formalin-fixed, paraffin-embedded (FFPE) samples[1]. We analyzed a total of eight breast clinical and investigative protein markers: Estrogen Receptor (ER), Progesterone Receptor (PgR), Epidermal Growth Factor Receptor 2 (HER2/neu), Ki67, p53, p21, p16 and Cox2, on a breast cancer tissue microarray (TMA) consisting of 75 benign and invasive breast cancers in duplicates (Pantomics, Richmond, CA). IHC of each single marker was also conducted on serial sections and scoring determined by our pathologists. ***Results:*** Protein multiplex imaging of breast cancer TMA using MxIF with a total of 11 antibodies (investigative and segmentation), consisting of 7 staining, imaging and bleaching rounds, has been completed. Using imaging software provided by GE GRC and algorithms developed in our lab, we will present quantitative data on the number of cancer cells that express each protein marker, and signatures of protein markers, in each breast cancer core. We will evaluate the distribution of cells with different protein signatures, and compare them to the clinical annotation based on current guidelines for pathological evaluations. ***Conclusions:*** Our explorative study will provide quantitative measures of the cellular heterogeneity in breast cancer. Future investigation using breast cancer cohorts with long-term outcome analysis will be instrumental to evaluate the impact of cellular heterogeneity on prognosis or the response to treatment.

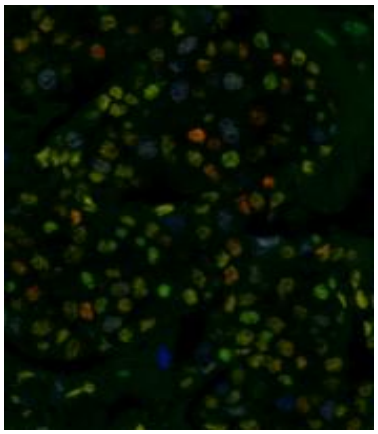

Left: An example of MxIF staining of a breast cancer – PgR, red; ER, yellow; Ki67, blue; p53 cyan illustrating the cellular heterogeneity of breast cancer.

References: 1. Gerdes MJ et al. ***PNAS*** 110(29):11982-7 (2013).

Facilitating Lu^{177} Personalized Dosimetry for Neuroendocrine Tumours

B. Driscoll [1,3], S. Breen[1,2] , A. Shessel [1] , I. Yeung[1,2,3] & R. Wong [1,2]

(1) Radiation Medicine Program, Princess Margaret Cancer Center, Toronto, Canada
(2) Dept Radiation Oncology, University of Toronto, Toronto, (3) Techna Institute, University Health Network, Toronto,, Canada

Introduction

Neuroendocrine tumours over-express cell surface somatostatin receptors (SSTRs) a feature which allows for the therapeutic application of somatostatin analogs (SSA). A Prospective Phase II, Single-Arm, Multi-Centre Study of the Efficacy and Safety of Lutetium-177 Octreotate (Lu-DOTATATE) Treatment in Patients with Somatostatin Receptor Positive Neuroendocrine Tumours was initiated at Princess Margaret Cancer Centre with participation from the London Health Sciences Centre, Odette Cancer Centre and Juravinski Cancer Centre. The 190 patients in the trial receive 4 cycles of Lu^{177} DOTATATE therapy using individualized dosimetry based on SPECT-CT imaging.

Facilitating the SPECT-CT calibration, multi-site image transfer and individualized dosimetry were all managed by the QIPCM (Quantitative Imaging for Personalized Cancer Medicine) team out of the TECHNA Institute at the University Health Network.

Methods

SPECT-CT scanners from all four sites were calibrated with a simple cylindrical phantom injected with a known quantity of Lu^{177}. Results from these phantom scans were used to calculate the sensitivity of each system for the dosimetry study.

Site	SPECT	Sensitivity (cpm/MBq)
TGH	Infinia T16	**727.13**
LHSC	Hawkeye 1	**296.95**
LHSC	Hawkeye 2	**464.09**
Hamilton	Hawkeye	**295.66**
Hamilton	Optima640	**286.11**
Sunnybrook	Optima640	**281.93**

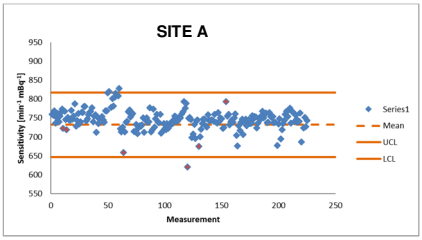

Figure 1 : (Left) Results of Multisite SPECT calibration results. (Right) Continuous syringe QC results from one site.

QIPCM set up CTP (clinical trials processor) pipelines at each site such that patient images could be anonymized and sent to QIPCM where they undergo quality control and are then sent for contouring and dosimetry report generation. The organs at risk from SPECT images are segmented in MIM (MIM Software) and then the images and regions of interest are sent to a dosimetry report generation extension written in MATLAB (The Mathworks). The report is then sent to a physician and medical physicist for review and sign off.

Results

All four trial sites have had their scanners calibrated and have begun treating patients with Lutetium-177 Octreotate. To date 51 patients have been treated and 129 individual dosimetry reports have been created using the QIPCM framework. 17 patients have successfully received all 4 cycles of treatment.

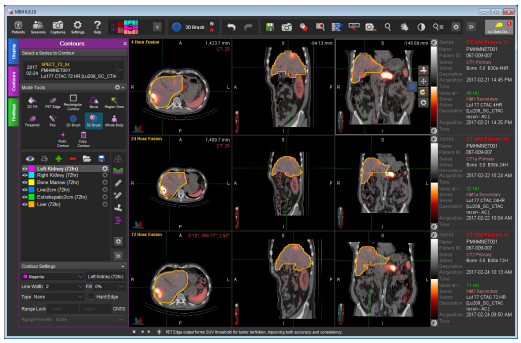

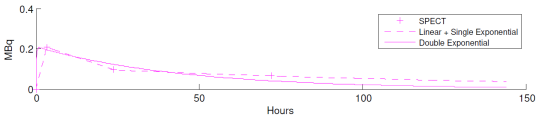

Quantitative SPECT Summary

Manufacturer	SPECT Unit	Acquisition Time	Sensitivity CPM/MBq	Scan Duration (min)	Total Counts	ROI Volume (cc)	Activity (MBq)
SIEMENS NM	INTEVO16	17–Jan–2017 13:38:20	755	30.0	4.71e+03	4.07	0.21
SIEMENS NM	INTEVO16	18–Jan–2017 10:17:42	755	30.0	2.16e+03	4.07	0.10
SIEMENS NM	INTEVO16	20–Jan–2017 10:25:14	755	30.0	1.48e+03	4.07	0.07

Absorbed Dose Summary

Model	Cumulated Activity (MBq x hr)	mean ROI Volume (cc)	mean ROI Mass (g)	Absorbed Dose (Gy)
Linear + Single Exponential	15.55	4.07	5.29	0.23
Double Exponential	9.25	4.07	5.29	0.14

Figure 2 : The individualized dosimetry report generation extension displaying contours (left) and a sample report (right).

Conclusions

QIPCM has successfully facilitated a very complex multi-centre clinical trial allowing the treatment for patients across Ontario with this novel and effective therapeutic.

Title: Automated image based registration of endoscopy to CT for improved tumor contouring in image guided radiation therapy

Souzan Mirza[1] (Primary Author), Runjie Shi[1], Jimmy Qiu MASc[2], Jonathon Irish MD, MSc, FACS, FRCSC [3], John Cho MD, PhD, FRCPC[4] , David Jaffray, PhD[1,2,4], Robert A. Weersink, PhD, MCCPM[1,2,4]
[1] Institute of Biomaterials and Biomedical Engineering, University of Toronto, Toronto, ON, Canada
[2] TECHNA Institute, University Health Network, Toronto, ON, Canada
[3] Department of Surgical Oncology, University of Toronto, Toronto, ON, Canada
[4] Department of Radiation Oncology, University of Toronto, Toronto, ON, Canada

Introduction

One of the largest uncertainties in radiotherapy treatment of head and neck squamous cell carcinomas (HNSCC) comes from errors in contouring the gross tumor volume (GTV), increasing the risk of negative health outcomes for the patient. Presently, endoscopy is only used in clinical exams of patients, but registering endoscopic images to treatment planning CT images is expected to improve contouring accuracy. A registration procedure is developed such that tumor margins viewed under endoscopy can be directly contoured on endoscopic images and projected onto the treatment planning CT.

Methods

We are developing an automatic endoscopy to CT registration procedure using electromagnetic (EM) sensors and image based registration (IBR) methods to minimize registration error between endoscopic and CT images. Inputs to the registration pipeline are the CT image, endoscopic images and EM tracker positions from the sensor embedded in the endoscope. A surface rendering is first generated from the CT image. The EM tracker position defines an initial camera pose with respect to this surface rendering; in combination these generate a virtual endoscopic image that should match the real endoscopic image. The real and virtual images are compared using image metrics. Using an automated global search routine, the virtual camera pose is optimized to find the best match between the real and virtual images. The registration accuracy was quantified using the feature registration error (FRE) measured between pairs of features picked in the real and virtual endoscopic images and the contour reprojection error (CRE) measured between the endoscopy-projected contour and the CT contour.

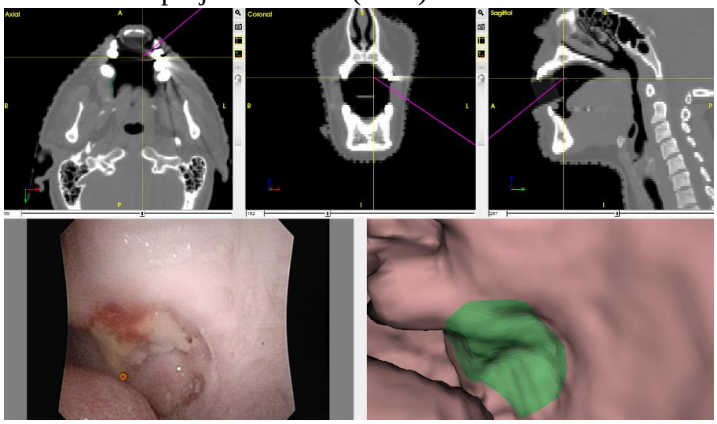

Figure 1: Endoscopy to CT registration interface showing orthogonal views of tumor with purple line representing the location of the endoscope (top row). Real endoscopic image with tumor visible (bottom left) and virtual endoscopic image with tumor contoured in green (bottom right).

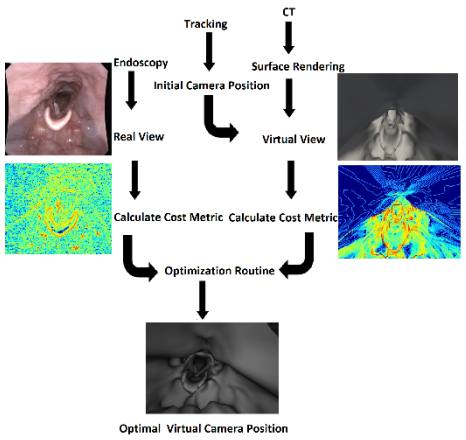

Figure 2: Registration pipeline takes endoscopic images and EM tracker positions as inputs and refines the registration using IBR by comparing image similarity of the real and virtual endoscopic images.

Results

On six images from two patient cases the FRE was 2.3mm-4.4mm after IBR. On a rigid phantom the CRE was measured to be 1.9-14.5mm on a simulated lesion.

Conclusion

An automatic pipeline for endoscopy to CT registration is feasible and can attain an FRE and CRE smaller than the acceptable clinical uncertainty margin of 5mm. Future work includes further research into IBR metrics and testing on more clinical data.

QIPCM Imaging Core Lab ï a Robust Solution for Multi-Center Clinical Trials

V. Iakovenko[1], I. Yeung[2,3], B. Driscoll[1,2], J.Publicover[1,2], T. Shek[1,2], W. Leong[1], C. Coolens[1,2,3], H. Keller[1,2,3], D.Vines[2,3], L. Brzozowski[1] and D.A. Jaffray[1,2,3]

(1) Techna Institute, University Health Network, Toronto,, Canada
(2) Radiation Medicine Program, Princess Margaret Cancer Center, Toronto, Canada
(3) Dept Radiation Oncology, University of Toronto, Toronto

Introduction

One of the major challenges in many clinical trials is the ability to route all the imaging data to one secure location.
Quantitative Imaging for Personalized Cancer Medicine (QIPCM) program aims to provide a central repository for large-volume functional and dynamic imaging data and analysis tools to ease the management for international multi-center clinical trials. QIPCM infrastructure was designed to help clinical investigators achieve systematic image collection and improved collaboration.

Methods

The QIPCM clinical trial data archiving and analysis platform consists of a customizable image anonymizer and secure transport pipeline (RSNAs Clinical Trial Processor, CTP), a dedicated remote analysis platform, and a dedicated server for the archival and storage of medical images.

Each clinical trial site is provided with a de-identification and image transfer pipeline to anonymize all trial images before they leave each site. Only anonymized images are sent to QIPCM, after which they are archived in the safe, secure and backed-up PACS. The images can then be analyzed either by QIPCMs dedicated team of imaging experts or remotely by the trial investigators.
Remote users can select from available customized image analysis tools or use their own custom applications on the virtual environment.

Results

The QIPCM team has established infrastructure and support services for multi-center clinical trials. The platform currently serves 30 clinical trials spanning 25 sites globally. The image store currently holds over 3.0 million images from 1523 imaging studies. QIPCM is a reliable system with robust backup, storage and processing capacity, capable to handle large volume functional and dynamic imaging data.

Conclusions

QIPCM system successfully supports global image transfer and remote connection for international central image review. QIPCM provides fast, customizable and easy-to-use computing platform for central image review where multiple trial investigators can securely and simultaneously review images by accessing them from anywhere in the world.

Investigating the Correlation Between Hyperpolarized ^{13}C-signal and Lactate Concentration

Casey Y. Lee[1,2], Benjamin J. Geraghty[1,2], Justin Y. C. Lau[1,2,3], Albert P. Chen[4], Yi-Ping Gu[2], and Charles H. Cunningham[1,2]

1. Dept. of Medical Biophysics, University of Toronto, Toronto 2. Physical Sciences, Sunnybrook Research Institute, Toronto 3. Cardiovascular Medicine, Radcliffe Department of Medicine, University of Oxford, United Kingdom 4. GE Healthcare, Toronto, ON, Canada

Introduction Hyperpolarized MRI is a technique that has undergone a rapid development in recent years, resulting in a number of successful human studies [1,2]. This technique commonly utilizes hyperpolarized [1-^{13}C]pyruvate as a contrast agent to measure the production of lactate in tumours, which is known to correlate with metastasis and radiation resistance, leading to poor clinical outcomes [3,4]. The tumoural total lactate pool size (or lactate concentration) has been proposed to be the dominant contributor to the pyruvate-to-lactate conversion measured with HP ^{13}C MRI in cells [5]. However, there are a number of molecular mechanisms aside from lactate pool size, such as rate of delivery, transporter and enzyme expressions (i.e. MCTs, LDHs), that concurrently influence the *in vivo* ^{13}C-signals in tumours [6]. In this study, the correlation between MRI-derived ^{13}C-signals and these biological factors will be investigated in a xenograft tumour model.

Methods Nine male Rowett nude (RNU) rats with subcutaneous xenografts of MDA-MB-231 human breast cancer cells (co-injected with MS1 mouse endothelial cells [7]) were scanned on a 3T GE MR750 scanner following the injection of 2ml of pre-polarized 80mM [1-^{13}C]pyruvate, co-polarized with 27mM HP001 (bis-1,1-(hydroxymethyl)-[1-^{13}C]cyclopropane-d_8), a metabolically non-reactive perfusion marker, over 12s via tail-vein catheter. Sequentially interleaved 3D images of lactate, pyruvate, and HP001 were acquired with spectral-spatial excitation followed by a dual-echo EPI readout (5s temporal resolution, 16 time points; axial; 64x8x6 cm^3) [8]. For anatomical reference, 2D fast spin echo (5s TR, 192x192 matrix, axial) images were acquired. Approximately 4.5 min after the initial [1-^{13}C]pyruvate injection, 80mM/2ml non-hyperpolarized [3-^{13}C]pyruvate was injected over 12s (to capture the active metabolism that occurs post-bolus pyruvate injection). The tumours were extracted and immediately flash-frozen approximately 1:30 min from the start of [3-^{13}C]pyruvate injection. The metabolite images were corrected for off-resonance shift based on the lactate frequency offset observed in the spectroscopy interleave and then summed over time to improve SNR. Signals of each metabolite within the tumour were determined by summing the signal within the tumour ROI that was drawn on the T_2-weighted image. For NMR analysis, metabolites were extracted from flash-frozen tumours in perchloric acid, lyophilized, and re-dissolved in 450Õl D_2O containing 5mM DMSO. Portions of each tumour were preserved in RIPA buffer for future analysis of transporter and enzyme expression. Proton spectra were acquired using binomial solvent suppression and 13C spectra were acquired using a proton-decoupled (WALTZ-16) ^{13}C sequence. The area-under-the-peak signals (SNR > 2) from sodium lactate and [3-^{13}C]sodium pyruvate concentration standards were compared to determine ópparentô total lactate pool size and [3-^{13}C]lactate concentration, respectively.

Results and Discussion Our data showed that for MDA-MB-231 xenografts, the tumours showed a positive trend between lactate pool size and Lac/Pyr (r = 0.64), but showed an opposite, negative trend when lactate pool size was compared to Lac/HP001 or [3-^{13}C]lactate concentration (r = 0.67 and 0.82, respectively). These contradictive trends suggest that, in addition to lactate pool size, other biological factors such as rate of ^{13}C-substrate delivery and transporter expression level may significantly attribute to *in vivo* ^{13}C-signals.

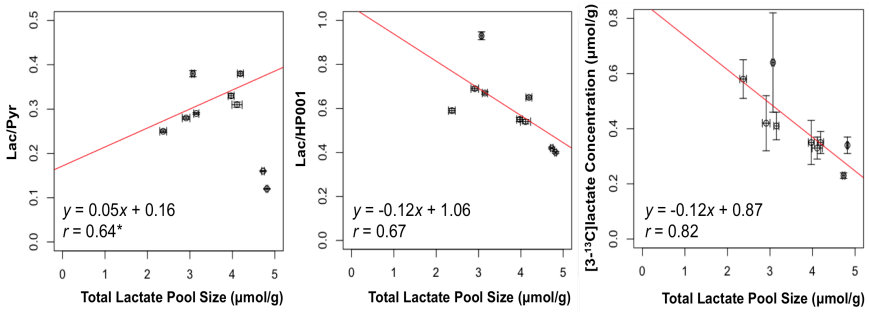

Fig. 1) The total lactate pool size in tumours were compared to Lac/Pyr, Lac/HP001, and [3-^{13}C]lactate concentration. The linear lines of best fit are shown with its equation and the Pearsonôs correlation coefficient (r). *2 outliers were excluded for the best fit in the total lactate pool size vs. Lac/Pyr plot.

Conclusion These results suggest that tumour lactate concentration is not the sole dominant factor determining the observed hyperpolarized ^{13}C-signals in the MDA-MB-231 xenografts used in this study. In the future, the correlation between ^{13}C-signals and the expression levels of transporters and enzymes (e.g. MCTs and LDHs) known to contribute to ^{13}C-signals will be further investigated using the preserved tissue samples.

Acknowledgements The authors thank Jennifer Barry for assistance with the animal handling. Funding support from the Canadian Institute for Health Research Operating Grant MOP-133544. **References** 1) Cunningham CH, *et al*. Circulation research. 2016. 2) Nelson SJ, *et al*. Sci Transl Med. 2013. 3) Walenta S, *et al*. Cancer Res. 2000. 4) Quennet V, *et al*. Radiother. Oncol. 2006. 5) Day SE, *et al*. Nat. Med. 2017. 6) Hurd RE, *et al*. JMRI. 2012. 7) Lau JYC, *et al*. NMR Biomed. 2016. 8) Geraghty BJ, *et al*. Magn. Res. Med. 2017.

Effect of optical clearing on melanoma microangiography with optical coherence tomography

Valentin Demidov[a, †, *], Layla Pires,[b,†] I. Alex Vitkin,[a,c,d]
Vanderlei Bagnato,[b] Cristina Kurachi,[b] Brian C. Wilson,[a,c]

[a]Department of Medical Biophysics, University of Toronto, Toronto, Canada
[b]São Carlos Institute of Physics, University of São Paulo, São Paulo, Brazil
[c]Princess Margaret Cancer Center, University Health Network, Toronto, Canada
[d]Department of Radiation Oncology, University of Toronto, Toronto, Canada

[†]Authors contributed equally to this work

We examine the effects of a topically-applied optical clearing agent (OCA) on the microvascular network imaging of melanoma tumors *in vivo* with optical coherence tomography (OCT). Melanoma is the most aggressive type of skin cancer, with a significant risk of fatality [1]. During the phase of vertical in-depth growth, it develops dense neovascularization that correlates with poor prognosis (worse overall survival, tumor ulceration and recurrence rates). Melanoma's heavy pigmentation results in high visible-light absorption, so that optical imaging techniques are limited to probing tissues only near the tumor surface, which is inadequate to evaluate the subsurface microvascular density. This also affects OCT, a non-invasive *in-vivo* imaging technique that enables volumetric depth-resolved cross-sectional imaging of subsurface tissue microstructure, using low coherence interferometry to enable spatial resolution approaching optical microscopy [2].

In order to decrease melanin absorption in the near infrared, a 1310nm central wavelength OCT was used for experiments. Also, to reduce the light-attenuating effects of tissue scattering, the use of OCA has been investigated. Speckle variance OCT imaging of microvasculature [3] was performed before and up to 4 hours after OCA application. Imaging was followed by OCT data processing to extract and characterize the structure of tumor and normal vasculatures. 3D microvascular maps were obtained at several time points following OCA application. The clearing effect was quantified using spatial texture analysis [4] of OCT image speckle patterns.

OCT was able to image the microvasculature in the pigmented melanoma tissue with ~15μm isotropic spatial resolution up to a depth ~300 μm without the use of OCA; improved contrast-resolution was achieved with optical clearing to a depth of ~750 μm in tumor [5]. These findings are relevant to potential clinical applications in melanoma, such as assessing prognosis and treatment responses, and may also facilitate the use of light-based treatments such as photodynamic therapy.

References

[1] R. Ria et al. Angiogenesis and progression in human melanoma. Dermatol. Res. Pract. 2010; 185687.

[2] J. Fujimoto et al. Optical coherence tomography: an emerging technology for biomedical imaging and optical biopsy. Neoplasia 2000; 2:9–25.

[3] A. Mariampillai et al. Speckle variance detection of microvasculature using swept-source optical coherence tomography. Opt. Lett. 2008; 33: 1530-1532.

[4] A. Lindenmaier et al. Texture analysis of optical coherence tomography speckle for characterizing biological tissues in-vivo. Opt. Lett. 2013; 38: 1280-1282.

[5] L. Pires et al., Optical clearing of melanoma in vivo: characterization by diffuse reflectance spectroscopy and optical coherence tomography. J. Biomed. Opt. 2016; 21: 0812101-9.

Remarkably High Stabilities of MnTCP: A Non-Gd Extracellular MRI Contrast Agent

Henry Tieu,[a,b] * Naixin Zhao,[a] Xiao-an Zhang [a,b,c] *

[a]Department of Physical and Environmental Science, [b]Department of Chemistry and [c]Department of Biological Sciences, University of Toronto Scarborough, Toronto, Ontario, Canada

Introduction: High thermodynamic stability and kinetic inertness are important characteristics for molecular imaging probes. Most clinical MRI contrast agents (CAs) currently used are gadolinium (Gd) based. There have been an increasing amount of reports of Gd release and deposition in vivo from Gd based contrast agents (GBCAs), as their complexes are kinetically labile[1]. Gd dissociation from its complex previously have been associated with nephrogenic systemic fibrosis (NSF), a rare but severe disorder in patients with renal dysfunction[2]. In addition, GBCAs are known to exhibit moderate sensitivity (measured as T_1 relaxivity or r_1) but decrease in r_1 as magnetic field increases to clinical field strength (>1 T). To address these issues, we developed manganese(III) porphyrins (MnPs) as a non-Gd alternative[3,4]. MnPs are more advantageous due to their abnormally high r_1 at higher clinical fields and biocompatibility with high stability. Among them, MnTCP is the first MnP-based extracellular agent. As the smallest water-soluble MnPs known to date, MnTCP exhibits the highest r_1 in clinical fields (1-3 T) among small T_1 agents with molecular weight below 600 Daltons. Here, we demonstrate the high thermodynamic stability and kinetic inertness of MnTCP in a variety of conditions.

Methods: Our experimental design involved three main conditions that cause metal dissociation: low pH, trans-metalation, and temperature. First, we looked at possible demetalation and precipitation of MnTCP by protonation. The Mn may fall out of the porphyrin at low pH conditions and the carboxylic functional groups can get protonated to reduce the solubility of the porphyrin in water. Second, we investigated the transmetalation of MnTCP with different bio-relevant metals at various pH levels. We investigated five different metals for their ability to replace manganese in the porphyrin; calcium, copper, iron, magnesium and zinc. Lastly, we tested at room temperature (23ęC) and at physiological temperature (37ęC) to see whether there are rate changes between the two temperatures. We designed our experiments to mainly use UV-vis spectroscopy and HPLC to measure the kinetic stabilities of MnTCP. Porphyrins have a characteristic UV spectra consisting of a high intensity Soret band and many low intensity Q bands. MnTCP exhibits a unique Soret band at 465 nm while its metal free complex has a Soret band at 407 nm (Figure 1b). Any changes in the concentration of the porphyrin will be observed as changes in the UV spectra, as either lower intensities through precipitation or the appearance of another band indicating the loss of manganese in the porphyrin. Once MnTCP was incubated in the specified conditions, aliquots were taken out and measured using UV-vis to obtain the corresponding spectra. The reaction was monitored over several weeks.

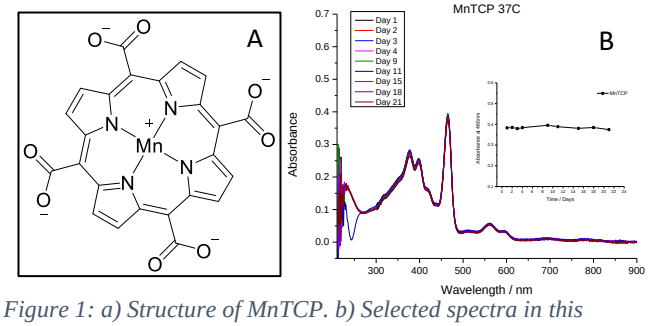

Figure 1: a) Structure of MnTCP. b) Selected spectra in this study: MnTCP monitored at 37˚C in citrate-phosphate buffer, pH 3, for 3 weeks.

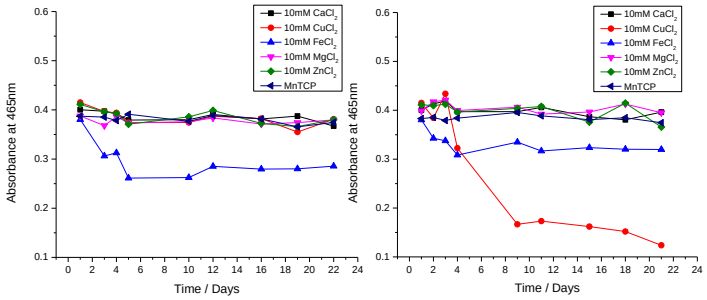

Figure 2: Selected kinetic traces of MnTCP incubated at 22˚C (left) and 37˚C (right) in citrate-phosphate buffer, pH 3 with no metal and 10mM metal salts.

Results: There were no significant changes for MnTCP at pH 3 (Figure 2). Metal concentrations were investigated up to 10X the MnTCP concentration and the no manganese dissociation was observed. Further, temperature did not have an effect on the rate of reaction observed so far (~3 weeks at pH 3). However, decreases in the Soret band was observed in all the iron concentrations and at 10mM of $CuCl_2$ (at 37ęC) after 3 days, but no metal-free and trans-metalated porphyrin signal observed, indicating some precipitation of MnTCP from solution which was also observed visually.

Conclusions: We demonstrated the high stability and kinetic inertness of MnTCP at low pH. It does not exhibit any transmetalation or demetalation in the conditions investigated.

References: [1] *Top Curr. Chem.* **2002**, 221. [2] *Biometals.* **2008**, 21, 469. [3] *J. Med. Chem.* **2014**, 57(2), 516. [4] *J. Magn. Reson. Imaging*. **2014**, 40, 1474.

Title: *In vivo* effects of stereotactic body radiation therapy (SBRT) on the perivascular microenvironment of pancreatic tumors.

Authors: Timothy Samuel[1,2], Azusa Maeda[1,2], Niloufar Khosravi[3], Sara Rapic[2], RALPH S. DACOSTA[1,2]

Affiliations: [1]Department of Medical Biophysics (University of Toronto), [2]Princess Margaret Cancer Centre, [3]Faculty of Dentistry

Abstract:

Stereotactic body radiation therapy (SBRT) is a recent advancement in radiotherapy for locally advanced pancreatic cancer (LAPC) treatment. It uses advanced volumetric imaging techniques to conformally deliver high doses of radiation (greater than 6 Gy) with high accuracy and precision. While growing evidence suggests that SBRT affects both tumor cells and their microenvironment, a better understanding of the biological changes from high dose irradiation may provide new insights into the mechanisms that influence radiation response. Perivascular cells (PVCs), which envelope the vascular endothelium throughout the body, play a well-known role in regulating vascular formation, stabilization, remodelling, and function. A PVC insufficiency is postulated to account for excessive tumor angiogenesis and cancer cell extravasation. Here we use a new preclinical experimental platform combining intravital optical microscopy for cellular-level longitudinal imaging, a small animal x-ray micro-irradiator for reproducible spatially-localized millimeter-scale irradiations, and laser-capture microdissection of ex vivo tissues for transcriptomic profiling. This preclinical study will characterize the impact of SBRT (1×24 Gy and 5×10 Gy) on tumor PVCs and microvascular stability. A custom image-processing platform is developed, using advanced techniques to quantify vascular function, PVC coverage, and other features of interest. This platform has the potential to solve unanswered questions regarding functional significance of the PVC-endothelial association in tumors and how it affects vessel integrity and permeability.

Do dominant intraprostatic lesions receive sufficient dose in high dose rate brachytherapy?

Christopher W. Smith, BSc [3], Douglas A Hoover, PhD [1,3], David D'Souza, MD[1], Derek W. Cool, MD, PhD [2], Zahra Kassam, MD [2], Glenn S. Bauman, MD [4], Aaron D. Ward, PhD [1,3]
1. Department of Oncology, 2. Department of Medical Imaging and 3. Department of Medical Biophysics, University of Western Ontario, London, Ontario, Canada

Introduction: Prostate cancer is clinically understood to be a heterogenous disease. It ranges from being very indolent with chronic, slow progression, to extremely aggressive and potentially lethal. The management of prostate cancer is made more difficult by two additional facts: 1) low-volume, sub-clinical disease is often located throughout the entire prostate, with additional foci of higher grade/aggressive disease, and 2) prostate biopsy, which is a common method used to identify regions of disease, has a notoriously high false-negative rate. Given these two facts, once the decision is made to treat, the standard approach is to treat the entire prostate gland as uniformly as possible (e.g. through complete surgical resection, or through radiation therapy). Current evidence indicates that local recurrence most often occurs at these foci of higher grade disease [1,2], termed the dominant intraprostatic lesions (DILs). Therefore, we hypothesize that the current clinical approach to prostate high dose rate (HDR) brachytherapy may provide suboptimal radiation doses to DILs in certain patients and thus contribute to treatment failure in those cases.

Methods: To measure the hypothetical radiation dose delivered to realistic DIL(s) within the prostate, 13 prostate cancer patients with DILs segmented by radiologists on magnetic resonance imaging (MRI) were each deformably mapped to treatment plans of three different prostate cancer patients who underwent transrectal ultrasound (TRUS)-guided HDR brachytherapy. An iterative closest point transformation was first performed to align the surface of the prostate on the MRI to the surface of the prostate on the TRUS. Next, a thin plate spline transform was used to deform the MRI prostate surface to match the shape of the TRUS prostate surface. The two transforms were applied to the DIL segmentations, thus placing the DIL(s) within the intra-procedural TRUS plan (Fig. 1). In certain cases, the transformed DILs had to be cropped so that they were entirely contained within the TRUS-defined prostate. These transformations were automated using custom scripts written for 3D Slicer 4.6.2 (www.slicer.org). Treatment plans were imported into MIM 6.6.9 (MIM Software Inc, Cleveland, OH, USA) and the D90 and D95 values were determined for each DIL. Overall, 53 DILs with a minimum size of 0.15 cc were evaluated.

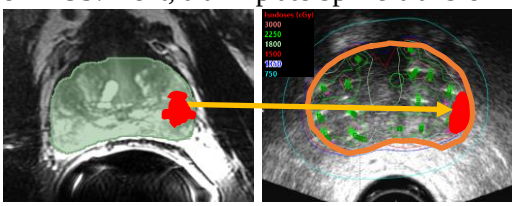

Figure 1. (A) A preprocedural T2W MRI with a DIL contour. (B) The dose distribution within the intraprocedural TRUS image, with co-registered red DIL.

Results: Of the 53 different DILs evaluated, nine did not receive the prescribed dose (15Gy) to 95% of the DIL volume (Fig. 2), while six of those nine also did not receive the prescribed dose to 90% of the DIL volume. The nine different DILs stemmed from 6 different MR patients evaluated on 6 different clinical plans.

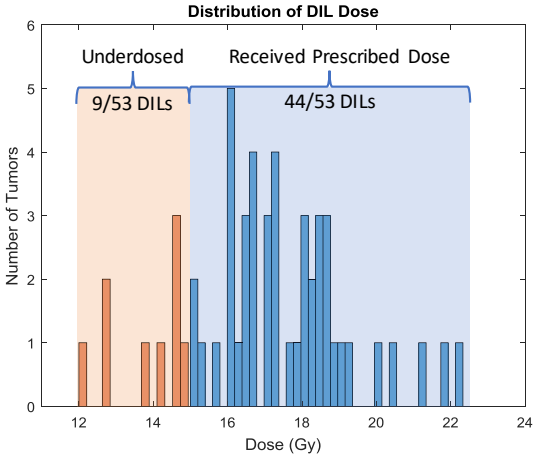

Figure 2. Histogram representing the number of DILs with their respective D95 doses. Red bars represent underdosed DILs.

Conclusion: This study suggests that the current whole-gland approach to HDR brachytherapy may leave patients susceptible to under-treatment of DILs and may be a potential cause of treatment failure. Future work will be to investigate the optimization of catheter placement and/or source dwell times to provide improved radiation doses to dominant intraprostatic lesions, as defined on pre-procedural multiparametric MRI fused to intra-procedural 3D TRUS.

References: [1] Int J Radiat Oncol Biol Phys. 2002 Jul 1;53(3):595-9. [2] Int J Radiat Oncol Biol Phys. 2012 Apr 1; 82(5): e787–e793

Development of a Computer Aided Diagnosis Model for Prostate Cancer Classification on Multi-Parametric MRI

R. Alfano[1,2,8], D. Soetemans[1,7,8], G. S. Bauman[2,6], E. Gibson[9], M. Gaed[3,4], M. Moussa[4], J. A. Gomez[4], J.L. Chin[5,6], S. Pautler[5,6], A. D. Ward[1,2,6,8]

1. Baines Imaging Research Laboratory, 2. Department of Medical Biophysics 3. Robarts Research Institute, Depts. of 4. Pathology and Laboratory Medicine, 5. Surgery, 6. Oncology, 7. Biomedical Engineering Graduate Program 8. Lawson Health Research Institute, London, Ontario, Canada, 9. Centre for Medical Image Computing, University College London, London, UK

Introduction: Prostate cancer (PCa) is one of the most prevalent non-cutaneous cancers among men. Diagnosis depends on a trans-rectal ultrasound (TRUS)-guided biopsy to estimate the stage and aggressiveness. The accuracy of this estimate is confounded by a high false negative rate due to a lack of consistent imaging characteristics that make the identification possible in the majority of cases and consequent use of a universal sextant needle targeting scheme for all patients. Multi-parametric magnetic resonance imaging (mpMRI) maps the prostate in 3D, but is relatively complex to interpret and suffers from inter-observer variability in lesion localization and scoring. Computer-aided diagnosis (CAD) systems have been developed as a solution as they have the power to perform deterministic quantitative image analysis. We measured the accuracy of such a system validated using accurately co-registered whole-mount digitized histology. [1]

Methods: Using a prostatectomy cohort of 40 patients with T2-weighted MRIs and ADC maps, we generated mpMRI texture maps. Cancer ROIs were defined by masks in the mpMRI coordinate system after fusion of the histologic contours to mpMRI. Healthy tissue ROIs wherein the pathologist did not identify the presence of cancer were selected. Twenty-two first and 33 second order texture features were extracted from each ROI for both the T2-weighted images and ADC maps. A logistic linear classifier (LOGLC), support vector machine (SVC), k-nearest neighbour (KNN) and random forest classifier (RFC) were trained in a three-part ROI based experiment as follows: 1) cancer vs. non-cancer, 2) high-grade (Gleason score Ó4+3) vs. low-grade cancer (Gleason score <4+3), and 3) high-grade vs. other tissue components (low-grade cancer and healthy tissue) by selecting the classifier with the highest area under the receiver operating characteristic curve (AUC) using 1-10 features from forward feature selection via 4-fold cross validation. This was performed in both the peripheral zone (PZ) and central gland (CG) for each case. The misclassification rate (MCR), false-negative rate (FNR), and false-positive rate (FPR) were reported at the ROC point with the lowest FPR and highest TPR, depicting ideal classification.

Results: In classification of cancer vs. non-cancer in the PZ, we found an AUC of 0.99 Ñ0.01 [0.04 Ñ0.03 FPR, 0.01 Ñ0.02 FNR, 0.02 Ñ0.03 MCR] for a 4-feature SVC and in the CG an AUC of 0.99 Ñ0.01 [0.00 Ñ0.00 FPR, 0.04 Ñ0.05 FNR, 0.02 Ñ0.02 MCR] for a 6-feature LOGLC. In classification of high-grade cancer vs. low-grade cancer in the PZ, we found an AUC of 0.55 Ñ0.05 [0.48 Ñ0.03 FPR, 0.39 Ñ0.03 FNR, 0.43 Ñ0.02 MCR] for a 5-feature RFC and in the CG an AUC of 0.56 Ñ0.12 [0.35 Ñ0.14 FPR, 0.50 Ñ0.10 FNR, 0.45 Ñ 0.08 MCR] for a 3-feature SVC. In classification of high-grade cancer vs. other tissue components in the PZ, we found an AUC of 0.73 Ñ0.05 [0.39 Ñ0.04 FPR, 0.21 Ñ0.08 FNR, 0.32 Ñ0.05 MCR] for a 1-feature SVC and in the CG an AUC of 0.78 Ñ0.10 [0.29 Ñ0.08 FPR, 0.20 Ñ0.16 FNR, 0.26 Ñ0.09 MCR] for a 9-feature SVC.

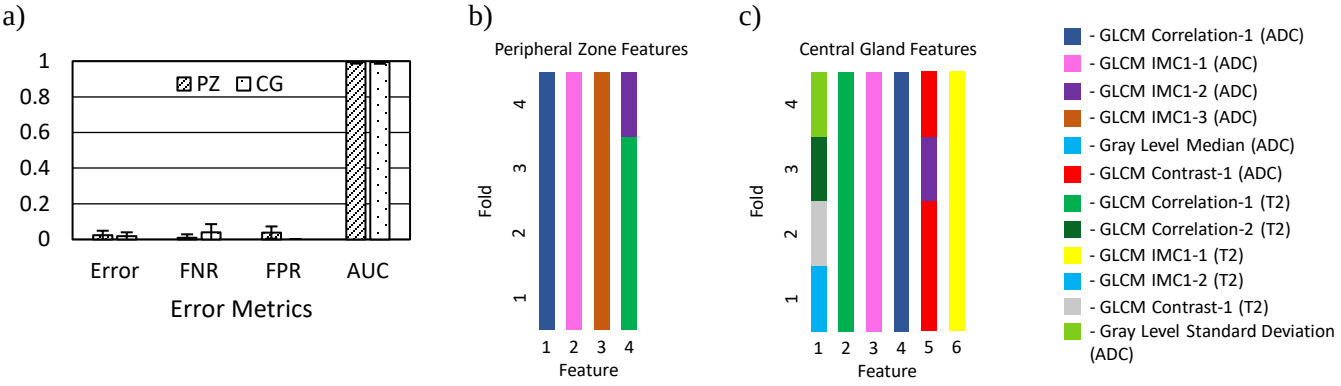

Fig. 1: Experiment 1: a) Error metrics for a 4-feature SVC classifier in the PZ and a 6-feature LOGLC classifier. Features selected in the b) PZ and c) CZ at each fold.

Conclusion: A computer aided diagnosis system assisting a radiologist has the potential to characterize PCa lesions with high accuracy. Our system was able to distinguish cancer from healthy tissue. This work has the potential to lead to a clinically accessible tool that can assist physicians in characterizing PCa lesions on mpMRI. Once fully validated, the system has the potential to improve treatment selection and image-guided biopsy for PCa patients.

References: [1] E Gibson IJROBP 96(1), 188-196, 2016

Signal Enhancement Volume Increase in DCE-MRI After Single Fraction SBRT of Early Stage Breast Cancer

Matthew Mouawad*, Heather Biernaski, Muriel Brackstone, Michael Lock, Anat Kornecki, Olga Shmuilovich, Ilanit Ben Nachum, Frank S. Prato, R. Terry Thompson, Stewart Gaede, Neil Gelman
Western University, Lawson Health Research Institute, London Health Sciences Center

Introduction: The SIGNAL trial is an ongoing phase I/II clinical trial assessing the utility of high dose radiotherapy in early stage breast cancer patients [Guidolin *et al*. 2015]. This provides a unique opportunity to use imaging to potentially assess tumour response to high doses of radiotherapy. One imaging modality shown to be useful in this context is dynamic contrast enhanced (DCE) MRI, which provides functional information related to angiogenesis, perfusion and extra cellular volume. In this study, we investigated changes seen in DCE-MRI imaging following high dose radiotherapy.

Methods: DCE-MRI breast images were acquired on a 3T-PET/MRI system (Siemens Biograph mMR) in five patients before and seven days after a single radiation dose of 21 Gy. 3-D fat suppressed fast low angle shot (FLASH) images were acquired (spatial/time resolution = 1.0x2.1x1.2mm/18s) which included a pre- and 28 post-contrast images. Motion was corrected using deformable registration [Mouawad *et al. ISMRM* 2017]. A rectangular box (volume of interest ï VOI) that encompassed the tumour was drawn for each patient, using the same sized box in the post-radiotherapy data. The signal enhancement (SE - ratio of post to pre-contrast image intensity) at three minutes was calculated voxel wise. The SE VOI signal was progressively thresholded from a value of one (post-contrast signal = pre-contrast signal) to five (post-contrast signal is 5x greater than pre-contrast) in increments of 0.05 and the volume of voxels was calculated at each SE threshold to generate SE threshold vs volume curves. The pre and post radiotherapy images were compared by calculating the fractional change in the area under the volume-SE threshold curve (AUC). In addition, the maximum SE threshold that contained 5% of the volume of voxels at SE = 1 was calculated in the pre and post radiotherapy data.

Results: Figure 1 shows a volume vs SE curve from a representative patient. For every patient at all SE thresholds there was a greater volume of tissue that was enhancing post radiotherapy. Table 1, shows the fractional change of the AUC (post/pre radiotherapy) and the maximum SE threshold for each of the five patients pre- and post-radiotherapy. On average, there was an mean (Ñstandard deviation) increase in the AUC of 2.8 Ñ1.70, with all greater than one. In all five patients, there was an increase in the maximum SE threshold, as seen in table 1.

Conclusion: Following high dose radiotherapy, there is a large increase in the volume of voxels that enhance, and an increase in the maximum SE threshold in the VOI. This may be due to tumour cell death/permeability increase in the vessels [Janssen *et al.* 2010] or potentially an acute inflammatory effect, as it is unlikely the tumour grew over this period of time. Further work will look to correlate the dose a voxel receives to the increase in SE, as well as acquire simulatenous FDG-PET/MRI to correlate perfusion with metabolic/inflammation markers.

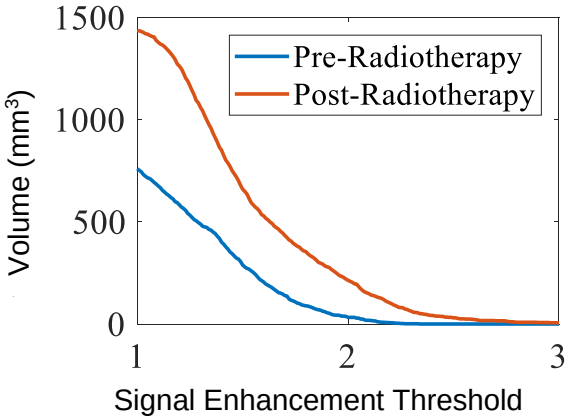

Figure 1 - Volume vs Signal enhancement threshold from a representative patient.

	Ratio of AUC (Post/Pre)	Max SE	
		Pre	Post
Patient 1	2.51	1.65	2.2
Patient 2	5.78	2.25	2.9
Patient 3	2.11	1.95	2.25
Patient 4	1.50	2.1	2.2
Patient 5	2.16	1.75	1.95

Table 1- Fractional Change in the area under the curve (AUC) and maximum SE threshold that contained 5% of the volume of voxels at SE = 1.

Human Prostate Cancer Lesion Characterization Using Tissue Sodium Concentration Assessed by 3.0-T Sodium MRI

N.C. Broeke[1], J. Peterson[1], A. Farag[1], J. Chin[2], S. Pautler[2], G. Bauman[2], A. Ward[1], R. Bartha[1,3], T.J. Scholl[1,3,4]

[1]*Medical Biophysics, Western University, London,* [2]*London Health Sciences Center, London,* [3]*Robarts Research Institute, Western University, London,* [4]*Ontario Institute for Cancer Research, Toronto*

Introduction: Prostate cancer is the most common non-cutaneous cancer in men, affecting on average one in seven men[1]. A significant problem with this disease is the overtreatment of prostate cancer[2,3], leading to reduction in quality of life due to treatment complications and increased healthcare costs[4,5]. Prostate gland under-sampling in standard prostate biopsy is a major concern, leading to uncertain Gleason grading—often forcing conservative decision making by clinicians when staging patients into either active surveillance or treatment. Non-invasive, reliable lesion characterization would be an invaluable tool to afford clinicians more confidence about cancer stage, reducing the instances of overtreatment. This study was preformed to demonstrate that *in vivo* tissue sodium concentration (TSC), assessed by non-invasive sodium MRI can discriminate between low- and high-grade prostate lesions.

Methods: We acquired *in vivo* data from multi-parametric MRI and sodium MRI at 3.0 Tesla from a cohort of ten patients with biopsy-proven prostate cancer prior to prostatectomy. Excised prostates were then sectioned and subsequently Gleason graded by a pathologist assistant prior to non-rigid registration using a validated registration pathway[6]. An example of graded prostate histology and sodium images with overlaid Gleason contours is shown in figure 1. Acquisition of sodium images was done using a custom built endorectal (ER) receive-only coil and an asymmetric transmit-only birdcage RF coil. Sodium data were normalized using the procedure of Axel *et al.*[7] to correct for the ER coil's receive sensitivity.

Results: Assessment of TSC was carried out for peripheral zone lesions as a percent change from healthy peripheral zone tissue (ΔTSC) using this formula: $100\% * \frac{(TSC_{Lesion} - TSC_{Healthy})}{TSC_{Healthy}}$. We report statistically significant increases in ΔTSC with Gleason grade, seen in both individual patients and cohort-averaged data. Spearman's non-parametric ranked correlation was preformed between all ΔTSC data and Gleason grade; yielding a correlation coefficient of 0.791.

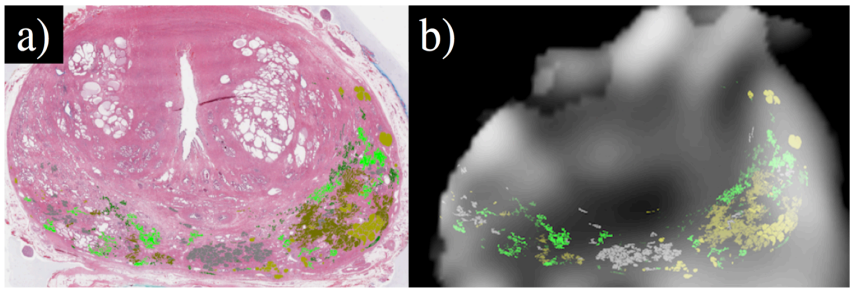

Figure 1. Axially sliced prostate histology sections with Gleason contours (a). Co-registered sodium image overlaid with Gleason contours (b).

Discussion: The monotonic increase in TSC with Gleason grade was observed to be statistically significant in individual men. These results suggest that TSC assessed by sodium MRI has utility to non-invasively characterize prostate lesions. The current gold standard for prostate cancer diagnosis is a 12-core biopsy, sampling less than 0.5% of the total gland. Low-risk Gleason 6 cancer is the most common diagnosis post-biopsy; it rarely metastasizes and has an extremely low associated mortality. However, uncertainties surround biopsy results since under-sampling may mean negative biopsies are missing potentially aggressive lesions. This leads to conservative decision making when staging patients with low-risk disease who otherwise would be streamed for active surveillance. Lesion characterization by TSC measured from sodium-MRI could improve risk stratification and treatment decisions at diagnosis and surveillance of low-risk disease. This will reduce the psychological burden of living with untreated prostate cancer and tip the scales to active surveillance for men with low-risk disease.

References: [1] Statistics CCSAC on Cancer Statistics. Canadian Cancer Statistics 2017. [2] Rouse P. *et al*., Urologia Internationalis, 2011, 87(1), 49-53, [3] Djavan B. *et al*., Primary Care, 2010, 37(3), 441-459. [4] Dragomir A. *et al*., CMAJ Open, 2014, 2(2), E60-E68, [5] Eisemann N. *et al*., Qual Life Res, 2015, 24, 128-128. [6] Ward AD. *et al*., Radiology 2012, 263, 856ï 864. [6] Axel L. *et al*., Amer J Roentgenol, 1987, 148, 418-420.

Non-invasive quantification of glomerular filtration rate for personalization of renal cleared cancer drugs

Fiona Li[1,3,4], Alexandra Hauser-Kawaguchi[2,5], Christopher McIntyre[3,4,5], Mamadou Diop[1,3,4], Keith St. Lawrence[1,4], Leonard G Luyt[2,4,5], James Koropatnick[4,5], Ting-Yim Lee[1,3,4,5]

[1]Medical Biophysics, Western University, London, Ontario
[2]Chemistry, Western University, London, Ontario
[3]Robarts Research Institute, London, Ontario
[4]Lawson Research Institute, London, Ontario
[5]London Health Research Institute, London, Ontario

INTRODUCTION: Kidney is the main excretory organ for many cancer drugs like carboplatin. Renal insufficiencies can lead to drug toxicity due to increased drug concentration in the blood. Therefore, it is imperative to measure kidney function for optimizing drug dosage while minimizing toxicity and complications. Existing methods of measuring kidney function is to determine its clearance rate of a substance filtered from blood as it passes through the glomeruli or glomerular filtration rate (GFR). GFR measurement requires collecting either blood or urine from a couple to 24 hours. In addition, determining the concentration or amount of the glomerular filtered substance in the collected samples can be time consuming leading to delay in reporting the measurement. The goal is to develop a point-of-care GFR measurement method without blood sampling or urine collection, can be performed at physiciansô offices within 30 minutes without any delay in the measurement results.

METHOD: Light transmission from NIR-TPDD at two wavelengths through an extremity is measured. One wavelength is tuned to the absorption maximum of the NIR dye Cy7.5-inulin, a GFR agent (synthesized by our collaborator Dr. Len Luyt). The other wavelength is in the red region of the visible spectrum where the absorption by Cy7.5-inulin is minimal. With every heartbeat, blood vessels in the extremity pulsate changing their thickness and hence attenuation of light. The recorded intensity of the transmitted light, thus, exhibit peaks and troughs. The ratio of the ratio of the peak and trough transmitted light at the two wavelengths can then be used to calculate the arterial Cy7.5-inulin concentration. The ratio of the ratio (RoR) method ignores scattering of light, we have extended TPDD theory to include scattering based on the theoretical model of Schuster.

RESULTS: Using data acquired with our in-house developed TPDD, the measured Cy7.5-inulin concentration curves based on the RoR method with and without scatter were almost the same. Furthermore, these curves were comparable to that measured by the commercially available Nihon Kohden (NK) TPDD.

DISCUSSION AND CONCLUSION: NK-TPDD cannot be used for measuring clearance of Cy7.5-inulin because it is optimized for measuring ICG which is excreted by the liver with a much faster clearance time. As such, the measurement time of the NK unit is limited to 15 minutes while the plasma half-life of Cy7.5-inulin is at least 60 minutes which necessitates a much longer acquisition time than 15 minutes. Our in-house developed TPDD will overcome this limitation to allow point of care monitoring of kidney function with the optical dye Cy7.5-inulin which will lead to accurate dosing of renal excreted cancer drugs for better therapeutic efficacy without excessive drug related toxicities.

Poster Presentation Abstracts

Session 5: Cardiovascular Imaging

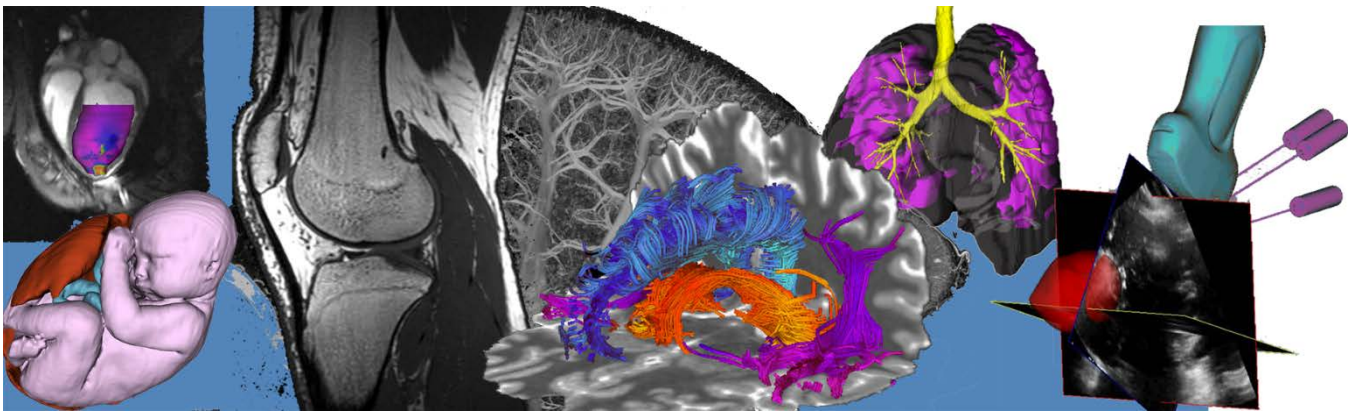

Effect of Image Resolution in T1-Mapping Cardiac Magnetic Resonance in Infarct Mass Quantification for Predicting ICD Therapy

Nadia A. Farrag[1], Venkat Ramanan[2], Graham A. Wright[2], Eranga Ukwatta[1]

[1]*Carleton University, Department of Biomedical Engineering, 1125 Colonel By Drive, Ottawa, ON, K1S 5B6*
[2]*Sunnybrook Research Institute, Sunnybrook Health Sciences Centre, 2075 Bayview Avenue, Toronto, ON M4N3M5*

Purpose: Patients with chronic myocardial infarct MI in the left ventricular (LV) myocardium are at increased risk of developing ventricular arrhythmias, and may therefore qualify for implantable cardioverter defibrillator (ICD) therapy. Indices based on infarct core (IC) and border-zone (BZ) masses are shown to be sensitive in predicting ventricular arrhythmic events. The aim of this study was to compare the MI masses determined by T1-mapping cardiac magnetic resonance (CMR) techniques to those of conventional late Gadolinium-enhanced CMR using inversion-recovery fast gradient-echo (IR-FGRE). We also aimed to investigate the effect of diminishing image resolution on quantification of MI mass and its ability to predict appropriate ICD therapy.

Methods: Thirty-eight patients with known MI underwent acquisitions of three CMR imaging techniques: multi-contrast late enhancement (MCLE) and modified Look-Locker inversion recovery (MOLLI) T1-mapping techniques, and conventional IR-FGRE after double-dose injection of Gadolinium. We post-processed images to quantify IC and BZ masses determined by each technique using a full-width half-maximum (FWHM) approach for IR-FGRE images and a fuzzy c-means algorithm for T1-mapping images. To determine the impact of spatial resolution in sensitivity of predicting ICD events, we artificially diminished resolution of MCLE images acquired from a separate group of 27 patients who had been followed up for ICD therapy and compared MI masses estimated from original and downsampled MCLE images (1.37x1.37 mm^2 and 2.47 x 2.47 mm^2, respectively).

Results: Twelve patients out of 27 (44%) received ICD therapy during the follow up stage. Computed IC masses did not differ between imaging methods, while BZ masses determined by MOLLI were greater compared to those determined by MCLE and IR-FGRE (*p*-value = 0.0025 and 0.0014, respectively). The BZ masses determined by MCLE were not significantly different from those determined by IR-FGRE; however, BZ masses determined by the downsampled MCLE were significantly higher than those determined by IR-FGRE and original MCLE (*p*-value = 0.0324 and 0.0121, respectively). The BZ mass estimated by original MCLE was greater in patients who had received ICD therapy compared to those who did not (*p*-value = 0.044); however, when spatial resolution of the MCLE images was diminished to that of MOLLI, BZ masses were not significantly different between patients with and without ICD therapy.

Conclusions: While estimated IC masses were consistent among all three techniques, the estimated BZ masses were not consistent, especially when spatial resolution of images differed between the techniques. In particular, our study showed that diminished image resolution caused an increase in estimation of the BZ mass, likely due to partial volume effects, which led to a reduced sensitivity in the prediction of appropriate ICD therapy.

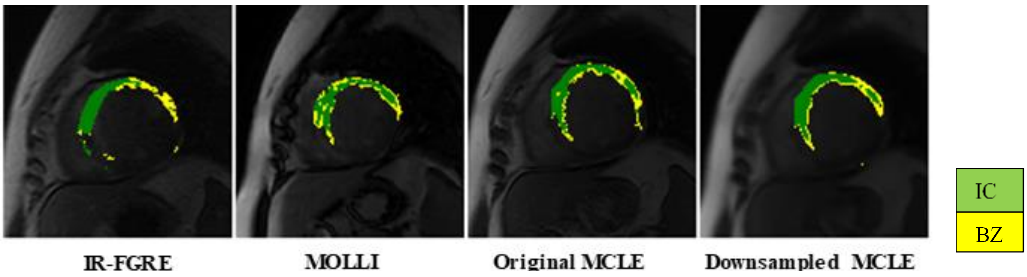

Quantifying Inflammation in Infarcted Myocardial Tissue with Severely Reduced Flow: A Hybrid PET/MRI Approach Using a Prolonged Constant Infusion of 18F-FDG and Gd-DTPA

Benjamin Wilk[1], Gerald Wisenberg[2], Jane Sykes[3], John Butler[3], Michael Kovacs[3], R. Terry Thompson[3], Jonathan D. Thiessen[3], Frank S. Prato[3].

[1]Western University, London, ON, Canada, [2]London Health Sciences Centre, London, ON, Canada, [3]Lawson Health Research Institute, London, ON, Canada

Introduction: Cardiovascular disease is the leading cause of death worldwide. Heart failure, specifically, is predominantly caused by disregulation of inflammation often seen after a heart attack *[1]*. MRI has shown promise in detecting characteristics that can increase the risk of heart failure, including: infarct size, presence of hemorrhage and presence and size of an area of extreme low blood flow within the infarct called the region of microvascular obstruction (MO) *[2]*. What is needed is an imaging method that can distinguish between pro-inflammatory (neutrophils and M1 macrophages) and anti-inflammatory (M2 macrophages) cells as disregulation occurs when the pro-inflammatory phase is prolonged. It has been shown that ^{18}FDG/PET can, in principle, distinguish between the pro- and anti-inflammatory cell types [3] however post heart attack there are three problems: a) ^{18}FDG cannot penetrate the MO after intravenous bolus injection, b) resting healthy myocardium also has uptake of ^{18}FDG and c) partial volume effects interfere with identification of MO tissue. A constant infusion may be able to penetrate the MO while simplifying kinetic modelling [4,5]. Here we present initial results addressing these three issues using a canine model of heart failure post heart attack and PET/MRI imaging during a simultaneous prolonged constant infusion of ^{18}FDG and an extracellular MRI contrast agent (a gadolinium chelate e.g. Magnevist).

Methods: Two animals were imaged at 5 days after a heart attack. During the 150-minute constant infusion of Magnevist and ^{18}FDG, MRI T1-maps and 3D T1 weighted were acquired every 10 minutes; PET images were binned in 3-minute frames. Suppression of ^{18}FDG uptake by cardiomyocytes was initiated at 40 minutes using a heparin injection and the start of a 50-minute lipid infusion.

Results:

a) The MRI T1-maps allow the identification of the infarcted tissue and the zone of MO with relatively little partial volume (figure 1B).
b) The MRI T1-maps can be used to infer the degree of penetration into the MO zone. In one animal, the MO was penetrated after 150 minutes (figure 1C) while the other did not have a visible infarct at any time (not shown).
c) The ^{18}FDG uptake in normal heart cells was eliminated after suppression.
d) The suppression of myocardial glucose uptake lasted at least 60 minutes after the lipid infusion was stopped (figure 1A and 1G).
e) The MRI contrast agent deposition in the infarcted tissue including the MO zone was not affected by suppression.
f) The ^{18}FDG uptake in infarcted tissue and the zone of MO was not affected by suppression.

Discussion: This PET/MRI protocol can be used in the canine model of heart failure to investigate therapies to regulate the inflammatory response. This PET/MRI protocol can be used in patients to detect disregulation of the inflammatory responses and to evaluate therapy.

Future Work: Additional animals need to be studied.

[1] Frangogiannis, NG. (2014). *Nat Rev Cardiol.* 11(5): 255ï 265.
[2] Kali A. (2016). *Circulation Cardiovasc Imaging*. 9(11): e004996.
[3] Thackeray, J. (2017). SNMMI 2017. *J Nucl Med*. 58:302.
[4] Prato, FS. (2015). *J Nucl Med.* 56(2): 299ï 304.
[5] Wilk, B. (2016). SNMMI 2016. *J Nucl Med*. 57:120.

Using Magnetosome Genes to Refine Gene-based Iron Contrast for Magnetic Resonance Imaging

*[1,2,3]Sun, Q; [1,2]Yanofsky, D; [1,2]Thompson, RT; [1,2,3]Prato, FS; [1,2,3]Goldhawk, DE
*Trainee, Supervisor
[1] Imaging Program, Lawson Health Research Institute; [2] Medical Biophysics & [3] Collaborative Graduate Program in Molecular Imaging, Western University, London, Canada

Introduction: Due to its superb spatial and temporal resolution [1], magnetic resonance imaging (MRI) is a great tool for tracking cellular activities that define early stages of disease. To improve current molecular imaging techniques, we are developing MRI reporter gene expression based on the magnetosome model. In magnetotactic bacteria (MTB), magnetosome formation allows the cell to compartmentalize and concentrate iron biominerals in membrane-enclosed vesicles [1]. Furthermore, magnetosome formation is a stepwise, protein-directed process that begins with vesicle formation and culminates with iron biomineralization. While the entire process is regulated by numerous genes [2], we have selected a subset of genes, specifically *mamI*, *mamL*, *mamB*, and *mamE*, deemed essential for the initial stages of magnetosome formation. While *mamI*, *mamL*, and *mamB* have a role in designating the magnetosome vesicle [2, 3], they may also provide docking site(s) for additional proteins, such as *mamE*, that facilitate biomineralization [4]. Refining the development of an MRI reporter modeled after the magnetosome will provide an endogenous magnetic resonance (MR) label [5] for long-term cellular and molecular imaging throughout the cellôs life cycle. In addition, expression of multiple magnetosome genes may provide distinct MR signatures that reflect the structure and subcellular location of a magnetosome-like particle.
Hypothesis: Magnetosome genes *mamI*, *mamL*, *mamB*, and *mamE* will co-localize on an intracellular membrane to form a rudimentary magnetosome-like structure in mammalian cells.
Methods: MTB genes *mamI*, *mamL*, and *mamE* were cloned into vectors with fluorescent protein tags to create Mam fusion proteins [6]. The human MDA-MB-435 melanoma cell line was transfected with each hybrid construct to develop stable expression systems. Synthesis of fluorescent Mam fusion proteins was verified by Western blot. Subcellular location of proteins was examined by epifluorescence and confocal microscopy. Immunocytochemical counter-staining distinguishes mammalian subcellular compartments. To investigate magnetic resonance (MR) signatures, cells were cultured in the presence or absence of an extracellular iron supplement (250 ÕM ferric nitrate) and mounted in a gelatin phantom [7]. Transverse relaxation rates were acquired at 3 Tesla. Changes in total cellular iron content were measured by inductively-coupled plasma mass spectrometry (Biotron Analytical Services, Western University).
Results: When expressed alone, GFP-MamI and GFP-MamE both displayed intracellular fluorescence in a mammalian cell model, with no apparent localization at the plasma membrane (Figure 1). MamI also showed donut-shaped fluorescence structures. While expression of Tomato-MamL was also intracellular, its red fluorescence was punctate.
Conclusions: We have shown that overexpression of three bacterial magnetosome-associated proteins, MamI, MamL, and MamE, are compatible with a mammalian cell system. Fluorescence microscopy demonstrated that these membrane proteins are localized in the intracellular compartment and not associated with the plasma membrane. Future comparison of these Mam proteins, alone and in combination, with iron-labelled MagA-derived activity [7], will indicate their potential for co-localization and modulation of MR measures, such as transverse relaxation rates.

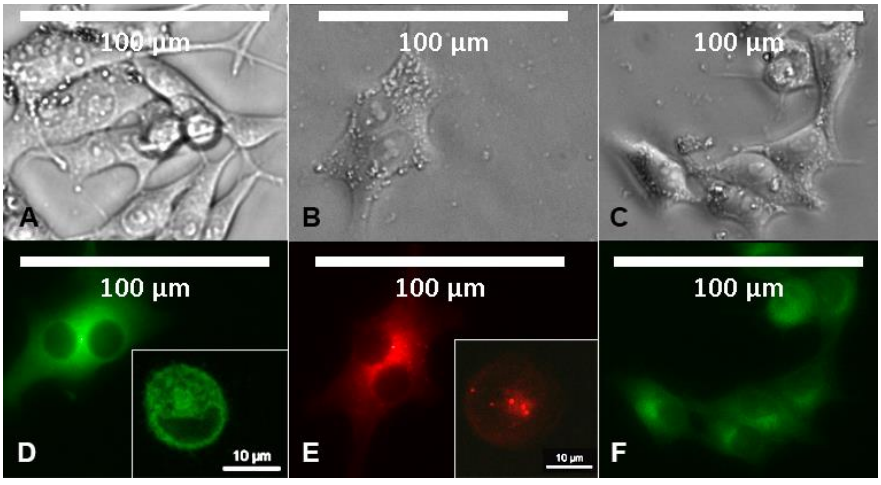

Figure 1. MDA-MB-435 cells stably express fluorescent Mam fusion protein. Panels A-C are bright field images of MamI-GFP, MamL-Tomato, and MamE-GFP, respectively. Panels D-F are the corresponding fluorescence images. Insets in panels D and E are confocal fluorescence images of the corresponding fusion proteins.

References:
[1] Goldhawk *et al* (2017) Design and Applications of Nanoparticles in Biomedical Imaging, pp 187-203 **[2]** Komeili, A. (2012) FEMS Microbiology Reviews 36, 232 **[3]** Murat *et al* (2010) PNAS 107, 5593 **[4]** Quinlan *et al* (2011) Molecular Microbiology 80, 1075 **[5]** Uebe and Schuler (2016) Nature Reviews: Microbiology 14, 621 **[6]** Sun *et al* (2016) Magnetotactic Bacteria 5th International Meeting **[7]** Sengupta *et al* (2014) Frontiers in Microbiology 5, 29

Using P19 Cells to Model the Influence of Macrophage Pro-inflammatory, Iron-handling Activity on MRI

[1,2,3]*Alizadeh, K; [1]McGuire, T; [1,2]Thompson, RT; [1,2,3]Prato, FS; [1,2] Gelman, N; [1,2,3]Goldhawk, DE
*Trainee, Supervisor
[1] Imaging Program, Lawson Health Research Institute, London, Canada; [2] Medical Biophysics & [3] Collaborative Graduate Program in Molecular Imaging, Western University, London, Canada

Introduction: Magnetic resonance imaging (MRI) is a non-invasive tool that may be used to track cellular activity in the body. Since the magnetic resonance (MR) signal is sensitive to iron-based contrast agents [1], MR may also distinguish changes in a particular cellôs iron metabolism [2]. For instance, inflammation involves downregulation of iron export in monocytes and macrophages by the hormone hepcidin [3], due to degradation of the iron export protein, ferroportin (Fpn) [4].We therefore examined the effect of hepcidin on transverse relaxation rates in multipotent P19 cells, which provide a convenient model of molecular activities present during inflammation owing to their high iron import and export activities, similar to macrophage [5].
Hypothesis: Pro-inflammatory signalling by hepcidin is detectable by MRI due to regulation of iron export.
Methods: Iron-exporting P19 cells were cultured under various conditions of iron supplementation, with (n=11) or without (n=25) 200 ng/ml hepcidin/medium. Cells were harvested; mounted in gelatin phantoms; and scanned at 3 Tesla [6]. Image-based measurements of total transverse relaxation rate (R_2*= $1/T_2$*) and the irreversible component ($R_2=1/T_2$) were performed [6] and used to calculate the reversible component, R_2' (R_2* ς R_2). Total cellular iron content was measured by inductively-coupled plasma mass spectrometry (ICP-MS). Expression of Fpn protein was examined by Western blot. Linear regression modelling was conducted to determine the correlation between relaxation rate, as the dependent variable, and total cellular iron content, as the independent variable (SPSS version 24). Independent Studentôs t-test was performed to compare linear regression slopes. Statistical significance was set at $p<0.05$.

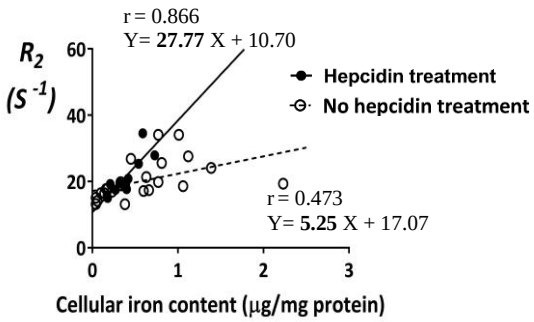

Figure 1. Hepcidin influences the linear relationship between transverse relaxation rate and total cellular iron content in P19 cells. Hepcidin interrupts iron export and significantly increases the slope of the line that correlates R_2* to the total cellular iron content ($p<0.05$).

Results: While hepcidin caused ferroportin protein degradation in P19 cells, it did not significantly alter the magnitude of transverse relaxation rates or total cellular iron content compared to no hepcidin treatment. However, hepcidin altered the correlation between transverse relaxation rates and total cellular iron content. Although the correlation between iron and either R_2 *or* R_2* was significant ($p<0.01$) in both treatment groups, the slope of this linear regression relationship in hepcidin-treated cells was significantly higher than in non-hepcidin treated samples by 3-4-fold ($p<0.05$, Figure 1). In addition, a significant correlation was observed between R_2' and total cellular iron content in non-hepcidin treated cells ($p<0.001$), while no correlation was found in the hepcidin-treated group.
Discussion: These results demonstrate how hepcidin-dependent interruption in iron export influences transverse relaxation rates. The increase in the slope of the lines lead us to conclude a potential higher diffusion effect after hepcidin treatment. This might be related to changes in cellular iron compartmentalization in response to hepcidin. This study indicates the potential for non-invasively monitoring such inflammation-related changes using MRI.
References:
[1] Goldhawk *et al* (2012) Wiley Interdiscip Rev Nanomed Nanobiotechnol 4, 378
[2] Goldhawk *et al* (2015) Magnetic Resonance Insights 8, 9
[3] Theurl *et al* (2008) Blood 111, 2392
[4] Nemeth *et al* (2004) Science 306, 2090
[5] Liu (2015) MSc., Western Univeristy
[6] Sengupta *et al* (2014) Frontiers in Microbiology 5, 29

Reproducibility and repeatability of cardiac ^{11}C-Hydroxyephedrine PET sympathetic nervous system imaging and kinetics

Kai Yi Wu[1], Tong Wang[1], Vincent Dinculescu[2], Robert Miner[1,3], Jennifer M. Renaud[1], Lisa Marie Mielniczuk[1], Rob Beanlands[1], Robert deKemp[1]
[1] Department of Medicine, University of Ottawa Heart Institute, Ottawa, ON, Canada,
[2] Radiology, Alberta Health Services, Calgary, AB, Canada,
[3] Carleton University, Ottawa, ON, Canada.

Objectives: Dysfunction in the cardiac sympathetic nervous system (SNS) has been associated with poor prognosis in patients with chronic heart failure. The purpose of this study was to characterize the reproducibility and repeatability of [^{11}C]-meta-hydroxyephedrine (HED) PET imaging of cardiac SNS function.
Methods: Dynamic ^{11}C-HED PET/CT scans were performed 47Ñ22 days apart at baseline and follow-up in 20 heart failure with reduced ejection fraction patients as part of another study. Three observers blinded to patientsô clinical data used FlowQuant to evaluate the intra- and inter-observer reproducibility and test-retest repeatability of ^{11}C-HED tracer uptake and clearance rates to measure volume of distribution (DV), myocardial blood flow (MBF), and retention index (RI). Since sympathetic denervation assessed using ^{11}C-HED PET has been shown to be a predictor of sudden cardiac death, regional % defects of DV and RI, which are measures of denervation, were assessed by the proportion of values <75% of the peak value in the LV. Both global and regional partial-volume corrections were performed. Reproducibility and repeatability were evaluated using intra-class-correlation (ICC) and Bland-Altman parametric and non-parametric coefficient-of-repeatability (NPC and RPC, respectively).
Results: All intra- and inter-observer correlations were excellent (ICC>0.89) and reproducibility values (NPC = 6-13%) were significantly lower than the test-retest values (NPC =11-48%). RI and % defect RI (NPC = 29% and 11%) exhibited the best test-retest repeatability compared to similar measures of DV and % defect DV (NPC = 17-48%). Global partial-volume corrected DV values (NPC = 17-44%) consistently showed improved repeatability over regionally corrected DV (NPC =21-48%). MBF exhibited the greatest test-retest repeatability of 59%.
Conclusion: ^{11}C-HED PET analysis can be performed reliably by different operators using a highly-automated program. Measures of global and regional SNS function were more repeatable using the retention index compared to distribution volume tracer kinetic model.

Accuracy of mitral valve imaging in dynamic computed tomography

Claire Vannelli*[12], John Moore[1], Aaron So[1], Wenyao Xia[1], Terry Peters[12]

*: first author, 1: Robarts Research Institute and 2: Biomedical Engineering Program Western University, Canada

INTRODUCTION: With the significant increase in life expectancy over the past century, valvular heart disease has been referred to as the next cardiac epidemic. Transesophageal echocardiography (TEE) is widely recognized as the standard of care evaluation technique to diagnose mitral valve disease (MVD). In most cases, TEE imaging is adequate for identifying pathology, however due to limitations such as signal dropout, limited resolution and user-variability in interpreting images, the diagnostic value of TEE is often limited. Dynamic cardiac computed tomography (CT) is emerging as a valuable tool for diagnosis and assessment of cardiac diseases, enabling surgeons to personalize their approach to intervention. However, application of dynamic CT to mitral valve imaging is particularly challenging due to the large and rapid motion of the mitral valve leaflets. Therefore, it is important to investigate the level of precision with which dynamic CT captures mitral valve morphology throughout the cardiac cycle.

METHODS: To mimics normal mitral valve morphology and motion patterns, we have created a valvular model which but can be arrested at precise cardiac phases. Valve motion is achieved by pulling on the chordae tendinae, controlled by a servomotor. To assess the accuracy of gated, dynamically acquired mitral valve images, we use a static valvular model against which we can compare the dynamic data. CT images of the valve are acquired in air, both with the valve in motion and at predefined static positions (Figure 1). Phase-matched time points from the dynamically-acquired scan are aligned to the corresponding static volumes with homologous-point landmark based registration. The valve leaflets and chordae are segmented in MATLAB using continuous max flow, the static flanges registered using iterative closest point and the segmented volumes compared using the average Euclidean surface distance (Figure 2).

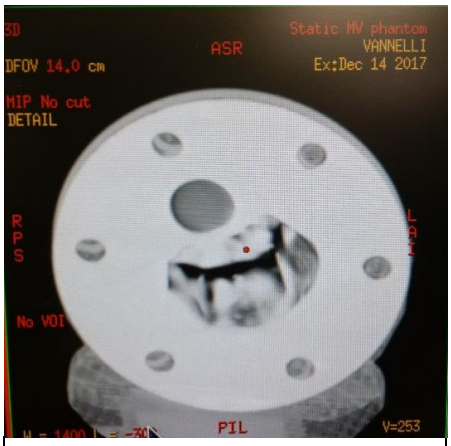

Figure 1: 3D volume rendering of arrested silicone mitral valve

RESULTS: Table 1: Evaluation of phase-matched static and dynamic datasets with mean Euclidean distance observed between the two models

ECG time point	Mean Euclidean Surface Distance (mm)
1: pre- to mid- P wave	1.80
2: mid- to post- P wave	2.91
3: Q wave	2.93
4: RST waves	3.21
5: post-T wave	3.52
6: pre- P wave	1.97

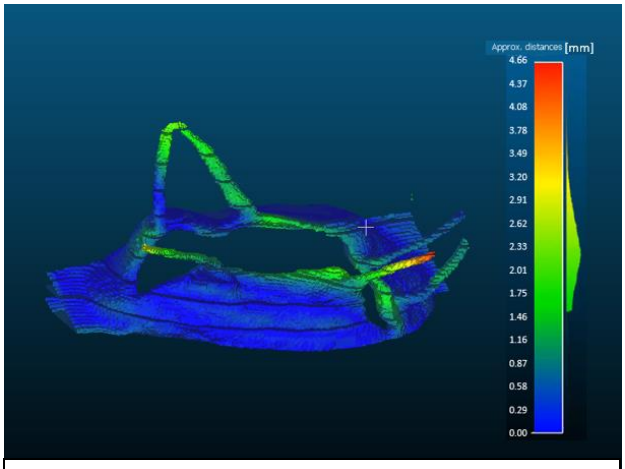

Figure 2: Cloud comparison of segmentation maps from static and dynamic datasets. Chordae can be visualized protruding outward from the leaflets

CONCLUSION: In order to assess the accuracy of dynamic CT for mitral valve imaging, we propose a workflow to compare gated, static CT images with dynamically-acquired images. Preliminary results from a proof-of-concept study demonstrate the need for further analysis and quantification of dynamically-acquired scan motion artifacts and image quality.

Novel T1-mapping based models for cardiac EP: a combined experimental and modelling study

Mengyuan Li[1,2], Maxime Sermesant[3], Sebastian Ferguson[2], Fumin Guo[1,2], Jen Barry[2], Graham Wright[1,2], Mihaela Pop[1,2]
[1]University of Toronto, [2]Sunnybrook Research Institute (Canada); [3]Inria Sophia-Antipolis (France)

Introduction: Computational models are powerful tools used in electrophysiology (EP) to predict arrhythmia associated with structural heart disease (such as infarct scar-related ventricular tachycardia, VT), a major cause of sudden cardiac death [1]. Our aim is to develop novel integrative technologies using advanced imaging methods (that efficiently probe the biophysical MR signal in chronically infarcted myocardium) and MRI-based computational heart modelling, for better identification and ablation therapy of arrhythmia substrate. Previously, we customized similar 3D models using electrical data obtained from optical imaging [2] or *real time* MR image-guided EP studies [3]. In this work we present our recently developed predictive T1-based heart models personalized using conventional X-ray guided EP data obtained in a preclinical pig model of chronic infarction.

Methods: 6 pigs (5 with chronic infarct and 1 healthy) underwent cine MRI on a 1.5T GE scanner. The infarcted pigs underwent *in vivo* multi-contrast late enhancement MCLE imaging (1x1x5mm resolution) for T1* mapping as in [3], followed by X-ray guided electro-anatomical EP studies. The EP maps were obtained using a CARTO-XP system (Biosense, J&J, USA) and a catheter that was inserted into the LV (left ventricle) cavity and recorded depolarization times (~100 points/map). For image analysis, we first segmented the 2D MCLE images and categorized the tissue into: dense fibrotic scar, healthy zone and grey zone, GZ (i.e., the arrhythmia substrate, a mixture of viable and dead myocytes). We then generated 3D volumetric meshes (~1.5 element size) using CGAL libraries from the stacks of segmented images, and assigned different electrical conductivity values per tissue zone: non-conductive (scar), normal and slow-conductive (GZ). Next, using fast numerical methods [1], we simulated the propagation of depolarization wave in each heart model in <1min on a 4,096(1x)MB machine, Intel® Core™ i3-2310M processor, 640 GB HD, NVIDIA® GeForce® 315M graphic adapter. Finally, we compared the simulated activation times with their corresponding electrical maps recorded during the EP study.

Results: Representative results from one infarcted case are shown in Figure 1. Fig. 1a shows the steady state SS and T1* map obtained from MCLE images, used as input to a fuzzy-logic segmentation algorithm for classifying tissue into: scar, healthy and GZ pixels. Fig 1b shows the 3D T1*-based model with the three zones. Fig. 1c shows the measured endocardial isochronal map projected onto the 3D model (visualized in *Vurtigo* [4]), as well as the corresponding 3D simulated activation time map, resulting in a small absolute mean error (i.e., ~10ms, between computed vs. mesured maps) over all endocardial nodes of the mesh. Most importantly, compared to the sparse and interpolated measurements of endocardial electrical signals, the predictive 3D heart models provide higher density maps, as well as transmural activation times (note: early depolarization times are in red).

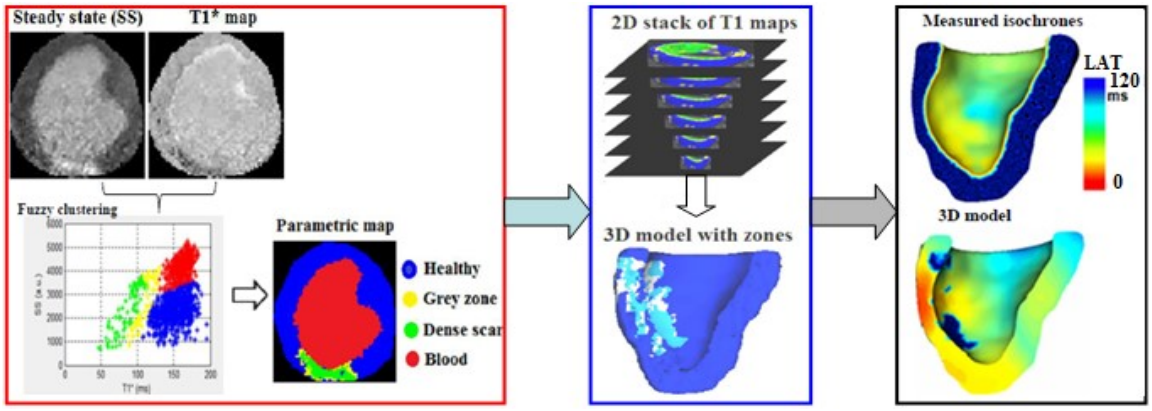

FIGURE 1 **(a)** **(b)** **(c)**

Conclusion: We have successfully developed novel T1*-based heart models that integrate conventional X-ray guided EP mapping data with computational modelling, allowing us to rapidly predict and visualize the electrical wave propagation in 3D through the heart. Future work will focus on improving image resolution and simulating VT inducibility. Such non-invasive predictions may be critical for planning the RF ablation of scar-related VT.

References: [1] Sermesant M *et al* 2005 IEEE Transactions in Medical Imagining; [2] Pop M *et al* Medical Image Analysis 2012; [3] Ferguson S *et al* ImNO 2017; [4] www.vurtigo.ca.

Gd-Free MRI Blood Pool Contrast Agents Based on Manganese(III) Porphyrin Dimers

Hanlin Liu[a,b], Piryanka Sasidharan[b], Vlad Constantinescu[b], Davesh Chauhan[b], and Xiao-An Zhang[a,b,c *]
[a]Department of Chemistry, University of Toronto. [b]Department of Physical and Environmental Sciences,
[c]Department of Biological Sciences, University of Toronto Scarborough.

Introduction: Classic MRI contrast agents (CAs) are mainly based on Gd complexes, and operate by the paramagnetic enhancement of NMR T_1 relaxation (r_1) of surrounding water protons. In MR angiography (MRA), to selectively enhance the visualization of the bloodstream, specialized CAs known as blood pool agents (BPAs) with long vascular retention are employed. The long circulation of BPAs, however, unavoidably increases the risk of the dissociation and accumulation of toxic Gd(III) ions in vivo. This problem has been magnified in patients with renal dysfunctions, as their impeded renal clearance causes in vivo retention of Gd-agents injected, which could lead to a severe adverse effect called Nephrogenic systemic fibrosis (NSF). In March 2017, the European Medicines Agency (EMA) recommended the suspension of the majority of Gd-based CAs with linear chelators from use in MRI. Prior to that, Gadofosveset was withdrawn from the market. Here, we present a series of dimeric Mn(III) porphyrin (MnP) platforms that utilize the significantly less toxic manganese ion and serve as biocompatible and more efficient alternatives to Gadofosveset.

Methods: The synthesized dimers **MnTriCPP2**, **MnP2**, and ***m*-MnP2** (Fig. 1a) were characterized by electrospray ionization-mass spectrometry (ESI-MS), UV-Vis spectroscopy, and ^{1}H-NMR spectroscopy where applicable, and their purities determined by high performance liquid chromatography (HPLC). The field-dependent r_1 was obtained with a fast field cycling NMR relaxometer (SMARTracerÊ) coupled with a cryogen-free superconducting magnet (HTS-110), covering magnetic fields from 0 to 3 tesla. CA binding affinity to human serum albumin (HSA) was acquired through optical studies with UV, fluorescence, and circular dichroism spectroscopies.

Results: The r_1 of all dimers showed promising results as potential BPAs (Fig. 1b). **MnTriCPP2**ôs r_1 increases after binding to HSA, indicative of a slowed-down tumbling of the CA. **MnP2**[1] and ***m*-MnP2** exhibited a mild decrease in r_1 after binding to the protein, caused by water coordination blockage. However, all three MnPs were shown to be more efficient than Gadofosveset at clinical field strengths. Moreover, in vivo studies of **MnP2** demonstrated its safety and efficiency by aiding the visualization of the lungs,[2] an organ often difficult to see under MRI due to low proton density.

Conclusions: Our results demonstrated the superior efficiency of the dimeric MnPs has over the traditional Gadofosveset. We also demonstrated the role of molecular geometry as well as polarity on relaxivity and HSA binding, which gives us insights on future rational design to further optimize the relaxivity and pharmacokinetics of the CAs. Overall, all MnP dimers exhibit higher r_1 at high fields compared to Gadofosveset, making them potential replacements for Gadofosveset and other Gd-based CAs. In the near future, in vivo studies will be performed on ***m*-MnP2** and **MnTriCPP2** to investigate their in vivo efficacy and toxicity.

[1]*J. Med. Chem.* **2014**, *57*, 516-520. [2]*Molecular Imaging* **2014**, *13*, 1-6.

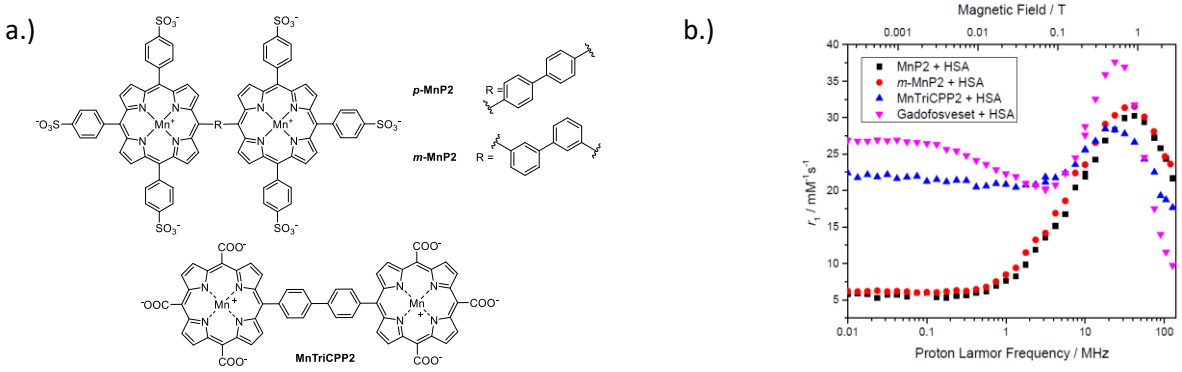

Figure 1. a. Structures of BPAs discussed in the above text. b. Selected nuclear magnetic relaxation dispersion (NMRD) profiles of CAs relative to that of Gadofosveset, all bound to HSA.

Fully Automatic SegmenTal myocardial Relaxometry (FASTR) - Initial results using T1 mapping

Nitishkumar Bhatt[1], Venkat Ramanan[2], Hayden Gunraj[3], LaBonny Biswas[2], Graham A. Wright[2,4], and Nilesh R. Ghugre[2,4]
[1] Systems Design Engineering, University of Waterloo; [2] Schulich Heart Research Program, Sunnybrook Research Institute; [3] Mechatronics Engineering, University of Waterloo; [4] Department of Medical Biophysics, University of Toronto, Toronto

Introduction: T_1 mapping and other relaxometry techniques such as T_2, T_2* have gained clinical importance in myocardial characterization of various cardiomyopathies for detection of edema and fibrosis. To investigate regional variations in T_1 and extracellular volume fraction (ECV) segment-wise, the endocardial and epicardial boundaries are usually drawn manually, which can be laborious and time-consuming, particularly for high volume data. Here we present a fully automated framework (FASTR) to calculate segmental T_1 values accurately and display them using the standard American Heart Association (AHA) model. Initial results are shown using both native and post-contrast T_1 maps with the partition coefficient (λ) computed and displayed.

Figure 1

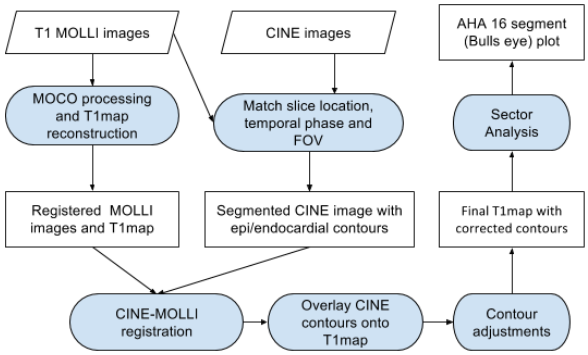

Methods: Pigs were imaged on a 3T scanner in healthy state (N=3) and at week 1 (N=2) following myocardial infarction. Imaging involved routine CINE SSFP, MOLLI T_1 mapping sequence and late Gd-enhanced imaging (LGE). Figure 1 (right) depicts the flowchart of our framework (FASTR). We start with a standard MOLLI T_1 map reconstruction using motion correction (MOCO) [1]. The closest CINE SSFP image in both slice-location and temporal-phase is selected for myocardial segmentation to detect epicardial/endocardial contours based on a previously published technique [2]. These contours are transferred to T1 maps and serve as ñinitialò guess for T1 map segmentation. Next, corrections are applied to ensure accurate contouring - 1) contour points are translated to the closest border point (edge) by applying an edge detection filter to exclude partial voluming from blood; 2) points are further shifted inwards towards the mid-myocardium to completely avoid the LV and RV blood pools and lung interface. The above process is conducted for both native and post-Gd T1 maps to arrive at the AHA segment-wise T1 and partition coefficient $\lambda = \frac{R_1 myo,post - R_1 myo,pre}{R_1 blood,post - R_1 blood,pre}$ where $R_1 = \frac{1}{T_1}$.

Results. Figure 2 shows a mid-cavity slice segmentation of T_1 maps with FASTR and the LGE image from an animal 1-week post-infarct. The AHA bullseye plots are shown for T_1 maps (native and post-contrast) and ɔ. Infarct was confirmed from the LGE image and FASTR performed well for identifying the myocardial region on both native and post-contrast T1 maps. In the presence of minor artifacts, the contouring remained robust. Segmental T1 and ɔ bullseye plots demonstrated expected deviations in the infarct region ï native T1 and ɔ were significantly elevated due to edema and scar, respectively while post-contrast T1 was reduced.

Conclusions. Here we have presented a novel method to automatically reconstruct and display myocardial segment-wise relaxometry parameters using CINE SSFP derived contours. FASTR offers relative insensitivity towards pathophysiological responses such as edema and fibrosis and provides an efficient framework for processing high volume data. Initial results have been shown using T1 mapping but the technique can be generalized and extended to T2 and T2* relaxation as well. Further studies are needed to validate the technique.

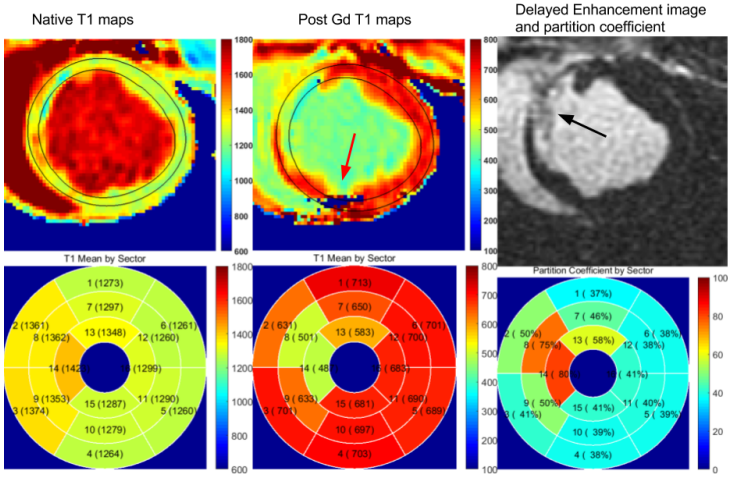

Figure 2: Results from an infarct model (1 week post-infarct, N = 2) are shown. First row: Final contours from native and post-contrast T1 maps show that robust contouring is achieved even in the presence of infarcts and T1map reconstruction artifacts (red arrow). The LGE image shows the extent of infarct in the septal region (black arrow). Second row: The AHA segment-wise plots display the native-T1 maps, post-contrast T1 maps and the partition coefficient (ɔ) respectively. We noted systematic increase in λ in infarct zone (>50%) relative to remote (<40%)

References: [1] Xue et al. MRM. 2012; 67:1644.
[2] Lu et al. Lec Notes CS, 2009. pp. 339.

Ultrasound Registration for Intra-cardiac Surgical Guidance: Proof of Concept

Hareem Nisar, John Moore, Terry Peters
VASST Lab, Robarts Research Institute, Western University

Introduction: Atrial fibrillation (AF) is a highly prevalent arrhythmic disease which is treated by trans-catheter ablation therapy. In about 60% of the patients, the arrhythmia reoccurs within a year[1]. Trans-septal puncture is a pre-requisite for AF ablation and is guided by intra-cardiac echocardiography (ICE). However, the recognition of cardiac structures and localization of exact puncture site is still challenging and inaccuracy can lead to recurrence of arrhythmia and puncturing of pericardium.

The recently introduced Conavi Foresight ICE[2] probe generates a cone-shaped surface image via rotating transducers. With a 360ę imaging field of view this 2.5D ICE system also acquires both side-looking and forward-looking views.

To address the challenges with intra-cardiac surgical interventions and improve visualization we propose to place the Conavi Foresight ICE in the context of 3D trans-esophageal echocardiographic (TEE) imaging.

The purpose of this abstract is to present the methodology of our proposed technique in order to generate discussion. We describe a proof-of-concept study aimed at allowing the Conavi Foresight ICE probe to be employed in conjunction with a 3D TEE volume to provide context for the ICE image during navigation and monitoring during catheter ablation.

Method: We developed a polyvinyl alcohol based model of the left atrium and imaged it using Conavi Foresight system. Imaging angle was kept greater than 70Üto ensure side viewing. 3D TEE data were acquired by imaging the same left atrium model using Philips iE33 echo machine. While the ICE and TEE images could potentially be registered by tracking each modality using magnetic tracking technologies, this approach adds additional complexity to the system. We therefore propose to use optimized image registration techniques to place the two image datasets in the same frame of reference. We will evaluate various registration metrics, including Normalized Mutual Information, Normalized Cross Correlation and Squared Sum of Differences, with respect to robustness, and speed to determine the most appropriate approach for this unique 2.5D to 3D registration process.

Result: Once the simulated images are successfully registered to the 3D TEE data, the results will be assessed in terms of the mean-squared error between the recovered transformations and those defined by initial displacements prior to registration, equivalent to comparing the translation and rotation of structures in the registered ICE image compared to those observed in the 3D TEE images.

Conclusion: This is preliminary study towards use of Conavi Foresight ICE system in surgical guidance and recognition of cardiac structures. We believe that visibility and navigation during minimally invasive intra-cardiac surgeries can be improved by using the high-speed Conavi Foresight ICE probe in conjunction with 3D TEE volume in real time.

[1] R. Weerasooriya et al., ñCatheter Ablation for Atrial Fibrillationò, Journal of American College of Cardiology, 57 (2) 160-166, 2011

[2] B. Courtney et al., ñTCT-104 Initial Pre-clinical and Clinical Use of Mechanical Intracardiac Echocardiography System with 3D Viewing, Color Doppler and Side-viewing Capabilitiesò, Journal of the American College of Cardiology, 70 (18 Supplement) B45-B46, 2017

Exploring the Effects of Dialysate Cooling on Liver Hemodynamics during Hemodialysis with CT Perfusion

Raanan Marants[1,2], Elena Qirjazi[3], Chris W. McIntyre[1,2,3,4], Ting-Yim Lee[1,2]
[1]*Department of Medical Biophysics, Western University, London, Canada*
[2]*Lawson Health Research Institute and Robarts Research Institute, London, Canada*
[3]*The Lilibeth Caberto Kidney Clinical Research Unit, London Health Sciences Centre, London, Canada*
[4]*Division of Nephrology, London Health Sciences Centre, London, Canada*

Introduction: Intradialytic hypotension is an independent predictor of mortality in hemodialysis (HD) patients. It has been shown that reducing the temperature of the dialysate is an effective intervention to reduce the frequency of intradialytic hypotension and ameliorate HD-induced circulatory stress. Dialysate cooling is a favorable intervention because it does not adversely affect dialysis efficiency, HD patients generally find it tolerable, and it is universally available and can be implemented at no additional cost. Studies have shown that dialysate temperature reduction is an effective hypothermic strategy for the heart and the brain, but its impact on intradialytic liver hemodynamics is unknown. The goal of this study was to use CT perfusion imaging to quantitatively assess liver blood flow under standard and cooled dialysate conditions during HD treatment. This is important to validate because if HD has the potential to cause recurrent hepatic dysfunction, interventions before, during or after the treatment may be initiated to reduce or prevent long-term liver damage. It was postulated that patients undergoing cooled dialysate HD will exhibit attenuated hepatic hemodynamic changes compared to their standard HD.

Methods: 15 patients provided written informed consent for the study and were randomized to receive either standard (36.5ÁC) or cooled (35ÁC) HD first in a 2-visit crossover study design. For each visit, CT perfusion imaging was performed at three timepoints (before, 3 hours into, and after HD) on a 256-slice CT scanner (GE Healthcare) without any interruption to HD treatment. Each scan was done without breath-hold for 118 seconds immediately following a bolus injection of iodinated contrast agent. The 3-hour measurement point was chosen because it represents peak intradialytic stress (defined from previous studies of HD-induced myocardial injury). Misalignment among CT perfusion images was minimized using non-rigid registration software, and parametric liver perfusion maps (total liver, hepatic arterial and portal venous blood flow) were generated from the registered CT images. Statistical analysis was performed using non-parametric tests.

Results: Preliminary analysis of 8 patients has been completed. The average liver blood flow results for the standard and cooled HD cases are presented below in Figure 1.

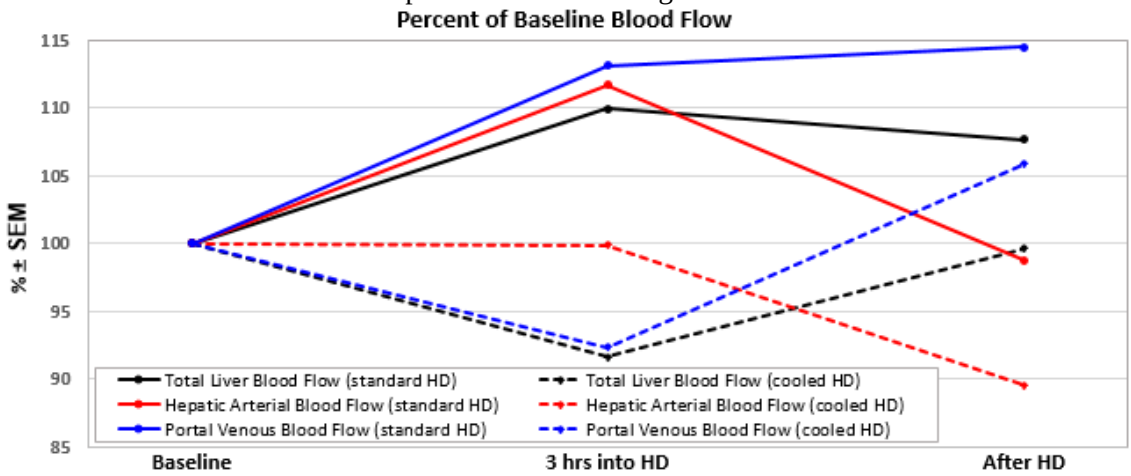

Figure 1: Percent of baseline liver blood flow before, 3 hours into, and after HD (standard = solid lines, cooled = dotted lines). Results are given as average Ñ SEM of all study patients for total liver blood flow (black curves), hepatic arterial blood flow (red curves) and portal venous blood flow (blue curves).

Conclusions: In a previous 15 patient study where only standard HD was used, it was found that dialysis had no effect on total liver blood flow, however, the hepatic arterial and portal venous blood flow demonstrated trends of increasing and decreasing, respectively, indicative of hemodynamic shifts in blood supply to the liver. This differs from the standard HD results of the present study, where all hepatic perfusion measures increased during dialysis. This discrepancy may be due to the preliminary nature of the presented results (i.e., only 8 patients analyzed so far). In addition, there was a clear difference in signal between the standard and cooled HD perfusion results with opposing trends at peak stress. It is also worth noting that the magnitude of perfusion changes from baseline was smaller for cooled HD compared to standard HD, suggesting that the cooled dialysate treatment successfully reduced the hemodynamic impact of HD.

Poster Presentation Abstracts

Session 6: Maternal – Fetal Imaging

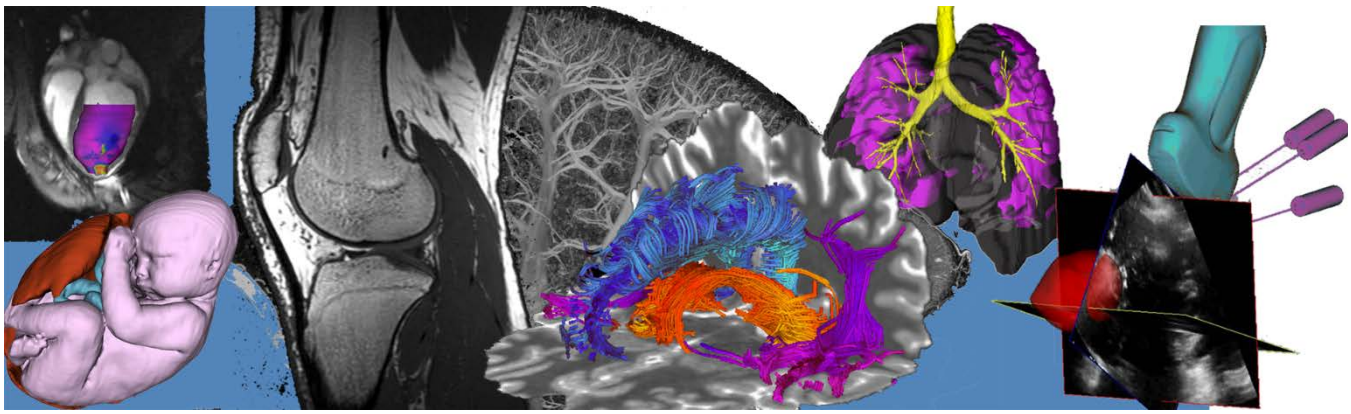

Multidimensional fetal flow imaging with MRI

Datta Singh Goolaub[12], Christopher W. Roy[2], Dafna Sussman[2], Mike Seed[34], Christopher K. Macgowan[12].
[1]Medical Biophysics, University of Toronto, Toronto. [2]Translational Medicine, The Hospital for Sick Children, Toronto. [3]Cardiology, The Hospital for Sick Children, Toronto ON, Canada. [4]Paediatrics, University of Toronto, Toronto.

Introduction

Velocity sensitive phase contrast (PC) MR is the gold standard for measuring blood flow in postnatal subjects and, using image-based cardiac gating, has enabled quantification of fetal blood flow in both normal pregnancies and fetal congenital heart disease[1]. Unfortunately, studies of fetal blood flow have been limited by motion, placing constraints on the achievable spatial resolution, temporal resolution, and number of dimensions of flow sensitivity[2]. Recent studies have overcome these limitations for anatomical imaging of the fetal heart by implementing a golden-angle radial acquisition, which enables intermediate real-time (RT) reconstructions for performing motion correction and image-based gating[2,3]. The motion-corrected and retrospectively gated data are then combined to produce a high-quality CINE reconstruction using compressed sensing (CS)[4,5]. Unfortunately, conventional PCMR requires repeating each radial spoke for each flow encode. This lowers the temporal resolution of the RT reconstructions relative to anatomical imaging, reducing the accuracy of image-based gating strategies. In this work, we propose an alternate strategy that increments both the golden-angle radial trajectory and the velocity encoding direction, synchronously, thereby preserving the temporal resolution of RT reconstructions. We combine this sampling strategy with translational motion correction, image-based gating (metric optimized gating, MOG)[2], and CS to reconstruct high-quality flow images from accelerated acquisitions. Experimental validation of this strategy is performed in an adult volunteer. Using this pipeline, we present the first multidimensional PCMR velocity maps of the human fetal heart.

Methods

Validation of the proposed acquisition and reconstruction strategy was performed in a healthy adult volunteer Ungated scans were performed, although the pulse gating signal was logged for subsequent comparison to MOG. MOG was performed on RT reconstructions[2,6] and final CS CINE reconstructions of the retrospectively gated data were performed. Quantitative evaluation of the proposed sampling and reconstruction scheme compared cardiac gating timing and flow parameters obtained using MOG versus those obtained using pulse gating. Feasibility of the proposed methods in the fetal population was assessed in two healthy pregnancies (32 weeks gestation). Acquisitions were motion compensated and then gated with MOG. Final CINE reconstructions were performed as in the adult.

Results

In adults, R-R intervals detected by MOG agreed well with pulse gating with a mean timing error of 35ms. The MOG and pulse gated flows had an RMSE of 5.1cm/s across all four acquisitions, and differed in peak flow by -0.1Ñ2.7cm/s. Reconstruction of fetal flow CINEs in four-chamber and three-vessel views show the complex hemodynamics within the fetal heart. Figure 1 illustrates this using velocity vectors of the in-plane flow only, depicting blood passage through the heart with in-plane speeds reaching 80cm/s during peak filling and contraction. The proposed sampling strategy allowed RT reconstructions at high temporal resolution, which was required for image-based gating. To achieve similar RT imaging quality with conventional PCMR sampling leads to unacceptable temporal resolution for fetal applications. This proposed approach may also be useful for multidimensional flow studies in uncooperative subjects, such as neonates or the elderly.

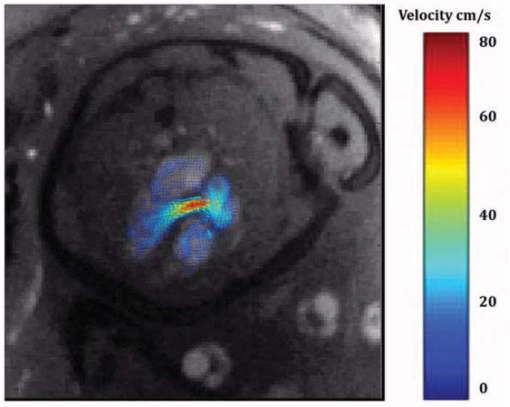

Fig. 1: In-plane velocity vector plot of the blood flow in the four-chamber view of the fetal heart (1x1x4mm3). The magnitude of in-plane flow components in the heart is color coded. The direction of the arrows depicts the direction of the in-plane blood flow.

Conclusions

We have proposed and demonstrated a novel sampling and reconstruction pipeline targeting fetal blood flow applications. This pipeline was validated in an adult study, and its feasibility tested in two fetuses resulting in the first multidimensional velocity maps of the fetal heart obtained using MRI.

1. Seed M et al. JCMR. 2012; 14:79. **2.** Roy C et al. MRM. 2017; 77(6):2125-2135. **3.** Chaptinel J et al. Proc 24th Annual Meeting ISMRM, Singapore;2016. **4.** Lustig M et al. MRM. 2007; 58(6):1182-95. **5.** Otazo R et al. MRM. 2015; 73(3):1125-1136. **6.** Jansz M et al. MRM. 2012; 64(5):1304-14.

Fat Quantification Using A High-Resolution Bipolar Gradient Water-Fat Sequence

Alireza Akbari[1,2], Lanette J Friesen-Waldner[1], Timothy R H Regnault[3,4], and Charles A McKenzie[1,2]
[1]Medical Biophysics, Western University, [2]Robarts Research Institute, [3]Obstetrics and Gynaecology, Western University, [4]Physiology and Pharmacology, Western University

INTRODUCTION Quantifying adipose tissue in guinea pigs, a model for studying obesity, is challenging because the fat tissue volume is much smaller than humans due to their small size. Hence, high-resolution images are required to reduce partial volume effects and minimize segmentation errors.[1] Conventional water-fat imaging based on quantitative IDEAL[2] uses several unipolar gradient echoes that are acquired over multiple repetition times (TRs) to achieve optimal echo-spacing. However, a bipolar water-fat imaging sequence would require fewer TRs to acquire the requisite gradient echoes, leading to a more time-efficient sequence.[3] In this work, we investigate how a high-resolution bipolar sequence would perform in quantifying fat *in vivo* compared to a conventional unipolar sequence.

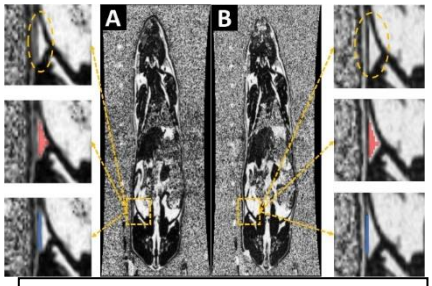

Figure 1. Representative unipolar (A) and bipolar (B) Proton Density Fat Fraction maps of a guinea pig. The box indicates the region selected to perform abdominal fat quantification. The red mask represents the ROI selected for abdominal fat quantification. The blue line represents the boundary region selected to assess partial volume effect.

METHODS Four guinea pigs were scanned using a 3T MR scanner (Discovery MR 750, GE Healthcare, Waukesha, WI) and 32-channel cardiac coil. Imaging parameters including scan time were kept the same for both sequences except resolution: bipolar sequence voxel-size = 0.94 x 0.86 x 0.9 mm^3(= 0.73 mm^3) and unipolar sequence 0.94 x 0.56 x 0.7 mm^3(= 0.37 mm^3). Proton Density Fat Fraction (PDFF) maps were produced for sequence comparison. To assess the partial volume improvement in bipolar PDFF maps, a region of interest (ROI) was drawn on the boundary between visceral (VF) and subcutaneous fat (SCF). The mean PDFF were computed and an unpaired two-tailed t-test was performed. Fat was quantified by drawing ROIs in VF on PDFF maps.

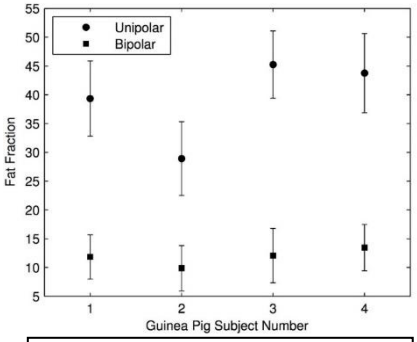

Figure 2. *In vivo* Proton Density Fat Fraction (PDFF) measurements in the boundary between visceral and subcutaneous fat regions in four guinea pigs. Unipolar PDFF measurements showed higher values as a result of partial volume effects ($p<0.001$).

RESULTS Examples of bipolar and unipolar images are shown in Figure 1. Figure 2 reports higher fat fraction measured in the boundary between VF and SCF in unipolar PDFF maps as compared to the same regions in bipolar PDFF maps ($p<0.001$). The measured fat fractions were the same per region between unipolar and bipolar images (Table 1).

DISCUSSION The bipolar sequence performs like unipolar for quantifying fat *in vivo* while doubling the image resolution. Higher resolution helps delineate the boundary between fat and other tissues where it is unclear due to partial volume effects. The boundaries between SCF and VF in unipolar PDFF maps suffer from partial volume effects as their mean fat fraction are higher compared to the same regions in bipolar PDFF maps. Therefore, the high-resolution bipolar sequence would be ideal for both manual and automated segmentation to produce more accurate quantitative results.

CONCLUSION Compared to unipolar, high-resolution bipolar water-fat imaging reduces partial volume effects without affecting fat quantification in the same imaging time.

REFERENCES **1.** Ranefall P, Bidar AW, Hockings PD. JMRI. 2009;30(3):554-60. **2.** Reeder SB, McKenzie CA, Pineda AR, et al. JMRI. 2007 Mar 1;25(3):644-52. **3.** Soliman AS, Wiens CN, Wade TP, et al. MRM. 2016; 75:2000ï 2008.

Table 1. In vivo abdominal and thoracic fat quantification in four guinea pigs using unipolar and bipolar water-fat imaging. The result of t-test for difference (unipolar minus bipolar) against 0 for fat volume was not significant ($p=0.314$), indicating the results were statistically similar.

Guinea Pig #	Unipolar/Bipolar	Region	ROI Volume [mm^3]	Number of Voxels	Mean Signal Intensity	Standard Deviation
1	Uni	Abdominal	121.6	524	85.3	11.9
	Bi		122.7	680	82.6	18.3
2	Uni		52.4	226	81.2	13.4
	Bi		50.5	280	82.7	16.7
3	Uni	Thorasic	89.1	384	86.0	9.1
	Bi		93.3	517	80.1	12.7
4	Uni		142.0	612	83.5	9.3
	Bi		147.1	815	82.3	12.2

Fatty Liver Assessment in Obese and Non-obese Pregnant Women with Water-Fat MRI

Stephanie A. Giza[1], Simran Sethi[1], Takashi Hashimoto[1], Barbra de Vrijer[2,3], Charles A. McKenzie[1,2]
[1]Medical Biophysics, Western University, [2]Division of Maternal, Fetal and Newborn Health, Children's Health Research Institute, [3]Obstetrics and Gynaecology, Western University, London, Ontario

Introduction: Assessment of metabolic health during pregnancy is indicative of the future health of both the mother and fetus. Non-alcoholic fatty liver disease (NAFLD) is the most common liver disease in the world, and is considered part of the metabolic syndrome. In non-pregnant Caucasian women, the age-adjusted prevalence of NAFLD ranges from 6.5% with normal body mass index (BMI) to 25.3-47.5% in women with obesity[1]. Approximately 29% of women of reproductive age are obese[2], suggesting that a large portion of the pregnant population may be affected by NAFLD.

Proton density fat fraction (PDFF) is an imaging biomarker of the tissue lipid concentration, and has been found to have high precision and accuracy for quantification of hepatic steatosis[3]. The objective of this study was to compare the mean hepatic PDFF in a group of pregnant women with normal pre-pregnancy BMI to a group of women with pre-pregnancy BMI in the obese range. We hypothesized that due to a greater expected prevalence in the obese group, the mean hepatic PDFF of the obese group would be greater than those with normal BMIs.

Methods: Volunteers with singleton pregnancies and gestational ages between 29 and 38 weeks were imaged in a wide-bore (70 cm) 1.5T MRI (GE MR450w). 3D water-fat MRI (TR 9.7-12.7 ms, flip angle 6-7Á, Field of View 50 cm, 160Ĭ 160 or 128Ĭ 128 pixels, slice thickness 4-6.5 mm, 42-78 slices, ARC acceleration 2x phase 2.5x slice and 32x32 calibration lines, acquisition time 12-24 s) was used to image maternal liver during breath hold. Volunteers were divided into a normal weight group (18 kg/m^2 < pre-pregnancy BMI Ò25 kg/m^2) and an obese group (pre-pregnancy BMI Ó30 kg/m^2). A 10 mm region of interest was placed in a vessel-free region of the lower right lobe of the liver using 3D Slicer (v4.7.0-2016-12-06)[4]. The mean PDFF was measured and compared between normal weight and obese groups using a Mann-Whitney test in GraphPad Prism (v7.03).

Results: Fifteen women had a normal BMI, and 10 women were obese. The Mann-Whitney test did not show a significant difference of mean hepatic PDFF between the normal BMI and obese groups (p=0.28) (Figure 1). One woman in the normal BMI group (Figure 2) and one in the obese group had hepatic PDFFs consistent with patients that have moderate and mild NAFLD[5] respectively. The observed prevalence of NAFLD may be lower than previously described using ultrasound techniques due to ameliorating effects of nutrition partitioning in pregnancy, lifestyle changes in obese pregnant patients or a selection bias towards metabolically healthy women who are more likely to conceive.

Conclusion: In conclusion, the mean hepatic PDFF was not elevated in a sample of obese pregnant women compared to those with a normal BMI.

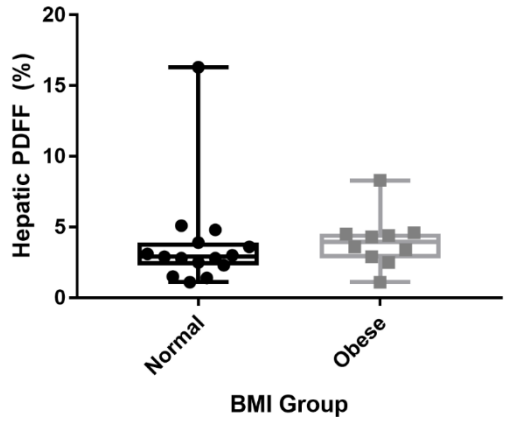

Figure 1. Box and whisker plot of hepatic PDFF for normal BMI and obese women.

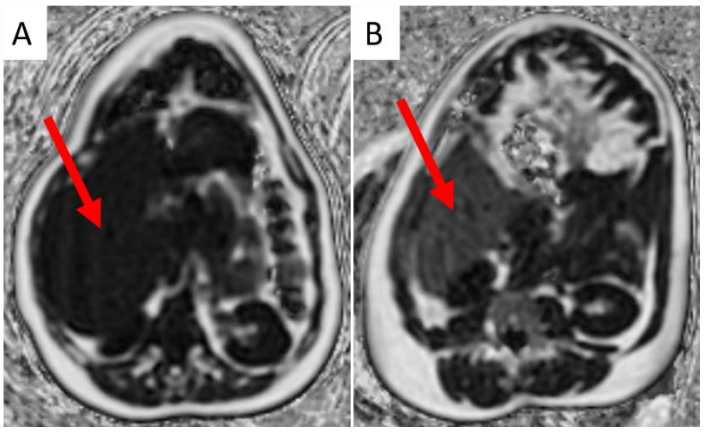

Figure 2. PDFF map with A) no fatty liver and B) moderate fatty liver. Red arrows indicate livers.

References: (1) Lazo, M., et al. Am J Epidemiol 2013;178(1):38-45. (2) Hedley, A.A., et al. JAMA 2004;291(23):2847-2850. (3) Hines, C.D., et al. J Magn Reson Imaging 2011;33(4):873-881. (4) Federov, A., et al. Magn Reson Imaging 2013;30(9):1323-1341. (5) Kuhn, J.P., et al. Radiology 2017;284(3):706-716.

A Novel Method for Registering left atrium Fibrosis from LGE-MRI to Electroanatomical Maps

Jieun Lee[1, 2], Rebecca Thornhill[2, 3], Pablo Nery[2], Rob DeKemp[2], Elena Pe¶a[3], David Birnie[2], Andy Adler[1], Eranga Ukwatta[1]

[1]Department of Systems and Computer Engineering, Carleton University, Ottawa, ON, Canada
[2]University of Ottawa Heart Institute, Ottawa, ON, Canada
[3]The Ottawa Hospital, Ottawa, ON, Canada

Abstract:

Abnormal electrical conduction and excitability in left atrial (LA) fibrosis may serve as a substrate for atrial fibrillation (AF). Therefore, determination of LA fibrosis by late gadolinium-enhanced magnetic resonance imaging (LGE-MRI) may aid in the AF cardiac ablation therapy. The purpose of this work was to develop a method for registering regions of low bi-polar voltage on Electroanatomical voltage mapping system (EAMS) with regions of hyperenhancement in LGE-MR images. Twenty patients with persistent AF participated in the study who underwent MRI scanning, and invasive procedure to obtain endocardial peak voltages using an intra-vascular cardiac catheter. An experienced radiologist manually segmented the LA image in MR. We utilized the segmented myocardium of the LA as the region of interest; several methods based on intensity thresholds were used to delineate areas of fibrosis on MR. We used the iterative closest points (ICP) algorithm for registering of endocardial surface in EAMS and segmented LA surface in MR. We then applied non-rigid ICP algorithms (NICP). Based on the spatial proximity, the points from MR images were aligned to the surface mesh of EAMS. For each patient image, the assessment for the registration was evaluated using manually chosen eight landmark points around all four pulmonary veins (PVs) of the LA using the Euclidean distance measurement. The target registration error using landmarks improved from 24.9 mm to 0.9 mm after NICP-based registration (see Fig 1). The results of landmarks distance demonstrate that our registration method reduces the target registration error significantly. The scar assessment resulting from registration using NICP suggests that there is a substantial spatial correlation between low voltage regions on EAMS and increased distribution of gadolinium on LGE-MRI (see Fig 2).

Fig1. A sample result of the suggested registration method. LA surface is displayed in 3D space under ParaView environment (Kitware Inc. New York, NY, USA). The distance value of the registration result shows both qualitative in color and quantitative in a numeric bar. The measurement of the unit is millimetre. A is a posterior and B is an anterior view of the LA.

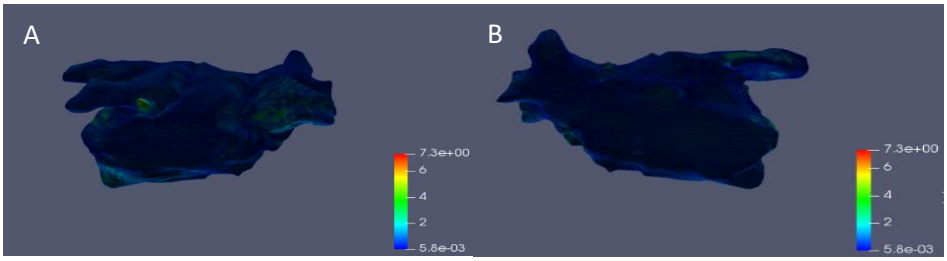

Fig2. A sample result for scar correlation between EAMS and LGE-MRI with three scar thresholds. Low voltage in EAMS and scar regions in LGE-MRI were displayed in the LA of EAMS. We chose a grey color for the LA to display MR scars and EAMS low voltage visibly. The red color represents low voltage with below 0.5 mV in EAMS and the blue color represents fibrosis in LGE-MRI. A is Full-width-half-maximum (FWHM), B is mean + 1 standard deviation (STRM1), and C is mean + 2 standard deviations (STRM2).

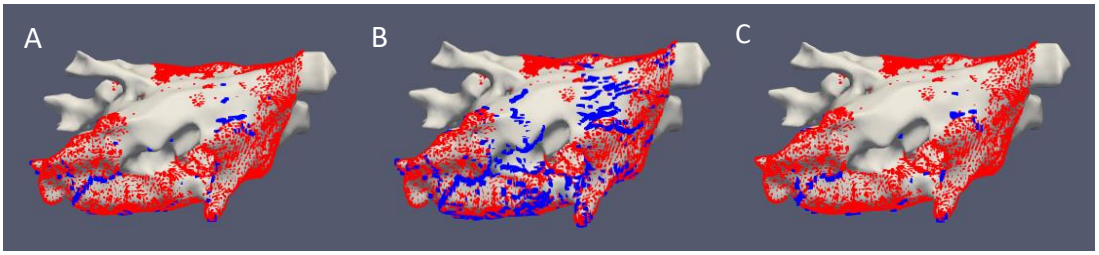

Poster Presentation Abstracts

Session 7: New Imaging Approaches

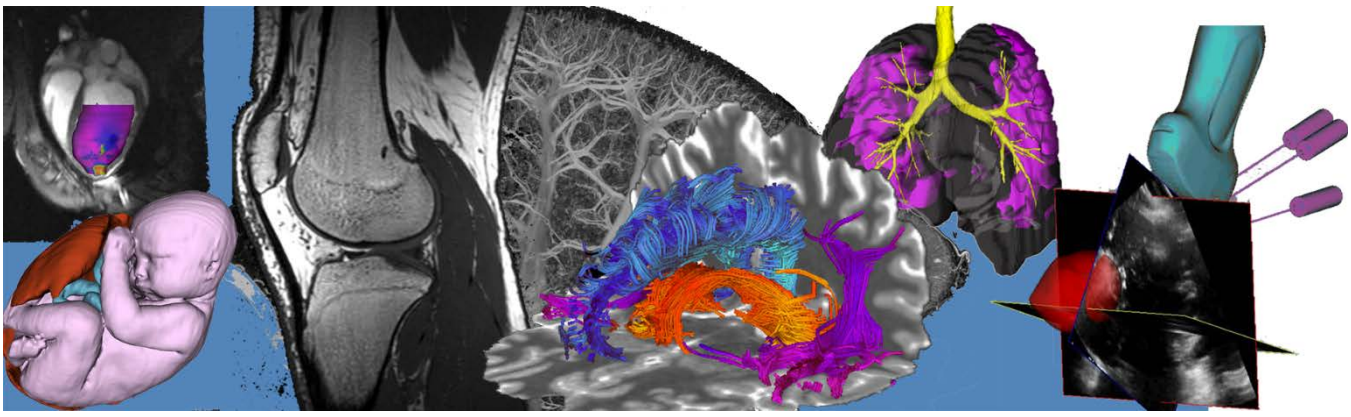

Dynamic Phosphorus Spectroscopic Imaging of Muscle using Flyback Echo Planar Imaging trajectories

Alejandro Santos Diaz[1], Diana Harasym[1], Michael D. Noseworthy[1,2]
1. School of Biomedical Engineering, McMaster University, Hamilton, Canada
2. Electrical and Computer Engineering, McMaster University, Hamilton, Canada

Introduction. Dynamic exercise-recovery studies of phosphocreatine (PCr) demand a high temporal resolution and thus are usually performed using single voxel ^{31}P-MRS [1,2] or ^{31}P-MRI [3,4]. A recent study showed implementation of spiral trajectories to perform ^{31}P spectroscopic imaging experiments of this kind at 7T [5]. In this preliminary study we show that flyback ^{31}P-EPSI is suitable for performing dynamic studies of PCr recovery in human calf muscles at 3T.

Methods. Experiments were performed using a 3T GE MR750 system (GE Healthcare, Milwaukee, WI) and a home designed/built 31P surface coil tune/matched specifically for calf muscles. Gradient trajectories were optimized to achieve a 2x2 cm^2 resolution over a 12x12 cm^2 FOV (slice thickness = 4 cm) and a spectral bandwidth of 1110 Hz. This configuration allowed us achieve a temporal resolution of 9 seconds with TR= 1500 [ms]. 5 Hz Lorentian apodization was applied to the spectra. The region of interest was shimmed on a T2-weighted proton image used as anatomical reference. One healthy volunteer (male, 20 years old) participated in the experiment. The protocol consisted on taking 8 temporal points as baseline, followed by three minutes of plantar flexion with a frequency of 0.5 Hz using a home designed/built ergometer and a load of 40% maximum voluntary contraction (MCV). Subsequently 16 temporal points were acquired during recovery. No acquisition was performed during exercise. Data was fitted using the OXSA package [6]. **Fig. 1** shows a diagram of the pulse sequence and the experimental setup.

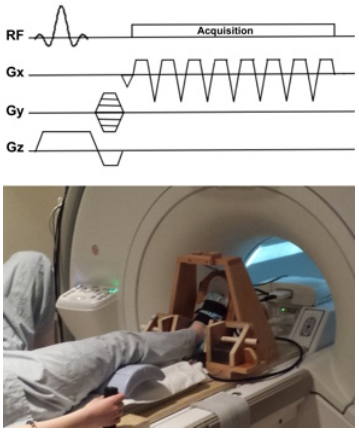

Fig 1. Diagram of the pulse sequence (Top) and experimental setting (Bottom)

Results. **Fig. 2** shows the imaging area and the PCr and Pi amplitudes over time. PCr signal dropped roughly 65% right after the exercise whereas Pi increased. Additionally, it was possible to detect a change in pH due to a lower chemical shift for Pi. **Fig. 3** shows spectra of the Gastrocnemius medialis position across time where the kinetics of PCr is clearly depicted.

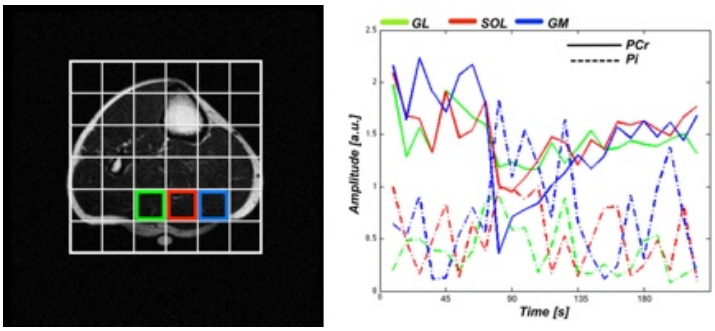

Fig 2. Imaging matrix (left) and temporal evolution of PCr and Pi signals through the experiment (right). GL: Gastrocnemius lateralis. SOL: Soleus. GM: Gastrocnemius medialis.

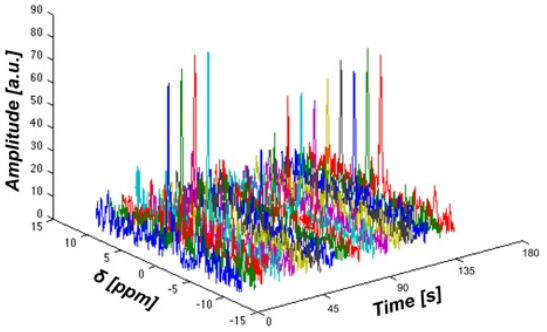

Fig 3. ^{31}P Spectra from the GM position across the experiment. Four baseline and 12 after exercise temporal points are shown.

Conclusions. We were able to track recovery of the PCr and Pi signals as well as the change in intracellular pH (lower chemical shift). Best fitting was achieved right after exercise showing corresponding values between PCr and Pi. In this preliminary work we showed the feasibility of performing dynamic studies of calf muscles using flyback Echo Planar Imaging readout trajectories.

References. 1. Chance B, et al. NMR in Biomedicine. 2006;19(7):904ï 926. 2. Fiedler GB, et al. Scientific reports. 2016;6:32037. 3. Parasoglou P, et al. Magnetic Resonance in Medicine. 2012;68(6):1738ï 1746. 4. Schmid AI, et al. 2016;75(6):2324ï 31. 5. Valkovic L, et al. NMR in Biomedicine. 2016;29(12):1825ï 1834. 6. Purvis L, et al. PLoS One 12:e0185356, 2017.

Acknowledgements

CONACYT NSERC CRSNG

Compressed sensing reconstruction with 23Na MRI

Paul Polak[1], Michael D. Noseworthy[1,2,3]

[1] School of Biomedical Engineering, McMaster University, Hamilton; [2] Department of Electrical and Computer Engineering, McMaster University; [3] Imaging Research Centre, St. Josephôs Healthcare, Hamilton ON.

Introduction: In vivo 23Na MRI is desirable due to sodium's essential role human metabolism (1ï 2), but its acquisition suffers from many inherent technical challenges. Among these are a low gyromagnetic ratio, short T1/T2 times, dedicated transmit/receive coils, non-standard pulse sequences, low signal and long acquisitions (3ï 4). Compressed sensing (CS) techniques (5) can be utilized in order to improve image quality without increasing scan times. We present here quantitative measures of compressed sensing 23Na MRI reconstructions in saline phantoms.

Subjects and Methods: Experiments were conducted using a General Electric 3T MR750 (GE Medical Systems, Waukesha, WI), using a custom designed and built birdcage head coil (resonant frequency=33.7 MHz). A saline phantom was constructed using 8 concentrations of NaCl in distilled water (430 mM, 215 mM ... 3.36 mM). Acquisition was via a 3D-radial, density adapted, projection sequence at differing acquisition window lengths (4 ms, 12 ms, 16 ms, and 25 ms). The projections were designed to have a resolution of 3x3x3 mm^3. The other sequence parameters were held identical ï TR: 120 ms; FOV: 180 mm; readout bandwidth: +/- 125 kHz; number of spokes: 11310; acquisition length: 22:42. Reconstruction utilized the Berkeley Advanced Reconstruction Toolbox (6). Tested reconstructions: non-uniform FFT (NUFFT); conjugate gradient l2-norm, regularization parameters of 25, 50, 100; total variation (TV), regularization of 1. Python was used to create NIFTI files were created from the reconstruction sampled to an in-plane resolution of 128x128. Signal to noise ratio (SNR) statistics were calculated from the images ï the results are in Figure 2.

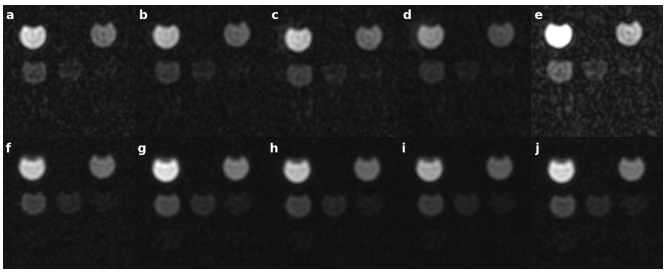

Figure 1: (a-e) reconstructed axial slices for 4 ms acquisition window, for NUFFT, l2/25, l2/50, l2/100, and TV. (f-j) reconstructed axial slices for 25 ms acquisition window, for NUFFT, l2/25, l2/50, l2/100, and TV.

Discussion: As expected, the l2-norm and TV reconstructions provide an increase in SNR for each level of undersampling. While the l2/100 gives the best SNR, there is a discernible loss in edge contrast at this level (Figure 1d and 1i). Of the methods shown here, the l2/25 appears to give the best trade-off in terms of increased SNR over the NUFFT method with acceptable edge contrast. Unsurprisingly, the best reconstructions were from the acquisitions with the most acquired data, with the CS-methods performance decreasing with the quality of the input data. It is worth noting that the 4 ms sequence acquired 6.25 time less data than the 25 ms sequence ï were this 6-fold saving in data acquisition translated into a reduced acquisition time, scan time would be < 4 minutes.

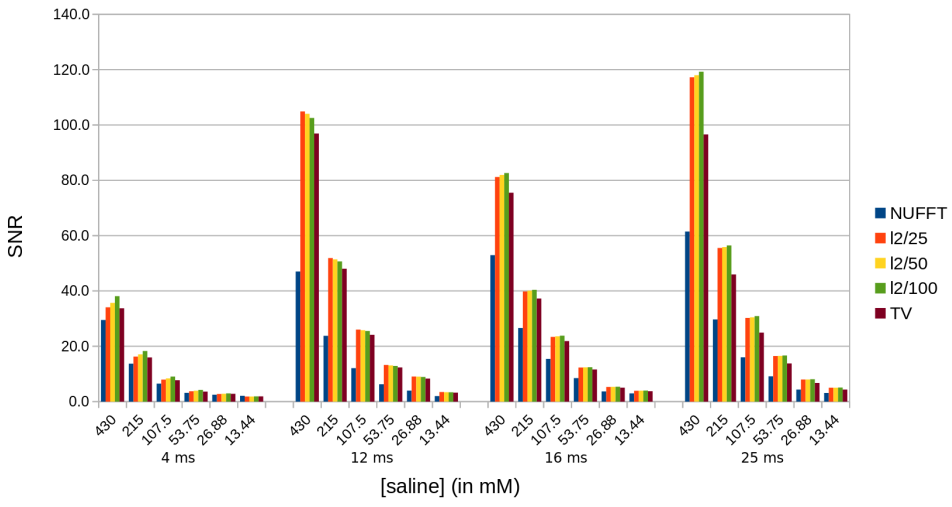

Figure 2: SNR measurements for the different reconstruction techniques, versus saline concentration and acquisition window.

Conclusions: This work demonstrates the performance and feasibility of CS reconstructions for 23Na MRI for levels of undersampling. CS methods are essential to overcome the inherent technical challenges for sodium MRI.

1. Rose AM, Valdes R. Understanding the sodium pump and its relevance to disease. Clin Chem 1994;40:1674ï 1685. 2. Skou JC, Esmann M. The Na, K-ATPase. J Bioenerg Biomembr 1992;24:249ï 261. 3. Madelin G, Lee JS, Regatte RR, Jerschow A. Sodium MRI: Methods and applications. Prog Nucl Magn Reson Spectrosc 2014;79:14ï 47. 4. Nagel AM, Laun FB, Weber M-A, Matthies C, Semmler W, Schad LR. Sodium MRI using a density-adapted 3D radial acquisition technique. Magn Reson Med 2009;62:1565ï 1573. 5. Lustig M, Donoho D, Pauly JM. Sparse MRI: The application of compressed sensing for rapid MR imaging. Magn Reson Med. 2007 Dec;58(6):1182ï 95. 6. Martin Uecker, Frank Ong, Jonathan I Tamir, Dara Bahri, Patrick Virtue, Joseph Y Cheng, Tao Zhang, and Michael Lustig, Annual Meeting ISMRM, Toronto 2015, In Proc. Intl. Soc. Mag. Reson. Med. 23:2486

Automating metal level selection in metal artefact correction

Ivailo Petrov[1], Alexandra Blokker[1,3], D. W. Holdsworth[1,2,3] and Maria Drangova[1,2]
[1]Robarts Research Institute, [2]Dept. of Medical Biophysics, [3]Biomedical Engineering Graduate Program
The University of Western Ontario, London, Ontario, Canada

Introduction: Computed tomography (CT) is an established, useful, and widely used medical imaging technique. Unfortunately, dense and/or thick materials in the field of view can cause severe image degradation and loss of information. This can be a significant problem in many medical applications that require high quality images of implants or hardware. Many different approaches have been implemented over the past forty years[1] with varying success. Metal artefact reduction (MAR) technique[3], developed previously, was successfully applied on several materials and scanners. The purpose of this study was to automate the selection of the global threshold needed for proper metal segmentation before MAR.

Methods: ***Objects:*** A fresh-frozen human cadaveric knee joint (age: 54, female, right)[2] and fresh-frozen porcine ACL were used to test the method. Zirconium dioxide (ZrO_2) beads (0.8 mm diameter) were embedded in various soft tissues throughout each specimen, and the porcine specimen was submerged in a saline bath.

Imaging: The two objects were scanned with a clinical CT scanner (O-Arm, Medtronic). High definition mode (750 projections) was used in the experiment (80 kVp, 50 mA for 26 s). Volumes (matrix size 1024 Ĭ 1024 Ĭ 384, with voxel dimensions 0.2075 Ĭ 0.2075 Ĭ 0.415 mm^3) were reconstructed off-line with the FDK algorithm.

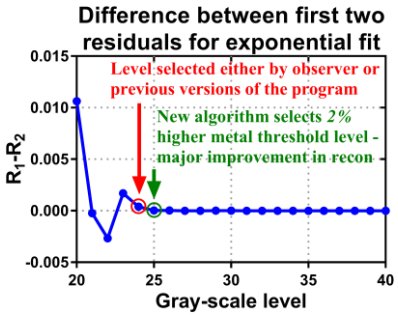

Fig. 1

Image post-processing: Data from the CT scanner were processed on a separate computer to avoid the automatic cut-off and binning. All calculations were done with MATLAB using custom scripts and *MIRT* toolbox[5].

Algorithm: Metal segmentation level is selected in two steps: the first one finds the global minimum of the derivative of the difference between the entropy and intensity density[3]; this is, then, used as an initial point for the ñfine-tuningò stage, where a function ($f_i(k) = a_i \cdot e^{-k \cdot b_i}$) was fitted to the histogram of the intensities of the selected volume over each level (total of 50 levels). When only the dense metal, causing the image artefact (Fig. 2) was selected, the histogram displayed good exponential behavior. The difference between the first two residuals (R_1-R_2) of the fit (Fig. 1), and its first and second derivatives, were used as sufficient criteria for level selection. Indication for a good fit would be small differences (close to zero) in the residuals. Additionally, having the derivatives of the residual difference small and close to zero, would suggest the least fluctuation of the fit (as a function of the gray-scale level). Thus, the algorithm first detected a stable sequence of low-valued (R_1-R_2) and then iteratively probed for an availability of a next even tighter epsilon for residual derivatives.

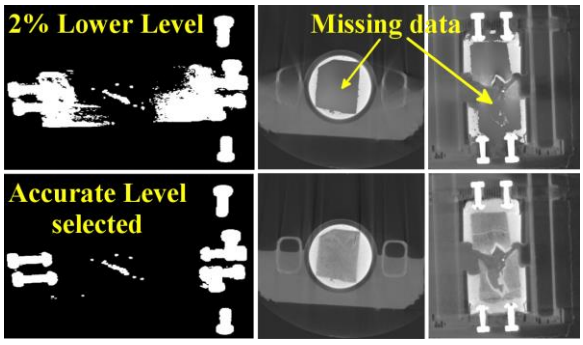

Fig. 2 Left - metal selection in projection space; Middle/Right ï 2 views of the reconstructed vol.

Results/Discussion: This method determined the optimal metal threshold before performing the ñinpaintingò in the projection space. The efficiency of MAR depends on the choice of the correct level, which is sensitive of the objectôs distribution, geometry and composition. This algorithm was stable and performed as well as, and often better than, visual selection. The workflow was considerably improved with the automatic selection, instead of a manual approach. This method was successfully tested on different objects (Fig. 2, 3), ranging from tiny beads and coils to hip implant and on two different CT scanners (results for the other scanner not shown).

Conclusions: Sometimes as little as 2% difference in the threshold had a profound difference in the reconstructed volume quality (Fig. 1, 2) but this algorithm could detect that. In most challenging cases (hip, series of metal rods), the final stage of the MAR removed most of the artefacts but introduced some new ones. The next MAR development will address this problem.

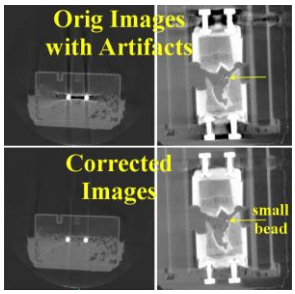

Fig. 3

References: [1] Gjesteby, L., et al. IEEEAccess, 2016. [2] Blokker, A., et al. ImNO, 2018. [3] Petrov, I., et al. ImNO, 2016. [4] Petrov, I., et al. SPIE Med. Imaging, 2011. [5] Fessler, J., Univ. of Michigan, 2012.

Spherical navigator echoes (SNAVs) correct for motion in PET and MR images on a hybrid PET/MR scanner

PM Johnson,[1] R Taylor,[2,3] T Whelan,[1] M Drangova[1]
[1]Imaging Research Laboratories, Robarts Research Institute, Western University, London, Ontario, Canada
[2] Lawson Health Research Institute, London, ON, Canada
[3] Siemens Canada, Oakville, ON, Canada

Introduction: Head motion during brain imaging with hybrid PET/MR degrades the diagnostic quality of both the PET and MR images. Simultaneous acquisition provides the opportunity for MR motion measurement techniques to be used for correction of the PET data. In this work spherical navigator echoes (SNAV) ï a 3D k-space navigator ï is interleaved within a turbo-flash sequence to enable simultaneous motion corrected PET and MRI. The SNAV technique can measure brain rotations and translations with sub-millimeter and sub-degree accuracies and has been applied successfully for retrospective correction of MR brain images.[1] In this work we demonstrate successful retrospective motion correction of simultaneously acquired PET and MR images using SNAVs.

Fig 1. Pineapple phantom with FDG-filled vials.

Methods:

SNAV sequence: SNAVs were incorporated into the turbo flash imaging sequence (tfl-SNAV) where the SNAV is acquired prior to each image TR. The SNAV is a spherical shell in k-space with a radius of 0.4 cm^{-1}; it is acquired in two shots ï one for each hemisphere ï with a TR of 30 ms.

Phantom experiment: The experiment was performed on a 3T PET/MR scanner. Seven 12-mm diameter vials were inserted into a pineapple (Fig. 1), known to be a suitable phantom for MR navigators,[2] and filled with FDG. Each vial contained 2 ml of FDG (20 kBq/mL). A 6-min reference PET/MR scan was acquired while the phantom was stationary, followed by three 6-min scans during which the phantom was manually repositioned several times. For each acquisition, tfl-SNAV data were acquired simultaneously with the PET list-mode data.

Motion measurement & correction: SNAVs were processed in Matlab; the rotations and translations were determined by comparing SNAVs acquired during the PET/MR scan to those acquired in a baseline scan. The SNAV motion estimates were then used to correct the MR data. A detailed description of this method can be found in Johnson *et al.* 2016.[1] The measured motion profile was then used to sort the list-mode data into six motion states. RTA reconstruction[3] was then performed in which each bin was reconstructed using the Ordinary Poisson model. The six images were finally transformed based on the measured motion and summed to form a final motion corrected image.

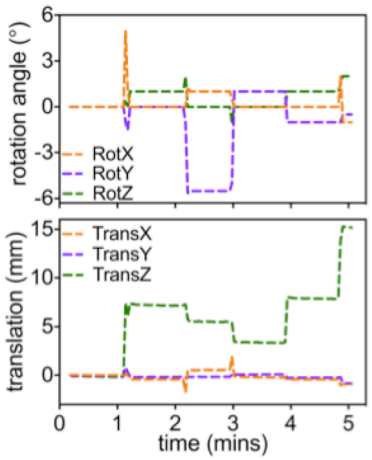

Fig 2. SNAV derived motion profile.

Results: An example SNAV-derived motion profile is shown in Fig. 2. Translations up to 15 mm and rotations up to 5° were measured. Axial and sagittal slices of the reference (left), uncorrected (center) and corrected (right) MR images are shown in Fig. 3a and 3b. The motion-related blurring is clearly seen in the uncorrected image, and the SNAV-corrected images have greatly improved image quality. A coronal slice of the reference, uncorrected and corrected PET images are shown in Fig. 3c. The motion-related distortion is clearly seen in the uncorrected image. The SNAV-corrected image closely resembles the reference image and the expected circular cross-sections of the vials are restored.

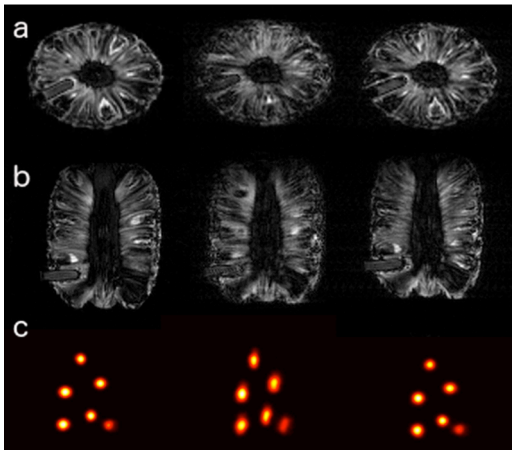

Fig 3. Example of SNAV motion correction. Reference (static), motion corrupted, and motion corrected images are shown in the first, middle and third columns, respectively. Axial (a) sagittal (b) slices are shown for the MR images and a coronal (c) slice is shown for the PET images.

Discussion/ Conclusions: Three-dimensional motion correction using SNAVs successfully removed blurring due to motion from the MR and PET images. Evaluating motion correction in-vivo, and with an anthropomorphic brain phantom is the focus of on-going work. We are also implementing prospective MR motion correction, which is expected to improve the motion correction of MR images by eliminating the need for interpolation of image data.

References: [1] PM Johnson et al., Magn Reson Imag, 2016 [2] van der Kouwe et al., Magn Reson Med, 2006 [3] Picard et al., IEEE Trans Med Imag, 1997

Suppressing Broadband Noise in Ultrasound Imaging

Natasha Alves[1], Naimul Khan[2] and Brian Courtney[1,3,4]
1 – Physical Sciences, Sunnybrook Research Institute
2 – Dept. of Electrical and Computer Engineering, Ryerson University
3 - Department of Cardiology, Sunnybrook Health Science Centre
4 – Conavi Medical, Toronto

Introduction: Medical imaging with ultrasound relies on detecting low-amplitude signals, typically in the 2 MHz to 60MHz range. Signals in minimally invasive ultrasound imaging systems tend to be very weak since signal amplitude is limited by the small size of the transducer, the small size of the probe which restricts the use of electronics that can boost signal amplitude at the source, and attenuation along the conductors that carry the electrical signal from the transducer out of the body. Ultrasound image quality is also greatly influenced by many noise sources, such as radio transmitters, power electronics and transmission lines. Noise can be difficult to suppress once it has entered the ultrasound system. Narrow-band filtering can be applied to limit the imaging signal to those portions whose frequencies lie within the operational bandwidth of the ultrasound transducer. However, noise that lies within the imaging band remains challenging to remove. A method for identifying and actively removing in-band noise from imaging signals will be very useful.

Methods: We propose a method to reduce broadband noise in ultrasound systems by exploiting the fact that imaging energy predominantly lies within a selective imaging band, while broadband noise can be detected both within the imaging band (in-band noise) and outside of the imaging band (out-of-band noise). The relationship between in-band noise and out-of-band noise is determined in an initial 'characterization' stage, when the system is receiving noise energy but is not receiving imaging energy. In a subsequent 'imaging' stage, i.e. when the system is receiving imaging energy, an estimate of the in-band noise is made based on out-of-band noise measures. The received ultrasound signal is then altered to generate a signal that estimates the desired imaging energy in the absence of the estimated in-band noise.

Results: Noise introduced into a mechanically scanning intracardiac echo system (Foresight ICE, Conavi Medical) from an electro-anatomical mapping system (Carto3, Biosense Webster) was processed in real-time by an on-board FPGA programed with the above noise-suppression algorithm. A 6dB improvement in signal-to-noise ratio was observed (see Fig1). The algorithm was also effective in reducing other sources of broad-band noise, for example, noise from the motor that mechanically rotates the imaging transducer.

Conclusions: We have developed algorithms that can reduce noise in imaging systems by processing the portion of the noise that lies outside the imaging band. These methods have been demonstrated for ultrasound imaging, but may be easily be extended to other imaging modalities, such as MRI or MEG, where weak signals are detected in the presence of broadband noise from undesired sources.

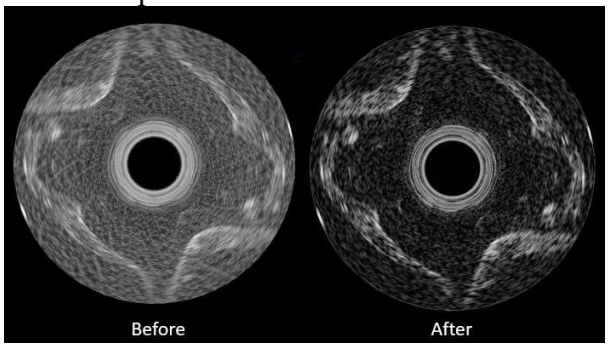

Figure 1. Improvement in SNR of an ultrasound image contaminated by noise from an electro-anatomical mapping system.

A Covalent MRI Tag Based on Manganese(III) Porphyrin as Building Block for Bioconjugation

Keith Tang[1,2], Hanlin Liu[1,2], Lida Tan[2], Edmond Wong[2], Xiao-an Zhang[1,2,3 *]
[1]Department of Chemistry, University of Toronto. [2]Department of Physical and Environmental Sciences,
[3]Department of Biological Sciences, University of Toronto Scarborough.

Introduction: The distinction between healthy and diseased tissues in MRI may sometimes require administration of contrast agents (CAs) that chemically improve sensitivity (characterized by T_1 relaxivity or r_1) and enhance the tissue contrast. Currently, MRI CAs available to the clinic are mainly gadolinium (Gd) based, which have several drawbacks such as risk of in-vivo toxicity upon Gd-dissociation and decreasing sensitivity at clinically relevant fields (1-3T). The pursuit for MRI scanners that operate at higher magnetic field strengths has made manganese(III) porphyrin (MnP) platform a more appealing choice due to its abnormally high r_1 at clinically relevant fields, as well as better biocompatibility over Gd.[1] The challenge remains in optimizing target specificity and improving sensitivity of these compounds. The tunable structural diversity of the MnP platform allows flexibility in the design for targeted molecular imaging in the form of bioconjugates (Fig. 1) and controlling pharmacokinetics in the form of small monomers/oligomers (Fig. 2). Here we report the first generation covalent MRI tag ï MnTPPS$_3$NCS and its conjugation to a polymer backbone (Fig. 1a). This molecular design would enable linkage of the backbone to bio-macromolecules, i.e, antibodies, capable of targeting diseases or specific cells, while maintaining the high sensitivity obtained from the MnP bioconjugate. We attempt to quantify the sensitivity of newly synthesized MnP conjugates and evaluate its potential application for in vivo imaging.

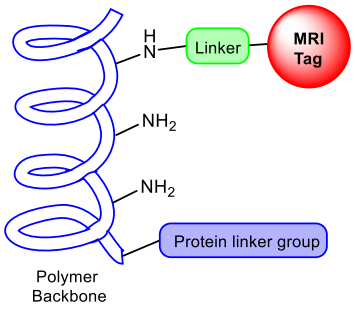

Figure 1: Molecular design of Mn(III)-porphyrin bioconjugates with large macromolecular backbone with amine functionalized moieties for covalent linking to isothiocyanate MRI tag.

Methods: The synthesis of MnP-based MRI tag (Fig. 2) was modified based on previous methods.[2] The structure of the compounds were confirmed by ^{1}H NMR, ESI-MS, UV-vis, and HPLC when applicable. Sensitivity of contrast agents was evaluated based on r_1 (mM^{-1} s^{-1}), measured in 25 mM HEPES buffer (pH 7.2) at 25ÁC on a SMARTracerÊ Fast Field Cycling NMR Relaxometer and coupled to a variable high-field (HTS)-110 NMR system

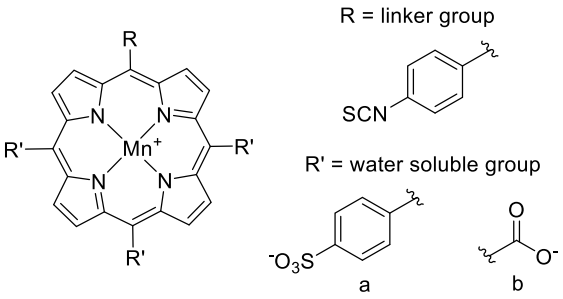

Figure 2: Proposed structures of contrast agent bearing an isothiocyanate linker group for polypeptide conjugation, with (a) first generation MRI tag with phenyl sulfonate groups for water solubility or (b) smaller second-generation tag with carboxylate groups for increased polarity and water accessibility

Results: Preliminary r_1 data of monomeric MnTPPS$_3$-NH$_2$ and MnP-PLL conjugate demonstrated a considerable increase in r_1 upon linking with polymer across higher magnetic field strengths (1-3T), agreeing with optimization of the molecular tumbling rate (τ_R) through attachment to a large biomolecule, as predicted by the classic SBM model.[3] However, aggregation at physiological pH limits the potential application in vivo. We then have synthesized and are currently working towards characterizing a second generation covalent MRI tag with smaller molecular weight and more polar functional groups for greater water accessibility (Fig. 2b).

Conclusion: The design of a novel covalent MRI tag shows potential towards high relaxivity contrast agent with molecular targeting ability. Improvement in the r_1 at higher magnetic fields upon conjugation of the MRI tag has a dual-function in increasing sensitivity and providing a molecular scaffold for our MRI tag for attachment onto biomarkers. Reduced solubility of the contrast agent leads room for improvement, which is addressed in our second generation covalent MRI tag with smaller molecular weight and increased polarity.

References: [1] *Magn Reson. Med.* **1984**, 1, 478ï 495. [2] *J. Med. Chem.* **2014**, 57, 516-520. [3] *J. Magn. Reson. Im.* **1992**, 100, 491ï 516.

Multi-image polarimetric Mueller matrix feature extraction

Jared Westreich[1], Adam Gribble[1], [2]Mohammadali Khorasani, and I. Alex Vitkin[1,3,4]
[1]Department of Medical Biophysics, University of Toronto, Toronto, Ontario, Canada
[2]Division of Surgical Oncology, Department of Surgery, University of Toronto, Toronto, Ontario, Canada
[3]Department of Radiation Oncology, University of Toronto, Toronto, Ontario, Canada
[4]Division of Biophysics and Bioimaging, Princess Margaret Cancer Centre, Toronto Ontario, Canada

Introduction: Polarimetry is a promising optical method to noninvasively assess biophysical characteristics of tissues. As polarized light propagates through tissue, its polarization state is altered as dictated by the optical properties of heterogeneous scattering bio-structures. A potential application is in intra-operative margin assessment to identify regions suspected to contain tumor and then using mass spectrometry (MS) to obtain a definitive classification. The information to characterize tissue is contained within the Mueller matrix (MM), a complete mathematical description of its interaction with polarized light. In wide-field polarimetry, the MM is calculated for every pixel. Biophysical quantities derived from the MM, such as depolarization (a measure of tissue heterogeneity) and birefringence (its (a)symmetric/ anisotropic nature) can help differentiate healthy and tumorous tissue. [1] However, a wealth of information within the MM goes unused as it is difficult to know which elements are of the most bio-physical relevance.
Methods: To demonstrate the feasibility of using polarimetry for tumor margin assessment, we will design a setup that optimizes resolution, speed, and field of view. We will then determine the best way to combine the MM elements at each pixel to optimize contrast between tissue types. Although widely used, it is not clear that the standard decomposition metrics (depolarization, birefringence, etc.) are the best way to use the information contained within the MM. We will determine whether machine learning (ML) algorithms can combine the MM elements in a way that improves tissue contrast compared to decomposition. We can use the MM elements, along with ground truth segmented histology, as the training data and let the ML algorithms learn the hidden patterns. Possible algorithms for this application include random forest, logistic regression, and artificial neural networks. The MMs and labels of neighboring pixels can also be used to assist with the training and image processing techniques can help detect misclassified regions. A separate validation set will be used to prevent overtraining. Polarimetry for guided MS requires high sensitivity but a lower specificity may be acceptable. This is because a “false alarm” will be subsequently tested with MS but a false negative would result in undetected tumor. Receiver Operator Characteristic (ROC) curves will be used to optimize the threshold to meet the sensitivity/ specificity balance for this application. Once the method is proven with transmission polarimetry, it can be adjusted for reflectance mode, which is more clinically relevant. Our method will then be compared with the current intra-operative margin detection best practices in terms of speed, sensitivity, and specificity.
Results: The expected results are Dice Scores quantifying the ability of decomposition methods and our ML algorithms to differentiate between tumor and healthy tissue. These will then be compared with the current intra-operative margin assessment techniques in terms of speed, sensitivity, and specificity.
Conclusion: If sensitive and specific, this tool could reduce the number of patients who require a second surgery, which is now approximately 20% [2].

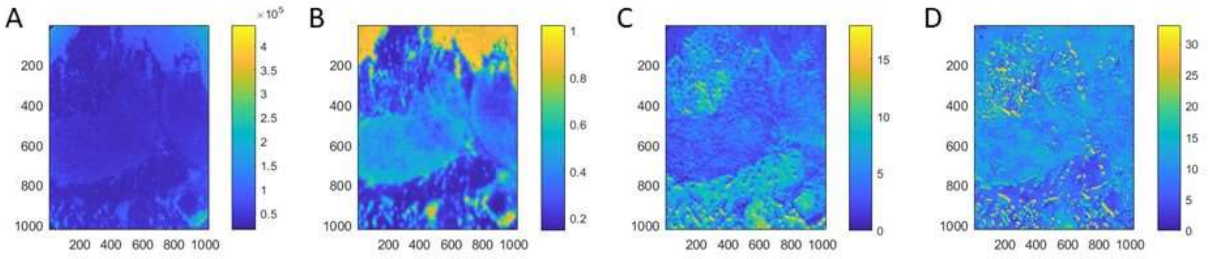

Figure 1 Polarimetry images. a) Raw image with horizontal input and output, b) Transmission derived from MM, c) Depolarization, d) Linear Retardance

[1] A. Tata, A. Gribble, M. Ventura, M. Ganguly, E. Bluemke, H. J. Ginsberg, D. A. Jaffray, D. R. Ifa, A. Vitkin and A. Zarrine-Afsar, "Wide-field tissue polarimetry allows efficient localized mass spectrometry imaging of biological tissues," *Chemical Science,* vol. 7, no. 3, pp. 2162-2169, 2016.

[2] E. R. St John, R. Al-Khudairi, H. Ashrafian, T. Athanasiou, Z. Takats, D. J. Hadjiminas, A. Darzi and D. R. Leff, "Diagnostinc Accuracy of Intraoperative Techniques for Margin Assessment in Breast Cancer Surgery," *Annals of Surgery,* vol. 265, pp. 300-310, 2017.

Polarimetry imaging for breast cancer analysis

Adam Gribble[1], Michael Woolman[1], Michael Pinkert[2], Kevin Eliceiri[2], Arash Zarrine-Afsar[1], Alex Vitkin[1,3,4]

[1]Department of Medical Biophysics, University of Toronto, Toronto, Ontario, Canada
[2]Laboratory of Optical and Computational Instrumentation, University of Wisconsin ï Madison, Madison, Wisconsin, USA
[3]Division of Biophysics and Bioimaging, Princess Margaret Cancer Centre, Toronto Ontario, Canada
[4]Department of Radiation Oncology, University of Toronto, Toronto, Ontario, Canada

Introduction: Polarimetry imaging is a fast, label free, optical technique that differentiates tissues based on their interactions with polarized light. Here, two breast cancer applications are investigated: breast cancer margin detection, and visualization of collagen organization.
Margin detection: Intraoperative pathology assessment for breast cancer patients is imperative to determine that the entire tumour has been removed. If tumour margins are ill-defined and there is residual cancer following surgery (incomplete recession), there is an increased risk of recurrence, and additional surgery is likely required. Thus, there is an unmet need to improve intraoperative histology through faster and more sensitive techniques that identify pathologic tissue. To address this problem, we investigate the ability of polarimetry to distinguish breast cancer from healthy tissue. This may be useful as a standalone technique, or as rapid guidance for more sensitive analysis methods (such as mass spectrometry imaging).
Collagen organization: In addition to cellular changes, collagen organization plays an important role in breast cancer. Second harmonic generation (SHG) microscopy, a multiphoton imaging technique, is highly sensitive to collagen and has been used extensively to study collagen structure and organization. SHG has revealed tumor associated collagen signatures (TACS) - associated with poor prognosis in humans, that may facilitate tumor cell migration from primary tumors to surrounding tissue. Thus, understanding collagen organization may be diagnostically beneficial, and may provide opportunities for new treatment strategies. However, despite high collagen sensitivity and specificity, SHG is slow and has a limited field of view (FOV). The recent interest in *bulk collagen organization* provides an intriguing case for studying collagen over a larger FOV. Polarimetry is well suited for this, as it can detect birefringent structures such as collagen, and can be adapted to image large FOVs.

Methods: Margin Detection: Human breast cancer cells were injected into the quadriceps muscle of mice. Following tumour growth, sections of tissue containing the tumour and a margin of healthy surrounding tissue were excised and sliced to be imaged with polarimetry, Mass Spectrometry imaging, and histology.
Collagen organization: Wide-field (~cm scale) polarimetry and SHG were both used to image tissue samples from a mouse model of breast cancer (PyVT model). The two imaging techniques are directly compared.

Results: Margin detection: Polarimetry revealed that depolarization is reduced in cancerous regions compared to the surrounding healthy muscle tissue. Agreement was observed between polarimetry, histology, and mass spectrometry imaging.
Collagen organization: Polarimetry was shown visualize regions of highly aligned collagen, as supported by complimentary SHG imaging.

Conclusion: Polarimetry can reveal multiple types of tissue contrast in breast cancer, revealing tumor margins, and collagen organization. This may have implications for intraoperative pathology assessment (stand-alone technique, or rapid guidance for more sensitive techniques like mass spectrometry), and the study large-scale collagen organization in breast tissue.

Optimization of Slow-Proton-Exchange (SPE) Magnetic Resonance pH Sensor and Application for Monitoring Enzyme Activity

Ontario Institute for Cancer Research Smarter Imaging Program: An Ontario Imaging Consortium
Ryan Correa[a,b], Loise Perruchoud [a b], and Xiao-An Zhang[a,b,c *]
[a]Department of Chemistry, University of Toronto. [b]Department of Physical and Environmental Sciences, [c]Department of Biological Sciences, University of Toronto Scarborough.

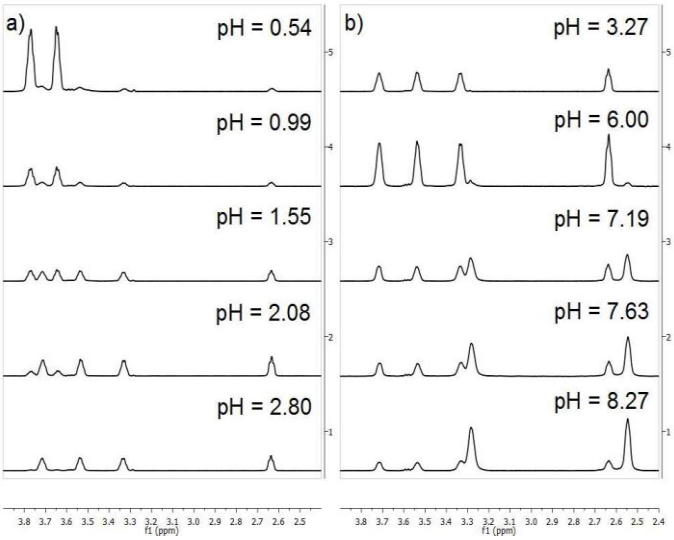

Figure 1: Selected ^{1}H NMR spectra for the titration of **SPE2**. a) at pH values near pK_{a1} (1.57). b) at pH values near pK_{a2} (7.30).

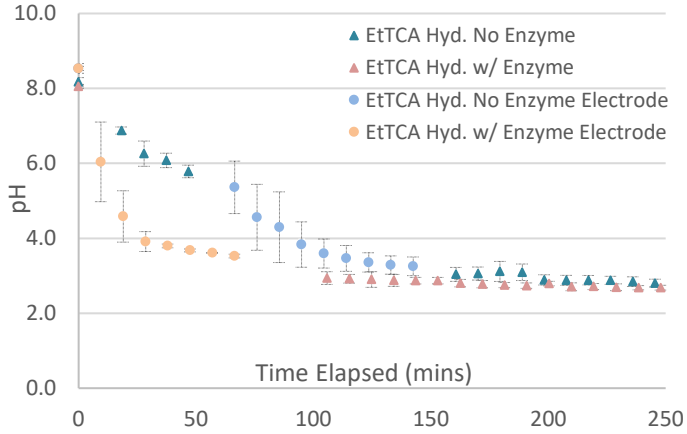

Figure 2: Monitoring the hydrolysis of ethyl trichloroacetate (+/- esterase) by pH change, using **SPE2**. A pH electrode was used to complement data in the pH windows not covered by **SPE2**.

Introduction: Noninvasively monitoring pH change with deep penetration and high accuracy holds great promise for precise detection of various diseases, including cancer. Magnetic resonance based techniques, such as NMR and MRI, are preferred choices. However, classic MR-based methods for pH measurement are compromised by low sensitivity and accuracy, partially due to rapid proton transfer beyond NMR time scale. We developed a novel Slow Proton Exchange (SPE) strategy for measuring pH using a ratiometric NMR pH sensor, **SPE1**.[1] With this method, unprecedented accuracy of NMR pH measurement (æpH = 0.02) was achieved. **SPE1** is biocompatible and can be used for real-time monitoring of pH dynamic of live cells, but its pK_a (~7.72) is sub-optimal above common physiological pH. In this study, a second-generation pH sensor, **SPE2**, is developed and applied for monitoring enzymatic reactions in real-time.

Methods: Through rational structural modification, **SPE2** was designed with a lower pK_a than **SPE1**, thus better suited for biological applications. Unlike **SPE1**, which exhibits an apparent single pK_a due to positively cooperative protonation, **SPE2** is expected to have separate two step protonation and consequently a broader operating pH window. **SPE2** was chemically synthesized and structurally characterized. The protonation behaviour and pK_a values were determined by NMR titration. **SPE2** was incubated with an esterase to monitor the enzymatic ester hydrolysis by NMR.

Results: **SPE2** exhibits proton exchange rate slower than NMR timescale in the same vein as **SPE1**. The NMR pH titration of **SPE2** revealed two well-separated protonation steps, with apparent pK_a values of 7.30 and 1.57 respectively (Figure 1). Therefore, **SPE2** can measure pH over a much wider range, in contrast to **SPE1**, including biologically relevant pH windows. For example, the enzyme-catalyzed ester hydrolysis could be monitored by **SPE2** in real time (see Figure 2) and was found to be accurate when compared to potentiometric measurements. **SPE2** was demonstrated to have resistance to environmental changes in ionic strength, proving robustness and accuracy of this method.

Conclusions: **SPE2** is a second generation slow-proton-exchange NMR sensor, with high accuracy and optimized pK_a and wider operating pH windows. We have demonstrated the effectiveness and potential for future biomedical applications.

1. Perruchoud, L. H., *Chem. Sci.*, **2015**, *6*, 6305.

Poster Presentation Abstracts

Session 8: Neuroimaging

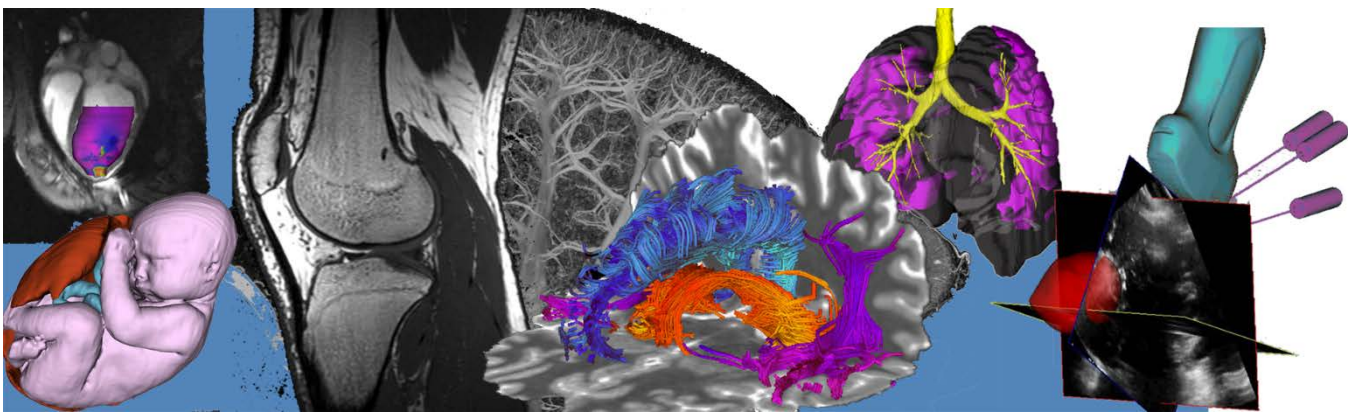

Correlations between ΔB_0, ΔB_1^+, and Physiological Noise in the Spinal Cord for MRS Approaches

Nicholas Maurice Simard[1], Aimee J Nelson[2], and Michael D. Noseworthy[1,3]

[1]School of Biomedical Engineering, McMaster University, Hamilton, ON, Canada, [2]Department of Kinesiology, McMaster University, Hamilton, ON, Canada, [3]Department of Electrical and Computer Engineering, McMaster University, Hamilton, ON, Canada

Spinal cord 1H MR Spectroscopy (1H-MRS) can provide insight into the biochemistry of spine-specific metabolites. However, due to the spine's anatomical location there is a significant degradation of signal quality due to changes in B_0 and B_1 due to pulsatile and respiratory motion at or near the spinal cord [1]. Although there have been measurements and protocols to identify ΔB_0 and ΔB_1^+ in spinal cord MRS [2], there have been no comprehensive assessments of changes relating to physiological disturbances. Therefore, in this work, the goal is to measure ΔB_0 and ΔB_1^+ during the length of a typical MRS scan while recording physiological data to quantify the impact of noise in the area of interest and further improve the acquisition quality in spinal cord MRS.

Experiments were performed using a 3T GE MR750 scanner (General Electric Healthcare, Milwaukee, WI) along with a home designed/built phantom and 4 healthy human subjects. B_0 and B_1 field maps were acquired over a 10 minute timespan at the cervical spinal cord (C4) (Fig.1). The integrated body-coil was used for transmission and a GE Head Neck and Spine, with a Brachial coil was used for reception. The B_0 (TE=4.6ms) and B_1 sequences (TE=13.9ms) were auto-shimmed only at the beginning to properly maintain the shim for the duration of the scan. Pulsatile flow was acquired using a pulsed oximeter whereas respiratory motion was acquired using a thoracic bellow and both physiological measures were recorded during the collection of the maps scans at a sampling rate of 10Hz and 25Hz, respectively.

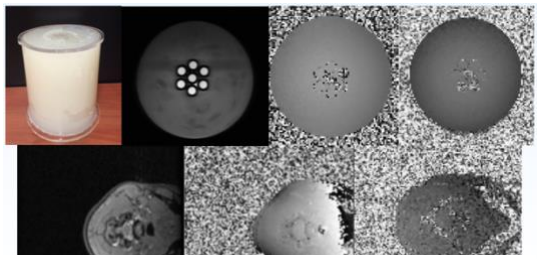

Fig. 1 : *Top* (*from left to right)*, phantom, anatomical scan, B0 map, B1 map. *Bottom* (*from left to right)*, anatomical scan of human cervical spine, B0 map, B1 map

Data analysis was performed using 1x1cm ROIs in the B_0 and B_1 field maps to mimic voxel dimensions of MRS in the spinal cord. Significant standard deviation of ΔB_0 (mean ± SD) 48.5 ± 2.7Hz and ΔB_1 21.4 ± 4.61 ^{0}/flip angle was calculated in the human spinal cord The acquired pulsatile flow data underwent a Fast-Fourier transform (FFT) and Power Spectral Density (PSD) calculation to identify the frequency contribution. Respiratory motion contribution was calculated using a sliding standard deviation window. Physiological data was further analyzed with Principal Component Analysis (PCA) to identify sources of variation (Fig.2). The principal component in ΔB_0 was attributed to pulsatile flow and yielded a correlation coefficient of 0.71. Whereas in ΔB_1, the principal component was respiratory motion and yielded a correlation coefficient of 0.52. Data was not normally distributed and additionally analyzed using kurtosis, skewness, and Jarque-Bera tests.

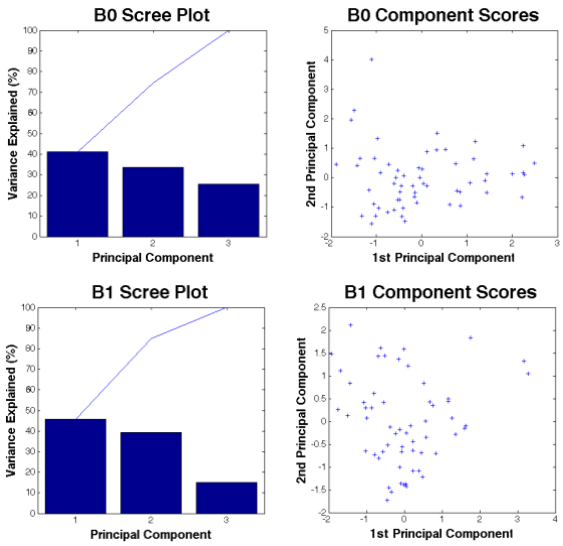

Fig. 2 : PCA Analysis

There are significant links between physiological data and ΔB_0 and ΔB_1^+ within the spinal cord. However, further exploration is needed between ΔB_0 and ΔB_1^+ and respiratory/cardiac motion to establish equations that can reduce additional motion artifacts. Further research should include larger sample sizes and more component variables in PCA such as temperature, shim, and MR noise.

[1] Henning A., et al., Magn Reson Med, 2008;59(6):1250-8.
[2] Cooke F.J. et al (2004) MRM 51:112281128

Reliability of Freesurfer Reconstruction For 7T T1-weighted Images

Yaojie Zhou[a], Hossein Rejalia[a], Lena Palaniyappan[a,b,e], Ali R. Khan[a,c,d,e]

[a]Robarts Research Institute, [b]Department of Psychiatry, Schulich School of Medicine and Dentistry, [c]Department of Medical Biophysics, Schulich School of Medicine and Dentistry, [d]Brain and Mind Institute London, Ontario, Canada, [e]Co-senior authors: contributed equally to the supervision of this study

Introduction: Prior research has shown that there is a reduction in grey matter in the early stages of schizophrenia [1], which is related to the damage of normal intra-cortical myelin. Investigating intra-cortical myelin is possible with the longitudinal relaxation rate (R1), however, accurate reconstruction of the cortical surface is required to sample R1 in the cortex. FreeSurfer has been a gold standard for many researchers as an automated neuroimaging processing tool as it has provided a reliable reconstruction for 1.5T and 3T T1-weighted images [2]. Neuroimaging with 7T MRI provides greater SNR and potentially greater sensitivity to detect subtle abnormalities, however, artifacts that include signal non-uniformities and drop-outs are more prevalent. Thus, as a first step we aimed to evaluate the reliability of surface reconstruction, and the impact and necessity of manual correction. We hypothesized that summary morphometric measurements (volume and thickness) would not be significantly different between manually corrected reconstructions and fully-automated reconstructions. **Method:** *Data acquisition:* High resolution 7T T1-weighted images and T1 maps were acquired using a MP2RAGE sequence (0.75mm resolution) for 10 patients with schizophrenia unmedicated, as part of an ongoing study. *Analysis:* FreeSurferôs cortical map reconstruction was obtained for each subject. Next, we manually edited the reconstructed images by using the recommended reconstruction workflow, consisting of skull stripping, control points addition, and white and pial surface fixation. We evaluated the reliability by investigating three quantitative metrics including the whole brain cortical volume, and right and left cortical mean thickness for both original and corrected cortical maps. Furthermore, surface group analysis with Qdec produced by FreeSurfer was applied. **Result:** All images underwent the automatic reconstruction (Fig.1) and manually editing (Fig.2). The data of three metrics were computed from FreeSurferôs automatic calculation, and Wilcoxon signed-rank test was performed for each variable. The analysis for three metrics showed no significant difference (P>0.05) between standard and manual-edit cortical maps(Fig. 3.4.5). Qdec also showed no statistically different regions between the standard and manual corrected groups. **Discussion:**Our study indicates that the cortical map reconstructed by Freesurfer for 7T T1w-images agreed with that of manual corrected reconstruction. The results support the usage of FreeSurfer as the automatic reconstruction for the 7.0 Telas T1-weighted images. However, due to the limited number of subjects available further investigation may be needed to confirm our results. **Reference:** [1]. Palaniyappan L et al. Neuropsychopharmacology. April 2013. Doi:10.1038/npp. 2013.80. [2].Cardinale F et al. Neuroinformatics. 2014 Oct;12(4):535-42. Doi: 10.1007/s12021-014-9229-2.

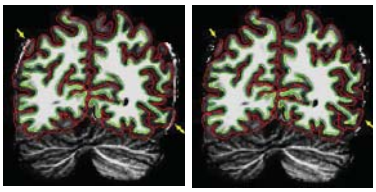

Fig. 1 (left), Fig,2 (right): show the reconstruction of 7T T weighted images. Red contour: pial surface; Green contour: white surface; yellow arrows: manual edit.

Figure 3,4,5 Paired t-test results: show no significant differences between the two procedures

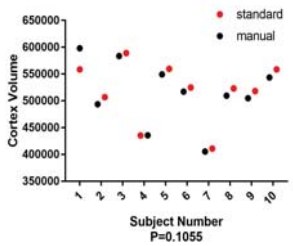

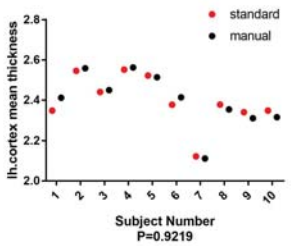

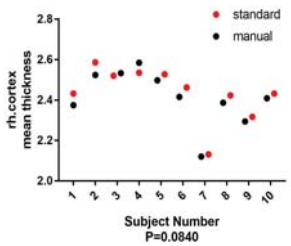

Investigating anatomical regions in which myelin abnormalities occur in schizophrenia using quantitative R1 maps

*Hossein Rejali[1,2], Penny Gowland[5], Peter Liddle[6,8], Ali Radaideh[7], Lena Palaniyappan[2,4], and Ali R. Khan [1-3]
[1]Robarts Research Institute, [2]Dept. of Medical Biophysics, [3]Dept. of Biomedical Engineering and [4]Dept. of Psychiatry, Western University, London, Ontario, Canada
[5]Dept. of Physics, [6]Dept. of Psychiatry, [7]Dept. of Medical Imaging and [8]Dept. of Medicine and Health Sciences, University of Nottingham

Introduction: MRI is conventionally used to examine myelin content based on quantitative mapping of longitudinal relaxometry, T1, or 1/R1. It is well known that there are myelination abnormalities present in schizophrenia from ex-vivo studies, although validation of such abnormalities currently has not been investigated using in-vivo data in high-resolution MRI. Our objective is to investigate common anatomical areas in which myelination abnormalities arise in schizophrenia using high resolution quantitative R1 data. To explore the myelin anomalies seen in schizophrenia, we examined the quantitative R1 maps of the cortex at a 0.2mm and 50% distance from WM/GM boundary. The 50% projected fraction is assumed to correspond to layers II and III of the cortex, while the 0.2mm distance corresponds to deeper layers in the cortex. The projected depths are where abnormalities are typically seen and investigated. In particular, we have focused a portion of our analysis in the part of the frontal lobe which consists of the rostral middle frontal cortex (RMF), caudal middle frontal cortex (CMF), pars opercularis, pars orbitalis, and pars triangularis. Also, we explored other commonly affected ROIôs such as the insula, anterior (ACC) and posterior cingulate gyrus (PCC). We hypothesize that quantitative R1, which measures myelin content, would be reduced in patients with schizophrenia compared with controls.

Methods: *Data acquisition*: Limited field of view (FOV) high resolution 7T quantitative R1 maps were acquired along the axial direction covering majority of temporal lobe. R1 Maps were collected for 20 controls (15 male, 5 female) and 21 diagnosed with schizophrenia (16 male, 5 female) ranging from 20 to 50 years of age. Two subjects were excluded from the analysis due to the quality of the scan and lack of data. *Preprocessing*: Individual R1 maps were registered to a common space using FreeSurfers fsaverage atlas, and the mean intensity in each ROI was calculated. *Analyses:* To account for extraneous variables known to affect myelin content such as age, we modelled R1 using a general linear model (GLM) similar to the quadratic model used in [1] which modelled intracortical myelin in subjects in their late adolescence to middle adulthood using T1 weighted images. In addition to the model in [1], our model included a discrete group variable, control or schizophrenia, as a covariate affecting myelin. We then tested for differences in R1 intensities between control and patients with schizophrenia in the specified mean ROIs using F statistic hypothesis testing.

Results: In this work we analyzed 8 ROIs at a projected distance of 0.2mm and 50% projected fraction from the WM/GM boundary. Our preliminary results showed no significance ($p<0.05$) between the two groups. Table 1 shows the significance level for each ROI at a projected distance of 0.2mm from WM-GM boundary. Similar results were seen in the 50% projected fraction of the R1 surface.

	ACC	**PCC**	**Insula**	**RMF**	**CMF**	**Pars Opercularis**	**Pars Orbitalis**	**Pars Triangularis**
P-Value (LH)	0.1996	0.8512	0.3137	0.2409	0.0715	0.2751	0.9957	0.4280
P-Value (RH)	0.2713	0.9309	0.3059	0.2127	0.2454	0.2819	0.7000	0.4537

Table 1: P value table for specified ROIôs at 0.2mm depth from the WM-GM boundary for both left and right hemispheres, testing hypothesis that there is a difference in R1 between control and patients with schizophrenia

Conclusion: In this work, we have presented a study of high resolution quantitative R1 maps in schizophrenia and controls in areas of the cortex in which myelin has been commonly reported to be affected by the disease. Our results suggest that there is no significant evidence for myelin reduction in patients with schizophrenia in the areas examined, this may be due to the limited number of subjects and FOV. Further analysis and investigation is required to validate what has been stated by previous literature.

References: [1] C. D. Rowley *et al.*, ñAge-related mapping of intracortical myelin from late adolescence to middle adulthood using T1 -weighted MRI,ò *Hum. Brain Mapp.*, Apr. 2017

Ventricular expansion in Alzheimer's Disease: relationships with small vessel disease and cognition.

Sabrina Adamo[1,2], Joel Ramirez[1,2,3], Melissa F. Holmes[1,2], Fuqiang Gao[1,2,3], Sandra E. Black[1,2,3,4]
[1]L.C. Campbell Cognitive Neurology Research Unit; [2]Hurvitz Brain Sciences Research Program, Sunnybrook Research Institute; [3]Heart & Stroke Foundation Canadian Partnership for Stroke Recovery, Sunnybrook Health Sciences Centre; [4]Department of Medicine, Division of Neurology, University of Toronto, Toronto, Canada.

Introduction

Alzheimer's disease (AD) is the most common irreversible cause of dementia. In addition to standard cognitive testing, such as the Mini-Mental State Examination (MMSE), previous studies suggest that atrophy measured by ventricular expansion[1] and small vessel disease measured by white matter hyperintensity (WMH) burden[2] may have potential utility as an MRI-based biomarker. The current study examined changes in ventricular cerebrospinal fluid (vCSF) and WMH volumes as they relate to cognitive changes in AD patients relative to healthy elderly controls in order to determine its feasibility as an outcome measure for clinical trials in AD.

Methods

We examined AD patients (n=133) with varying degrees of small vessel disease, and normal elderly controls (NC: n=47) from the Sunnybrook Dementia Study. All participants had undergone baseline and follow up MRI (1.5T) and cognitive testing (MMSE), with a mean interscan interval of 1.7 years. Each participant's vCSF, deep and periventricular (d/pWMH) volumes were measured at both time points using a previously validated segmentation pipeline which produces growth, shrinkage, and stable dynamic progression volumetrics.[3] An analysis of covariance was used for group comparisons of the progression metrics and partial Pearson r correlations were used to examine the relationship between changes in vCSF, WMH, and MMSE. All analyses accounted for age at baseline, sex, and years of education.

Results

Dynamic progression analyses revealed that AD patients exhibited significant increases in vCSF volume compared to NC ($p<0.0001$). Pearson r analyses revealed vCSF growth was significantly correlated with pWMH ($r=0.4$, $p<0.0001$) but not dWMH ($p=0.285$). Additionally, vCSF growth exhibited a moderate correlation with change in MMSE score ($r=0.372$, $p<0.0001$) over the same time period.

Conclusions

As expected, patients with AD showed a greater progression of ventricular atrophy compared to cognitively normal elderly. Additionally, vCSF expansion in AD patients from their baseline to follow up scans was consistent with their small vessel disease burden and decline in cognition. These findings suggest that ventricular change is a promising biomarker that may be used as viable outcome measure for novel treatment strategies aimed at halting progression and restoring cognitive function in AD.

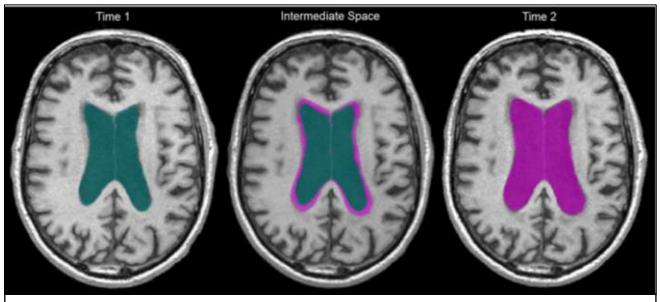

Figure 1: Two year ventricular expansion in a 60 year old man living with AD. Baseline vCSF = 83.6 cc, follow-up vCSF = 119.0 cc. Green indicates baseline vCSF voxels, pink indicates follow-up (right) and growth (middle). WMH within vCSF growth regions were subsequently removed to account for ventricular expansion

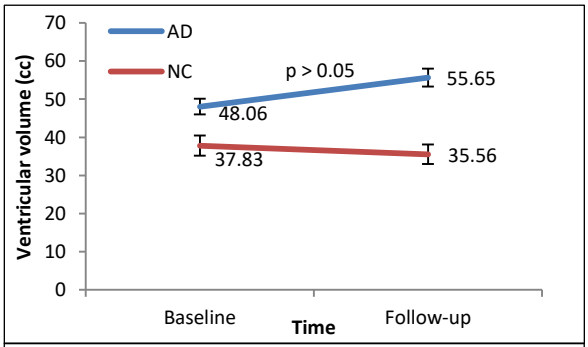

Figure 2: Mean (± SEM) ventricular change in Alzheimer's disease (AD; n=133) and normal controls (NC; n=47) after ~1.7 years.

1 Nestor SM, Rupsingh R, Borrie M, Smith M, Accomazzi V, Wells JL *et al.* Ventricular enlargement as a possible measure of Alzheimer's disease progression validated using the Alzheimer's disease neuroimaging initiative database. *Brain* 2008; **131**: 2443–2454.
2 Lee S, Viqar F, Zimmerman ME, Narkhede A, Tosto G, Benzinger TLS *et al.* White matter hyperintensities are a core feature of Alzheimer's disease: Evidence from the dominantly inherited Alzheimer network. *Ann Neurol* 2016; **79**: 929–39.
3 Ramirez J, McNeely AA, Berezuk C, Gao F, Black SE. Dynamic progression of white matter hyperintensities in Alzheimer's disease and normal aging: Results from the Sunnybrook dementia study. *Front Aging Neurosci* 2016; **8**: 1–9.
4 Edwards JD, Ramirez J, Callahan BL, Tobe SW, Oh P, Berezuk C *et al.* Antihypertensive Treatment is associated with MRI-Derived Markers of Neurodegeneration and Impaired Cognition: A Propensity-Weighted Cohort Study. *J Alzheimer's Dis* 2017; **59**: 1113–1122.
5 Dementia numbers in Canada. Alzheimer Soc. Canada. 2016.

Multivariate hippocampal subfield analysis of PET, DTI and ASL in MCI and AD

Maged Goubran[1,3], Benoit Caldairou[3], Philip DiGiacomo[1], Audrey Fan[1], Praveen Gulaka[1], Steven Chao[1], Andrew Quon[1], Andrea Bernasconi[2], Neda Bernasconi[2], Greg Zaharchuk[1], Minal Vasanawala[1], Michael Zeineh[1]

[1] Richard M. Lucas Center for Imaging, Department of Radiology, Stanford University, CA, USA
[2] Neuroimaging of Epilepsy Lab, Montreal Neurological Institute, McGill University, QC, CA
[3] LC Campbell Cognitive Neurology Research Unit, Sunnybrook Research Institute, ON, CA

Aim: AD has been shown to selectively affect the hippocampal subfields[1]. FDG imaging and fused PET-MR have previously demonstrated hypometabolism within the hippocampus in patients suffering from AD[2]. However, metabolic characteristics within subfield structures have not extensively been explored with PET largely due to poor spatial resolution and the complexity of spatial alignment of small structures. We present an analysis of metabolism, perfusion and diffusion changes in the subfields, using simultaneous PET-MR and a robust feature sampling approach that minimizes partial volume effects.

Methods: 13 subjects with memory complaints were recruited as part of an ongoing study. Based on the clinical dementia rating (CDR), 4 subjects had probable AD (68Ñ4 yr), 4 had MCI (65Ñ5 yr) and 5 had no evidence of MCI/AD and were considered controls (70Ñ6 yr). Patients underwent a 75-min FDG scan on a 3T PET-MR (SIGNA, GE, WI, USA) following a 5 mCi injection of 18F-FDG. We simultaneously acquired high-resolution T1/T2-weighted images, arterial spin labeling (ASL) and diffusion tensor imaging (DTI) sequences. Cerebral glucose uptake maps (CMRGlc) were computed based on kinetic modeling of the dynamic PET. Subfields were segmented using T1-w and T2-w images with *Automatic subfield hippocampal segmentation (ASHS)*[3], into the following subfields: cornu ammonis (CA) 1, CA2, CA3, dentate gyrus (DG), subiculum (SUB) & entorhinal cortex (ERC). To minimize partial volume effects, imaging features were sampled along the central manifold of each subfield by extracting the skeleton running along its central path (***Figure 1***)[4]. Statistical analysis was performed for subfield thickness, CMRGlu (relative to cerebellar metabolism), CBF (relative to cerebellar perfusion), FA, and MD.

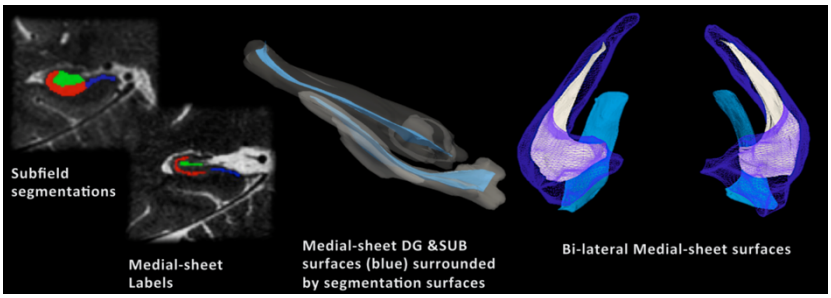

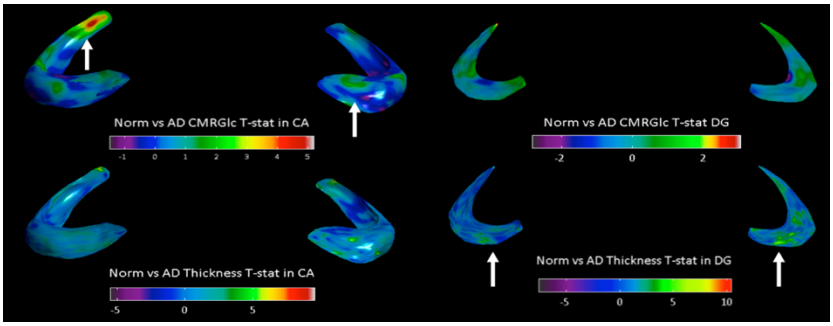

Results: *Whole hippocampus*: Analysis did not yield significant results between the groups for thickness, CMRGlu, CBF, FA, or MD. S*ubfield specific*: Both the dentate gyrus and subiculum showed thickness reduction in AD relative to controls (cluster p = 0.0269, cluster p=0.024). CMRGlc demonstrated a trend of reduction in AD and MCI patients with the highest effect for metabolic change seen in CA (max. T-statistic = 5.184) (***Figure 2***). FA was significantly reduced in the anterior hippocampal body portion of all subfields in AD patients compared to controls. A trend of reduction in CBF in AD and MCI was also found in the subiculum (max. T-stat = 3.70).

Conclusion: Our preliminary results demonstrate that structural and metabolic changes within the hippocampus can be simultaneously assessed at the subfield level and *that subfield analysis may be more sensitive to these pathological changes than global hippocampal assessment*. This study highlights the potential of this multivariate technique in disentangling structural and metabolic derangements accompanying dementia in the hippocampus.

References:

[1] West et al., Neurobiol Aging 2004;25:1205-1212. [2] Mosconi et al., Neurology 2005;64:1860-1867
[3] Yushkevich et al., Human Brian Mapping 2014; 36:258-287 [4] Kim, Hosung, et al. MICCAI 2014. Springer International Publishing, 2014. 170-178.

Improved Freesurfer Parcellation of Structural MRI in VCI population with Inclusion of Masks for Infarcts and White Matter Hyperintensities.

Ozzoude M[1, 2], Holmes MF[1, 2], Scott CJM[1, 2], Raamana P[3], Ramirez J[1, 2, 4], Swartz R[2, 4, 5], Black SE[1, 2, 4, 5], on behalf of the Ontario Neurodegenerative Disease Research Initiative

[1]L.C. Campbell Cognitive Neurology Research Unit, Sunnybrook Research Institute; [2]Hurvitz Brain Sciences Research Program, Sunnybrook Research Institute; [3]Rotman Research Institute at Baycrest Health Science; [4]Heart & Stroke Foundation Canadian Partnership for Stroke Recovery, Sunnybrook Health Sciences Centre; [5]Department of Medicine, Division of Neurology, University of Toronto, Toronto, Canada.

Introduction: Current software packages in brain imaging have allowed researchers to examine changes in brain structures in vascular cognitive impairment (VCI) patient populations [1]. However, the presence of small vessel disease and cortical infarcts pose a challenge in imaging analysis tools as they tend to increase misclassification errors [2]. FreeSurfer (FS) is a software package used for parcellation and analysis of cortical and subcortical brain regions from MRI (http://surfer.nmr.mgh.harvard.edu/). Interestingly, the FS method not only depends on the intensities and probabilities of a voxel belonging to a given region, but also depends on the reliability of the neighboring voxels [3]. This dependency may account for the segmentation failures in the presence of large infarcts and significant white matter hyperintensities (WMH) commonly observed on MRI of VCI patients. The aim of this study was to reduce FS segmentation failures in a VCI cohort, by integrating lesion and skull-stripped brain masks from our in-house software called Lesion Explorer (LE) [4]. **Methods:** 155 VCI patients underwent MRI as part of the Ontario Neurodegenerative Disease Research Initiative (ONDRI) study. Tissue segmentation and WMH were quantified using LE [4] (Fig. A), and cortical infarcts were manually traced on T1 and co-registered FLAIR images (Fig. B). LE outputs (skull-stripping, WMH) and infarct image masks were integrated into FS v6.0 as shown in Figure C. The FS outputs (brain mask, white matter segmentation, and subcortical segmentation) were visually evaluated before and after modifications. **Results:** 73.5% (114/155) failed using FS alone at first pass due to intensity normalization and infarcts (Fig. D). Out of 114 failures at first pass, 26 needed intensity correction using auto control points, 49 infarcts were to be filled, and 39 scans needed auto control points and infarct filling (Fig. E). Including LE outputs into FS improved the overall FS outputs as shown before (Fig. F) and after modification (Fig. G). Figures H&I represent FS brain parcellation of VCI patient with large left hemisphere infarct and error in intensity normalization. The inclusion of stroke mask showed significant improvement in the parcellation (Figs. J&K). **Conclusions**: Our findings suggest that accounting for cortical infarcts and WMH might serve as a possible solution for researchers who may encounter similar issues that arise when examining VCI populations using FS.

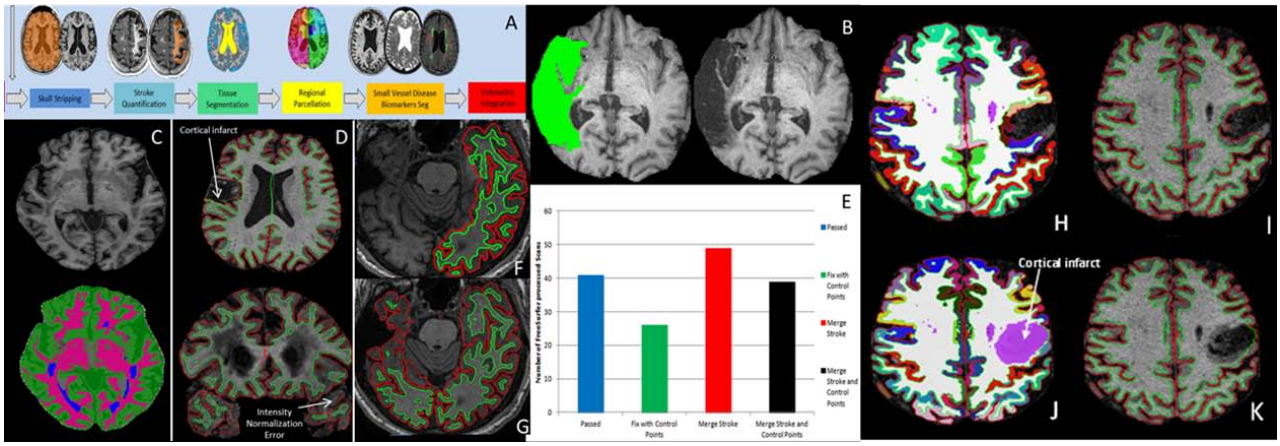

References: [1] Brodtmann, A., Pardoe, H., Li, Q., Lichter, R., Ostergaard, L., & Cumming, T. (2012). Changes in regional brain volume three months after stroke. *Journal of the neurological sciences*, *322*(1), 122-128.[2] Kabir, Y., Dojat, M., Scherrer, B., Forbes, F., & Garbay, C. (2007, August). Multimodal MRI segmentation of ischemic stroke lesions. In *Engineering in Medicine and Biology Society, 2007. EMBS 2007. 29th Annual International Conference of the IEEE* (pp. 1595-1598). IEEE. [3] Fischl, B., Salat, D. H., Busa, E., Albert, M., Dieterich, M., Haselgrove, C., ... & Montillo, A. (2002). Whole brain segmentation: automated labeling of neuroanatomical structures in the human brain. *Neuron*, *33*(3), 341-355. [4] Ramirez, J., Gibson, E., Quddus, A., Lobaugh, N. J., Feinstein, A., Levine, B., ... & Black, S. E. (2011). Lesion Explorer: a comprehensive segmentation and parcellation package to obtain regional volumetrics for subcortical hyperintensities and intracranial tissue. *Neuroimage*, *54*(2), 963-973.

Segmentation of Multiple Sclerosis Lesions using Dictionary Learning in Feature Space

Grey Kuling[1], Dr. Yunyan Zhang[2], and Hongmei Zhu[3]

[1]Faculty of Medical Biophysics, University of Toronto, [2]Department of Radiology, University of Calgary, [3]Faculty of Mathematics, York University

Introduction: Multiple Sclerosis (MS) is the most common neurological disease in Canada. In the diagnosis, management and evaluation of clinical trials for MS, manual segmentation is used to localize lesions in multi-weighted magnetic resonance imaging (MRI) of the brain; specifically T1w, T2w, Proton Density weighted (PDw) and Fluid Attenuated Inversion Recovery (FLAIR). However, manual segmentation suffers from inter and intra observer discrepancies [1]. Automatic segmentation has been proposed using a Machine Learning algorithm called Dictionary Learning (DL [2]. DL creates dictionaries of examples for different classes that a test subject is compared to, in order to determine which class the test belongs with. Up until now, DL segmentation has been done using the voxel intensity as the only information used from the scan, but recent works have shown that there are image texture differences between MS lesions and white matter (WM) [3]. Therefore, we explored using DL to segment MS lesions using a texture quantified feature space.

Methodology: Conventionally, the method of DL for MS lesion segmentation has classified each voxel of interest (VOI) by taking a localized patch of 5x5x5 voxels that here we will call a large patch feature space. Then, the test is classified by comparing it to dictionaries for WM, gray matter (GM), cerebral spinal fluid (CSF), and lesions. We found that quantifying these dictionaries by using texture features improved the segmentation capability. We found a texture feature space that includes the intensity of the VOI, the mean and standard deviation of a 3x3x3 patch, and the entropy of a 5x5x5 patch centred around the VOI, gave more favorable results than the large patch feature space. We present the results of simulations on the simulated patient scans of Brainweb from McGill University [4], and quantified the success using the Dice Similarity Score (DSC).

Results: We present the results of the texture feature space in contrast to the large patch feature space. Each method was tested on 15 slices from 3 lesion loads(mild, moderate, and severe), and the average and error of DSC for all 45 slices are shown on the y-axis of Figure 1. On the x-axis we show the variation in DSC in the presence of increasing noise (N) and intensity inhomogeneity (IIH). Noise is the random variation in intensity levels determined by using a white Gaussian noise generator, and intensity inhomogeneity is a simulation from Brainweb to reflect the radio-frequency inhomogeneity of an MR scanner.

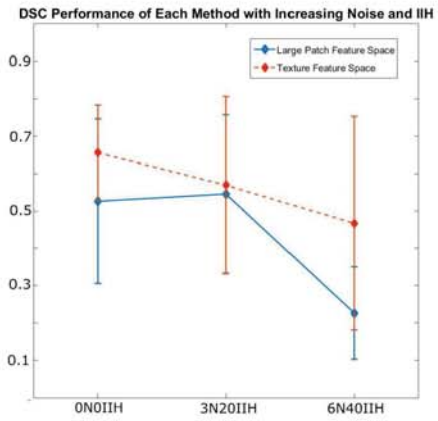

Figure 1: A graph of the Average DSC of each method, versus image distortion.

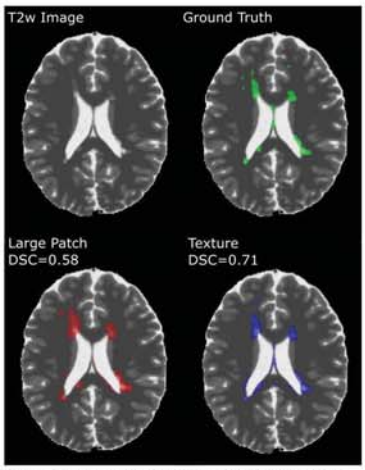

Figure 2: Example results on 0N0IIH slice of the moderate MS lesion load

Figure 2 shows an example slice from the 0N0IIH scans with moderate lesion load. We can see that the large patch method results in over segmentation compared to the ground truth, resulting in a poorer DSC than the texture feature space.

Conclusion: We have presented here that the texture feature space outperforms the large patch feature space in this case, and thus should be explored for future use on a database of real patient MR scans. Acknowledgements: NSERC, and the MS society.

References: [1] C. A. Cocosco, et al. Brainweb: Online interface to a 3dmri simulated brain database. Citeseer, 1997. [2] H. Deshpande, et al. Classification of multiple sclerosis lesions using adaptive dictionarylearning. Computerized Medical Imaging and Graphics, 2015. [3] X. Llado, et al. Segmentation of multiple sclerosis lesions in brain mri: a review of automated approaches.InformationSciences, 2012. [4] Y. Zhang. Mri texture analysis in multiple sclerosis.Journal of Biomedical Imaging, 2012.

Automated pipeline for analysis and visualization of spinal cord tracts from diffusion tensor imaging

Vignesh Sivan, Jason Leung, Cari Whyne PhD, Stewart McLachlin PhD, Michael Hardisty PhD, Pierre Olivier Quirion, Julien Cohen-Adad PhD
Orthopaedic Biomechanics Laboratory, Sunnybrook Research Institute, Toronto, Ontario, Canada

Introduction. Magnetic resonance diffusion tensor imaging (MR-DTI) tractography is a valuable tool for visualization of the locations of white-matter tracts, specifically for applications related to neurosurgery. Most commonly applied in the brain, the goal of this work is to extend this technique into the spine, specifically to create tools to aid in the planning of complex spinal surgeries where there may be anatomical distortion as a result of pathology (tumour, degeneration, etc.). Processing of DTI data for surgical planning requires many steps, as outlined below, including registration and streamline calculation. These steps are integrated into image processing pipelines in clinical software for neurosurgical planning and medical interpretation. The processing steps required take significant computational time and require site specific anatomical knowledge. We have developed software that creates an automated spinal cord DTI processing pipeline that generates tractography streamlines and could be used in a surgical planning workflow and future spine DTI research.

Methods. Computational tools were created using both the 3D Slicer platform and functionality from the Spinal Cord Toolbox library for automated processing of MR-DTI data to generate and verify tract specific DTI streamlines from known anatomical tract locations. Additionally, this pipeline automates the generation of streamlines and computation of spatial-correspondence metrics. The pipeline has four stages: (1) segmentation of T1-weighted MRI and atlas-based labelling, (2) deformable registration of diffusion MRI volumes to the atlas and T1 image, (3) tensor fitting, and (4) warping of the tensors to the anatomical space to display 3D visualization of tract structures against the original T1 volume.

The processing pipeline and algorithm were evaluated in the cervical spine (C2-C6) of ten healthy subjects by examining spatial correspondence of DTI derived streamlines with anatomical tract labels (atlas-based segmentation of T1 images). To examine streamline continuity, tractography was seeded at a cranial and caudal vertebral considering 1, 2, and 3 levels skipped. This was done to evaluate possible clinical scenarios of geometric distortions due to pathology at focal vertebral levels. Spatial correspondence was evaluated by calculating the Dice coefficient, the Hausdorff Distance, the number of streamlines within the anatomical tract label and the 95 percentile distance between the anatomical labels and streamlines.

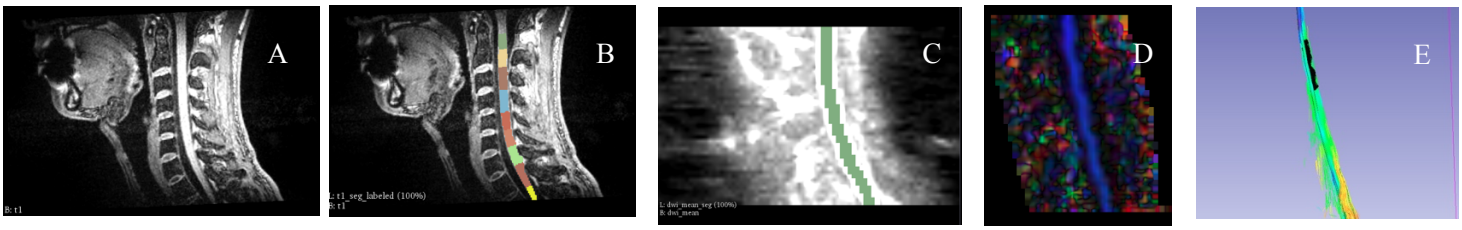

Fig. 1. A: T1-weighted image of subject with healthy anatomy. B: Segmented and labelled spinal cord from A C: Segmented average DWI Image. D: Computation of diffusion tensor image (DTI). E: Streamlines generated from DTI

Results. It was found that the processing pipeline can be run in about 18 minutes on a system with a 3.3GHz Intel Xeon CPU with 8GB RAM. Streamlines were generated for DTI data obtained from ten subjects with healthy anatomy (Fig. 1). Dice coefficients and Hausdorff distances of the streamlines and atlas-labeled T1 images from the skipped vertebral levels were computed. With an anatomic tract probability threshold of 0.3, it was found that the dice coefficient was greatest for one level skipped at 0.767. The average Hausdorff distance was also computed for each level skipped and it was found to be lowest for a single level skipped at 0.431 mm.

Conclusion. This work developed an integrated pipeline for the processing of diffusion MRI data of the spinal cord, allowing for consistent and efficient visualization of specific white matter tracts within the spinal cord. Further we examined the spatial correspondence between the anatomic labels and tractography-based streamlines with custom developed tools. The performance of the pipeline was consistent with technique being potentially useful for neuro-navigation of the spine pending further rigorous validation in cases with pathology.

7T Magnetic Resonance Spectroscopy in the Hippocampus of MRI Normal Temporal Lobe Epilepsy Patients

John Adams[1,2], Simona Nikolova[3,4], Suzan Brown[5], Robert Bartha[1,2], and Jorge G Burneo [5,6]

[1] Centre for Functional and Metabolic Mapping, Robarts Research Institute, University of Western Ontario, London, ON, Canada; [2] Department of Medical Biophysics, University of Western Ontario, London, ON, Canada; [3] Department of Physics and Astronomy, University of California, Irvine, CA, USA; [4] Center for the Neurobiology of Learning and Memory, Department of Neurobiology and Behavior, University of California, Irvine, CA, USA; [5] Epilepsy Program, London Health Sciences Centre, London, ON; [6] Department of Clinical Neurology, University of Western Ontario, London, ON, Canada

Introduction: Pre-surgical identification of epileptic regions in patients has been shown to improve post-surgical outcomes for patients who require such procedures to control their seizures. Magnetic resonance spectroscopy (MRS) has previously been explored as a technique to identify metabolic changes indicative of epileptic tissue in patients with normal appearing MRI brain scans. However, MRS is difficult to acquire in the hippocampus due to magnetic field inhomogeneities, limiting its usefulness in identifying one of the most common forms of intractable epilepsy, temporal lobe epilepsy (TLE).[1-3] The improved signal to noise ratio (SNR), and spectral dispersion that comes with ultra-high field strengths, along with improved shimming hardware on 7T systems, combine to produce high quality spectra in the hippocampus. The purpose of the current study was to examine MRI normal TLE patients on a 7T MRI system to evaluate the utility of 7T MRS in identifying epileptic tissue within the hippocampus.

Methods: Eight unilateral focal TLE patients (4 female, 4 male, average age= 36± 13 years) were recruited though the Epilepsy Program at London Health Sciences Centre, London, ON, Canada. Eleven age, sex, and handedness matched healthy participants were recruited to serve as a control group (5 female, 6 male, average age= 29± 8 years). All patients were diagnosed with drug resistant TLE and were deemed to have normal MRI brain scans when imaged on a 1.5T clinical system as part of routine clinical care. Seizure lateralization for each patient was determined using a combination of clinical EEG recordings and seizure semiology. All participants were scanned on a 7T Siemens head-only MR system, with spectroscopic data collected using a semi-LASER single voxel acquisition (TE= 60 ms, TR= 7.5s, voxel size 2.7x1.7x1.7 cm^3). Both a water suppressed metabolite spectrum (64 averages) and a water spectrum (4 averages) were acquired from each hippocampus separately. Metabolite concentrations were then calculated using software coded by our lab.[4,5] A one-way ANOVA was used to compare metabolite levels from hippocampi ipsilateral to seizure focus, contralateral to seizure focus, and from healthy controls.

Results: Metabolites with a coefficient of variation of less than 35% in our control group were included in our statistical analysis; the metabolites which met this criterion were *N*-acetylaspartate, total creatine, total choline, myo-inostol, glutathione, and combined glutamate plus glutamine. In our ANOVA analysis, we saw a trend in the absolute concentration of creatine, which trended lower in hippocampi ipsilateral to seizure focus compared to the contralateral side ($p = 0.067$). No other noteworthy metabolite changes were found.

Conclusions: While disruption of energy metabolism in TLE is commonly observed in FDG-PET images,[6] an absolute reduction in the concentration of total creatine has not been reported using ^{1}H-MRS. This may be part due to the common use of creatine as a reference signal for calculating the concentration of other metabolites. Recruitment is ongoing, to improve sample size and confirm these findings.

Acknowledgements: This research was made possible by funding from the Ontario Brain Institute, Canada First Research Excellence Fund, and the Brain Canada Foundation.

References:

1) Pan J, et Al. Epilepsia. 2013;54(9): 1668-1678.
2) Xu M, et Al. J Neuroimaging. 2015;25: 1030-1037.
3) Chernov M, et Al. Journal of the Neurological Sciences. 2009;285: 212-219.
4) Bartha R, Drost DJ, Williamson PC. NMR Biomed. 1999;12: 205-216.
5) Rupsingh R et Al. Neurobiology of Aging. 2011;32: 802-810
6) Cendes, Fernando. Continuum. 2013;19(3): 623-642.

Confirmation of A Derivative Hyperspectral NIRS Method for Measuring Oxygen Saturation by Comparison to Time-Resolved NIRS

Matthew Kewin[1, 2], D. Milej[1, 2], A. Abdalmalak[1, 2], A. Rajaram[1, 2], M. Diop[1, 2], S. de Ribaupierre[2, 3], K. St. Lawrence[1, 2]

[1]*Department of Medical Biophysics, University of Western Ontario, London, ON, Canada*

[2]*Imaging Division, Lawson Health Research Institute, London, ON, Canada*

[3]*Department of Clinical Neurological Sciences, University of Western Ontario, LHSC, London, Ontario, Canada*

mkewin2@uwo.ca

1. Introduction

Brain injury during preterm infancy can cause serious intellectual and behavioural disability, as such, reliable monitoring of cerebral health in the neonatal intensive care unit is a sought-after practice. Near-infrared spectroscopy (NIRS) is an ideal candidate for this purpose because it is non-invasive, portable, and can provide a continuous measure of cerebral oxygenation. Commercial systems are available for neuromonitoring in the neonatal intensive care unit; however, these systems only provide relative measurements, making it difficult to establish critical thresholds that can be applied across patients. More advanced NIRS technologies, specifically time or frequency domain systems, can overcome this limitation, but these systems are more expensive and complex. An alternative approach that is both inexpensive and quantitative is continuous wave (CW) broadband NIRS. Hyperspectral data enables multiple chromophores to be measured. Furthermore, we have shown how absolute chromophore concentrations can be extracted from the data using derivative spectral analysis. Concentrations of oxy and deoxyhemoglobin (HbO2 and Hb), can be used to calculate tissue oxygen saturation. The aim of this study was to investigate the ability of broadband NIRS to quantify optical properties and measure cerebral oxygen saturation (ScO_2) under different physiological conditions. Experiments were conducted using a simple tissue-mimicking phantom and an animal model (piglets) in which measurements were acquired at different cerebral oxygenation states. Measurements were also acquired with time-resolved (TR) NIRS for comparison.

2. Methods

2.1 Characterization of CW NIRS system

The broadband NIRS system consisted of a halogen light source (Ocean Optics, Dunedin, Florida) and a custom-built spectrometer (P&P Optica, Waterloo, Ontario). Experiments were performed on a liquid phantom consisting of a mixture of 20% Intralipid with water. Small amounts of diluted India Ink were added to the phantom to increase light absorption. Spectra were acquired at each addition of ink at a source-detector distance of 3 cm.

2.2 In vivo demonstration

Using the same NIRS system and source-detector separation described in 2.1, spectra were acquired from piglets with the probes fixed to the head. The inspired oxygen fraction was reduced from 60% to moderate hypoxia (16%) in 8 steps. Spectra were acquired at each step to measure the reduction in ScO_2. For comparison, changes in ScO_2 were also measured using a TR NIRS system that acquired reflectance data at 670 and 760 nm. The arterial partial pressure of oxygen (PaO_2) and arterial oxygen saturation (SaO_2) were measured at each step by withdrawing arterial blood samples for gas analysis.

3. Results

Analysis of the measured absorption spectrum from the liquid phantom spectrum prior to adding India ink, correctly estimated the expected water fraction of 99%. Ink titration showed a strong linear correlation between the phantom absorption coefficient and ink concentration (R^2=0.98). Finally, the extracted absorption spectrum of ink was in good agreement with the spectral extinction coefficient of ink obtained from literature data.

Across three animals, blood gas measurements showed that average PaO_2 and SaO_2 decreased from 200 to 26 mmHg and 100 to 33%, respectively. Hb and HbO_2 concentrations were quantified at each step and the resulting ScO_2 values dropped from 76% at normoxia to 19% at the lowest inspired O_2 fraction. This trend of deceasing ScO_2 values was confirmed by the TRNIRS results.

4. Conclusion

Broadband NIRS has the capability to quantify cerebral oxygen saturation at the bedside for patients in the NICU, and is a simple but quantitative alternative to current NIRS systems that only provide relative measurements. Further animal studies are ongoing to confirm these promising preliminary findings.

Development of a Self-calibrated DCS System for Tracking Absolute Cerebral Blood Flow

Mahro Khalid[1,2*], Daniel Milej[1,2], Ajay Rajaram[1,2], Androu Abdalmalak[1,2], Mamadou Diop [1,2], Keith St Lawrence[1,2]

[1]*Department of Medical Biophysics, University of Western Ontario, London, Ontario, Canada N6A 5C1*
[2]*Imaging Division, Lawson Health Research Institute, London, Ontario, Canada, N6A 4V2*
* mkhali56@*uwo.ca*

Introduction: Diffuse correlation spectroscopy (DCS) is an emerging non-invasive optical technique for monitoring cerebral blood flow (CBF) [1]. Although the blood flow index (BF_i) obtained by DCS has been shown in multiple validation studies to be linearly proportional to CBF, the conversion to units of blood flow is not trivial as it depends on the mean vessel diameter [2]. Here, we present a multi-distance DCS approach that has the capability of performing dynamic contrast-enhanced (DCE) measurements to determine absolute CBF in addition to standard BF_i monitoring. With this modification, CBF can be continuously monitored by DCS alone without requiring the combination with a separate NIRS system for DCE measurements [3].

Methods: The self-calibrated DCS method required replacing a dedicated hardware correlator with a software version in order to access the photon counts, and to record data at multiple source-detector distances. The effective attenuation coefficient (μ_{eff}) was determined from light intensity measurements acquired at different distances using the principle of spatially resolved NIRS. The corresponding autocorrelation curves (g_2) acquired across the distances were analyzed using the solution to diffusion equation for a semi-infinite homogeneous medium and incorporating the measured μ_{eff} to determine the reduced scattering coefficient (μ_s') and baseline BF_i. From the baseline optical properties, the differential pathlength (DP) was calculated, which was used to convert time-varying changes in light intensity caused by the passage of indocyanine green (ICG) through the cerebral vasculature into an ICG tissue concentration curve.

For demonstration of the approach, experiments were conducted using newborn piglets in which CBF was increased by change P_aCO_2 from normocapnia to hypercapnia. During the former, baseline intensity and g_2 data were acquired to extract baseline optical properties and DP. The DCE protocol required an IV bolus injection of ICG (0.1 mg/kg), followed by acquiring serial intensity measurements for 120 s. The corresponsing arterial ICG concentration was measured non-invasively by dye densitometry, Baseline CBF was calculated by standard kinetic modelling analysis. P_aCO_2 was then increased and multi-distance light intensity and g_2 data recorded to measure changes in light absorption and CBF.

Results: Fig 1 shows the CBF time course during a 5-min hypercapnic challenge. Plotted is the BF_i time course that has been converted to CBF by the DCE baseline data. As expected, CBF increased after the switch from normocapnia to hypercapnia at the 5-min mark.

Discussion and Conclusions: Data presented show that multi-distance DCS can track changes in absolute CBF with high contrast to noise. This was achieved by quantifying baseline optical properties from light intensity and g_2 curves measured at multi-distances, which were subsequently used to determine CBF by converting DCE data into ICG concentration. This study shows that a stand-alone DCS system is capable of calibrating BF_i measurements, which eliminates the need of combining DCS with another NIRS system. Incorporating measurements at multiple wavelengths would enable tissue oxygenation to be measured for determining the cerebral metabolic rate of oxygen as well.

References:

[1] T. Durduran et. al, "Diffuse correlation spectroscopy for non-invasive, micro-vascular cerebral blood flow measurement," *NeuroImage*, 2014.
[2] D. A. Boas, et al., "Establishing the diffuse correlation spectroscopy signal relationship with blood flow," Neurophotonics, 2016.
[3] M. Diop, et. al, "Calibration of diffuse correlation spectroscopy with a time-resolved near-infrared technique to yield absolute cerebral blood flow measurements," Biomed. Opt. Express, 2011.

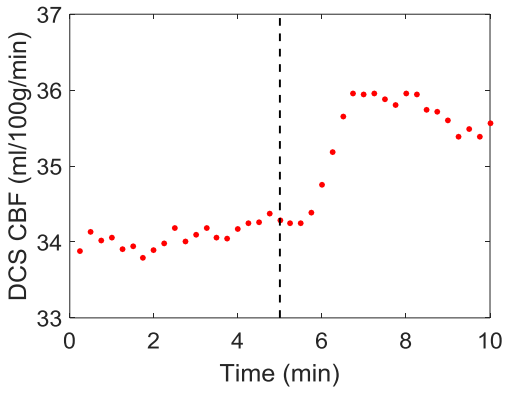

Fig 1: Change in CBF (dotted line) as a small concentration of CO_2 was introduced in an animal's inhaled gas mixture.

Brain Diffusion Tensor Imaging Metrics in Cerebral Tissues and Ischemic Lesions

Seyyed M. H. Haddad[1], Christopher J. M. Scott[2], Miracle Ozzoude[2], Stephen R. Arnott[3], Richard H. Swartz[4], Dar Dowlatshahi[5], Stephen C. Strother[3], Sandra E. Black[2], Sean Symons[6], Manuel Montero-Odasso[7], Robert Bartha[1], and ONDRI Investigators

[1]Robarts Research Institute, University of Western Ontario, London, Ontario, Canada, [2]L.C. Campbell Cognitive Neurology Research Unit, Sunnybrook Health Sciences Centre, Toronto, Ontario, Canada, [3]Rotman Research Institute, Baycrest Centre for Geriatric Care, Toronto, Ontario, Canada, [4]Sunnybrook Health Sciences Centre, University of Toronto, Stroke Research Program, Toronto, ON, Canada, [5]Ottawa Hospital Research Institute, Ottawa, ON, Canada, [6]Department of Medical Imaging, Sunnybrook Health Sciences Centre, Toronto, ON, Canada, [7]Parkwood Institute, London, Ontario, Canada

Introduction

Diffusion Tensor Imaging (DTI) is an MRI-based imaging technique sensitive to the translational motion of water molecules in the body. Diffusion measurements provide detailed information about the microstructure of brain tissue, especially white matter (WM) tracts, as it is sensitive to the type and configuration of microscopic cerebral tissue constituents. While a sensitive technique for studying brain tissue microstructure, DTI suffers from serious artifacts such as motion, eddy current induced distortions, echo-planar imaging (EPI) artifacts, and low signal to noise ratio (SNR) due to the method of data acquisition, requiring careful processing of this MR modality within sophisticated DTI processing pipelines.

Method

As part of the Ontario Neurodegenerative Disease Research Initiative (ONDRI), we have developed a fully automatic DTI processing pipeline based on the well-known ENIGMA DTI protocols. In our image processing pipeline, we performed three major processing procedures on the brain DTI data: 1) conversion of the raw DTI data to NIFTI/NRRD formats, 2) quality control and artifact removal, and 3) calculation of the voxelwise diffusion tensors and then DTI scalar metrics, mainly fractional anisotropy (FA) and mean diffusivity (MD), maps throughout the brain. Realization of this pipeline was achieved using well-known freely available image processing toolkit/software packages such as FSL, ITK, 3D Slicer, Camino, and ANTs. It is noteworthy that the total processing time for one DTI dataset using the proposed pipeline is ~90 minutes on a regular computer (16 GB RAM, Intel Core i7-6800K 3.4 GHz CPU).

To test our pipeline, we considered DTI datasets from six patients with vascular cognitive impairment (VCI) available in the ONDRI database, and then used our pipeline to calculate FA and MD maps throughout their brain. Cerebral tissue lesion masks obtained in part by manual segmentation of the corresponding T1-weighted images were used to calculate the DTI metrics in 12 types of cerebral tissues and lesions including stroke lesions, deep WM hyperintensities, periventricular WM hyperintensities, deep lacunae, periventricular lacunae, normal appearing gray matter, normal appearing WM, left and right hemisphere hippocampal tissues, periventricular spaces, sulcal CSF, and ventricular CSF, to determine how DTI metrics vary in these tissue types.

Results and Conclusion

Fig. 1 shows the FA and MD maps obtained from the developed DTI processing pipeline for a VCI subject along with corresponding T1-weighted image and lesion mask.

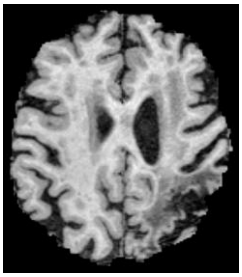

Fig. 1a) T1-Weighted Image

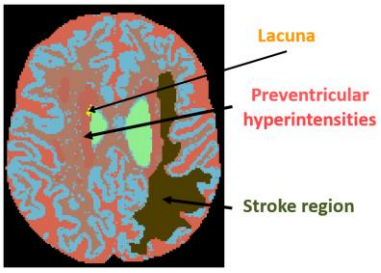

Fig. 1b) Corresponding Lesion Mask

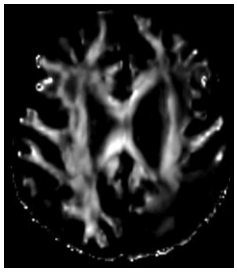

Fig. 1c) FA Map

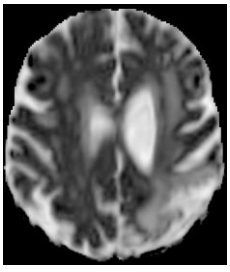

Fig. 1d) MD Map

FA values were significantly lower (Fig 1c), and MD values were significantly higher (Fig 1d) in stroke, periventricular lacunae, and WM hyperintensities compared to normal tissues, both indicating cerebral tissue (WM) disintegration in the abnormal regions consistent with the literature [1]. This automated pipeline will be applied to all ONDRI datasets to assess diffusion differences between neurological conditions.

[1] T. A. G. M. Huisman, "Diffusion-weighted and diffusion tensor imaging of the brain, made easy," *Cancer Imaging*, vol. 10, no. 1A, pp. S163–S171, Oct. 2010.

Title: Correcting the Arterial Input Function for Dynamic ^{18}F-FEPPA PET in Transgenic Fischer 344 Rats with Manual Blood Sampling

Authors: Qi Qi[1,2,5], Matthew S. Fox[1,2,5], Alexander Levit[3,4], Shawn N. Whitehead[3], Ting-Yim Lee[1,2,5,6], Jonathan D. Thiessen[1,2,5].

Departments of [1]Medical Biophysics, [2]Molecular Imaging, [3]Anatomy and Cell Biology, [4]Schulich School of Medicine & Dentistry, The University of Western Ontario; [5]Imaging Program, Lawson Health Research Institute; [6]Robarts Research Institute, London, Ontario, Canada

Introduction: A mitochondrial translocator protein (TSPO) is upregulated in activated microglia and reactive astrocytes during neuroinflammation. A TSPO-targeting positron emission tomography (PET) radiotracer, ^{18}F-radiolabelled phenoxyanilide (^{18}F-FEPPA), has been synthesized at our site to image neuroinflammation. Kinetic analysis is essential to accurately measure the uptake of the radiotracer and estimate the extent of inflammatory response. Blood sampling and analysis plays an important role in estimating the amount of unmetabolized radiotracer left in the plasma, which is then used to correct the arterial input function and provide an accurate estimate of tracer kinetics. We have developed a blood sampling method that can provide accurate information about free and metabolized forms of ^{18}F-FEPPA at multiple time points for dynamic PET imaging in rats.

Methods: Transgenic Fischer 344 rats (TgF344AD, n = 5) homozygous for mutant human APP gene were used in this study. Manual blood sampling was performed to measure the amount of unmetabolized ^{18}F-FEPPA in blood over time. Oasis HLP 1cc Vac Cartridges were used to separate distinct types of metabolites in blood (Katsifis et al. 2010). Each cartridge was conditioned using 1 mL of ethanol followed by 1 mL of distilled water. During a dynamic PET acquisition (Siemens Inveon), 5 arterial blood samples (0.4-0.5 mL each) were acquired from the tail artery of each subject at approximately 2, 8, 16, 64, and 90 minutes after the ^{18}F-FEPPA injection. Initially, 0.05 mL of blood was drawn, mixed with 0.25 mL of distilled water and collected in a test tube and labeled as whole blood (WB). The remaining 0.35-0.45 mL of blood was centrifuged to separate plasma from red blood cells. 0.05 mL of plasma was drawn, mixed with 0.25 mL of distilled water and transferred to a test tube and labeled as plasma (P). Another 0.05 mL of plasma was drawn, mixed with 1 mL of distilled water, applied to conditioned cartridges, washed with 20% acetonitrile and 80% acetonitrile consecutively to obtain mostly hydrophilic metabolites (M1), less hydrophilic more hydrophobic metabolites (M2) and mostly hydrophobic metabolites (M3 – corresponding to the unmetabolized FEPPA fraction), respectively. The cartridge was labeled as R (residual) at the end of elution. The samples were loaded in a high-purity Germanium well counter to measure the radioactivity of each sample. The blood-to-plasma ratio (BPR) and unmetabolized FEPPA fraction were calculated and plotted using a customized MATLAB script.

Results and Conclusion: The blood-to-plasma ratios, the radioactivity fractions of different metabolites (M1, M2, M3 and R) and the remaining unmetabolized FEPPA fraction plots are shown in **Figure 1**. This is a fast, low-cost, and reproducible method for deriving a corrected arterial input function for dynamic ^{18}F-FEPPA in rat models of disease.

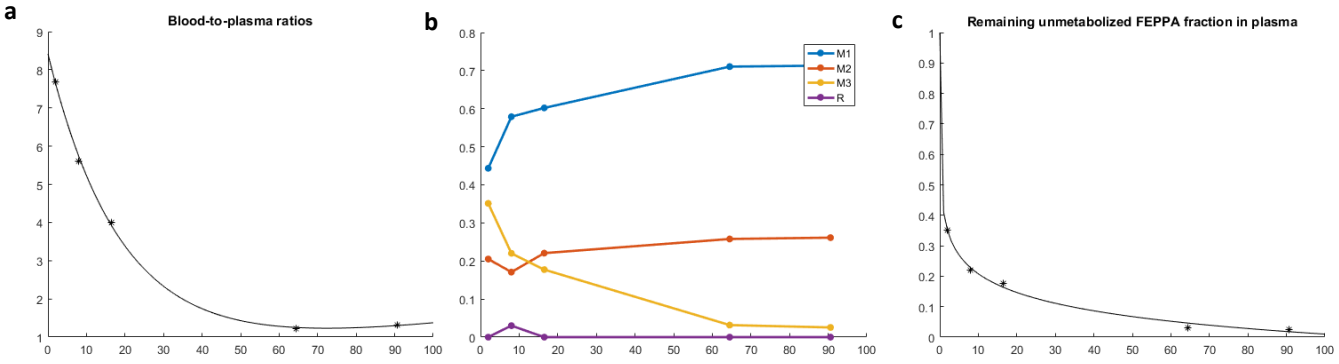

Figure 1: The blood-to-plasma ratios (**a**), the activities fractions of different metabolites (**b**) and the remaining unmetabolized FEPPA fraction (**c**) plots are shown above.

Poster Presentation Abstracts

Session 9: Instrumentation and Technology Development

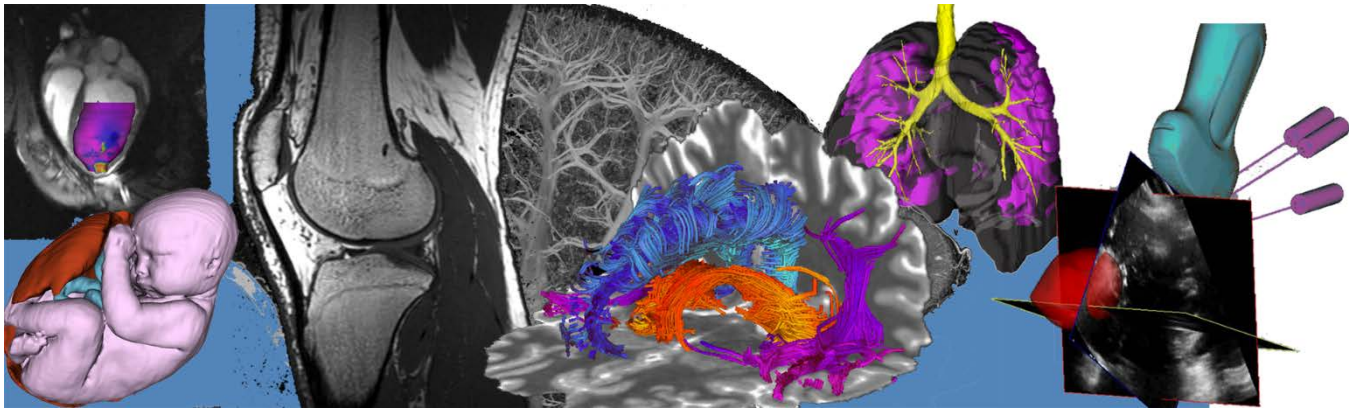

Component fusion in a webcam based optical tracker for interventional navigation

Mark Asselin, Andras Lasso, Tamas Ungi, Gabor Fichtinger
Laboratory for Percutaneous Surgery, School of Computing, Queen's University, Kingston, Canada

INTRODUCTION: In computer assisted surgery, it is very common to make use of the tracked position of a tool to guide surgical intervention. Many techniques exist to track surgical tools, but one of the most accurate is optical tracking. Commercially available surgical navigation systems that use optical tracking can track tools using reflective spheres or active infrared LED markers mounted on the tool in an asymmetric geometry. Such systems are highly accurate, but can be large and prohibitively expensive for surgical training or procedures where lower accuracy is acceptable. In this paper we develop an open source system which uses a laptop webcam or an off the shelf webcam with an additional infrared depth sensor to create an optical tracker which is both low in cost and convenient in form factor.

METHODS: We selected the Intel RealSense SR300 camera (Intel, Santa Clara, CA, USA) to perform this experiment because it had the combination of a fixed-focus RGB sensor and an infrared laser depth scanning sensor. We extended the PLUS toolkit [1] to incorporate the ability to acquire pixel-matched RGB video and depth point cloud data from the SR300. Using the RGB frame we applied the ArUco marker tracking toolkit [2] to acquire an RGB only pose of the tracked marker. We then extracted the depth point cloud data corresponding to the ArUco marker (pictured on the right in Figure 1) and performed a least squares plane fit to identify the center of mass of the marker plane. We setup the experiment in Figure 1 to determine the accuracy of the two different methods of computing the marker position in the direction perpendicular to the camera sensor plane. The results of this prompted us to fuse the two tracking streams by component fusion, selecting the components in the plane of the image sensor from the RGB stream and the remaining component from the depth stream.

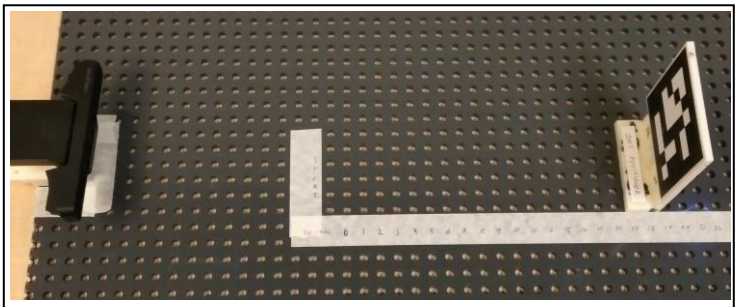

Fig 1. Setup to compute error in depth measurement

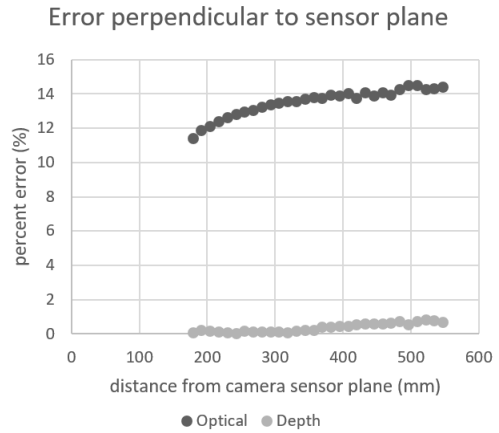

Fig 2. Percent error in position component out of sensor using ArUco and the depth data algorithm

RESULTS: Using the SR300, the ArUco based RGB only pose tracker had errors of 11% to 15% in computing the depth of the marker with respect to the camera (Figure 2). Using the point cloud data obtained from the SR300's laser infrared depth sensor we were able to compute the depth of the marker with less than 1% error in the position of the marker in the direction perpendicular to the camera. The use of component fusion improved the accuracy of the SR300 based tracker by using the depth stream to increase the accuracy of measuring marker depth relative to the camera.

CONCLUSIONS: Component fusion provides improvement to the accuracy of the SR300 at resolving the depth of a marker; however, this system does not yet have the accuracy to be viable for use in clinical procedures.

ACKNOWLEDGEMENTS: This work was funded, in part, by NIH/NIBIB and NIH/NIGMS (via grant 1R01EB021396-01A1 - Slicer+PLUS: Point-of-Care Ultrasound) and by CANARIE's Research Software Program.

REFERENCES: [1] A. Lasso, et al. "PLUS: open-source toolkit for ultrasound-guided intervention systems," IEEE Transactions on Biomedical Engineering, 61(10), 2527-37 (2014). [2] S. Garrido-Jurado, et al. "Automatic generation and detection of highly reliable fiducial markers under occlusion." Pattern Recognition, 47(6), 2280-2292 (2014).

Characterization of a cooled-CCD sensor for optical molecular imaging

David W Holdsworth,[1,2,3]
Development of Novel Therapies for Bone and Joint Diseases Consortium
[1]Department of Surgery, Western University, [2]Robarts Research Institute, [3]Department of Medical Biophysics, Western University, London, Ontario, Canada

Introduction: Optical imaging systems for bioluminescent molecular imaging typically employ a cooled CCD sensor to acquire very low-noise images of low-intensity specimens and animals. Proper functioning of these devices depends on consistent operation of the detector system, *i.e.* stability of focus, electronic gain, electronic read noise, and dark current. Although these parameters are usually specified by the manufacturer, there is typically no routine method for operators to evaluate these parameters as part of a quality assurance program, or after upgrades or repairs. We describe a low-cost technique for accurately evaluating the performance characteristics of a cooled CCD, using a purpose-built calibration device for low-intensity optical imaging.

Methods: This approach uses a calibration system that has been previously described.[1] Briefly, the calibration device is based on a 1.8" diagonal LCD TFT display (ST7735R) with 128x160 pixel resolution and an 18-bit colour display. The display is controlled by a dedicated microcontroller system (Arduino Uno), which controls the pulse-width and duty cycle for the transistor-controlled LED backlight display. In this manner, the light intensity that is displayed during a time-exposure acquisition can be varied linearly over five orders of magnitude. The display can present intensity patterns (such as spatial resolution tests) or uniform intensity patterns over a wide range of mean values. The latter capability can be used to characterize the system gain, read noise and dark current, using the mean-variance technique that has been previously described.[2] By presenting varying intensity levels to the sensor over the entire dynamic range, it is possible to derive the system gain (in ADU electron^{-1}) from the slope of the mean-variance curve, and the read noise (in electrons) from the intercept. Testing was carried out in a commercially available optical imaging system (FX-Pro, Carestream) using standard image acquisition settings. This device employs a 2048 x 2048 pixel monochrome, interline-transfer, thermoelectrically cooled CCD, with specified operating parameters of <7 electrons read noise and 0.003 electrons pixel^{-1} s^{-1} dark current, at its normal operating temperature of -29°C.

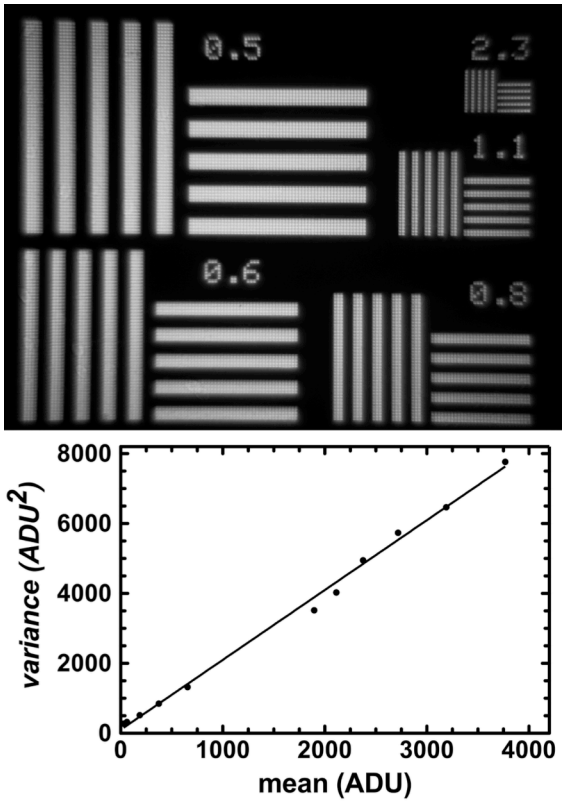

Fig. 1: Results from characterization of spatial resolution (upper) and mean-variance analysis (lower).

Results: Images of spatial resolution test patterns were acquire over a range of fields of view (FOV), from 35 to 200mm. Maximum spatial resolution at 35mm FOV was better than 2.3 line-pairs mm^{-1} (Fig. 1), maintained at better than 1.1 line-pairs mm^{-1} at 200mm FOV. Mean-variance analysis indicated a system gain of 1.99 ADU electron^{-1}, 5 electrons read noise, and dark current of 0.001 electrons pixel^{-1} s^{-1}.

Conclusions: An optical calibration system, based on a conventional backlit TFT display has been developed and implemented to characterize the performance of a cooled CCD sensor. The device that was tested (Kodak Carestream FX-Pro) exhibited performance parameters that were within the manufacturers specifications.

References: **1.** Holdsworth, D.W. "Low-intensity calibration source for optical imaging systems," *SPIE Proceedings Volume 10137, Medical Imaging: Biomedical Applications in Molecular, Structural, and Functional Imaging,* 101371L (2017); **2.** Sperline, R.P. "Read-noise characterization of focal-plane array detectors via mean-variance analysis," *Applied Spectroscopy* 59; 1315-1323, (2005).

Title: Cardiac Ballistic Gel Phantom for Ultrasound Imaging

Authors*: Angela Kim, Talha Javed, Amy Thu Do, Jeremy Tan, Natasha Alves-Kotzev and Brian Courtney

*All authors affiliated with Sunnybrook Research Institute

Abstract:

Cardiac ultrasound phantoms are important tools for training physicians and supporting the development of new imaging devices. However, most phantoms lack small details and features that can be important landmarks within the heart structure. We have attempted to overcome these limitations through a new construction method, and have successfully constructed an anatomically realistic cardiac ultrasound phantom using synthetic ballistic gel, a styrene-ethylene-butylene-styrene block co-polymer. Our model was developed based on image segmentation techniques applied to a patient's set of CT scans, produced using conventional plastics molding techniques, and evaluated by a trained cardiologist using a commercial intracardiac echocardiography probe.

Our phantom is unique in that it is a complete organ model which captures the major cavities and lumens of the heart; both ventricles and atria, aorta, superior vena cava and inferior vena cava. Detailed anatomic features were formed using 3D printed parts to produce silicone molds. Two sets of silicone molds were formed: one to capture the exterior geometry of the model, and a second that forms sacrificial core parts to create the interior geometries. To produce the phantom, ballistic gel was melted and mixed with scatterer and poured into prepared molds. After it has solidified, the sacrificial cores were removed.

We then qualitatively assessed the function of our phantom. First, anatomic features of the cardiac model were confirmed to be present by a cardiologist. We then tested if our tissue-mimicking material was an adequate replicant of cardiac tissue. Ballistic gel was found to have several benefits over commonly used tissue-mimic materials; it is temporally stable, low-cost, durable, and readily formed into complex geometries. It is anticipated that our developed methodology in the construction of ballistic gel phantoms will have broad applicability as a research and training tool, especially in the development of patient-specific models.

Development and clinical translation of a new handheld imaging device for 5-ALA-induced fluorescence guided breast conserving surgery

Christopher Gibson,[1,2] Dr. Kathryn Ottolino-Perry,[2] Dr. Wey Leong,[2] Dr. Alexandra Easson,[2] Dr. Susan Done,[2] Dr. Ralph DaCosta[1,2]

Introduction: Twenty-three percent of patients who undergo breast conserving surgery (BCS) for early stage breast cancer require reoperation within 1y to remove residual tumour cells not detected in the initial surgery [1]. Re-excisions increase discomfort, stress, adjuvant delay, medical costs, and local recurrence [2]. The purpose of this project is to develop a new custom-designed handheld fluorescence imaging device that allows real-time visualization of residual breast tumour within the surgical cavity. We hypothesize that fluorescence-guided resection using this device with 5-aminolevulinic acid (contrast agent) will improve BCS resection completeness compared to the standard of care.

Methods: 5-aminolevulinic acid (5-ALA) is an oral prodrug that promotes tumour-specific accumulation of protoporphyrin IX (PpIX), which primarily fluoresces (glows) bright red when excited with 405 nm (violet) light. We have previously demonstrated a proof-of-concept to image breast tumour margins intraoperatively based on 5-ALA-induced PpIX fluorescence in resected tissues (clinicaltrials.gov ID NCT01837225). Clinical user feedback from this ongoing trial has informed the design of an optimized fluorescence imaging prototype device that will be tested in tissue phantoms painted with PpIX. Following initial validation of the new device, we will test our hypothesis in a recently funded Phase III Pan-Canadian multicentre randomized clinical trial ("The Canadian FIGHT Breast Cancer Surgical Trial"; PI: R. DaCosta).

Results: We built a new proof-of-concept imaging device (RPi-Cam) which captures and streams fluorescence images wirelessly to a computer in real-time. We have successfully demonstrated detection of PpIX in pork tissue with RPi-Cam. Additionally, RPi-Cam includes white light illumination for enhanced surgical cavity visualization and anatomic colocalization of PpIX. Next steps include preparing RPi-Cam for trial readiness by miniaturizing into a clinically-informed housing design.

Conclusions: In its early stages, RPi-Cam provides a number of benefits over competing technologies. We anticipate the results of this study will elucidate the clinical applicability of intraoperative fluorescence image guidance for BCS.

References

1. Porter G et al. Rates of breast cancer surgery in Canada from 2007/08 to 2009/10: retrospective cohort study. *CMAJ Open*. 2014;2(2):E102-E108.
2. Clough KB et al. Oncoplastic Surgery: Pushing the Limits of Breast-Conserving Surgery. *The breast journal*. 2015.

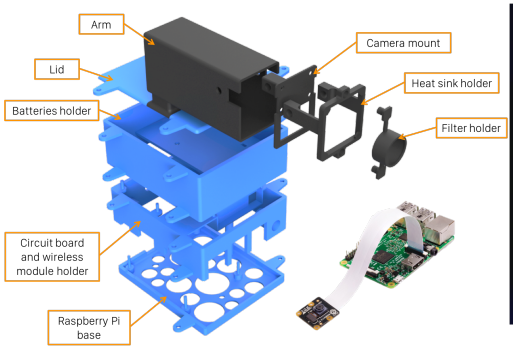

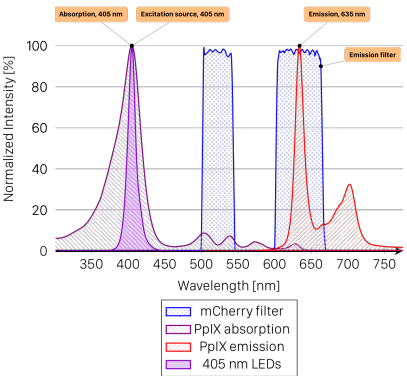

[1]Department of Medical Biophysics, University of Toronto; Toronto, ON
[2]Princess Margaret Cancer Centre, University Health Network; Toronto, ON

A mixed-reality user interface for gross anatomy learning

Fady Said[1*], David Burbidge[2*], Mustafa Haiderbhai[1], Sheila Esmeralda Gonzalez-Reyna[1], Mina Zeroual[3], Michel Désilets[1], Pascal Fallavollita[1]

[1]Faculty of Health Sciences, University of Ottawa
[2]Faculty of Health Sciences, Carleton University
[3]Faculty of Medicine, University of Ottawa
* *equal first author contribution*

Introduction: The Magic Mirror system is an anatomy learning technology developed in collaboration with the Technical University of Munich, Johns Hopkins University, and the University of Ottawa. The system comprises a Kinect sensor, a TV display, and custom in-situ visualization software making it a low-cost enabling technology. The system allows visualization of medical data directly on the user body, and a gesture-based user interface (UI) allows direct interaction with this data. However during interaction, the gesture UI was both cumbersome and imprecise at times as it required the user to utilize both arms/hands when switching between organ systems during the anatomy learning. The objective of this work was to redesign the Magic Mirror system by reducing complexity of the user-interactions and tailoring the gestures for specific organ systems. This was achieved during a pilot study with students during gross anatomy learning, and user-interface development feedback from two Anatomy Professors.

Methods: We redesigned the Magic Mirror user interface to a button-based control. The button-based controls were used when interacting with the traditional anatomy systems, taught to students in their first year of studies, namely: skeletal, cardiovascular, lymphatic, urinary and respiratory systems. Since these anatomy systems can be visualized in both 2D and 3D, OpenGL was used for our interactive graphics applications. We then reconfigured the Magic Mirror menus using a nano-graphical user interface (NanoGUI), which is a minimalistic cross-platform widget library for OpenGL. It supports automatic layout generation and makes it easy to instantiate widgets, and set layout constraints. With the addition of the NanoGUI, users can now switch between anatomy systems by selecting the various options with a mouse. The keyboard was used for more precise movement of the model along with the scroll on the mouse for zooming in and out. On the NanoGUI, additional added features included pre-set zoom regions of interest, adding bones to the various organ systems, text labels in both French and English language, and switching the anatomy viewpoint from front to back.

Results & Conclusion: User interfaces are not works of art but they are meant to be functional tools to allow users to easily accomplish the required task. The purpose of this work was to improve the Magic Mirror's usability and anatomy learning features for future medical students at our partner's medical schools. In the current pilot study, twenty-two students participated interacted with the refurbished Magic Mirror gesture-user interface. The users had an easier time navigating through the anatomy systems during the gross anatomy learning. Future studies will aim at measuring the effect of the button-based controls to user performance and ability to learn gross anatomy.

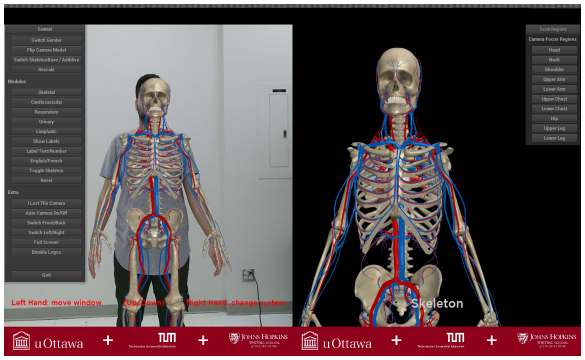

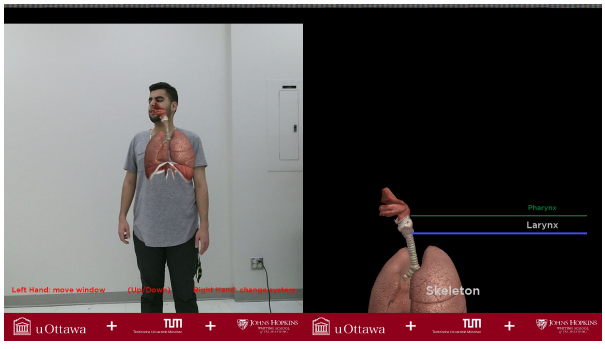

A system for stimulating live cells with high-frequency oscillatory fluid shear during real-time microscopy

Lorusso, D. [123], Nikolov, HN. [1], Soon, K. [4], Poepping., TL. [4], Sims, SM. [23], Dixon, SJ. [23], Holdsworth, DW. [1356]

1 Imaging Research Laboratories; Robarts Research Institute; 2 Department of Physiology and Pharmacology; 3 Bone and Joint Institute; 4 Departments of Physics and Astronomy; 5 Medical Biophysics; 6 Surgery
Schulich School of Medicine & Dentistry

The University of Western Ontario, London, ON, Canada

Primary Author: Lorusso, D. **Research Supervisor**: Drs. S.J Dixon and D.W. Holdsworth

Introduction: Mechanotransduction is the process by which cells sense – and respond to – the local mechanical environment. This ability to react to external loads and forces is a critical component of physiology and is essential for normal functioning of our bones, lungs, and blood vessels; yet, the underlying mechanisms are not fully understood. A form of mechanical stimulation that is commonly implicated in mechanotransduction is fluid shear stress (FSS). Recently, high-frequency oscillatory fluid shear (OFS) has been identified as a physiologically relevant stimulus, but the equipment does not yet exist to apply OFS to live-cells during real-time monitoring. Our goal is to observe the immediate responses of cells to high-frequency OFS. Here, we describe the development and validation of microfluidic platform for applying OFS to live-cell cultures at frequencies up to 90 Hz with shear between 1 and 3 Pa, and is compatible with real-time optical microscopy and photometry.

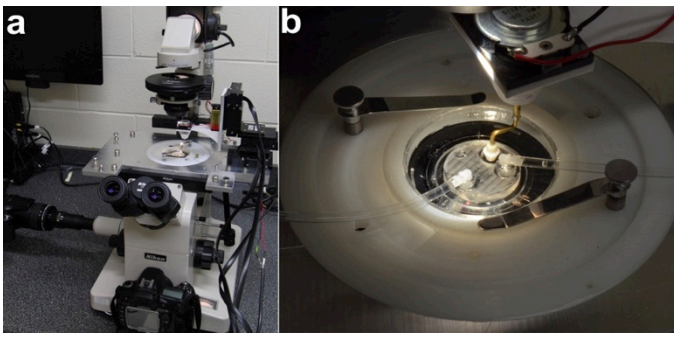

Fig. 1 The high-frequency oscillatory fluid shear platform mounted on an inverted Nikon microscope **(a).** Visible are key components of the device, including the micro-manipulator stage on the right side of the microscope, and **(b)** the electromagnetic actuator interfaced with the microfluidic device on-chip pump.

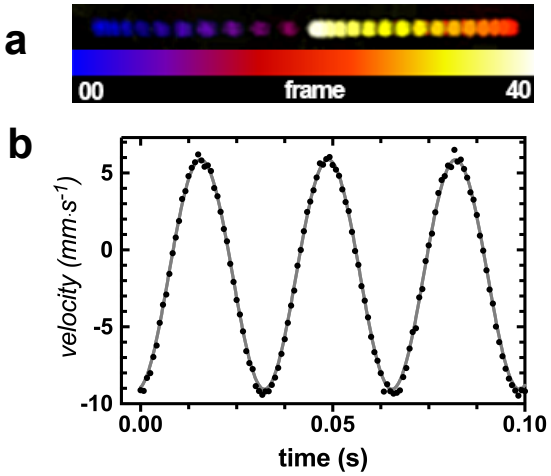

Fig. 2 (**a)** Maximum intensity projection of 1/2 cycle (40 frames) of a 6 μm marker bead oscillated sinusoidally at 30 Hz in concert with 15 μL/min steady flow and imaged on an inverted microscope with a high-speed camera (1200 FPS). (**b)** Position over time of the particle from Fig. 3. The grey curve indicates the result of non-linear regression performed to fit a sine curve to the data. Peak velocity of the particle was found to be 7.461 ± 0.14 mm/s, with an average frequency of 30.14 ± 0.09 Hz ($R^2 = 0.95$).

Methods: The system was comprised of 3 main components: a microfluidic device with an on-chip pump, an electromagnetic (EM) actuator to interface with the on-chip pump, and a motorized micro-manipulator (Sutter Instruments) to precisely position the EM actuator; all of which was assembled on an aluminum plate and then mounted on an inverted microscope (Nikon). The microfluidic device was of a novel design and fabricated from the silicone polymer PDMS using a method described previously (Lorusso et al. *Biomedical Microdevices* 2016). Steady flow was introduced to the device with a syringe-pump (NewEra) and the flow waveform was modulated with a sinusoidal oscillation using the on-chip EM pump. To observe flow velocities, marker beads are pumped through the channels and imaged at high-speed with a micro-particle image velocimetry system. To validate the application to cells, MC3T3-E1 cells were seeded into the device, loaded with fluorescent calcium dye fura-2 and imaged.

Results: During operation above 30 Hz and 1 – 3 Pa, sinusoidal motion of flow waveforms were observed, with velocities in the millimeters per second range. Cells were successfully seeded in the device, loaded with fura-2, and imaged.

Conclusions: We have developed, fabricated, and tested a microfluidic system capable of – for the first time – delivering physiologically relevant high-frequency oscillatory fluid shear stress to live-cells during real-time microscopy and photometry.

Detecting walking asymmetries automatically with a portable system in patients with knee osteoarthritis

*Riley A Bloomfield[1,4,5], Megan C Fennema[2,4,5], Brent A Lanting[3], Kenneth A McIsaac[1], Matthew G Teeter[2-5]
[1]Dept. Electrical & Computer Engineering, [2]Dept. Medical Biophysics, [3]Dept. Surgery,
[4]Robarts Research Institute, Western University; [5]Lawson Health Research Institute

Introduction: Asymmetries observed during walking can indicate movement impairments and the progression or severity of many health conditions including Parkinson's, stroke, and osteoarthritis (OA). Knee OA is most prevalent of all weight bearing joints, and has been linked to gait differences in the frontal and sagittal plane even at mild to moderate stages of the disease [1]. Quantification of between limb asymmetry during select weight bearing activities can produce relevant measures of knee impairment which may persist after total knee arthroplasty [2]. Traditional measurement during weight bearing activities requires a complex and often expensive motion capture system or sensor environment but low-cost wearable sensor systems have also been proposed for instrumenting patients. This study proposes a method of detecting and quantifying asymmetries during walking stages of the timed-up-and-go (TUG) test while instrumented with a wearable sensor system for ambulatory use.

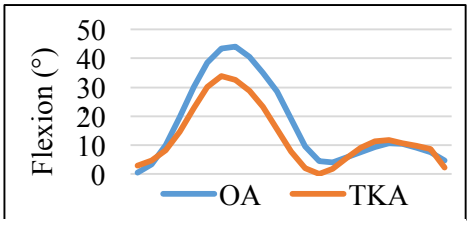

Figure 1: Average patient's steps, TKA knee and contralateral with severe OA. (flexion range asymmetry: 10.4°).

Methods: Representative patients (n=10) at one and two-year TKA follow-up appointments were asked to complete the TUG test while instrumented with wireless inertial sensors on the upper and lower segments of both legs. These tests were logged and the difference in limb segment orientation was used to compute flexion angles of the knee using a custom portable application [3]. Logged tests were segmented autonomously into five stages: sit-to-stand, walking-to-goal, turning-at-goal, walking-to-chair, and stand-to-sit using absolute limb orientations relative to the initial test start position (sitting in the chair). Times were recorded for each test stage independently. To detect walking asymmetries, steps were autonomously extracted from walking stages of the TUG test using a template matching technique. Prior to this study, a step template was found by combining 135 manually selected flexion patterns from previously recorded patient tests. The template was translated along recorded data sets and a Pearson correlation of over 0.8 was determined to be a step match. Since inertial sensors were mounted in pairs on each limb, steps from each leg could be analyzed independently. Flexion range, max flexion, max extension velocity, max flexion velocity, max extension acceleration, and max flexion acceleration were computed for each step, and a mean average of each statistic for each patient was computed.

Results: Patients took on average 3.9±1.9s walking 3m from a standing position and 4.1±1.6s after turning to walk back to the start position. Mean step flexion asymmetry across patients ranged 15.5° with a minimum of 2.3° and maximum of 17.7°. The mean difference in max flexion between limbs ranged 12.38° between patients. Extension and flexion velocity varied 105.0°/s and 150.0°/s and acceleration asymmetry ranged 1672.7°/s^2 and 1394.2°/s^2 respectively. An example of average between-limb step asymmetry for a single patient is depicted in Figure 1.

Conclusions: Segmentation successfully separated all TUG tests into all five stages confirmed with visual inspection of the test flexion data. For this study, step detection was accomplished using a fixed-length template. Consequently, all detected steps are the same length in number of samples (template length). Future work will employ machine learning techniques to better detect patient steps with a varying number of samples and possibly allow examination of step duration. In addition, further investigation and segmentation of detected steps could examine parameters in different gait cycle stages. Results obtained during this study have confirmed that flexion angle asymmetries during instrumented functional testing can be detected autonomously using a wearable sensor system. Further research will determine the significance of these results compared to a larger sample of knee OA patients. This measurement method can be deployed in many environments without any additional setup or facilities required. Autonomous generation of these statistics from instrumented functional testing permits clinicians to view results immediately following execution of the test, allowing individualized recommendations.

References: [1] K. Mills *et al.*, "Between-Limb kinematic asymmetry during gait in unilateral and bilateral mild to moderate knee osteoarthritis," Arch Phys Med Rehab, vol. 94, no. 11, pp. 2241–2247, 2013. [2] C. Christiansen and J. Stevens-Lapsley, "Weight-Bearing asymmetry in relation to measures of impairment and functional mobility for people with knee osteoarthritis," Arch Phys Med Rehab, vol. 91, no. 10, pp. 1524–1528, 2010. [3] R. Bloomfield *et al.,* "Proposal and Testing of a Minimal Calibration Knee Measurement System for Patients with Osteoarthritis," IEEE Trans. Biomed. Eng., Manuscript under revision.

Inside the TUG test: Wearable sensors identify new metrics related to function in post-TKR patients

Megan C Fennema[1,2,3], Riley A Bloomfield[1,2,4], Douglas D Naudie[2,5], James L Howard[2,5], Brent A Lanting[2,5], Matthew G Teeter[1,2,3,5]
[1]Robarts Research Institute; [2]Lawson Health Research Institute; Depts. of [3]Medical Biophysics, [4]Engineering, and [5]Surgery, Western University, London ON

INTRODUCTION: Wearable sensor technology has become an increasingly prevalent platform for digital monitoring. The diverse technology available presents an exciting opportunity for applications in the clinical world for more intelligent and individualized assessment of patients. The timed-up-and-go (TUG) test is a functional test that has been previously demonstrated to be an appropriate clinical tool to assess patient function after total knee replacement (TKR) [1]. However, the most common outcome metric for this test is solely the time to complete. With the use of novel wearable sensor technology, we can identify quantitative metrics of movement within the TUG test that may provide insight into the mechanics of patients post-TKR.

METHODS: Data were collected for n=33 TKR patients (male/female: 14/19) at 1- or 2-year post-operative appointments. Participants completed outcome questionnaires including: SF-12, WOMAC, KSS, and UCLA Activity Score. Subjects were affixed with four inertial measurement units, with one proximal and one distal to the knee joint on the anterior side of both legs. Subjects then underwent a TUG test in which they stood up from a chair, walked 3 meters to a measured goal, turned around, walked back, and sat back down in the chair. Knee flexion angles were calculated using orientation data from the proximal and distal sensors on each respective leg [2]. Time segments from the tasks within the TUG tests could be obtained from the sensor orientations (ie. total-test, sit-stand, walk-to-goal, turn-at-goal, walk-to-chair, stand-sit). GraphPad Prism 7.00 software was used to obtain Pearson correlation coefficients and P values.

RESULTS: Significant correlations were observed between sensor metrics and patient reported measures of physicality, where shorter durations were associated with improved outcome scores (**Table 1**). These correlations were found for total-test, walk-to-goal, turn-at-goal, and walk-to-chair time segments, but not for the sit-stand or stand-sit sensor time segments. Significant correlations were also observed between patient reported scores of satisfaction and sensor walk-to-goal and turn-at-goal time segments (R=-0.41, P=0.03; R=-0.40, P=0.04).

CONCLUSIONS: While the sensor-identified total-test, walk-to-goal, turn-at-goal, and walk-to-chair time segments all significantly correlated to patient reported measures of function, the sit-stand and stand-sit time segments did not. Greater correlations with reported functional outcomes were observed in the walk-to-goal and turn-at-goal time segments than the total TUG test time. This highlights the potential for more quantitative metrics derived from wearable sensors than the presently reported total TUG test time. Interestingly, the walk-to-goal and turn-at-goal segments also significantly correlated to patient reported satisfaction. Upon further investigation this may provide insight into the underlying mechanics of dissatisfied patients. While only temporal parameters were extracted from these quantitative TUG test data for this report, these novel sensor techniques may provide additional insight into patient function through the identification of gait- or flexion-based parameters. **Figure 1** below shows example knee flexion waveforms for two patients who reported very different functional scores. While the most notable difference in these two subjects is the total test time, this does not consider any individualized gait characteristics or strategies that the subjects may have employed to complete the test. In the future, we will determine the merit of gait- and flexion-based parameters derived from the quantitative TUG test to provide a more complete picture of function in TKR patients.

REFERENCES: [1] Poitras et al. *BMC Musculoskelet. Disord.* (2016). [2] Bloomfield et al. *IEEE Trans. Biomed. Eng.* (under revision).

***Table 1**: P Values and Pearson R coefficients for significant sensor temporal metrics vs. questionnaire scores of physicality*

	Total-test	*Sit-stand*	*Walk-to-goal*	*Turn-at-goal*	*Walk-to-chair*	*Stand-sit*
SF-12 Physical Score	R = -0.51, P = 0.005	ns	R = -0.55, P = 0.002	R = -0.63, P = 0.0003	R = -0.37, P = 0.05	ns
WOMAC Function Score	R = -0.52, P = 0.004	ns	R = -0.60, P = 0.001	R = -0.58, P = 0.001	R = -0.43, P = 0.02	ns
UCLA Activity Score	R = -0.50, P = 0.003	ns	R = -0.52, P = 0.002	R = -0.52, P = 0.002	R = -0.47, P = 0.006	ns
KSS Function Score	R = -0.49, P = 0.01	ns	R = -0.61, P = 0.001	R = -0.58, P = 0.002	R = -0.53, P = 0.006	ns

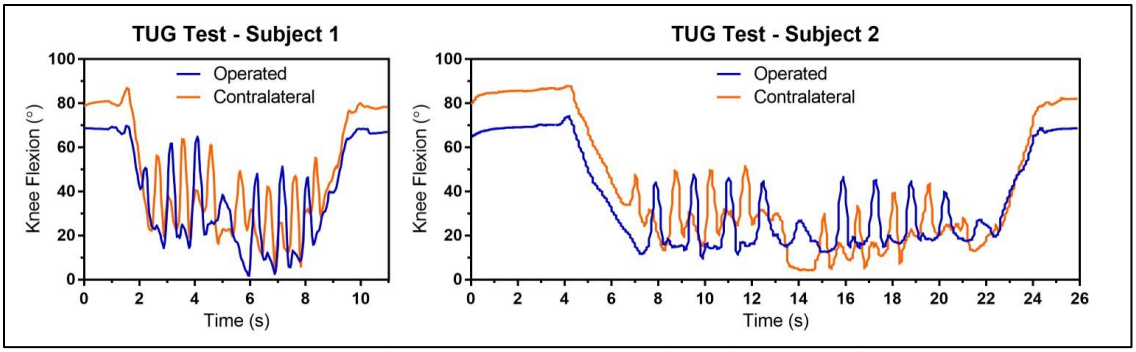

***Figure 1**: Example sensor flexion outputs during TUG test for two functionally different subjects*

Wearable sensors: Identifying quantitative metrics to better assess pre- and post-operative TKA patient functional status

H.A. Williams[1,2], R.A. Bloomfield[1,3], X. Yuan[1], J.L. Howard[4], B.A. Lanting[4], M.G. Teeter[1,2,4,5]
[1]Robarts Research Institute; [2]Department of Medical Biophysics; [3]Department of Electrical and Computer Engineering; [4]Department of Surgery, Western University, London, Canada; [5]Lawson Health Research Institute, London, Canada

Introduction: Total knee arthroplasty (TKA) is the current standard of care treatment for end-stage arthritis of the knee joint. Patient-reported questionnaires (PROMs) are used to evaluate physical function pre- and post-TKA as they are inexpensive, easy to administer, and can be completed from home [1]. Osteoarthritis is diagnosed through radiographic images, but time to surgery is largely dependent upon subjective complaints of pain and functional performance. While pre-operative functional performance is predictive of post-operative success, self-reported measures have a limited capacity to accurately represent a patient's functional capability [2]. The Timed-Up-And-Go (TUG) test is a reliable and simple physical performance measure for TKA patients which focuses solely on time to complete. Through the use of wearable sensors, TUG performance can be further quantified and used in conjunction with PROMs to accurately evaluate patient functional status. The objective of this prospective study is to examine correlations between new quantitative TUG test metrics and self-reported outcome measures in order to better assess the functional status of TKA patients both pre- and post-operatively.

Methods: Data was collected for n=24 patients at the pre-operative TKA time point (male/female: 13/11). Eleven of the 24 patients have returned to the clinic for their 2-week and 6-week post-TKA follow ups (male/female: 5/6). At the pre-operative and 6-week time point patients completed the following outcome questionnaires: 12-Item Short-Form Health Survey (SF-12), The Western Ontario and McMaster University Osteoarthritis Index (WOMAC), Knee Society Score (KSS), and the UCLA Activity Score. At 2-weeks post-op, patients completed the UCLA Activity Score. At all clinic visits the TUG test was completed. Patients were required to rise from a chair, walk 3 metres, turn around, and return to a seated position in the chair. Knee flexion angles were calculated through orientation data obtained from sensors placed distal and proximal to the knee joint on both the operative and non-operative limbs. Sensor data was segmented in order to obtain more detailed quantitative metrics of the TUG test.

Figure 1: Example of wearable sensor positioning

Results: Significant correlations were observed at the pre-operative time point between the WOMAC Joint Stiffness Score and total-test time (r=0.45, p=0.026), time-to-goal (r=0.5, p=0.013), turn-time (r=0.55, p=0.005), and stand-to-sit time (r=0.42, p=0.042). Additionally, significant correlations were observed between the WOMAC Function and TUG starting (r=0.54, p=0.007) and ending (r=0.463, p=0.023) knee flexion angle of the operative leg. WOMAC Total Score was significantly correlated with starting knee flexion angle (r=0.47, p=0.021) of the operative limb. Total-test time significantly decreased from the 2-week to 6-week time point (p=0.014). Mean difference between TUG total-test time pre-operatively to 6-weeks post-op was 1.99 seconds. While nonsignificant, a two second improvement on a pre-op mean time of 15.33 seconds could play a clinically significant role in reducing post-operative fall risk.

Conclusion: The WOMAC Joint Stiffness is a strong indicator of the ease of joint movement. Intuitively, those with stiffer joints would have an element of slowness associated with their movement and report higher WOMAC Joint Stiffness scores and longer TUG test times. Moreover, the significant correlation between pre-operative knee flexion angle and WOMAC Function score can be understood due to the dependence of the WOMAC Function score on knee range of motion (ROM). A moderate correlation between knee ROM and WOMAC Function before TKA amongst an older patient population has been reported, with stronger correlation for the younger members of the cohort [3]. Joint-specific scoring systems which accurately characterize joint flexibility allow for more accurate characterization of a patient's ability to utilize their prosthetic joint in activities of daily living. The observed increase in mean TUG performance time 2-weeks post-op is likely a result of the acute pain and swelling patients experience following surgery. As pain and swelling decreases, and muscle strength increases, functional performance improves and can be observed as an improvement in total test time [4]. Using this technology, we will be able to more accurately assess patient functional status both pre- and post- TKA. Looking forward, we hope to assess the correlations between TUG test performance spatial metrics and patient reported outcome measures.

References: [1] Mizner et al. J Arthroplasty (2011). [2] Swinkels A, Allian TJ. Physiother Theory Pract (2013). [3] Miner et al. J Arthroplasty (2003). [4] Petterson et al. Arthritis & Rheumatism (2009).

Index

O = Oral Presentation P = Poster Presentation

The Scientific and Organizing Committee for ImNO 2018 Annual Symposium would like to thank you for attending and acknowledge our supporting consortia and sponsors.

We invite you to attend the 17th ImNO Annual Symposium in March 2019 in London, Ontario.